Optimization and Implementation of Fiber Optic Sensors for Traffic Classification and Weigh-Motion Systems

(Phase 3) Final Report

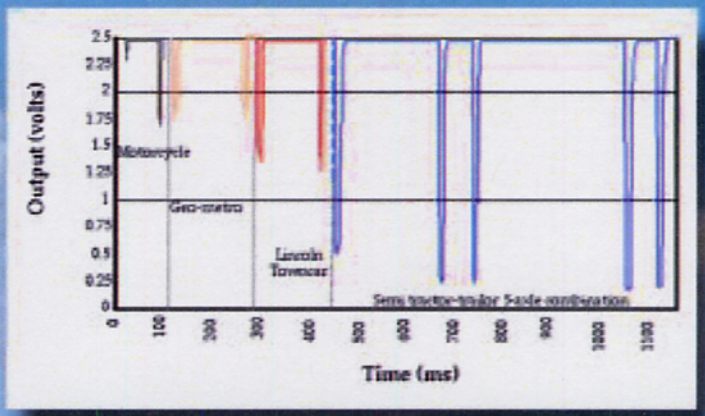

Florida Tech

Florida Institute of Technology
150 W. University Blvd.
Melbourne, Florida 32901-6975
(321) 674-7555 • www.fit.edu

September 25, 2000

Paul J. Cosentino, Ph.D., P.E., Principal Investigator
Barry G. Grossman, Ph.D., Co-Principal Investigator

Submitted to:
Administrator
Transportation Statistics Office
Florida Department of Transportation, Tallahassee, Florida 32399-0450
(800) 399-0450 • SunCom: 278-4111 • Fax: (850) 488-4752
WPA Item Number 0510726 • Contract Number BB-038 • State Job Number 99700-3383-119

Technical Report Documentation Page

1. Report No.	2. Government Accession No.	3. Recipient's Catalog No.
FL/DOT/RMC/06650-7754		

4. Title and Subtitle	5. Report Date
Optimization and Implementation of Fiber Optic Sensors for Traffic Classification and Weigh-in-Motion Systems (Phase 3)	October 2000
	6. Performing Organization Code
7. Author's	8. Performing Organization Report No.
P. J. Cosentino, B. G. Grossman	
9. Performing Organization Name and Address	10. Work Unit No. (TRAIS)
Florida Institute of Technology (321) 674-7555 Civil Engineering Program 150 West University Blvd. Melbourne, FL 32901-6975	11. Contract or Grant No. BB-038 WPI # 0510726
12. Sponsoring Agency Name and Address	13. Type of Report and Period Covered
Florida Department of Transportation 605 Suwannee Street Tallahassee, Florida 32399-0450	Final Report September 1998 to May 2000
	14. Sponsoring Agency Code *99700-7601-119*

15. Supplementary Notes

16. Abstract

This research included laboratory and field-testing that enabled optimizing and implementing fiber optic traffic classifying/ weigh-in-motion (WIM) sensors. The work was conducted for the Florida Department of Transportation.

Nearly 50 fiber-optic microbend sensors were placed in 5 fields sites in Brevard County Florida. Four of the sites were flexible pavements and the fifth was a rigid pavement. Sensors were 6-feet long and had fiber optic leads. They were encapsulated with relatively soft materials that were not temperature dependent. Sensors were successfully placed in both horizontal and vertical orientations. Two of the sites are FDOT telemetry sites used for vehicle classification, where sensors installed in December 1998 and September 1999 have been functioning under normal traffic conditions. Sensors installed in the access roads of two local plants with heavy truck traffic were used for signal evaluation.

Falling weight deflectometer tests were conducted on sensors installed in the rigid and flexible plant access roads to evaluate the accuracy of the fiber-optic sensor signals for weigh-in-motion applications. Sensors were installed using two geometries, two encapsulation materials in the two pavements. Of the variables investigated, the interaction between the encapsulant material and the sensor orientation had the greatest effect on fiber optic traffic sensor signal

Several laboratory sensor characterization tests have been developed. These tests were designed to produce data on the behavior under static and pneumatic loading conditions similar to those encountered in the pavement. Data was obtained on the load versus sensor light loss under both static and pneumatic loads. Data was also obtained on the load versus deflection versus light loss under pneumatic loads.

The load-deflection-light loss data was input into several finite element models that were used to study the sensor pavement interaction. According to these models when the sensors are placed in vertical grooves they have an optimal placement zone near the surface.

Scanning electron microscope photographs were taken of segments of the fiber-optic traffic sensors as the load varied. The microbend contact stresses were analyzed using Hertz' equation for the contact stresses between two cylindrical bodies. It was concluded that the fiber used for the sensor would fail at a compressive load of approximately 700 kPa (100 psi) and that Hertz' equation could be used to predict the length of the elliptical failure contact area.

These fiber optic traffic sensors are ready for implementation into traffic classification systems. The sensors are immune to electromagnetic interference, corrosion resistant and reliable. The installation procedure is simple; with the groove requiring only a masonry blade in a standard saw for cutting.

17. Key Words	18. Distribution Statement
Fiber Optic, Traffic Classification, Weigh-in-Motion, Sensors	Document is available to the U.S. public through the National Technical Information Service, Springfield, Virginia 22161

19. Security Classif. (of this report)	20. Security Classif. (of this page)	21. No of Pages	22. Price
Unclassified	Unclassified	221	

Form DOT 1700.7 (8-72)

Reproduction of completed page authorized

Executive Summary

This research included laboratory and field-testing that enabled optimizing and implementing fiber optic traffic classifying/ weigh-in-motion (WIM) sensors. The work was conducted for the Florida Department of Transportation.

Nearly 50 fiber-optic microbend sensors were placed in five fields sites in Brevard County, Florida. Four of the sites were flexible pavements and the fifth was a rigid pavement. Sensors were 6-feet long and had fiber optic leads. They were encapsulated with relatively soft materials that were not temperature dependent. Sensors were successfully placed in both horizontal and vertical orientations. Two of the sites are FDOT vehicle classification telemetry sites, where sensors installed in December 1998 and September 1999 have been functioning under normal traffic conditions. Due to this research these sites are not currently providing data for the Traffic Statistics Office. Sensors installed in the access roads of two local plants with heavy truck traffic were used for signal evaluation.

Falling weight deflectometer tests were conducted on sensors installed in the rigid and flexible plant access roads to evaluate the accuracy of the fiber-optic sensor signals for weigh-in-motion applications. Sensors were installed using two geometries; two encapsulation materials in the two pavements. Of the variables investigated, the interaction between the encapsulant material and the sensor orientation had the greatest effect on fiber optic traffic sensor signal

Several laboratory sensor characterization tests have been developed. These tests were designed to produce data on the behavior under static and pneumatic loading conditions

similar to those encountered in the pavement. Data was obtained on the load versus sensor light loss under both static and pneumatic loads. Data was also obtained on the load versus deflection versus light loss under pneumatic loads.

The load-deflection-light loss data was input into several finite element models that were used to study the sensor pavement interaction. According to these models, when the sensors are placed in vertical grooves they have an optimal placement zone near the surface.

Scanning electron microscope photographs were taken of segments of the fiber-optic traffic sensors as the load varied. The microbend contact stresses were analyzed using Hertz' equation for the contact stresses between two cylindrical bodies. It was concluded that the fiber used for the sensor would fail at a compressive load of approximately 700 kPa (100 psi) and that Hertz' equation could be used to predict the length of the elliptical failure contact area.

These fiber optic traffic sensors are ready for implementation into traffic classification systems. The sensors are immune to electromagnetic interference, and are corrosion resistant and reliable. The installation procedure is simple; the groove requires only a masonry blade in a standard saw for cutting.

Table of Contents

List of Figures

List of Photographs

List of Tables

Chapter 1

Introduction

1.1 Traffic Monitoring Through Classification and Weigh-in-Motion

Information on the type, size, weight, speed and density of traffic is required for the proper design and maintenance of highways. Sophisticated sensing systems are used to collect this data. They include sensors embedded in the pavement, computers with specialized software for recording and sending the data to a centralized location and solar panels to supply power to the systems. Highway engineers use this information to develop traffic and pavement management schemes for all state and federal highways. The management schemes are tied to federal budgets that require legislative approval.

Traffic monitoring may be divided into three different categories: traffic light detection, traffic counting, and traffic classification [Peek Traffic, Inc., 1992]. The U.S. Department of Transportation defines traffic classification as "the observation of highway vehicles and the subsequent sorting of the resulting data into a fixed set of categories [USDOT Traffic Monitoring Guide, 1992] (i.e. vehicle type, speed, headway, gap, length, and weight)."

Presently, the Florida Department of Transportation (FDOT) utilizes a combination of electromagnetic loops, piezoelectric sensors and data acquisition systems to obtain classification and weigh-in-motion (WIM) data (Figure 1.1). Reports from field personnel indicate that the piezoelectric sensors corrode, are destroyed by sharp objects being dragged

across them, and are affected by power surges and vehicles in adjacent lanes [Cosentino and Grossman, 1997]. When these factors are combined with the high truck tire pressures and extreme temperature and moisture variations, the sensor's working environment becomes severe [Cosentino and Grossman, 1994].

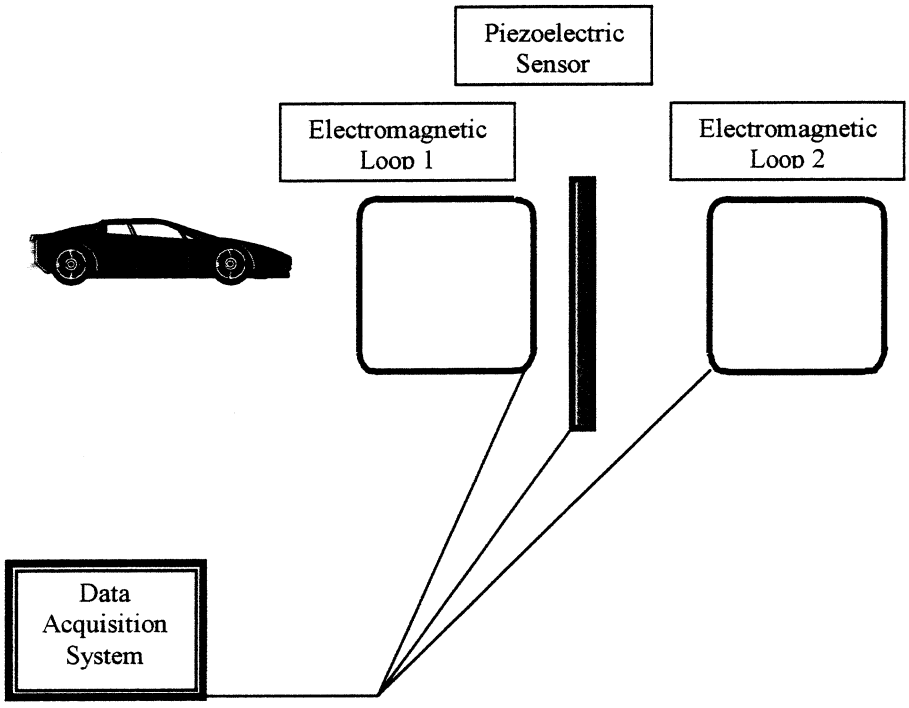

Figure 1.1 Typical Electromagnetic Loops and Piezoelectric Sensor Layout for Vehicle Classification and WIM [Taylor, 1995]

FDOT currently manages approximately 350 traffic classification sites. Traffic data, which includes axle counts, vehicle classes and axle weight, are telemeteried by modem to FDOT's Traffic Statistics coordination office in Tallahassee. These sites include thousands of sensors, which need to be maintained and replaced when failure occurs. Extremely high costs associated with sensor repair have prompted an interest within FDOT to find new techniques in traffic monitoring. To replace piezoelectric sensors, low-cost fiber optic, microbend sensor technologies have been explored.

1.2 Optical Fibers

An optical fiber consists of a glass or plastic core, a cladding layer that is also either glass or plastic, and an acrylic buffer layer (Figure 1.2). Plastic, Kevlar or metallic cables in turn protect these layers. Optical fibers are typically 250 or 500 μm thick, and without the protective cables are very fragile. They have been used extensively in communications because of their immunity to electrical surges.

All optical fibers have light rays focused into the core and cladding using either lasers or light emitting diodes (LED's). To make the fiber into a sensor, some outside perturbation must cause changes in light intensity. For example, a force that bends the fiber will cause light to refract out of the core, or a color change around the cladding will also cause light to refract differently within the fiber. The fiber then becomes a sensor when a reliable calibration curve is developed, correlating changes in light intensity with changes in the perturbation.

1.3 Advantages of Fiber Optic Sensors

Fiber optic sensors have important advantages over current techniques. Their small size makes them ideal for *in situ* monitoring, they are immune to corrosion and electromagnetic interference, they cannot cause fires, and multiple fiber optic sensors can be placed in series on one optical fiber (i.e., multiplexing) [Kim and Shaw, 1989], [O.S. Wolfbeis, 1989]. They are flexible, moisture insensitive, reliable and rugged. Another unique advantage is the chemical stability of the plastics and glasses that make up the optical fibers. Fiber sensors used in areas contaminated with hazardous compounds are immune to chemical breakdown. These advantages, along with the economics of fiber-optic sensors, have led to a significant research effort aimed at developing fiber-optic sensors [Ansari, 1993], [Cosentino and Grossman, 1994].

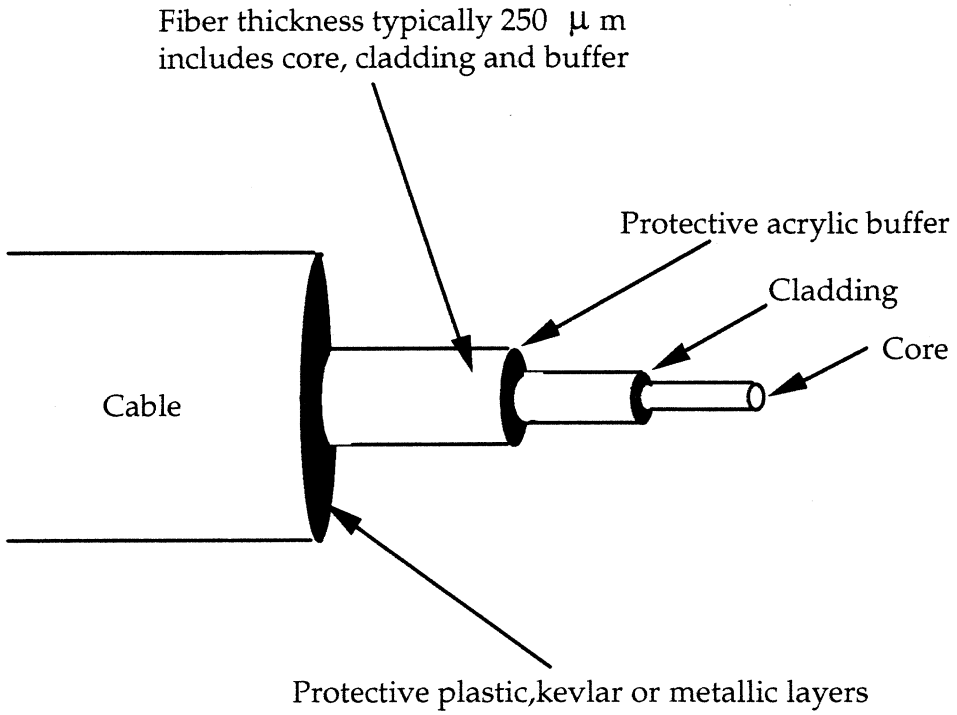

Figure 1.2 Typical Fiber Wrapped In Cabling Material [Grossman *et al.*, 1994].

1.4 Fiber Optic Traffic Sensors

Building upon the benefits of an optical fiber's characteristics, a Fiber Optic Traffic Sensor (FOTS) has been developed. This sensor is sealed from the environment, flexible, and installed below the roadway in an encapsulating material that prevents water intrusion and sensor damage. This report summarizes the results from phase III of a cooperative effort between FDOT and Florida Tech. The final results from phases I and II are summarized below. Phase I was a 12-month project and phase II an 18-month project.

1.4.1 Phase I Results

A rugged, reliable fiber optic sensor-based traffic classification system has been developed and successfully deployed below the pavement surface at three field sites in Florida. The sensors are immune to electromagnetic interference and do not provide a metallic conductive path to the electronic interface. This property minimizes the likelihood of lightning damage

to the electronic systems. This system incorporates fiber optic sensors that detect vehicle axles and provides an electronics interface to Peek's TrafiCOMP® III Model 241. Four generations of sensors were developed. Both laboratory and field-testing was conducted. The laboratory testing included load versus light intensity tests, cyclic strain tests, cyclic temperature tests and extreme compression tests. The Generation Three sensors proved to be very rugged, but had inconsistent properties due to the composite materials used. The Generation Four sensors were constructed of aluminum and had consistent light loss properties. These sensors were installed in pavement sections on the Florida Tech campus and on SR 507, Melbourne, Florida. Data from both sites showed accurate counts of vehicle axles and vehicle classifications. Over 250,000 axles were counted within one month of installation. These fiber optic sensors were compared to piezoelectric loop traffic classifiers installed in the same lane and gave comparable results. Additionally, the analog signal from the Generation Three and Four sensors could be directly correlated to axle weights, because both the magnitude and duration of the signal varied with load.

1.4.2 Phase II Results

Flexible fiber optic sensors were successfully deployed in both flexible and rigid pavements subjected to heavy truck traffic. Vehicles were classified and weighed in both pavement types. The sensors, manufactured in any desirable length are about 0.25 inches (7 mm) wide by 0.0625 inches (1.7 mm) thick. For vehicle classification and WIM, sensors are typically constructed six to seven feet (1.8 to 2.1 m) long. These sensors were epoxied into pavement grooves, covered with a flexible filler material and the leads were connected to a specially designed optical-electronic box. The optical-electronic interface contains LEDs that focus the light into the core of the optical fiber and photodetection equipment that converts light intensity to voltage. Voltage can then be used either for WIM or vehicle classification. Sharp, clear signals were obtained using the system developed, showing changes in light intensity for each single or dual tire assembly that passed over the sensor. The intensity changes vary according to the load on the tire and the vehicle speed. The fiber-optic system can be manufactured at a cost comparable to piezoelectric sensor systems. It is non-corrosive and unaffected by power surges.

Laboratory tests were developed to categorize the engineering behavior of the sensors and the materials used in sensor construction. A static compression test was developed that yielded load versus light intensity curves at any location along the length of the sensors. A second test was developed to categorize the variation in sensor response along its length. A motorized and weighted cart was guided along the sensor, while light intensity variations were monitored. This test yielded light intensity versus sensor position data that showed the repeatability of the signal versus location on the sensor. A new fiber failure test was developed to determine the breaking strength of the various fiber/mesh microbend combinations. An optical time domain reflectometer was used to determine the load at which the optical fiber would break during compression. The test results showed that Tefzel® mesh was preferred over polypropylene, nylon and polyester meshes because it yielded the highest fiber failure load.

Five sensors were placed in field sites subjected to controlled heavy truck repetitions. In January 1997, three sensors were placed in the Portland cement concrete entrance road of a local ready-mix concrete plant. About 1,000 trucks monthly use this road. To date over 8,000 trucks have passed over these sensors. In June 1997, two sensors were placed in the asphalt-concrete entrance road of a local hot-mix plant that rents space to a second ready-mix concrete company. Approximately 2,000 trucks monthly use this access road. These sensors experienced from 2,000 to 4,000 heavy trucks. As of August 21, 1997, three of the five sensors had failed. One sensor, placed 0.3 inches (9 mm) below the surface, in the rigid pavement failed in mid-August. The two remaining sensors were placed at depths of 0.5 (13 mm) and 0.85 (26 mm) below the surface. Both sensors placed in the asphalt-concrete pavement failed within a two-month period. Cause of the failures are under investigation, but may have resulted from the heavy loads, or poor field installation techniques.

1.4.3 Microbend Sensors

The Florida Institute of Technology's FOTS design was developed using the microbend theory. Microbend sensors function by periodically mechanically deforming the fiber so that the light guided into the core of the fiber is coupled, or passed, out of the core into the cladding layers (Figure 1.2) [Powers, 1993]. When a microbend sensor is deflected, the

intensity of the light exiting the sensor will be less than it was when the sensor was left free of external forces. The exiting light intensity, as the sensor is being deformed, is then compared to the intensity of the light when the sensor was free of stress, creating a percentage of light intensity remaining in the sensor.

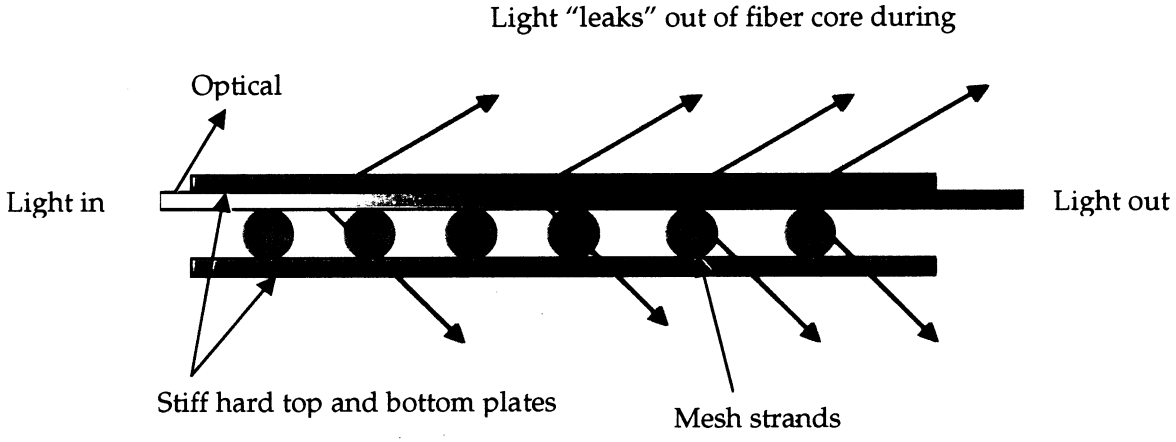

Figure 1.3 Light Losses Due to Single-Sided Deformation [Cosentino *et al*, 1994]

1.5 Objective

The project objective is to design, construct and deploy fiber optic traffic classifying and/or WIM sensors: 1) capable of detecting the presence and number of vehicle axles in the desired traffic lane for input into standard Federal Highway Administration (FHWA) classification software; 2) for substantial time in order to prove that this new technology is ready for implementation; and 3) with signals that can be used for WIM. The system will be immune to electromagnetic interference, expandable to detect traffic in multiple lanes, embedded below the pavement surface, and be deployable in both flexible and rigid pavements. It will also be economical and installed using procedures similar to those used with existing piezoelectric sensors.

Chapter 2

Background and Approach

2.1 Literature Search

The focus of the literature search was to be able to evaluate sensors' field performance and their associated field-testing programs. Information was obtained from various sources including manufacturer brochures and published reports.

2.1.1 Currently Used Weigh-In-Motion Sensors

Bending plates, load cells and piezoelectric sensors are the current types of WIM systems used by the U.S. DOT: WIM stations generally have similar components: loop detectors are used as on/off switches, axle detectors are used for vehicle speed detection, whereas the weighing devices differ between systems. Each has its benefits, weaknesses and ranges of error [ERES, 1987].

Bending plate WIM systems use plates with strain gauges bonded to the underside. Several of these plates are placed perpendicular to the direction of travel. As the vehicle passes over the bending plates, the sensors measure strain. The calibration system converts the strain into a static load using calibration parameters that account for known influence factors, such as pavement characteristics, vehicle speed, etc. [ERES, 1987].

Load cell WIM systems use a single load cell with two scales to detect total weight on the left and right side of the axle, simultaneously. As the vehicle passes over the load cell, the

independent scales record axle weight. The operating system sums the weights to obtain the total axle weight [ERES, 1987].

Piezoelectric WIM systems use piezoelectric sensors, usually encased in an epoxy-filled aluminum channel, placed across the traffic lane. As a vehicle travels across the sensor, pressure transferred to the sensor causes the piezoelectric material to produce an electrical charge. The WIM system records the resulting voltage change and converts the signal into a dynamic load. Again, calibration parameters and the dynamic weight are used to estimate the vehicle's static weight [ERES, 1987].

2.1.2 Evaluation of WIM Site Performance

According to the Federal Highway Administration, a weigh-in-motion site should detect axle loads for vehicle classification types I, II and III, within 20 percent, 30 percent and 15 percent error, respectively [ERES, 1987]. Depending on the type of sensor used for weight collection, the performance requirement may be difficult to achieve. For example, piezoelectric sensors perform at the very border of the acceptable level of error for detecting vehicle gross weight [ERES, 1987]. An inexpensive, more accurate alternative would be an improvement to the current piezoelectric sensor, which has a reported yearly failure rate of 20 percent [ERES, 1987].

Regarding the source of error for WIM stations, Cunagin suggested, "the random error is strongly influenced by the pavement profile" [USDOT & FHA, 1994]. Therefore, a more refined calibration procedure for WIM sensor systems could be developed to account for the pavement surface.

Fiber-optic traffic sensors could be used to replace the piezoelectric sensor if FOTS performance were calibrated to a high level of accuracy. Therefore, it would be essential to improve accuracy by identifying which factors (pavement type, encapsulant, etc.) have the greatest effect on FOTS signal generation. From this information a complex calibration procedure could be developed for a FOTS WIM system.

2.2 Lab and Field Testing Program Approach

To meet the project objectives, thorough laboratory and field-testing programs were performed in conjunction with a finite element analysis. The laboratory program included the development of static, pneumatic and cyclic compression tests on the sensor. It also included a scanning electron microscope (SEM) analysis of stress on the optical fiber. The analytical modeling was conducted using a series of finite element models of the sensors and the sensor embedded into pavement. The field program included installing sensors in five field sites in Brevard County. Sensors were exposed to heavy truck traffic and tested for WIM usage using Falling Weight Deflectometer (FWD) testing.

2.2.1 Laboratory Program

Developing a comprehensive laboratory-testing program for the FOTS required understanding the variables that controlled the sensors' laboratory and field response. The main variables include load, temperature, pavement materials, sensor components, sensor orientation and sensor encapsulation materials.

- Tire pressures can range from 70 to over 700 kPa (10 to over 100 psi) making it difficult to manufacture a microbend sensor with a linear response over this large range.
- Pavement temperatures vary over vary large ranges [Yoder and Witzak, 1975]. As the pavement stiffens during periods of low temperature, and softens during period of high temperatures, the signals from the FOTS may be affected.
- The pavement's materials properties vary both within a site and between sites. Traffic classification and WIM systems must be installed in both rigid and flexible pavements.
- There are numerous encapsulating materials available with long and short set times (i.e. minutes to days), low and high stiffness' and with elastic moduli from 500 to over 100,000 psi (3,500 to 700,000 kPa). They can be complicated to mix and hazardous to handle.

To cause the microbend effects, an infinite combination of fibers and deformers could be used. Throughout the duration of the Phase I and II research, sensor components have been refined to materials that are relatively insensitive to the temperature changes typically found in the pavements. Therefore, during this phase only minor changes to the sensor components were made. It was found that the heat shrink used to protect and seal the sensor was producing non-uniform sensor responses along the sensors length. This material was subsequently replaced by fiber-embedded strapping tape. Figure 2.1 shows the components of the current FOTS.

Sensors can be placed either horizontally or vertically in the pavement as shown in Figure 2.2. Both configurations yield useful signals, although the stresses imparted to the sensors vary for each scenario.

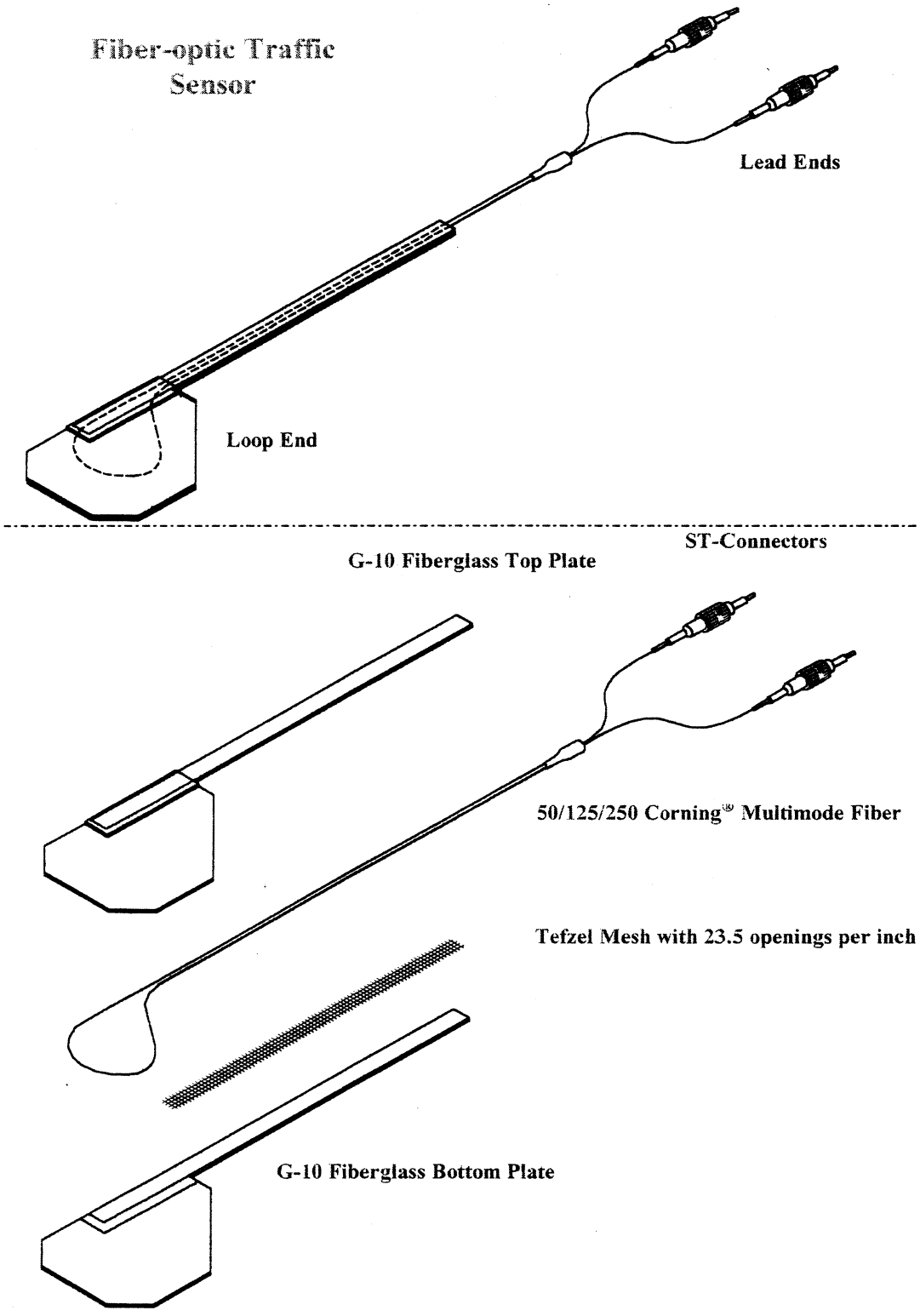

Figure 2.1 FOTS Components [Eckroth, 1999]

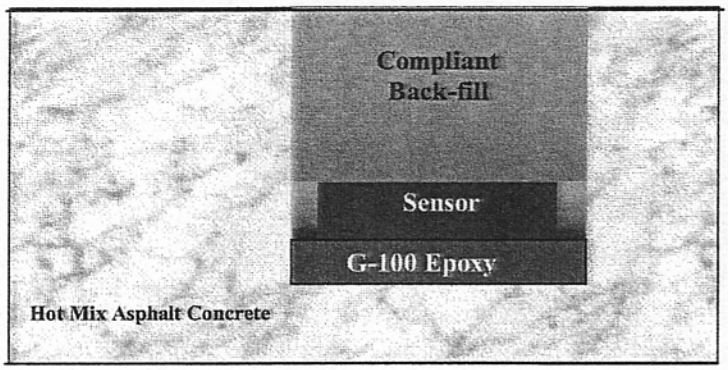

Horizontal Sensor Placement in HMA

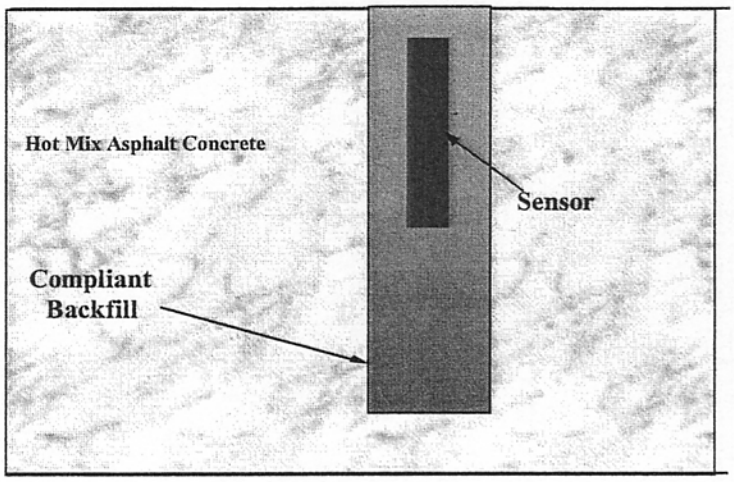

Vertical Sensor Placement in HMA

Figure 2.2 FOTS Placement Options [Eckroth, 1999]

2.2.1.1 Sensor Testing Methods

Static and pneumatic compression tests were developed to evaluate sensors. The static-compression test enabled sensors of varying lengths to be tested at loads up to 227 kg (500 lbs). Statically, sensors were characterized using their load at which 50 percent of the propagating light was lost. This value was determined by measuring the force applied by a rigid platen over a 6.45 cm^2 (1in^2) area, over the length of the sensor. Figure 2.3 shows the static testing equipment.

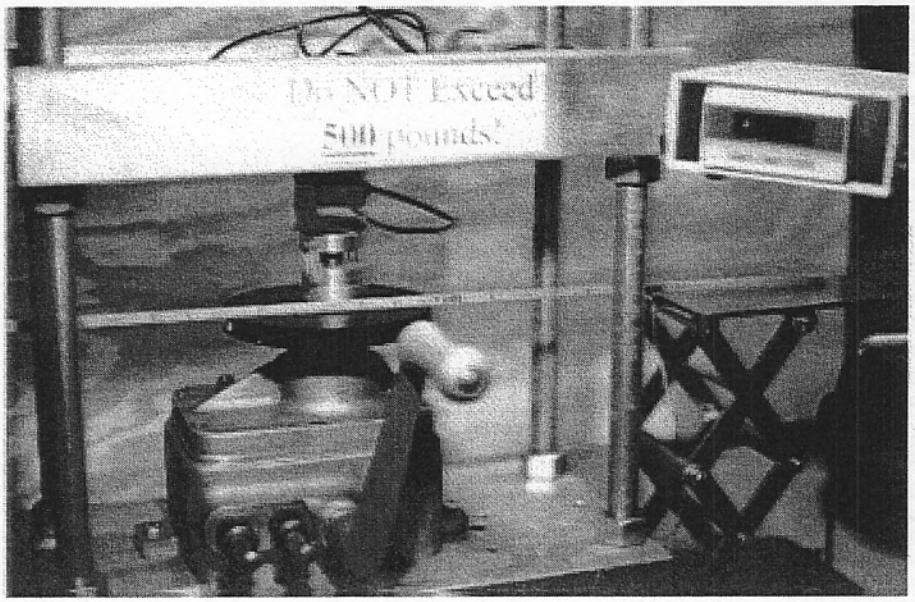

Figure 2.3 Static Compression Testing

The pneumatic testing chamber was developed to allow sensors up to 60.9 cm (2 ft) long to be pressurized using an impulse load (Figure 2.4). This clear PVC allows for a maximum pressure of 700 kPa (100 psi) to be applied to the sensor. Placing the sensor in a pressure vessel and applying air pressure allowed for pneumatic sensor characterization. The pneumatic characterization allowed for a complete pressure versus light intensity curve to be developed. This information was used to determine the sensors responses under free and encapsulated conditions.

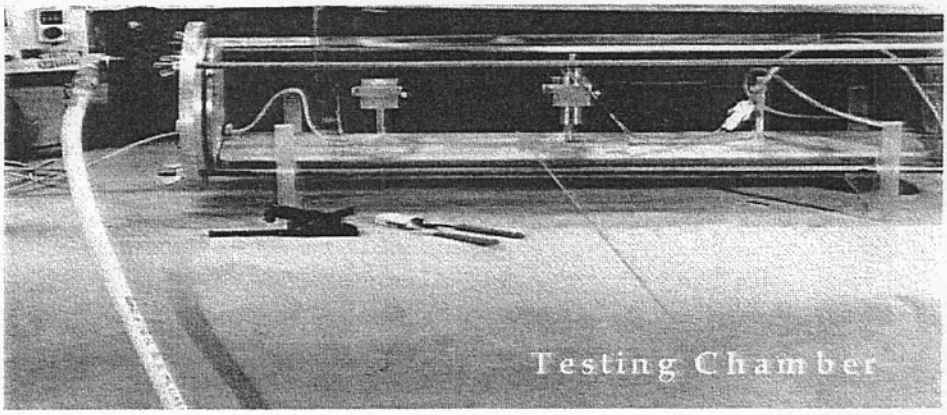

Figure 2.4 Pneumatic Testing Chamber [Eckroth, 1999]

2.2.1.2 Interface Electronics

To convert the microbends' sensor light intensity signal to a voltage for the data acquisition systems, an opto-electronic interface was developed. The interface electronics needed to be stable with temperature and sturdy enough to withstand the rigors of field usage. Several versions of the system were developed. One system allowed two fiber inputs (Figure 2.5) and a second allowed up to four complete sensor inputs (Figure 2.6). This device was constructed from off-the-shelf electronic components and was used to acquire data both in the lab and field.

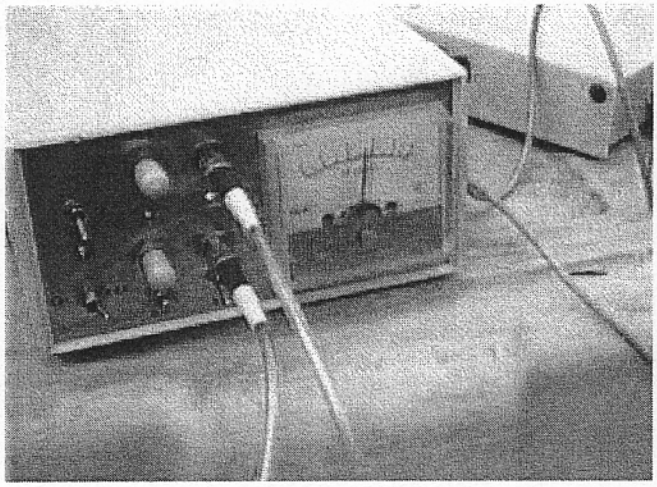

Figure 2.5 Two Channel Opto-Electronics Box

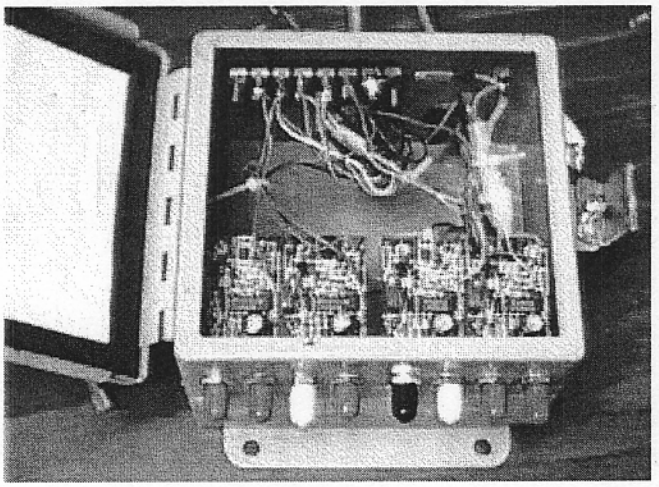

Figure 2.6 Four Channel Opto-Electronics Box [Call, 2000]

2.2.1.3 Sensor Static Compression Calibration Program

In order to categorize the traffic sensors linear and non-linear response ranges, a calibration process was established. Sensors of varying lengths were tested using the static compression testing system; by loading them until 100 percent light loss was recorded. This testing was

used to compare sensors being used in both the lab and field. Sensors were placed between the two platens of the compression machine and loaded using a hand crank. A typical load versus light loss is shown in Figure 2.7. This curve has a slight "S-shape" with a linear portion in its central portion.

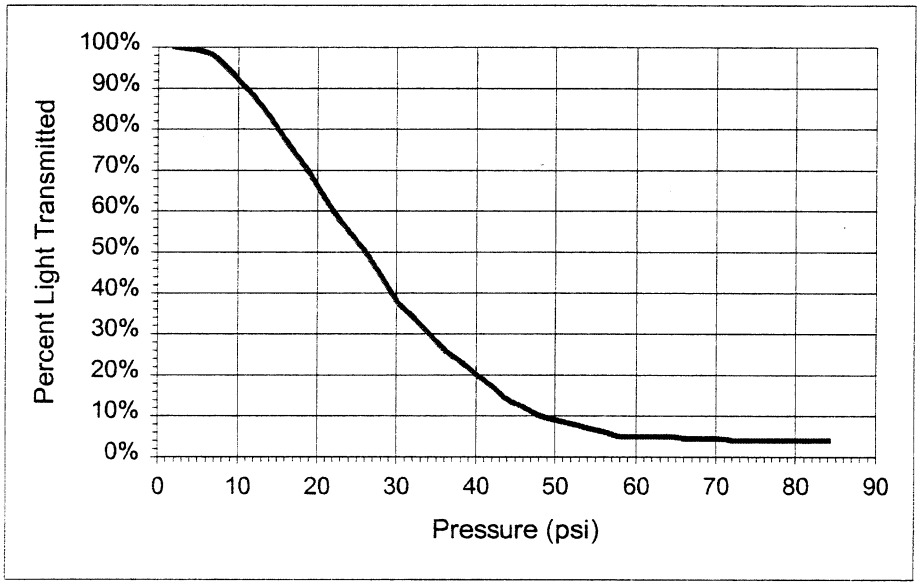

Figure 2.7 Typical FOTS Static Calibration Curve

2.2.1.4 Analysis of the Stresses Imparted to the Optical Fiber

The failure modes of the Corning ® optical fibers used in the microbending could result from excessive creep, shear, tensile, torsion or compressive stresses. Castro [1997] evaluated the effects various materials had on the sensor and concluded that the softest mesh material Tefzel® would produce the most efficient sensor. The Tefzel® mesh is a woven plastic with a modulus of elasticity of $2758*10^6$ Pa (400,000 psi). There are about 7.87 openings per centimeter (20 per inch) used to squeeze light out of the sensor during loading. Taylor's work (1996) indicated that the microbend sensor with Corning® 50/125/250 acrylate coated fiber functions best with a mesh containing about 7.87 openings per centimeter (20 per inch).

The Corning® fiber has acrylate coatings that protect the glass core from excessive stresses. The outer acrylate coating is relatively hard with an elastic modulus of 84,000 psi (590,000 kPa). However, the inner acrylate coating is soft, with an elastic modulus of 246 psi, (1720 kPa) and acts as a cushion absorbing stresses before they reach the glass core. The elastic modulus for all of the layers in the fiber is given in Figure 2.8. It was assumed that the glass core in the fiber would fracture in a relatively short time once the outer acrylate coating had cracked. Therefore, a testing program was developed to enable visual inspection of the acrylate after it was subjected to a series of increasing loads.

In 1895, Hertz developed a method of estimating the maximum contact stresses between two perpendicular cylinders [Roark, 1943]. It was assumed that the two cylinders were equivalent to the Tefzel® mesh contacting the Corning® fiber. Using this model, Castro [1997] predicted the stresses experienced by a fiber in a FOTS. A conservative prediction occurs if it is assumed that the glass in the fiber takes all the stresses.

2.2.1.4.1a Objective

This study had two main objectives. First, to determine the maximum load allowed by the acrylate coat of the optical fiber before failure. Secondly, to conclude if the theoretical Hertz equation to predict the stress between two perpendicular cylinders could be used to model the fiber-mesh contact.

2.2.1.4.1b Approach

To evaluate the fibers structural capacity during microbending, a laboratory test was developed to estimate the failure load of the acrylate layer of the fiber. The sensor was compressed at different loads, and the fiber was examined for cracks with SEM photos. Hertz' theoretical model was then used to determine if the failure load was realistic.

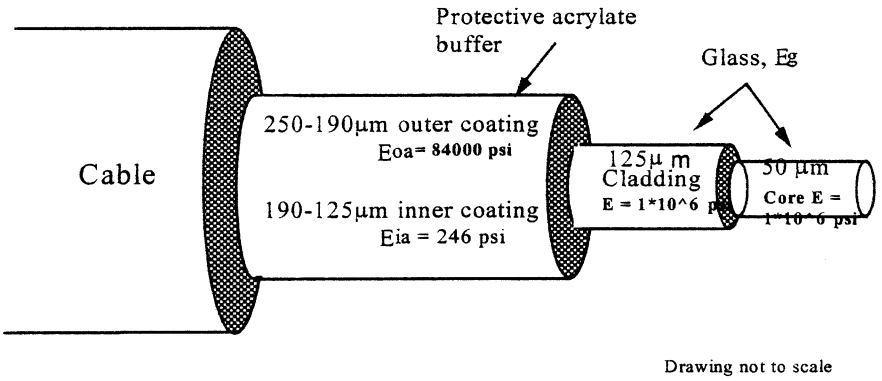

Figure 2.8 Corning® Fiber with Dimensions and Elastic Properties

Figure 2.9 shows the optical fiber contacting the woven mesh. This SEM photo was taken after a portion of a sensor was constructed, loaded and disassembled. Spray adhesive was used during assembly to keep the various layers properly aligned. It can be seen in the photograph as particulate on the fiber and mesh.

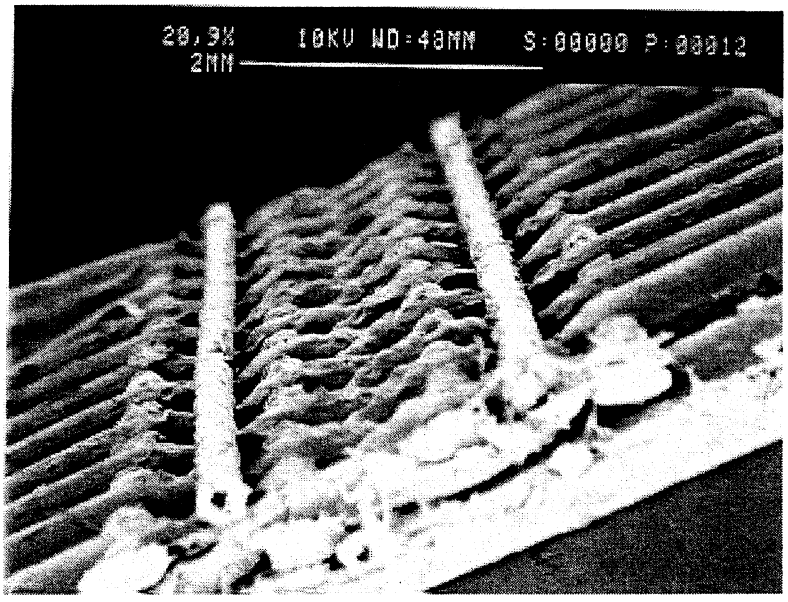

Figure 2.9: SEM View Showing Two Optical Fibers on Top of Tefzel® Mesh.

2.2.1.4.2 Optical Description and Properties

Corning's optical fiber is composed of four main layers: an inner and outer acrylate coat, a glass cladding and a glass core (Figure 2.8). A SEM photograph, Figure 2.10, illustrates the glass core with the buffer and cladding. This fiber has a 50 μm (0.12 mil) diameter glass core, a 125 μm (0.32 mil) glass cladding and a 250 μm (0.64 mil) outer acrylate coating. Figure 2.8 also indicates that an inner acrylate coating with a diameter of 120 μm (0.30 mil) is present.

Both the core and cladding glass components have elastic moduli of $6.89*10^9$ Pa (1,000,000 psi) (Figure 2.8). The acrylate coatings, with much lower moduli ($5.79*10^8$ (84,000 psi) and $1.69*10^6$ (246 psi)), absorb all the energy and protect the glass. The modulus of elasticity of the inner acrylate coating is very small because its role is to stop all the energy transfer when the fiber is loaded (Figure 2.8).

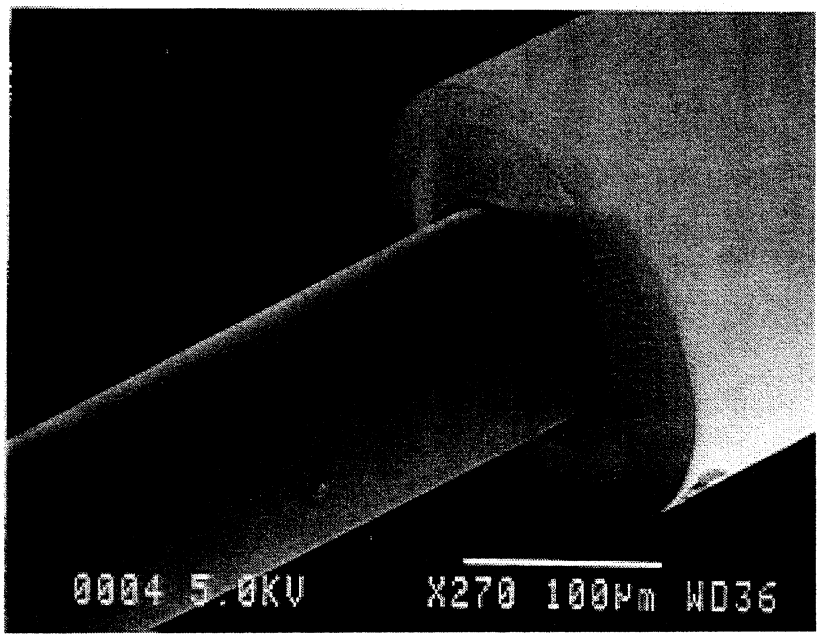

Figure 2.10: SEM Photo Depicting Fiber Core Surrounded by the Cladding and Buffer Layers.

2.2.1.4.3 Test Description

The testing apparatus, a standard compression-testing machine, is depicted in Figure 2.11. An 18-inch sensor was constructed and prepared for the experiment by defining the location along the surface on which each load would be applied (Figure 2.12). For each applied loading point, two specimens were selected to check for repeatability of the results.

The 2224 N (500 lb) load cell on the compression machine had an accuracy of $\pm$ 4.48 N ($\pm$1 lb), however, controlling the load using the hand operated crank resulted in an accuracy of about $\pm$ 44.8 N ($\pm$ 10 lb). Nine different 112 N (25 lb) load increments from 896 N (200 lb) to 1680 N (375 lb) were applied to the sensor at desired locations. The rectangular upper plate, 3.1 cm long (1.22 in) and 1.04 cm width (0.41in) is depicted in Figure 2.13.

After the loads were applied, the sensor was removed from the testing machine and small specimens were cut out of the sensor. Each load increment produced two fiber samples, since there is both an input and output fiber in the sensor (Figure 2.2). The mesh and the fiber were carefully removed ensuring that only the damage from the test-load would be analyzed. Samples were transported to the SEM where photographs were developed. Each photo was labeled with its corresponding load, and all 18 pieces of fiber were studied visually to evaluate the damage.

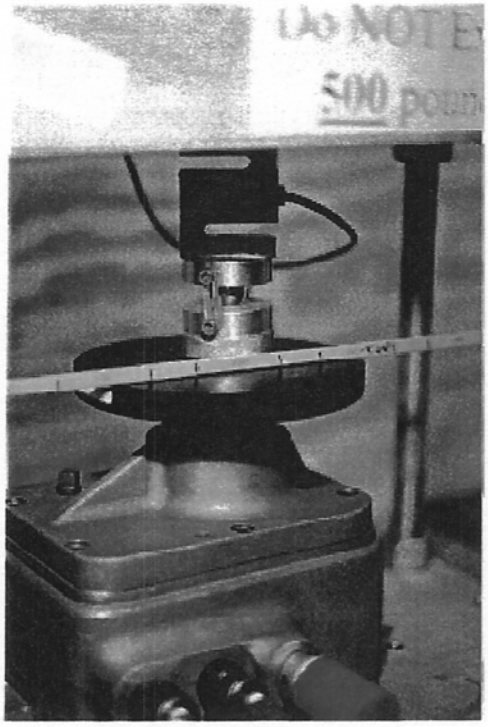

Figure 2.11: Compression Machine with 45.72 cm (18 inch) Sensor Being Prepared for Testing.

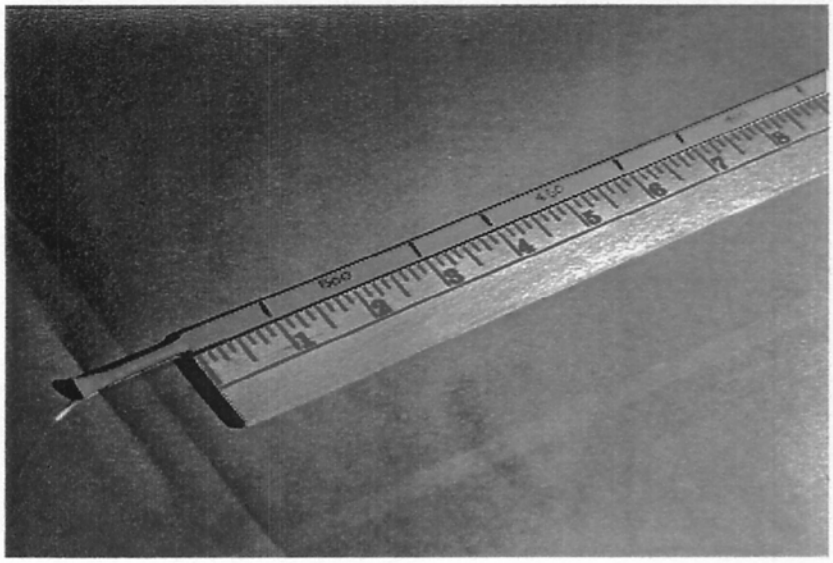

Figure 2.12: Sensor Prepared for the Testing.

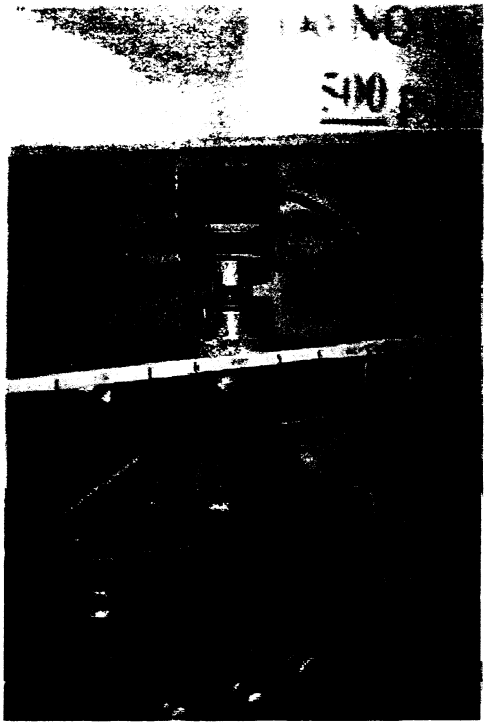

Figure 2.11: Compression Machine with 45.72 cm (18 inch) Sensor Being Prepared for Testing.

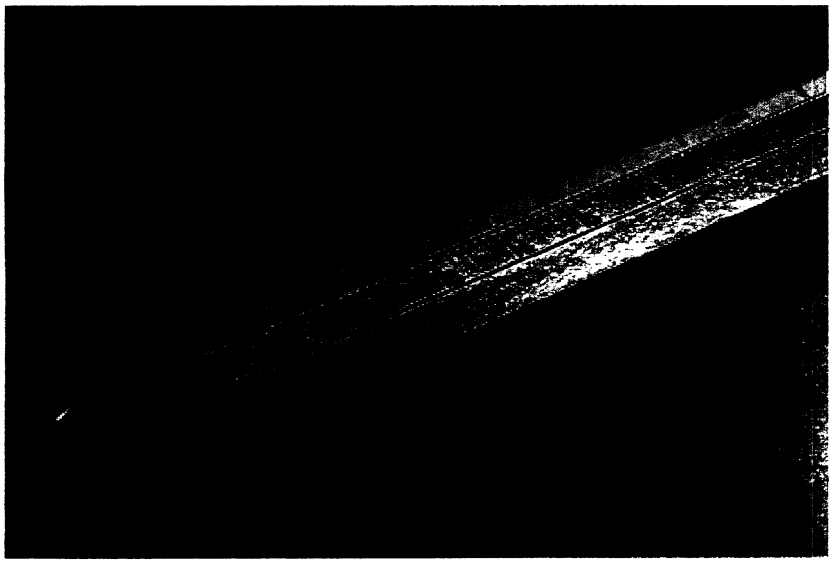

Figure 2.12: Sensor Prepared for the Testing.

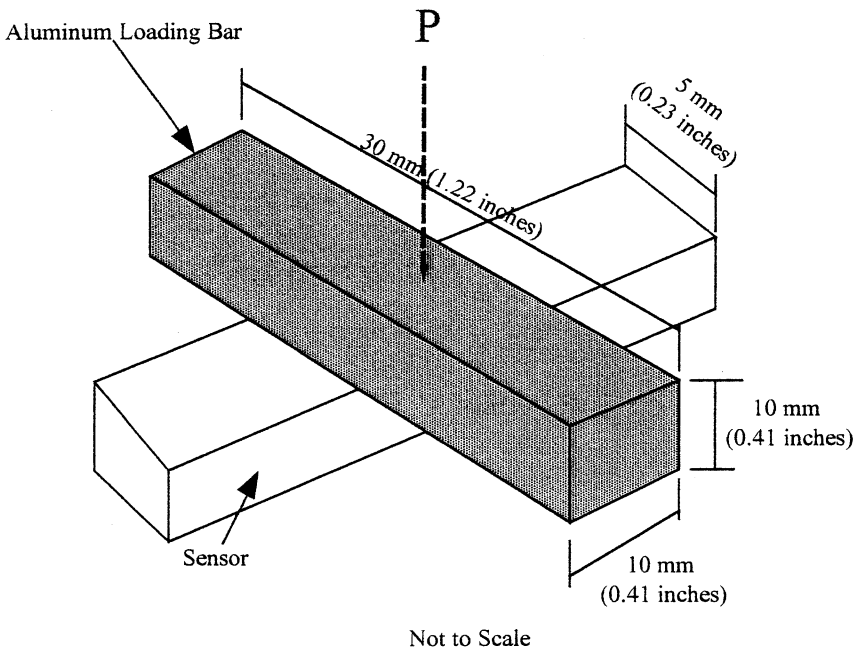

Figure 2.13: Schematic of the Aluminum Bar and Sensor.

2.2.1.5 Encapsulating Materials Testing Program

A laboratory-testing scheme was developed to evaluate candidate-encapsulating materials. The literature indicated that a large number of materials exist in the category of sealants. Based on the findings from Phases I and II, the list of available materials was narrowed to six. The encapsulants needed to be unaffected by temperature, easy to work with and pliable enough to allow the sensor to function properly.

An encapsulant was used to encase the fiber-optic traffic sensor in the pavement, thereby increasing sensitivity and improving the performance lifetime. The encapsulation material had to be strong enough to prevent damage to the sensor, yet soft enough to allow external tire pressures to compress the sensor. In addition, factors such as temperature, number of loading cycles, and decay should have limited affect on the encapsulation material's modulus of elasticity.

In order to select the best encapsulants, information was gathered from three sources: Center for Transportation Research (CTR), encapsulant research performed by Florida Institute of Technology researchers, and evaluations of Florida Tech FOTS telemetry sites. Laboratory testing by Criss produced an understanding of what range of values were desirable for a modulus of elasticity [1998]. Until such time, Florida Tech researchers selected many encapsulants from literature searches and field trials.

2.2.1.5.a CTR Review of Encapsulants

A research report from the CTR provided a summary of various bonding materials currently in use for installing piezoelectric sensors, plus a complete materials testing program [Carrasquillo, 1994]. Nine materials were tested for properties such as compressive and flexural strength, thermal expansion, set time, viscosity, etc. In addition, the materials were evaluated on their ease-of-use in the field. Encapsulants that have excellent material properties, but were extremely difficult to use in the field, did not rank well in the overall

evaluation. Testing performed during this investigation resulted in the list of candidate materials shown in Table 2.1.

Table 2.1 Study of Initial Candidates for Encapsulation Materials [Criss, 1998]

	Source	Elastic Modulus
Sikadur 22 Lo-Modulus	Sika (Tucker, GA)	42,000 kPa (6,000 psi)
Sikadur 35	Sika (Tucker, GA)	82,600 kPa (11,800 psi)
Type III Steep Roofing Asphalt	Gulfside Supply Co. (Melbourne, FL)	1,575 kPa (225 psi)
Slygard 170 (DC-170-2) Silicon Elastomer	Dow Corning (Essex Brunnel, Orlando, FL)	2,212 kPa (316 psi)
Sylastic M RTV Silicon Rubber	Dow Corning (Essex Brunnel, Orlando, FL)	3,500 kPa (500 psi)
Flexane 80 W/Flexadd (A-48)	Devcon (Grainer Co., Melbourne, FL)	3,150 kPa (450 psi)
Flexane 80 W/Flexadd (A-48)	Devcon (Grainer Co., Melbourne, FL)	5,600 kPa (800 psi)
Flexane 94 Two-Part Urethane	Devcon (Grainer Co., Melbourne, FL)	15,400 kPa (2,200 psi)
Flexane 94 Two-Part Urethane	Devcon (Grainer Co., Melbourne, FL)	70,000 kPa (10,000 psi)

2.2.1.5.b Objective

The objective of the encapsulation research was to experimentally determine a relationship between the modulus of elasticity of different sensor encapsulating materials and the percentage of applied dynamic impulse stress transmitted to sensors placed in the bottom of rigid channels. This program was designed to simulate conditions the sensors would experience, if they were placed in the pavement at various depths with various encapsulation materials.

2.2.1.5.c Approach

To achieve this objective, a laboratory-testing scheme was developed, enabling six candidate-encapsulating materials and their effects on the FOTS output, to be evaluated. Sensors were tested pneumatically in a clear PVC testing chamber (Figure 2.4) [Eckroth, 1998]. The six materials were evaluated by comparing signals from bare sensors to signals

from the same sensors after encapsulation. Data, in the form of light intensity versus pressure, was used to determine the percent stress transferred through the encapsulating material to the sensor. Encapsulation materials tests were conducted with sensors placed at three depths, 1.27 cm, 2.54 cm, and 3.81 cm (0.5 in, 1.0 in, and 1.5 in) in an aluminum channel (Figure 2.14) [Criss, 1998]. By selecting aluminum, which has an elastic modulus of 70,000,000 kPa (10,000,000 psi) as the medium for sensor placement, it was assumed that only the candidate-encapsulating materials would deform during pressurization.

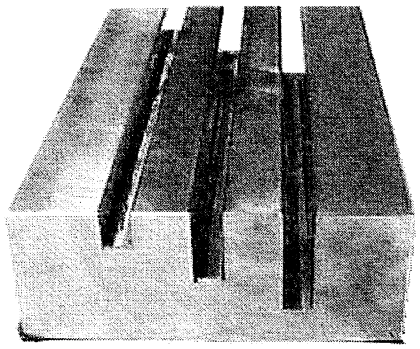

Figure 2.14 Aluminum Block for Pneumatic Chamber Testing [Criss, 1998]

2.2.1.6 Sensor Pneumatic Compression and Cyclic Testing

The pneumatic testing chamber was developed to allow sensors up to 60.9 cm (2 ft) long to be pressurized using an impulse load (Figure 2.4). This clear PVC allows for a maximum pressure of 700 kPa (100 psi) to be applied to the sensor. Placing the sensor in a pressure vessel and applying air pressure allowed for pneumatic sensor characterization. Linear Variable Differential Transducers (LVDT's) could be placed inside the chamber and on the sensors to measure deflections. The pneumatic characterization allowed for a complete pressure versus light intensity curve to be developed. Cyclic pressures up to 60 psi could be applied pneumatically every 30 seconds with the duration of loading during a cycle being about 1.2 seconds. This information was used to determine the sensors response under free and encapsulated conditions.

2.2.2 Analytical Program

To increase our understanding of the FOTS' behavior, a finite element analysis was performed to simulate the sensor being installed vertically in a flexible pavement. After the proposed pavement was modeled, the sensor alone was modeled, and then the FOTS embedded into a flexible pavement was modeled. The models were based on static loadings of a linear elastic system.

2.2.3 Field Program

The field analysis program included both classification and weigh-in-motion. Sensors were installed in five sites and monitored over time. Several modifications were made to the sensors, the encapsulants and the installation procedures during the research.

2.2.3.1 Site Selection

The sites chosen included both flexible and rigid pavements with light and heavy truck traffic. They were located within approximately 20 minutes of the Florida Tech campus.

Site 1 was the access road for APAC MacAsphalt Division, Melbourne, Florida, where over 20 sensors have been installed and monitored throughout the project. The plant is located about 20 minutes north of the campus off U.S. 1.

Site 2 was located on SR 507, Babcock Street, at FDOT Telemetry Site # 345, where six sensors were installed in the four-lane asphalt pavement surface course on July 27, 1998. Four of the sensors were placed in series with existing loop detectors and two were placed in the northbound slow lane to evaluate encapsulants.

Site 3 was located on the two-lane portion of A1A, south of Melbourne Beach at telemetry site # 284, where 10 sensors were installed on December 7, 1998. This site was also an asphaltic pavement. Eight of the sensors were installed to study sensor response, groove geometry effects, encapsulation material effects, while the other two sensors were installed as part of the existing traffic classification system.

Site 4 was again located on SR 507, Babcock Street, at FDOT Telemetry Site # 345, where four sensors were installed in the 4-lane asphalt pavement surface course on September 2, 1999. These sensors were installed to improve the site classification and to study encapsulants.

Site 5 was the access road for CSR Rinker's Palm Bay Ready Mix Concrete facility. This road is constructed from concrete and allowed the sensors response in rigid pavement to be compared to flexible pavements.

2.2.3.2 Sensor Construction

In general, the sites contained 6-foot-long sensors attached to optical fiber leads that ended in the roadside cabinets. The leads were connected to the opto-electronics box with output cables connected either to a data acquisition system or a traffic classifier.

2.2.3.3 Sensor Characterizations

Prior to installation, sensors characteristics were evaluated in the lab by testing them along their 6-foot lengths to determine the load required to cause a 50 percent light loss. This value was used as a benchmark to evaluate whether the sensors were constructed properly.

2.2.3.4 Installation Procedure

Field installation required a preliminary site visit so that sensor locations and lead lengths could be predetermined. Once the appropriate layout was established, sensor construction was started.

2.2.3.5 Field Monitoring

Once the initial installation was complete, data was recorded to ensure all the sensors were functional. Data was recorded either using compact (Class 2) vehicles or with nondestructive testing equipment such as the FWD or Dynaflect. The field monitoring continued until the end of the project.

Chapter 3

Laboratory Program Results

Sensors were constructed in lengths from 8-inches to 6-feet, depending upon their use. Sensors used in the lab were typically 8-inches, while the field sensors had to be 6-feet in length. The major differences between the construction of the short and long sensors was the loop ends. For the 8-inch sensors the fiber at the loop ends was left uncovered, while for the 6-foot sensors the loop was encased in G-10 fiberglass.

3.1 Sensor Materials

All materials selected for the FOTS were low cost and readily available. The fiber chosen was the acrylate-coated optical fiber manufactured by Corning® with core, cladding and buffer diameters of 50 μm, 125 μm, and 250 μm, respectively (Figure 1.2) [Taylor, 1995]. During Phase II of this research, testing demonstrated this fiber possessed the desired sensitivity when used as a single-sided microbending sensor [Cosentino, Grossman, 1994].

The microbending mesh was chosen to match the optimum microbending period of the fiber. This period causes the largest amount of light to be refracted out of the core during microbending, resulting in a very sensitive configuration. Again during Phase II, the optimum period of the Corning® fiber was experimentally determined to be 1.06 mm or 24 microbends per inch. Tefzel® a woven fiber mesh with 23.5 strands per inch was chosen from a group of several soft plastic mesh candidates, because it was the closest to the ideal 24 of all the candidate meshes. Testing also proved that Tefzel® provided the most reproducible sensitivity of the candidate materials [Cosentino, Grossman, 1994].

To protect the mesh, 0.64 mm (0.025 in) thick G-10 flame-rated fiberglass was used. This material also had sufficient stiffness to allow the desired sensor response.

3.2 Laboratory Sensor Construction

To construct the 8-inch laboratory sensors, a single layer of mesh and the optical fiber were sandwiched between two layers of 0.64 mm (0.025 in) thick by 7.62 mm (0.3 in) wide pieces of G-10 flame-rated fiberglass (Figure 2.1) [Eckroth, 1999]. These materials were temporarily held together using a spray adhesive and a 6.35 mm (0.25 in) strip of epoxy at either end. Once the adhesive and epoxy dried, the sensor was sealed using 2.54 mm (1 in) wide nylon reinforced cellophane packing tape. Once the sensor was longitudinally taped, the looped end of the fiber was sealed with a five-minute epoxy. The lead-in, lead-out end of the sensor was sealed using a layer of heat shrink with a light application of epoxy to join the sensor to the protective cable (Figure 2.1).

3.3 Field Sensor Construction

For each sensor, two 1.8 m (6 ft) long strips, of 7.6 mm (0.3 in.) wide G-10 fiberglass were cut, serving as the plates for the body of the sensor. G-10 fiberglass ends were cut for the loop ends/flags. Figure 3.1 shows the protective flag for a horizontal sensor, without the top cover plate.

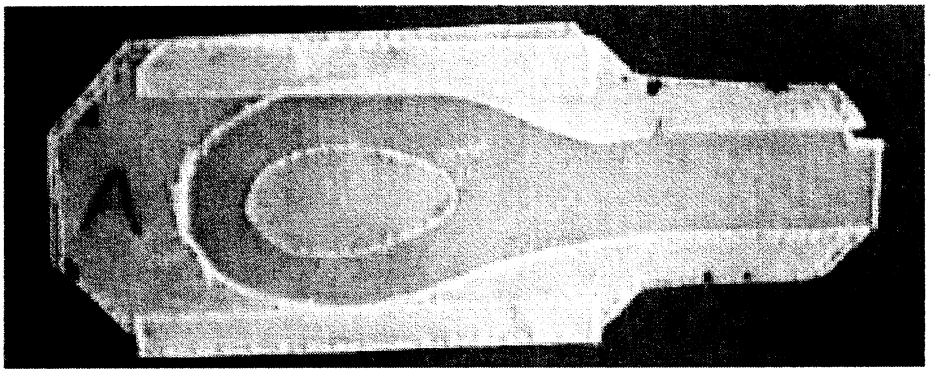

Figure 3.1 Protective Loop End Constructed of G-10 for Horizontal Sensor [Call, 00]

A 5-minute epoxy was used to construct the flags and affix them to the end of the fiberglass plates. A strip of Tefzel® mesh the width of the G-10 plate was cut, containing five rows of microbenders, termed 'tracks'. The mesh was adhered to the bottom G-10 plate using spray adhesive taking care to keep mesh rows in a straight line. The center of an appropriate length of 50/125/250 multimode fiber was glued to the loop. Find the center of an appropriate length of 50/125/250 multimode fiber and use spray adhesive to glue the loop onto the flag. Spray the Tefzel® with adhesive and affix the fiber strands to tracks 2 and 4. A schematic of this configuration is shown in Figure 3.2

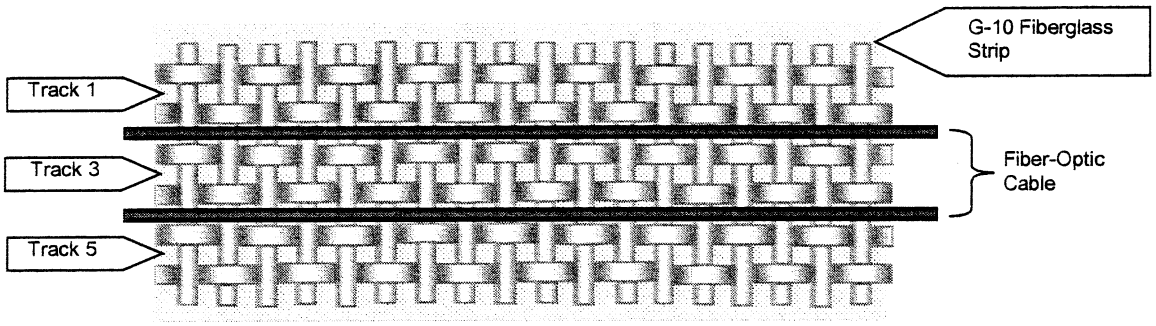

Figure 3.2 Fiber-Optic Cable Placed in Tefzel® Mesh Tracks 2 and 4 [Call, 00]

Once again, a thin coating of adhesive was applied to the fibers and covered with the top strip, while compressing the plate against the fiber. The center of the one-inch wide strapping tape was then adhered, without forming any creases, to the sensor's top plate. One side of the tape was folded onto the edge of the sensor and the procedure repeated for the opposite edge. The bare fiber ends were then fed into the protective, orange bifurcation tubing. A 3.1 cm (2 in.) strip of heat shrink was cut and drawn over the point where the bifurcation tubing meets the fiberglass end of the sensor. A heat gun was used to constrict the heat shrink in place. The heat shrink was coated in 5-minute epoxy and covered with a second piece of heat shrink. Each bare fiber end was stripped of the protective coating, coated with epoxy and secured into a ceramic ST-connector. After the bead of epoxy on the end of the connector dried, the end of the ST-connector was wet-polished for optimal coupling of light into the fiber.

3.4 Encapsulation Material Results

Materials tested were selected from various sources. Steep Type III Roofing Asphalt and E-Bonds G-100 were used at four Florida Tech field sites. Field tests with E-bonds G100 epoxy, which has a modulus of about 2,800,000 kPa (400,000 psi), indicated that the sensors response would not be large enough to activate the axle counter. Therefore, candidate materials were chosen with much lower moduli for this study. ArkDOT and OkDOT officials suggested several Flexane products. However, the most comprehensive information was presented in a TxDOT study, which summarized the properties of nine candidate piezoelectric sensor encapsulants. In order to provide a representative range of elastic moduli, six candidate materials were chosen from the available literature (Table 3.1) [Criss, 1998]. Moduli values ranged from 3500 kPa (500 psi) for Sylastic M RTV, to 70,000 kPa (10,000 psi) for Flexane 94. Five of these materials had been used successfully to install piezoelectric sensors. The ProSeal 6006 is currently being used for piezoelectric sensor installations in Florida. Only the Silastic M, which was the softest and most expensive, had not been used.

Table 3.1 Chosen Encapsulating Materials [Criss, 1998]

Product	Source	Elastic Modulus
Sylastic M RTV Silicone Rubber	Dow Corning (Essex Brunnel, Orlando, FL)	3500kPa (500psi)
Flexane 80 w/Flexadd (A-62)	Devcon (Grainger Co., Melbourne, FL)	5600kPa (800psi)
Bondo 7084 F	Dynatron/Bondo Corp. (Atlanta, GA)	9450kPa (1350psi)
Flexane 80 Two-Part Urethane	Devcon (Grainger Co., Melbourne, FL)	15,400kPa (2200psi)
Pro-Seal 6006 Two-Part Polyester Resin	RAI Products (Santa Fe Technologies, Gainesville, FL)	18,900 to 21,000kPa (2700 to 3000psi)
Flexane 94 Two-Part Urethane	Devcon (Grainger Co., Melbourne, FL)	70,000kPa (10,000psi)

3.4.1 Analysis of Encapsulation Results

For each of the six materials, the pneumatic pressure testing data was reduced to plots of percent light loss versus applied pressure. The maximum pressure applied to the channel ranged between 630 and 665 kPa (90 and 95 psi). These plots were termed calibration plots for the encapsulated sensors. They were compared to the calibration plots developed from testing the bare sensors in the chamber (Figure 2.3). Figure 3.3 depicts typical bare and encapsulated calibration curves. Comparing the plots for a given material and sensor at similar percent light losses (e.g. 75%) enabled a ratio between the pressures for the free (p_f) and encapsulated (p_e) sensors to be determined (Figure 3.3) ($\mathbf{p_f/p_e}$). This ratio was converted to a percentage and plotted versus sensor depth in the channel.

The data was used to determine the percentage change in the sensor response from the free state to the encapsulated state.

In order to compare the free and encapsulated curves over a range of intensity losses, comparisons were made from 99 to 50 percent losses. Only Sylastic M RTV and Bondo 7084F produced data that allowed levels below 90 percent to be used. In the other four cases, comparisons at losses between 95 and 99 percent light lose were made. A total of 11 plots were generated for the six materials. Each material was tested twice except Bondo 7084 F, which due to inconstant results was tested three times.

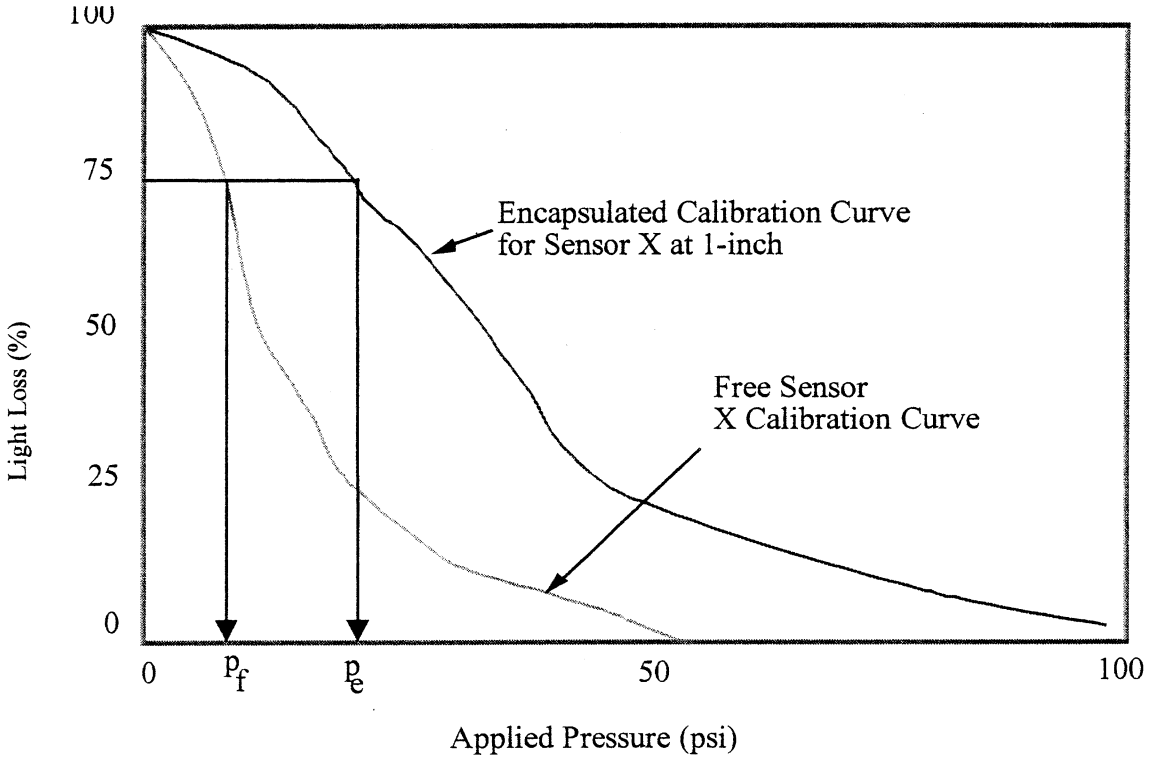

Figure 3.3 Typical Free and Encapsulated Calibration Curves for Determining Percent Change in Applied Pressure [Criss, 1998]

3.4.2 Percent Pressure Transmission Curves

Test date from the 11 plots was averaged to determine how the six materials affected the pressure delivered to the sensor. A plot of these averages was developed, showing percent load transferred to the channel bottom versus depth of groove (Figure 3.4). From this figure it can be seen that for each material there is a decreasing trend for the percent pressure transmitted to the bottom of the channel with respect to the depth of the groove. Also, it can be seen that Sylastic M RTV transmits significantly more light than the other materials. This is assumed to be due to the lower value of the modulus of elasticity. The Bondo 7084F and Flexane 94 averages were excluded. Bondo 7084's data yielded highly variable results when plotted. Bondo 7084 is a difficult material to mix properly due to the large portion of Hardener (48%) and Base (52%). If there is even a small error in the

mix proportions, the final product will have improper properties. Flexane 94's data was a straight line at zero percent pressure transmitted, indicating that it was too stiff to work with the microbend sensors.

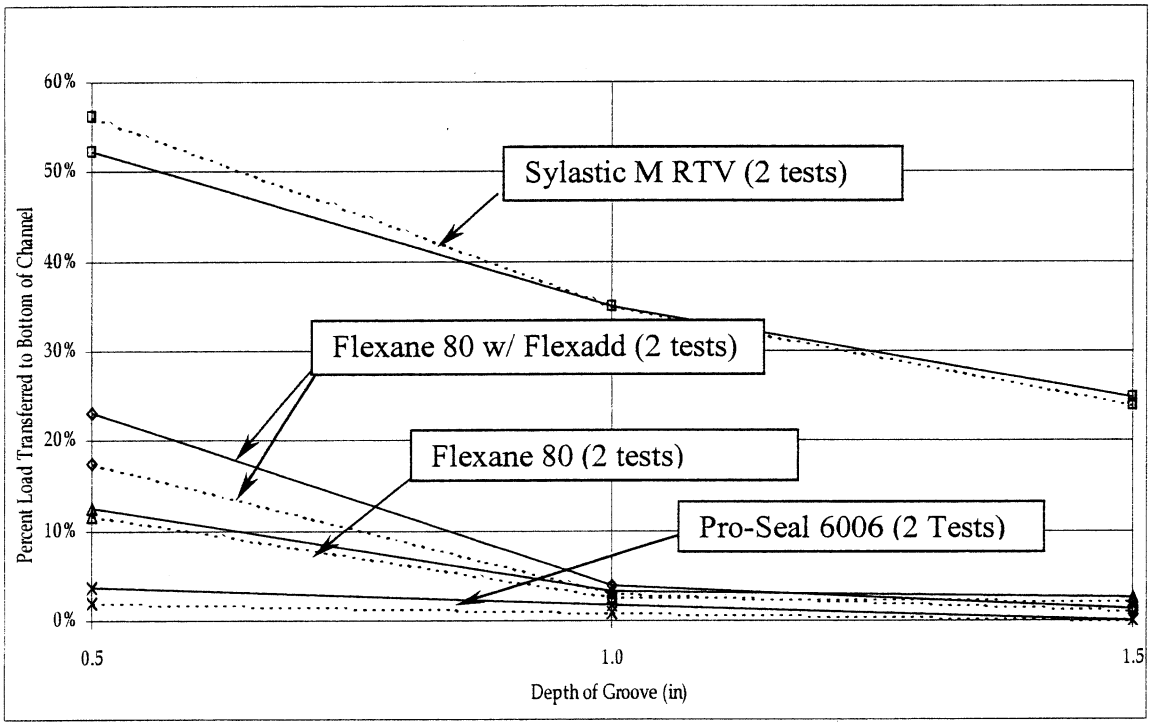

Figure 3.4 Average Percent Pressure Transmitted to Channel Bottom versus Groove Depth [Criss, 1998]

3.4.3 Defining and Calculating the Sensitivity Slope

A second method of data explication was adopted. Each material's sensitivity slope (M_s) was defined as the linear portion of the curve generated by the actuation of a sensor after encapsulation in a material (Figure 3.5). It has units of percent light transmitted divided by pressure in pounds per square inch (1psi = 7 kPa). The sensitivity slope for each material, at each depth was summarized in Table 3.2.

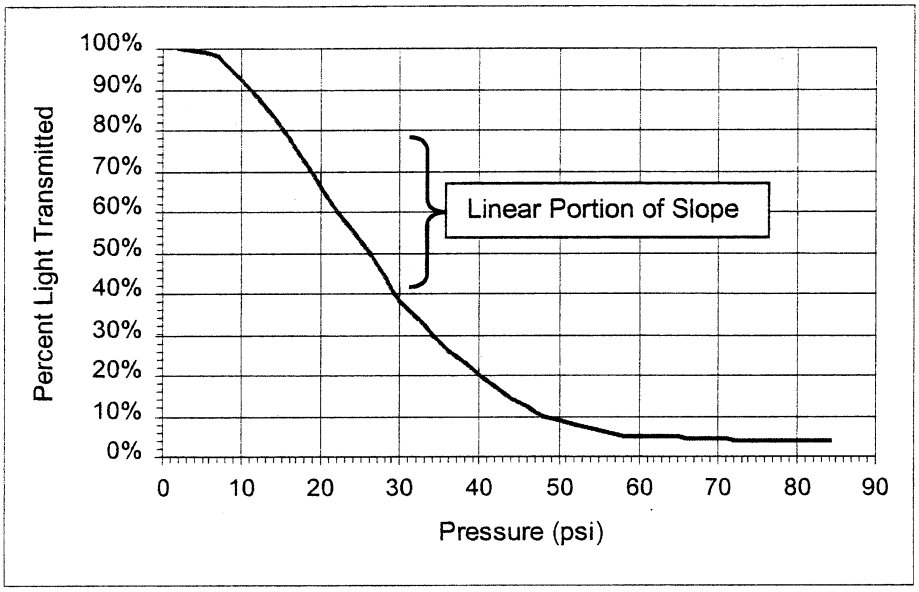

Figure 3.5 Typical Calibration Curve Depicting Linear Range Used for Determining the Sensitivity Slope (M_s)[Criss, 1998]

Five of the six M_s values presented in Table 3.2 were averaged, while only one of Bondo 7084F's M_s values were used. The other two sets of M_s values for Bondo 7084F were inconsistent and assumed irrelevant. In several cases, a change in the characterization of a sensor occurred after it was secured within its channel, and its sensitivity slope was adversely affected. When this occurred, there were typically one or two M_s values that followed the expected trend, and a single value that did not agree. In these cases, the questionable value was discarded and the remaining two were used for the average.

With the exception of Bondo 7084, the M_s results supported the earlier conclusion, that modulus of elasticity increases result in sensitivity decreases (Table 3. 2). Examination of the elastic moduli and M_s values for the 2.54 cm and 3.81 cm (1.0 in and 1.5 in) deep grooves indicates the sensitivity slopes were higher than expected (Table 3.2).

Table 3.2 Sensitivity Slope for Materials Tested [Criss, 1998]

Material	Modulus of Elasticity (psi)	Slope of Sensitivity (% /psi)		
		0.5" Depth	1.0" Depth	1.5" Depth
Sylastic M RTV Silicone	500	-3.00	-3.00	-3.30
Flexane 80 W/Flexadd (A-	800	-1.60	-0.77	-0.18
Bondo 7048 F	1,350	-1.58	-1.07	-0.66
Flexane 80 2-Part	2,200	-1.13	-0.13	-0.12
Pro-Seal 6006 2-Polyester	2,700	-1.07	-0.07	0.00
Flexane 94 2-Part	10,000	0.00	0.00	0.00

A second noticeable characteristic presented in Table 3.2 is that Sylastic M RTV and Flexane 94 could be considered to be the upper and lower boundaries for optimum sensor response. The Sensitivity Slope for both of these tests effectively does not change. This displays experimentally that when an encapsulating material has a modulus of elasticity near Sylastic M RTV there will be hardly any change in the percent stress transmitted to the bottom of the channel with respect to depth, up to 3.81 cm (1.5 in). Likewise, a material with a modulus of elasticity near Flexane 94 will allow for no stress transmittal to the bottom of the channel.

In an attempt to determine a relationship between M_s and the modulus of elasticity, a plot of the two was made (Figure 3.6). Three findings were noted from this plot. First, there was a strong linear relationship between the M_s and the modulus of elasticity, up to a modulus of 10,500 kPa (1500 psi). Secondly, both the 2.54 cm (1.0 in) and 3.81 cm (1.5 in) deep grooves yielded similar results. Increasing the modulus of elasticity past a value of 10,500 kPa (1500 psi) resulted in almost no pressure transmittal to the groove bottom.

Third, it was noted that the 1.27cm (0.5in) deep groove demonstrated the best response to all with respect to modulus of elasticity.

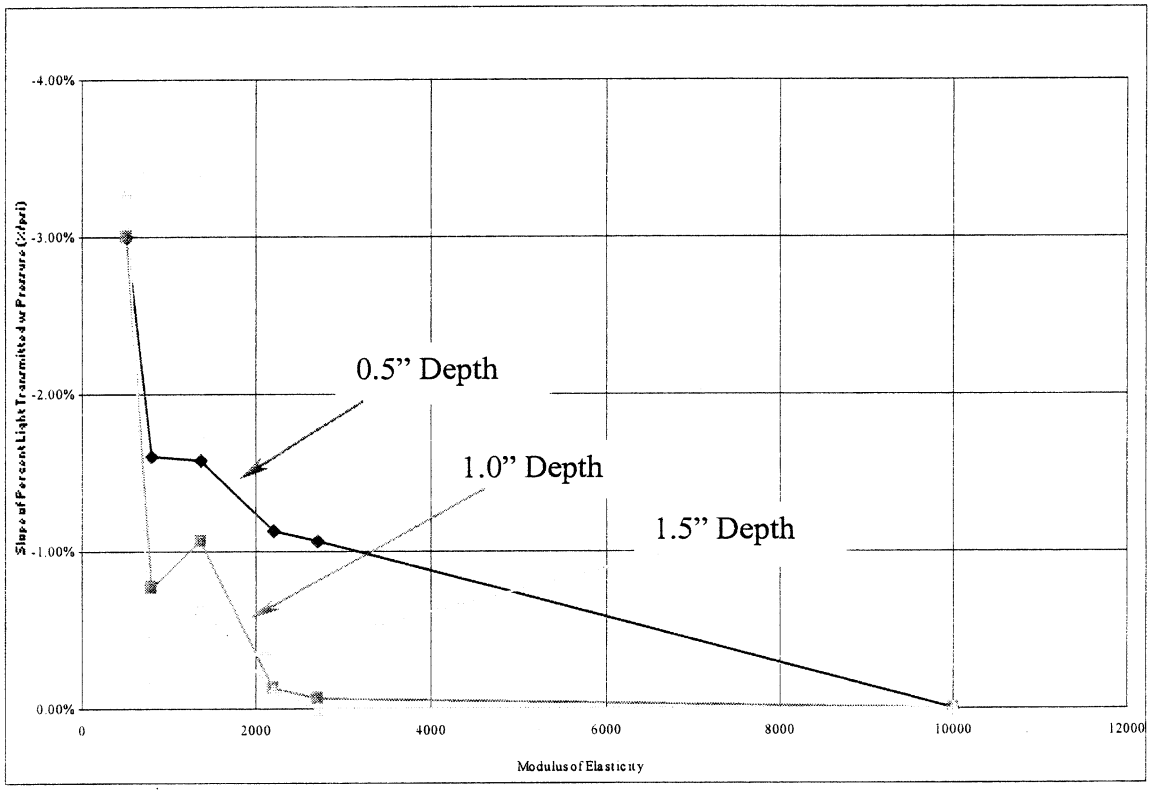

Figure 3.6 Sensitivity Slope versus Modulus of Elasticity [Criss, 1998]

3.5 Results from Failure Stress Testing

SEM photographs were taken of the loaded portion of the fiber. Facilities at both the Kennedy Space Center and Brevard Research Laboratories were used to complete this task. Each photo was visually inspected and the magnitude and severity of the fiber damage was documented.

3.5.1 Theoretical Failure Analysis of Acrylate

The acrylate was considered the most critical layer in the failure analysis of the fiber, because of its roll as an energy absorber around the glass. When acrylate failure occurs, little protection remains for the glass, allowing the fiber to suddenly break. The acrylate layers are flexible. Although the inner acrylate is very soft ($E_{ia} = 1.69*10^3$ kN/m^2 (246 psi)), which prevents stress concentrations from reaching the brittle glass.

Comparing the elastic moduli of the acrylate layers indicates that the outer layer is much stiffer. Although tests have yet to confirm its true role, it appears to function as a flexible outer layer that "contains" the softer inner acrylate. Once cracked, this outer layer causes the softer material to lose its confining abilities and the energy from stress concentrations can not be properly absorbed. Therefore, failure of the outer acrylate layer was considered sensor or fiber failure.

3.5.1.1 Theoretical Analysis Assumptions

The following assumptions were made to calculate the theoretical failure of the acrylate coat. First, it was assumed that the load was perpendicular to the fiber and the mesh, and therefore would result in pure compression at the point of contact. The second assumption was that the heat shrink and plastic coatings were incompressible compared to the fiber and mesh. This allows analysis to focus on of the fiber-mesh contact stresses. Third, to determine the modulus of elasticity of the fiber, it was assumed that Askeland's law of mixtures was

applicable [Askeland, 1989]. According to this law, a composite modulus of elasticity of the glass and the outer acrylate could be determined as follows:

$$\frac{1}{Ec} = \frac{Fg}{Eg} + \frac{Fa}{Ea} \tag{3.1}$$

where:

Ec: composite modulus of elasticity

Eg: modulus of elasticity of glass

Ea: modulus of elasticity of outer acrylate

Fg: volume fraction of glass

Fa: volume fraction of outer acrylate

Using the Askeland equation and assuming that the fibers' composite modulus was controlled by the outer acrylate with a modulus E_a of $5.79*10^5$ kN/m^2 (84000 psi)) and the optical glass with a modulus (E_g) of $7.24*10^7$ kN/m^2 ($1.05*10^7$ psi)) the fibers' composite modulus was (E_{fiber}) $7.72*10^5$ kN/m^2 (112,000 psi).

3.5.1.2 Application of Hertz's Law

Hertz's law was developed to analyze the contact stresses between two perfectly perpendicular cylinders. Castro [1997] applied it to the fiber mesh contact zone inside the sensor based on the following assumptions. The contact area is small when compared to the radius of the cylinder, which is infinitely long and perfectly perpendicular, resulting only in a compressive load.

The contact between the fiber and the mesh is shown in Figure 3.7. The fiber diameter (D1) and the mesh diameter (D2) are both 250 μm (0.64 mil). The stresses found using Hertz' equation are based on the assumption that the contact area changes from a point to an elliptical shape as the load increases.

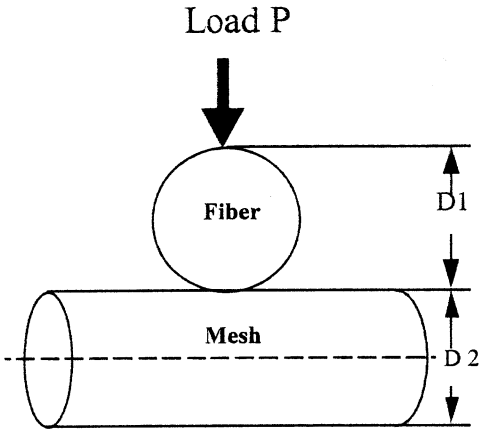

Figure 3.7: Schematic of fiber/mesh Contact (Roark and Young, 1975).

The equation to estimate this compressive stress is given as:

$$\sigma_c = \frac{1.5P}{\pi c d} \tag{3.2}$$

where;

σ_c is the compressive stress

P is the applied load and

c, d are the major and minor semi-axis of elliptical contact area

The major and minor axes can be found using:

$$c = \alpha \left[P * \frac{D1D2}{D1 + D2} \left[\frac{1-\nu_1^2}{E_1} + \frac{1-\nu_2}{E_2}^2 \right] \right]^{1/3}$$

$$d = c\beta$$

Where, α and β are constants that depend upon the ratio of the diameters (D1/D2), Young's modulus and Poison's ratio [Roark and Young, 1975].

Using Hertz' equation with the following input values;

- Poison's ratio of the fiber (ν_f) of 0.14,
- Poison's ratio of the mesh (ν_m) of 0.48,
- $\alpha = \beta = 0.908$.
- Young's Modulus of the Tefzel® Mesh, (E_m) of $2.75*10^6$ kN/m^2 ($4*10^5$ psi),
- Young's Modulus of the fiber, (E_{fiber}) of $7.72*10^5$ kN/m^2 (112,000 psi), and
- an applied failure load of 892 N (200 lb) per 18 fiber-mesh contacts under the upper rectangular plate or 49.5 N (11.11lb) per mesh contact

a maximum compressive failure stress of $6.89*10^5$ kN/m^2 (100,000 psi) was estimated.

3.5.2 Analysis of Results

The visual inspections of the SEM photographs revealed no visible damage to the fibers below the 896 N (200 lb) load level (Figure 3.8). The damage depicted in the photos above 896 N (200 lb) showed that contact between the fiber and the mesh formed an ellipse. When possible, the major and minor axis of the elliptical contact area was measured for the 896 N (200 lb) (Figure 3.8), 1232 N (275 lb), 1344 N (300 lb) and 1680 N (375 lb) load levels. These measured lengths were compared to the predicted contact lengths *c*, and *d*, from the Hertz equation. The photo of the 1680 N (375 lb) load-level presented problems with minor axis measurements because the cracks were not completely visible (Figure 3.9). Therefore, an estimated length was used.

Cornings' published data about fiber failure is based on tensile failures and reliability. This testing produced failures from compressive loads. Therefore, the failure stresses estimated from Hertz equation and the SEM results do not correlate with the published values.

A correlation between the contact area used by Hertz and the one on the SEM photos was not recommended because the photographs did not enable adequate precision in measuring the

contact area, specifically the contact widths. A plot of measured versus predicted contact area produced an R^2 coefficient below 0.2, implying no correlation was exists.

The major axis of the elliptical contact area was readable on the photographs. Therefore, a correlation between the major axis predicted by Hertz equation and the one measured from the photographs, was found. Figure 3.10 illustrates a linear relationship exists between the predicted and measured lengths with a relatively high R^2 value of 0.65. Therefore, Hertz equation can be use to predict the contact length of the elliptical failure surface.

The 896 N (200 lb) SEM photo shown in Figure 3.8 shows a break at 896 N (200 lb). The photograph shows three of the five cracks found in the 896 N (200 lb) fiber specimen. These cracks are small and longitudinal to the fiber. Cracks were detected for each fiber loaded above 896 N (200 lb) except for 1008 N (225 lb). If it is assumed that the failure load is 1123 N (250 lb), the estimated failure stress becomes $7.44*10^8$ Pa (107,850 psi). Therefore, the load does not significantly affect the failure stress. In summary, the estimated compressive failure stress is approximately 700,000 kN/m^2 (100,000 psi).

The SEM in Figure 3.9 represents the fiber after the 1680 N (375 lb) load was applied. This crack is significantly larger than for 896 N (200 lb) because the stress concentration caused the crack to propagate. The contact area was assumed to be the lighter zone in the central portion of the crack.

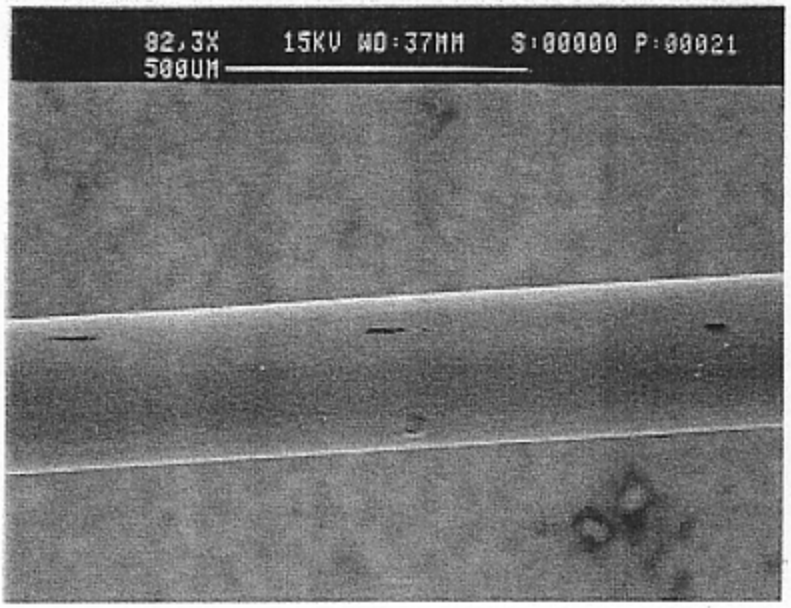

Figure 3.8: SEM Photograph Depicting Cracks on the Acrylate at a Load of 896 N (200 lb).

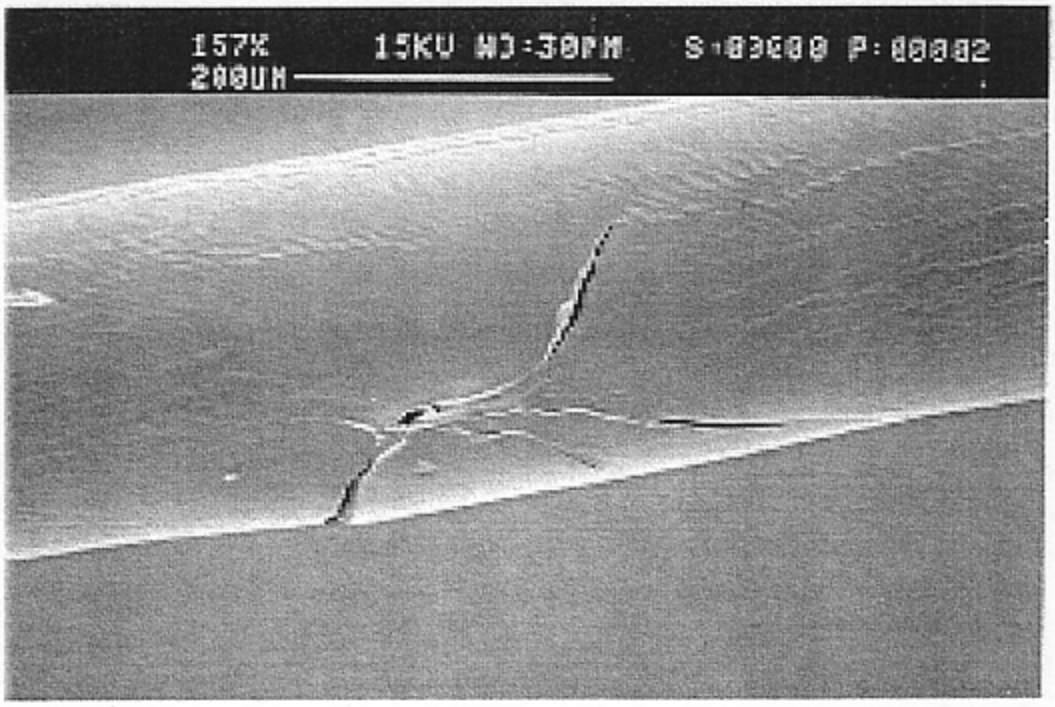

Figure 3.9: Cracks in the 1680 N (375 lb) Specimen.

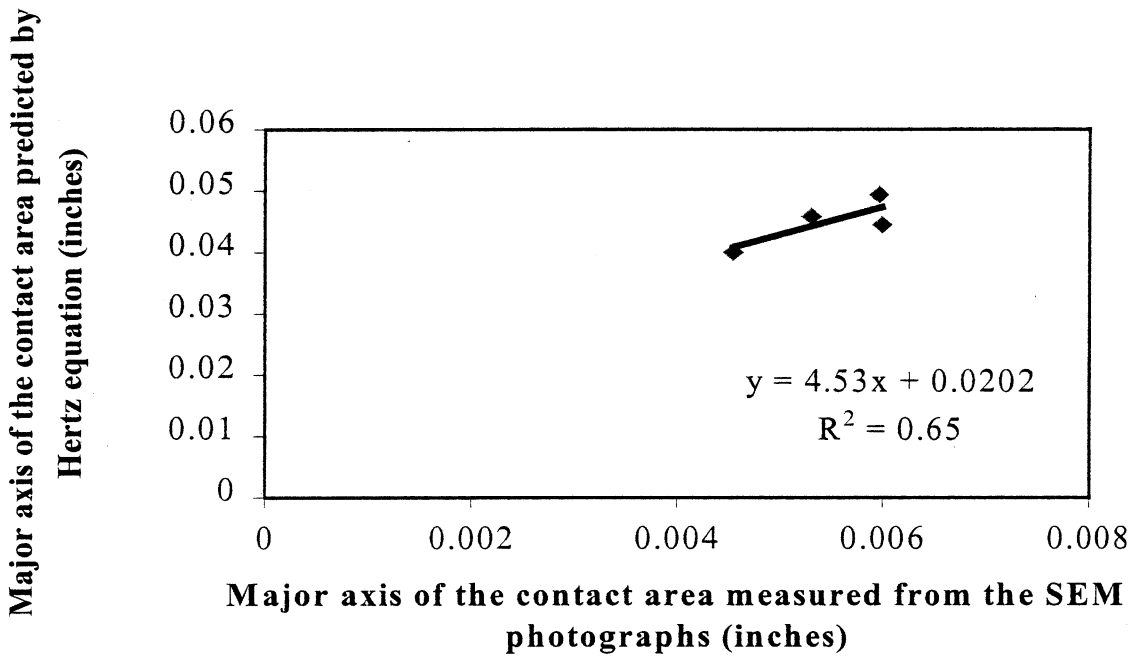

Figure 3.10: Major Axis of the Elliptical Contact Area Predicted by Hertz Equation versus Major Axis of the Elliptical Area Read on the SEM Photographs.

3.6 Microbend Sensitivity Versus Length

Transmissivity losses are a function of actuation pressure and the length over which that pressure is applied. Automobile tires have widths from 12 to 15 cm (4.5 to 6 inches) while truck tires can be 37.5 cm (15 inches) wide. Therefore, a relationship was required to estimate the change in signal response versus contact length. To develop this relationship eight sensors were constructed in varying lengths for evaluation in the pneumatic testing chamber (Figure 2.4). Sensors were placed in the testing chamber and connected to mode stripper to enable a clean signal to be evaluated. Pressures were increased from 0 to 210 kPa (0 to 30 psi) and light transmission losses were recorded. Figure 3.11 shows the resulting plots. The shortest sensors 12, 25 and 50 mm (1/2, 1 and 2 inch) have significantly different

response curves while all the sensors over 10 cm (4-inches) in length have very similar responses.

This testing indicates that contact lengths in excess of 10 cm (4-inches) do not affect the sensors signal response. The Tefzel® mesh has approximately 20 openings per inch indicating that approximately 100 contacts between the fiber and the mesh are required to ensure uniform signal responses. Since automotive tires are a minimum of about 12 cm (4.5 inches), all tires this width or larger with similar pressures would yield the same signal response each time they passed over the sensor.

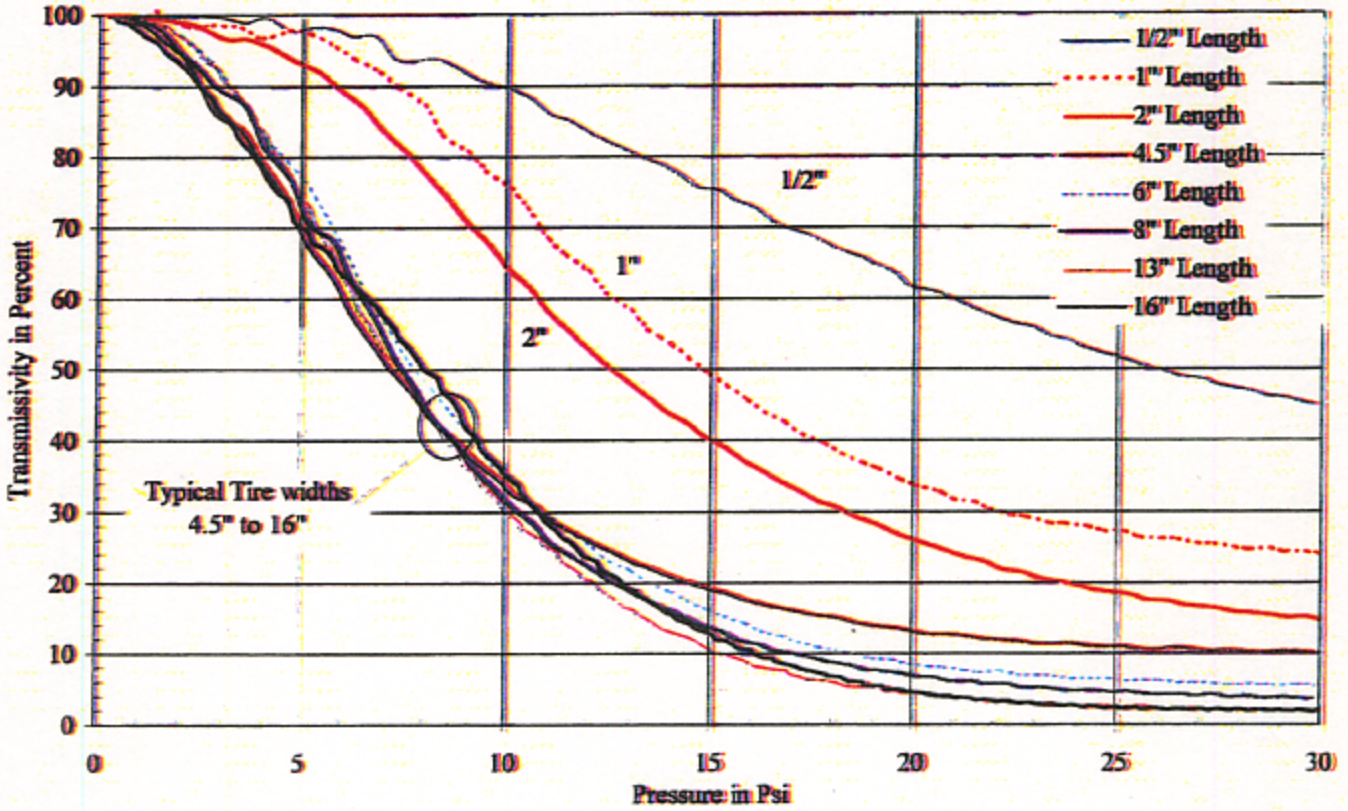

Figure 3.11 Sensitivity versus Actuation Length

Chapter 4

Analytical Program Results

To gain an understanding of the sensor-pavement interaction finite element modeling (FEM) was performed. Software, from MacNeal-Schwendler's Nastran for Windows® was used to generate a 2000 node mesh. In the field, the pavement and sensor system display nonlinear load-deformation characteristics that are a function of temperature, as well as load or stress level. There was no literature identified on analytical pavement-sensor models. Therefore, the load-deformation properties of the system were simplified as much as possible and assumed to be linear.

Three FEMs developed. First, the pavement in which the sensors were to be installed was modeled to predict the range of elastic moduli for its surface, base and subgrade layers. This model simulated the pavement at the APAC-MacAsphalt plant where the sensors were installed. FWD data were used to calibrate the model so that model deflections correlated to the deflections measured during the FWD tests.

The second model was used to isolate the stress-strain conditions of the fiber-optic sensor encapsulated with a probable bonding agent. Analytically, the model simulated the sensor epoxied horizontally to the bottom of a small structural channel, backfilled with a bonding agent that simulated the elastic properties of 3M's 5200 Marine Sealant. Model calibration was accomplished by changing the stiffnesses of the FOTS and bonding agent so that the model deflections were similar to the deflections measured using the pneumatic testing chamber (Photograph 4.1)

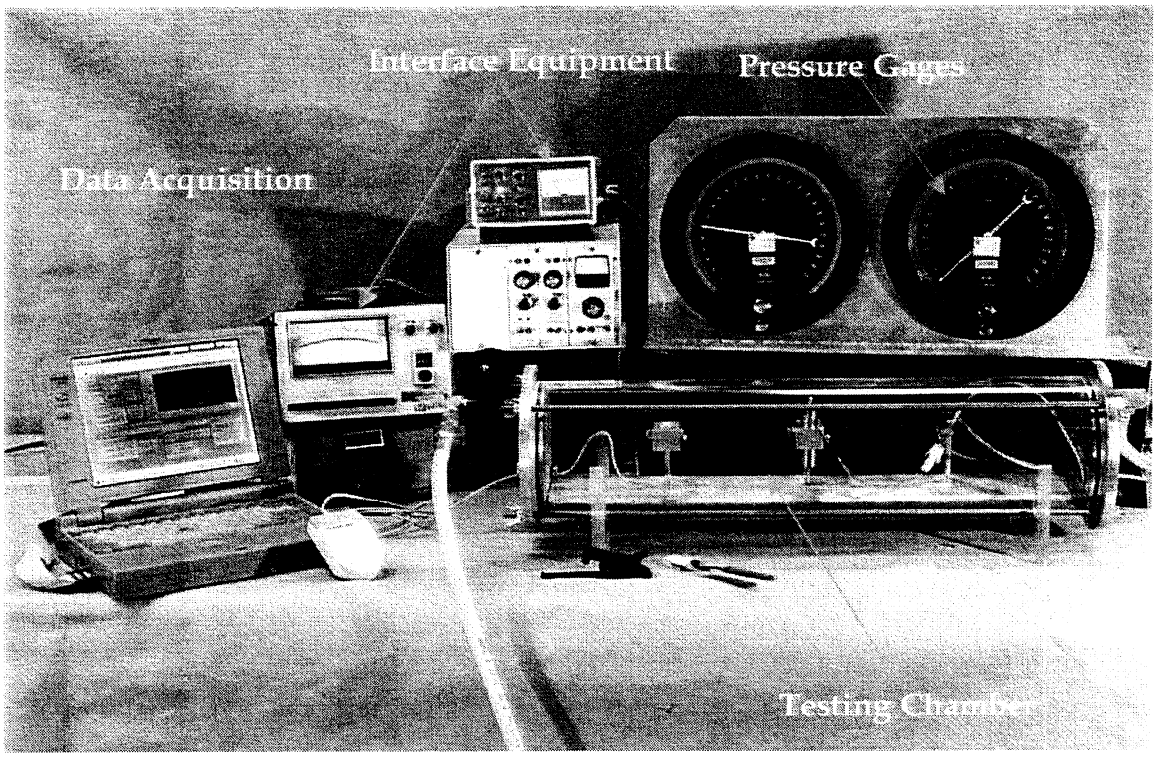

Photograph 4.1 Pneumatic Testing Equipment for Sensor Evaluation [Eckroth, 1999].

The third model was developed to simulate the sensor bonded with a material, similar to the 5200, in a narrow vertical groove (~1/8" wide by ~1" deep) cut into the pavement with elastic properties simulating those of the APAC MacAsphalt pavement. This model incorporated the material stiffness properties calculated from the two previous models. The predicted sensor deformations and associated light losses were correlated with light losses measured in the field. This third model enabled the stress distributions surrounding embedded traffic sensors to be evaluated.

4.1 Falling Weight Deflectometer Data Analysis

FWD data are typically acquired to determine the stiffness of the layers that constitute a pavement's structure and to predict the remaining structural life. FWD testing was performed on and around the sensors in the APAC pavement. This field-testing enabled the sensor response to direct impulse loads to be analyzed and gave an indication of how the

FWD deflection bowl would affect sensor response. The FWD data was also used to determine:

1. if the stiffness of the MacAsphalt field site was comparable to the stiffness of typical state roads,
2. if the stiffness values for the pavement layers at the MacAsphalt field site were reasonable for use in the finite element model and
3. if the fiber-optic traffic sensors could be actuated with the FWD

4.1.1 Comparing the MacAsphalt Pavement to Typical FDOT State Roads

The first item was addressed by acquiring FWD data on two roads. Data acquired at the MacAsphalt driveway were used to back-calculate the elastic moduli of the pavement layers and to determine the MacAsphalt driveway's stiffness. This was necessary to verify that the driveway was a good field-testing site. Additional data were acquired at State Road 507 (FDOT telemetry site number 345) for deflection bowl comparison to the MacAsphalt driveway. Because the pavement thickness was not determined at the SR 507 site, the layer stiffnesses could not be backcalculated. Personnel from FDOT traveled to these Melbourne, Florida sites (on 7/27/98) and performed tests at ten points near the sensors at the MacAsphalt driveway and tests at two locations near the sensors at the SR 507 site. The FWD tests consisted of releasing the same weight from four heights at a single station. Data were acquired from seven deflection transducers positioned along a straight line extending outward from the point of load contact. Photographs 4.2 and 4.3 depicts the transducers used for measuring the pavement's deflection and rubberized plate that acted as the interface between the falling weights and the pavement.

Data presented in Table 4.1 indicates that the average difference in loads between the Macasphalt and Babcock pavements was 1 percent while the average difference in deflections ranged from 6 to 11 percent. There is typically 15 percent error inherent during FWD testing. Therefore, the 6 to 11 percent variations were minimal and the relative stiffness of the two sites was assumed comparable. Because MasAsphalt's driveway stiffness was representative of state and county highways, it was concluded that this field site was

satisfactory for testing fiber-optic traffic sensors. The MacAsphalt site was tested at 138° F (1600 hr) while the Babcock site was tested at 100°F (2200 hr). The deflections at both sites, from all transducers, were similar, however, data from only three transducers are presented for comparison.

Photograph 4.2 Falling Weight Deflectometer Testing of Fiber Optic Sensors at MacAsphalt Site

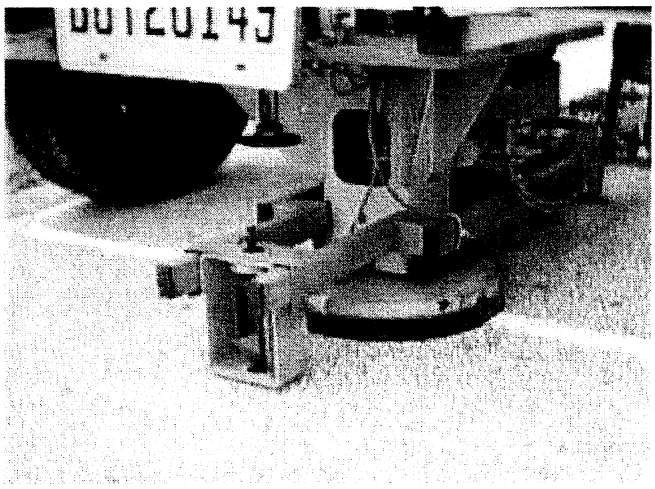

Photograph 4.3 Falling Weight Deflectometer Testing Plate and Geophones

Table 4.1: FWD Data from SR 507 and MacAsphalt Sites

Description	FWD Weight (lbs.)	FWD Deflections (inches)		
		Transducer 1, 0" from plate	Transducer 3, 12" from plate	Transducer 5, 23" from plate
SR 507	7144	0.01038	0.00527	0.00236
(test location 1)	10264	0.01491	0.00792	0.0037
	13032	0.01841	0.01017	0.005
	15672	0.02191	0.01218	0.00618
MacAsphalt	7032	0.00894	0.00462	0.00252
(test location 1)	10104	0.01305	0.00711	0.0039
	12880	0.01697	0.00953	0.00529
	15480	0.02051	0.01182	0.00655
Percent Difference	102%	116%	114%	94%
SR 507/Macasphalt	102%	114%	111%	95%
	101%	108%	107%	95%
	101%	107%	103%	94%
Averages	101%	111%	109%	94%

4.1.2 Determining the Elastic Properties of the MacAsphalt Pavement

The second question was addressed by using Texas Transportation Institute's MODULUS 5.0 software package. This program was used to back-calculate the elastic moduli of the hot mix asphalt (HMA), base, and subgrade layers at the MacAsphalt driveway. Accurate determination of the elastic moduli of the three layers was required because these values were used as input into the finite element model of the sensor embedded in the grove cut in the MacAsphalt pavement.

A portable core drill used to extract a specimen of HMA and crushed lime rock from the road (Photograph 4.4). The asphalt layer was 4-inches thick and the crushed limestone base was 8-inches thick. The photo shows the portable corer (with suction base) and its associated vacuum pump that held the drill against the pavement. Due to contractual difficulties coring was not performed at the Babcock site. The back-calculated values obtained from MODULUS 5.0 for MacAsphalt are presented in Table 4.2.

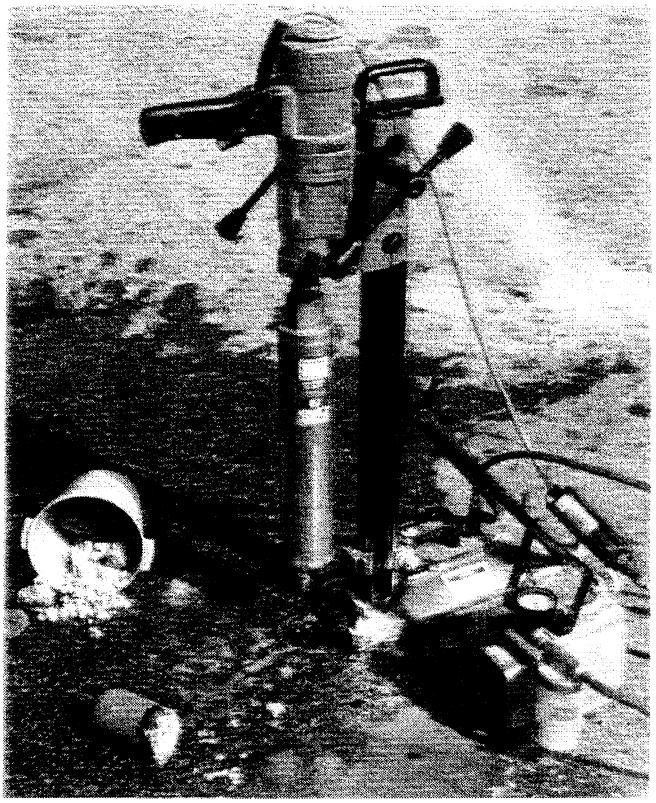

Photograph 4.4. Coring Equipment for Obtaining Pavement Samples at MacAsphalt

Table 4.2: Average Elastic Moduli Back-Calculated by MODULUS 5.0 for MacAsphalt Field Site

Average Load (kips)	Average Elastic Moduli (ksi) Poisson's Ratio = 0.35		
	HMA	Base	Subgrade
7	310	58.8	30.4
10	344	59.8	27.6
12	361	63.2	26.4
15	372	64.4	25.7

The HMA stiffness values steadily increased as the falling weight increased from 7 to 15 kips. This increase indicated strain hardening of the HMA occurred. The backcalculated

HMA moduli for the 10 drops ranged from 200 ksi to 400 ksi with an average of 310 ksi, which is comparable to literature values [Nazarian, et.al., 1988].

Laboratory unconfined compressive tests were performed on the HMA core to measure the variation in elastic moduli at 32° F, 72° F and 140° F. These results are presented in Figure 4.1. The elastic moduli decreased from 333 ksi at 32 °F to 16 ksi at 140 °F indicating that the stiffness of HMA was greatly affected by temperature. These moduli could be lower than field values due to the lack of confinement. Michalak and Scullion suggest that the asphalt could have an elastic modulus as low as 100 ksi at pavement temperatures of 110° F [1995]. Due to the inconsistencies in the lab and reported values, it was assumed that the 310 ksi backcalculated by MODULUS 5.0 for the HMA at MacAsphalt was appropriate for use in the FEA.

The backcalculated limerock base moduli values ranged from 39.2 ksi to 77.2 ksi, with an average of 59 ksi, which were again comparable to the literature values [Eckroth, 1999]. Again elastic moduli increased with increasing loads indicating a strain hardening of the limerock base.

The backcalculated subgrade sand moduli values ranged from 28.7 ksi to 34.7 ksi with an average of 30.4 ksi. These values were for the seven kip drop. Reported values for several types of sands ranged from 17 to 52 ksi, with the elastic modulus of well-graded dense sand reported as 28,000 psi [Lambe and Whitman, 1969]. Therefore, the average value was assumed reasonable for use in the FEM analysis. The elastic moduli for the sandy subgrade decreased with increasing loads, indicating that strain softening occurred.

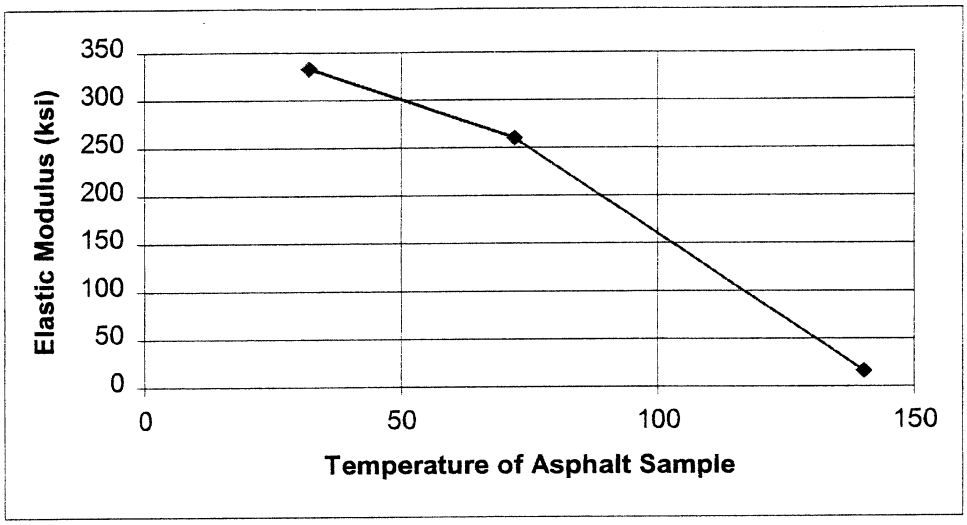

Figure 4.1 Asphalt Temperature versus Elastic Modulus [Eckroth, 1999]

Table 4.3 summarizes the elastic moduli values initially used as input to the finite element analysis for the three pavement layers. All three values were assumed reasonable for the pavement section under investigation.

Table 4.3: Initial Elastic Moduli Values Used in FEA

HMA = 310 ksi
Lime rock base = 60 ksi
Sandy subgrade = 30 ksi

4.1.3 Actuating the FOTS using FWD Tests

The third question was whether the sensor could be actuated by the FWD. A preliminary set of FWD tests was conducted to investigate this problem. Two six-foot fiber-optic sensors were tested using the FWD at the MacAsphalt field site. The lab calibrations performed on these sensors indicated that they required 12 and 35 psi to cause a 50% light loss. Half the length of each sensor was encapsulated with a 50/50 mix of Bondo® 7084F and the other half with a 65/35 Bondo® mix (part A to part B). The FWD test plan called for dropping the weights directly on top of a sensor and then dropping the weights one-inch to the side of the sensor. This process was repeated for each mix of Bondo® and for both sensors yielding a total of eight test locations near the two sensors. There were four-drop heights and associated

loads applied to the pavement at each of the eight test locations, yielding a total of 24 tests. Loads ranged from approximately 7,000 to 15,500 lbs. Test results from sensors loaded directly with the FWD indicated that light loss was a function of load level. While FWD tests near the sensor indicated that the loading plate had to be positioned within about 1-invch to produce a signal. Figure 4.2 is a summary of the light intensity losses for one of the sensors loaded directly and loaded to within 1-inch of the sensor. Light losses for the direct loading ranged from 35 to about 68 percent as the load increased, while losses for the other case ranged from 5 to 10 percent.

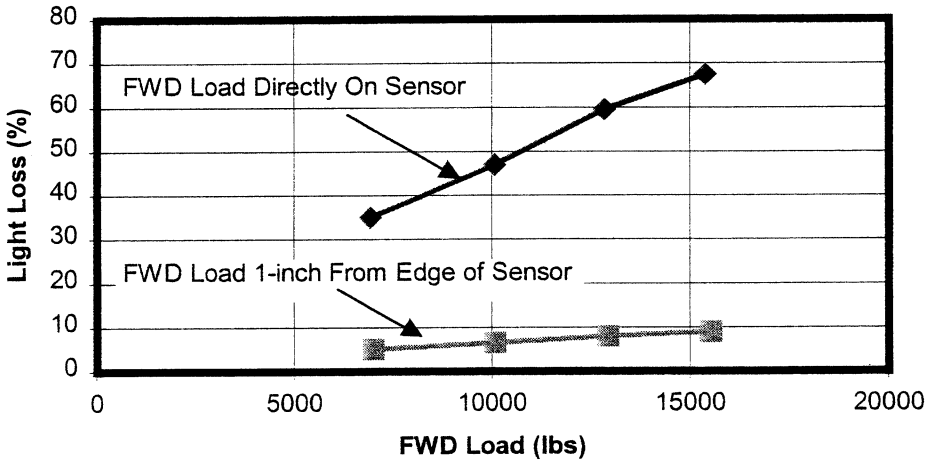

Figure 4.2 FWD Load versus Percent Light Loss

4.2 MacAsphalt Pavement Model Development and Results

The MacAsphalt pavement plane-strain model was designed with 1" by 1" square elements for the 4" thick HMA and 8" thick base layers, and 2" by 2" square elements for the 24" thick subgrade layer. This 48" long by 36" deep model was comprised of 937 nodes and 864 planar elements, which extended 1-inch into the z-direction. Boundary condition nodes

along the bottom of the subgrade layer were fixed. Nodes along each side of the model were allowed to translate in the vertical or Y-direction, which was direction of loading.

Loadings similar to the FWD loads were needed for input. FWD loads ranged from about 7,000 to 15,500 lbs, therefore, the equivalent pressures ranged from about 65 to 140 psi. It was assumed that simulating a heavy truck tire pressure would yield desirable results. The third loading level of nearly 13,000 lbs, which when distributed over the 5.91-inch diameter loading plate equated to approximately 117 psi was similar to a large truck tire. The 10,000 loads produced pressures of approximately 90 psi, which were standard truck tires. Therefore, the larger truck tire pressure was chosen for input and comparison to the model results.

The 117-psi pressures were equated to 117-pound points loads that could be applied through 11 nodes to duplicate the diameter of the FWD plate. Vertical (Y-direction) FEA deflections calculated at the center of the deflection bowl were compared to the measured deflections from the FWD transducers.

The model initial iterations used the elastic moduli presented in Table 4.3 as input. The resulting model deflections were 15 percent larger than the measured deflections at the center of the deflection bowl (i.e., 0.0207" FEA versus 0.018" FWD for 117 psi load). Numerous trials were conducted during which model deflections were compared to the measured deflection. Results of these iterations indicated that increasing the elastic modulus of one of the pavement layers decreased the deflections. By increasing the elastic modulus of the crushed lime rock base course from 60 ksi to 75 ksi the measured and predicted deflections agreed to within 5 to 9 percent (Table 4.4). Poisson's ratio for all three materials was assumed constant at 0.35.

Table 4.4: FEA Deflections versus Measured FWD Deflections at the Center of Deflection Bowl

Loads (lbs.)/ Pressure (psi)	FEA Deflection	FWD Deflection	Difference (FEA-FWD)
7,000 / 63	0.00921"	0.00972"	5.2%
10,000 / 91	0.0133"	0.01422"	8.6%
12,000 / 117	0.0171"	0.01806"	5.3%
15,000 / 140	0.0204"	0.02172"	6.1%

Figures 4.3 and 4.4 show the horizontal (or X-normal) stresses and vertical (or Y-normal) stresses for the model when the applied compressive stresses are 117 psi. The load is applied in the negative Y-direction; therefore, the stresses are in compression when a (-) sign is shown and in tension when no sign is given. In general, the stress distribution decreases from the 117 psi at the surface in a manner similar to Boussinesq's vertical stress distributions beneath a footing [Lambe and Whitman, 1969]. Figure 4.4 shows that the HMA undergoes the expected tension at the bottom of the 4-inch layer, as well as on the pavement's surface on either side of the distributed load.

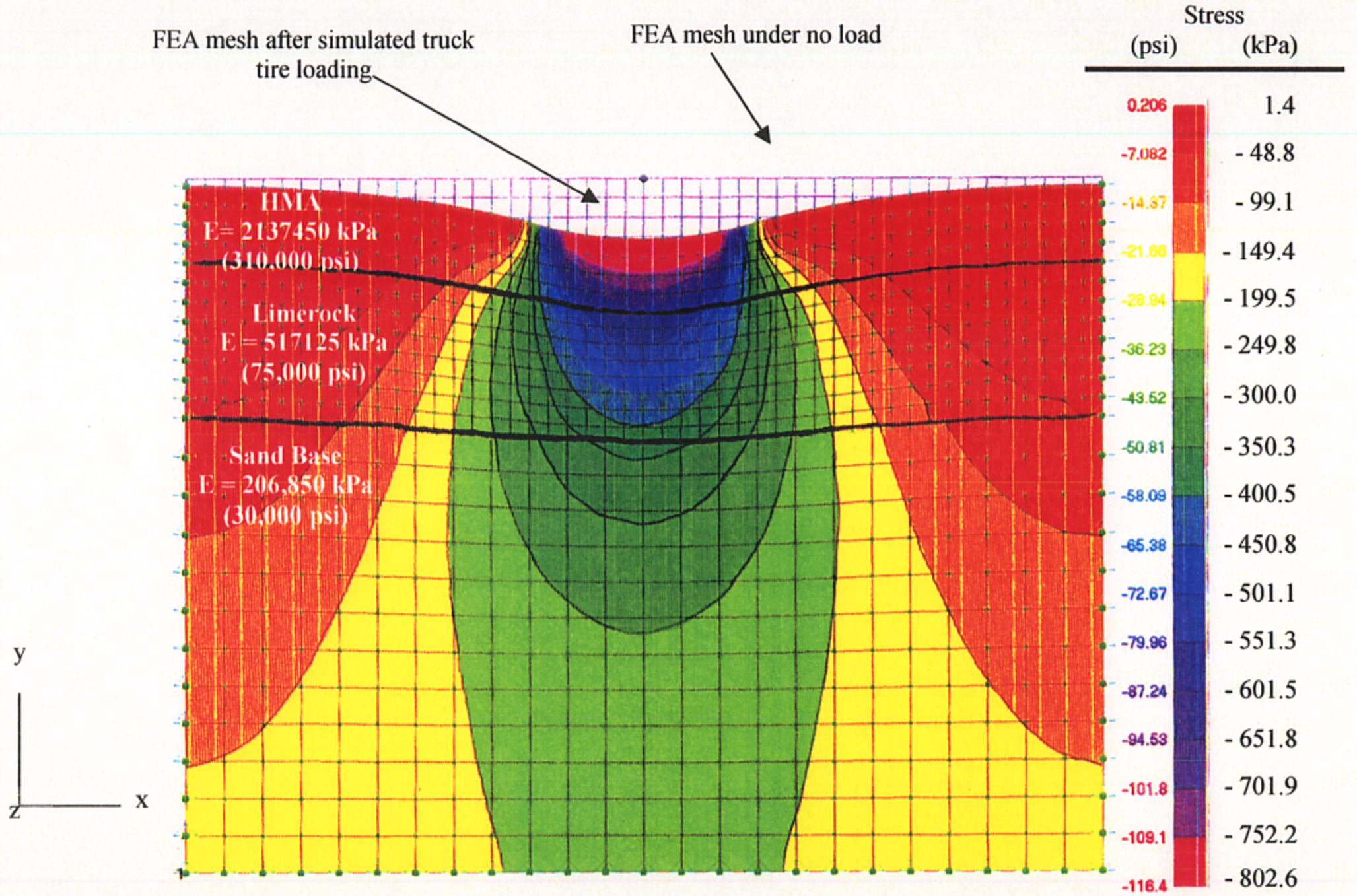

Figure 4.3 Model 1 FEA mesh and vertical stress distribution from 810 kPa (117 psi) applied stress on simulated Macasphalt pavement

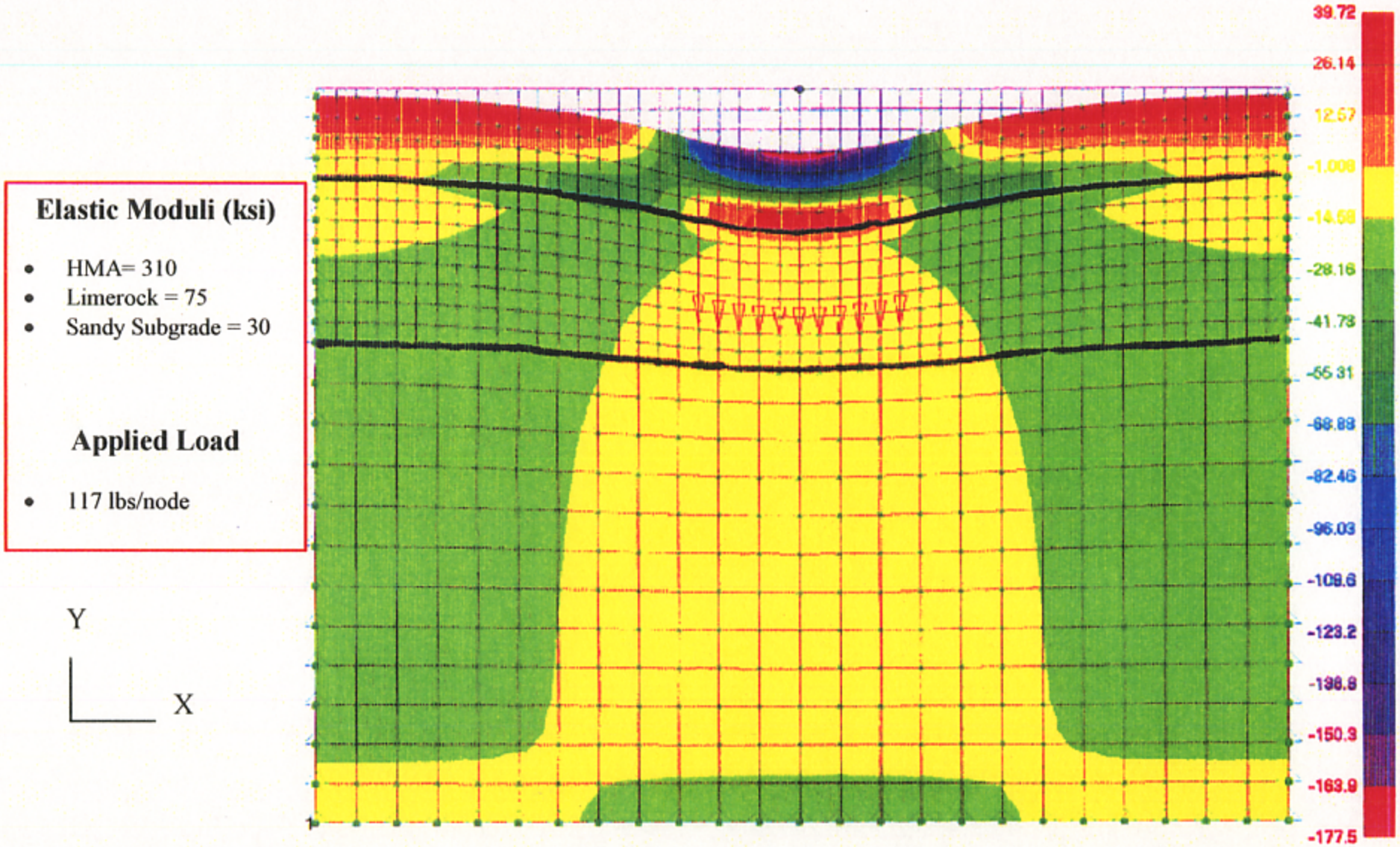

Figure 4.4 Vertical Stresses from FEA Flexible Pavement Model of MacAsphalt FOTS Site Subjected to Simulated Truck Tire loading of 117 psi

4.3 FEA Model and Results for a FOTS in a Channel

The purpose for this second FEA model was to determine the stiffnesses and Poisson's ratios of the FOTS and encapsulation material as they interacted. These stiffnesses were incorporated into the third model of the sensor embedded in the pavement. When the predicted deflections correlated to the measured deflections the model was assumed to be properly calibrated. This calibration was accomplished by changing the elastic moduli of the two materials.

4.3.1 Laboratory Testing Program for Bare and Encapsulated Sensor

The sensor-encapsulation testing was performed in two steps. Step one involved epoxying the bare sensor to the bottom of the aluminum channel (Photograph 4.5), placing the sensor in the pneumatic testing chamber (Photograph 4.1) and pressurizing the sensor to 45 psi. This pressure caused a 50 percent light loss. Deflection measurements were taken using a LVDT. Step two involved using the epoxied sensor and overlaying it with 3M 5200 Marine Sealant. The entire assembly was again placed in the pneumatic testing chamber and pressurized to 45 psi.

4.3.2 FEA Model for Bare and Encapsulated Sensor

The corresponding 3-D FEA model was developed using 0.5" by 0.5" elements, 0.020" square. Constraining the mesh's bottom coordinates simulated the properties of the aluminum channel. The lower left side as shown in Figure 4.5 was fixed while the lower right side was free to translate in the X-direction, but not in the Y - or Z-directions. Pressures equivalent to 45 psi were applied to the external faces of each surface element by applying 45 lb point loads to the entire surface. The 1352 nodes and 625 solid elements used to construct the mesh used in this model are shown in Figure 4.5.

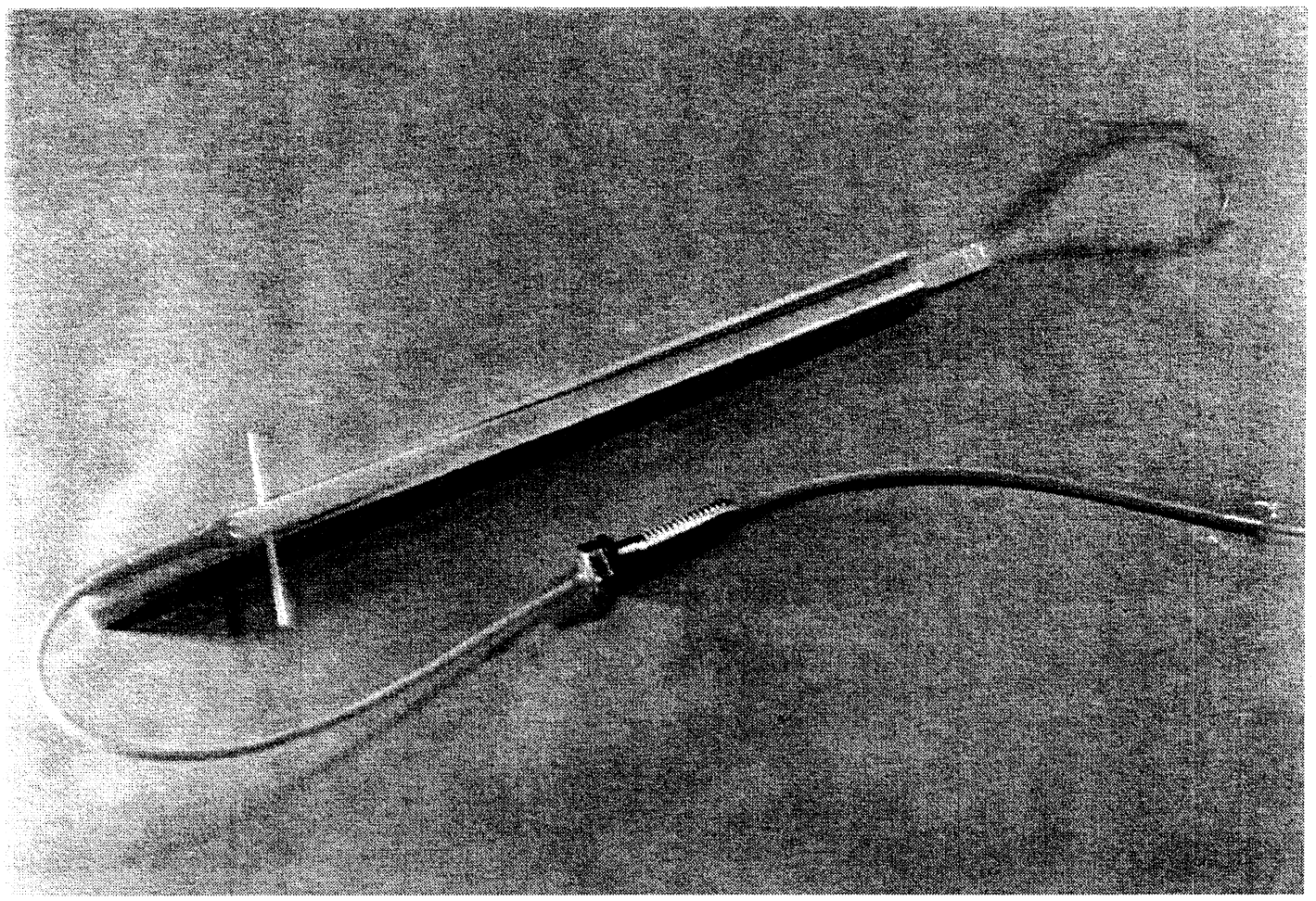

Photograph 4.5 Bare Fiber Optic Traffic Sensor [Eckroth, 1999]

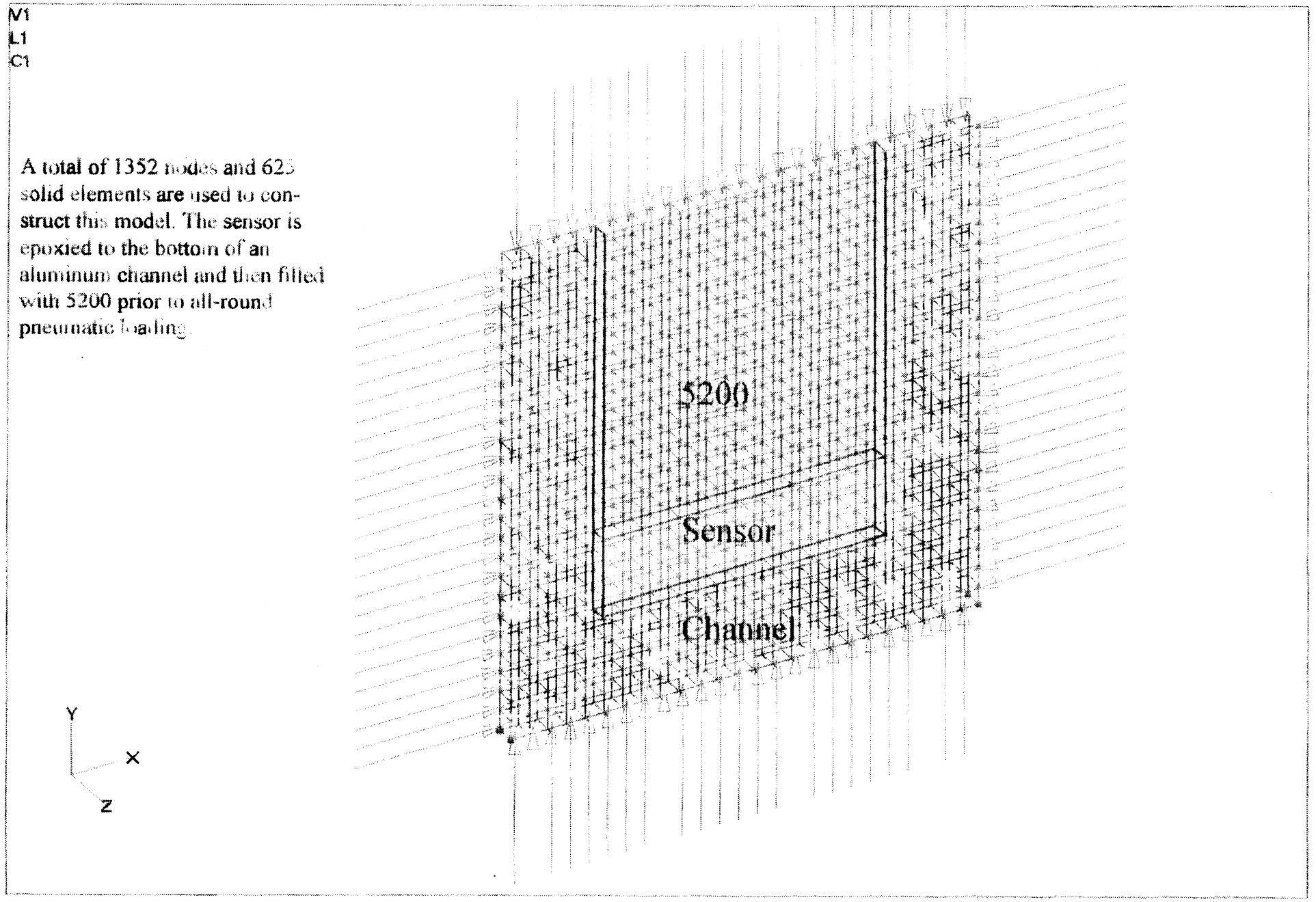

Figure 4.5 FEA Mesh of the FOTS/Encapsulant/Channel

Two assumptions were made in the design of this second model. The first assumption was that the pressure was equally distributed over the top of the sensor, when the sensor was pressurized without the 5200 layer. It was secondly assumed that the pressure distribution near the center elements was equal to the pressure applied to the optical fiber.

The sensor's thickness was modeled using four square solid elements, each having an edge dimension of 0.020-inches. The actual sensor had a thickness of 0.075-inches therefore; the model incorporated a sensor that was 0.080-inches thick. This resulted in a difference of about 6.7 percent. All other dimensions were modeled exactly. Once the encapsulant was placed over the top of the sensor and the pressure reapplied, the modeled stress distribution at the top of the sensor was non-uniform. It was largest near the middle and decreased to zero psi near the edge of the channel. Figure 4.6 shows the location of the fiber within the sensor. The contours display the deformations propagating into the compliant 5200 and the sensor. The maximum deflection at the surface of the 5200 was estimated to be approximately 0.011-inches. The deflection at the top of the sensor was estimated to be about 0.0007-inches. The majority of the deformation occurs in the 3M 5200, implying that it also absorbs nearly all of the stresses. The channel is considered a relatively wide groove in the pavement.

4.3.3. Laboratory Testing Results for Bare and Encapsulated Sensor

To compare the FEA results to lab data. A series of tests were conducted with the sensor first epoxied to the bottom of the aluminum channel and pressurized, and then overlaid with the 3M 5200 and pressurized. Figure 4.7 presents transmissivity and deflection data for the sensor prior to overlaying with 5200. Sensor deflections were measured at three locations along the 8-inch length using LVDT's. From this testing, the sensor was characterized, its elastic modulus was estimated and load-deflection data was collected. These three findings are summarized below.

1. The FOTS epoxied to the bottom of the channel lost 50 percent of the light when pressurized to 11.6 ± 0.7 psi (or $11.6 \pm 6\%$). The variation of 0.7 psi ($\pm$ 6%) was found through examination of Figure 4.7

2. The elastic modulus of the sensor epoxied to the channel bottom was 695 ± 35 psi (or 695 ± 5%). The variation of 35 psi (± 5%) was found through examination of the linear portion of the curves shown in Figure 4.7

3. The deflection of the sensor epoxied to the bottom of the channel, when loaded to 11.6 psi, was 0.00105" ± 0.0015" (or 0.00105" ± 14%). The variation of 0.00015-inches (± 14%) was estimated through examination of Figure 4.7 between 10.9 and 12.3 psi.

Figure 4.8 shows the load-transmissivity-deflections results for the 5200/FOTS system with deflections measured at the top of the 5200 for three data runs. Analysis of these data indicated that they were repeatable to within 10 percent. At a pressure of 45 psi the sensor lost about 50 percent of the light and the deflections at the top of the 5200 layer averaged 0.011-inches. Note that the FEA predicted deflections under 45 psi stresses were also 0.011-inches. This implies that while the system was pressurized to 45 psi, the sensor was being subjected to enough pressure to cause a 50 percent light loss and according to the results from Figure 4.7 that pressure should be 11.6 psi. By dividing the 11.6 into 45, it was estimated that the 3M 5200 absorbed about 75 percent of the stresses.

4.3.4 Elastic Moduli Temperature Testing Results for 3M 5200 Marine Sealant

Stress-strain testing was performed on the 5200. Pressures from zero to 30 psi were applied to a molded 2-inch diameter, 4-inch tall cylinder of this material. Deflections were recorded throughout the testing. A linear stress-strain relationship was observed with a slope, or elastic modulus, of 600 psi. This stiffness remained constant with respect to temperature as temperatures were varied from 32 to 140 °F. Based on this testing the initial model input value for the elastic modulus of 5200 was chosen as 600 psi.

4.3.5 FEA Sensitivity Analysis of FOTS-Encapsulant Model

A sensitivity analysis was performed using the FEA model, during which Poisson's ratio and elastic moduli of the FOTS and 5200 were varied to achieve the nodal deflections and element stresses presented in Table 4.5. Only one property value was changed at a time during an analysis run. Two critical locations were checked using measured and

predicted deflections, the surface deflection at the center of the 3M 5200, and the deflection at the center of the sensor. Table 4.5 identifies the corresponding critical nodes and elements where deflections were obtained from the output file. The measured deflections taken from Figures 4.7 and 4.8, respectively were 0.00105-inches at the surface and 0.0107-inches at the top of the sensor. The predicted deflections taken from Figure 4.6 were 0.0107-inches at the surface and 0.00103-inches at the top of the sensor. Table 4.5 indicates that the surface values agree to within 3 percent, however, the values at the top of the sensor agree to within 34 percent. At very small deflections such as the ones occurring at the top of the sensor, larger errors are expected. Therefore, it was concluded that the model was acceptable.

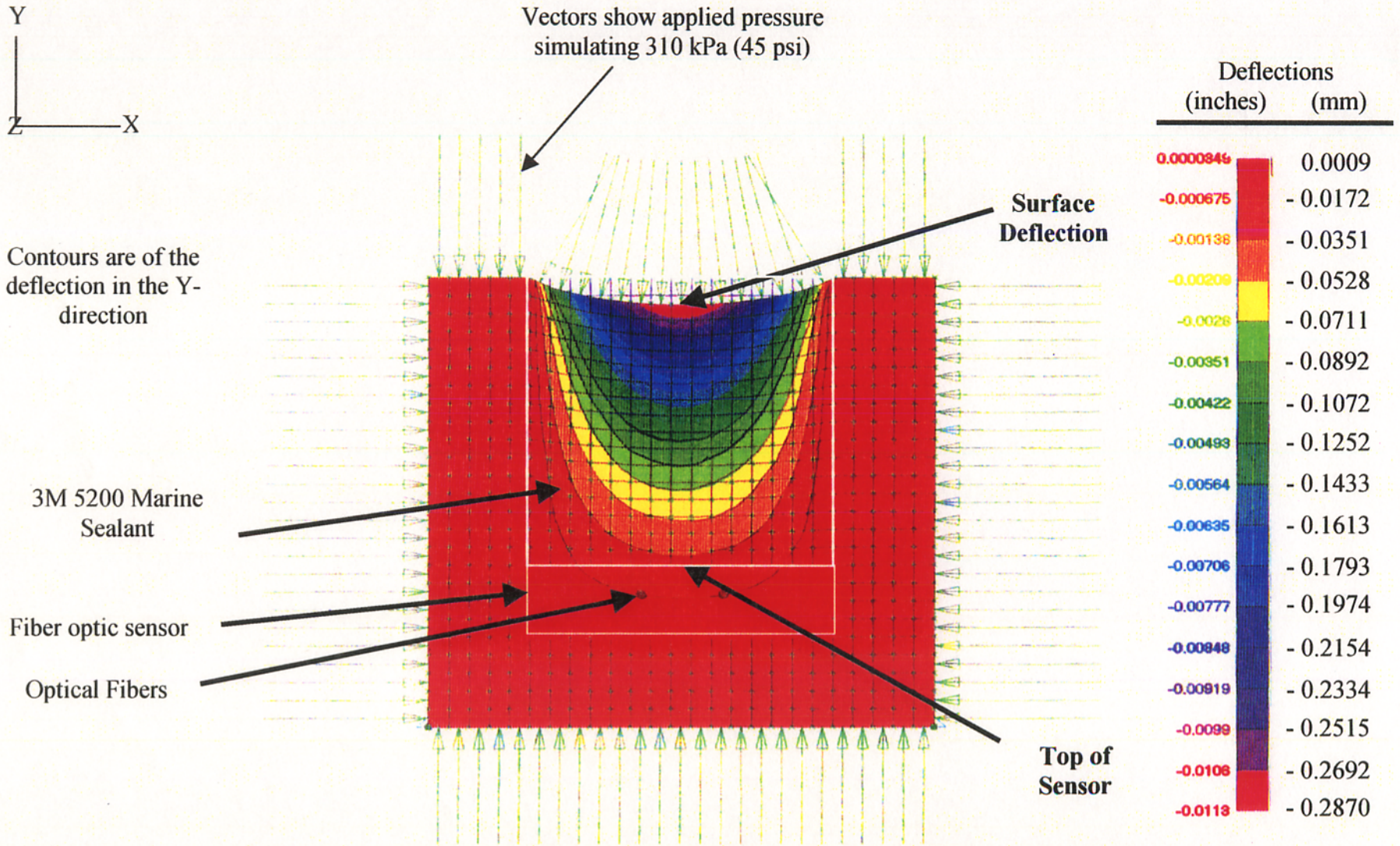

Figure 4.6 Model 2 Deflections from 310 kPa (45 psi) pressure on FOS overlaid with 3M 5200 Marine Sealant installed in a rigid channel

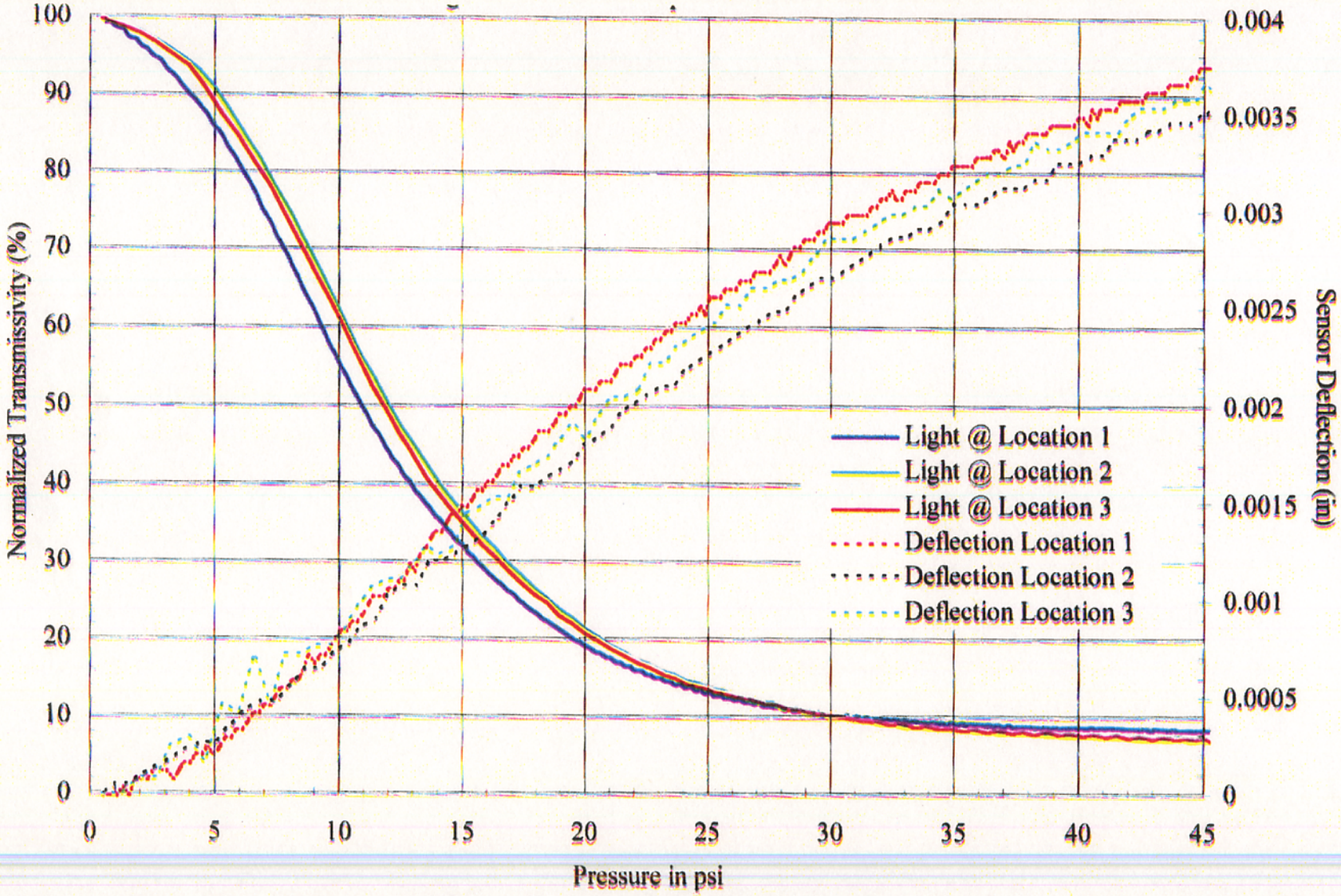

Figure 4.7 Sensor Epoxied to Bottom of Channel

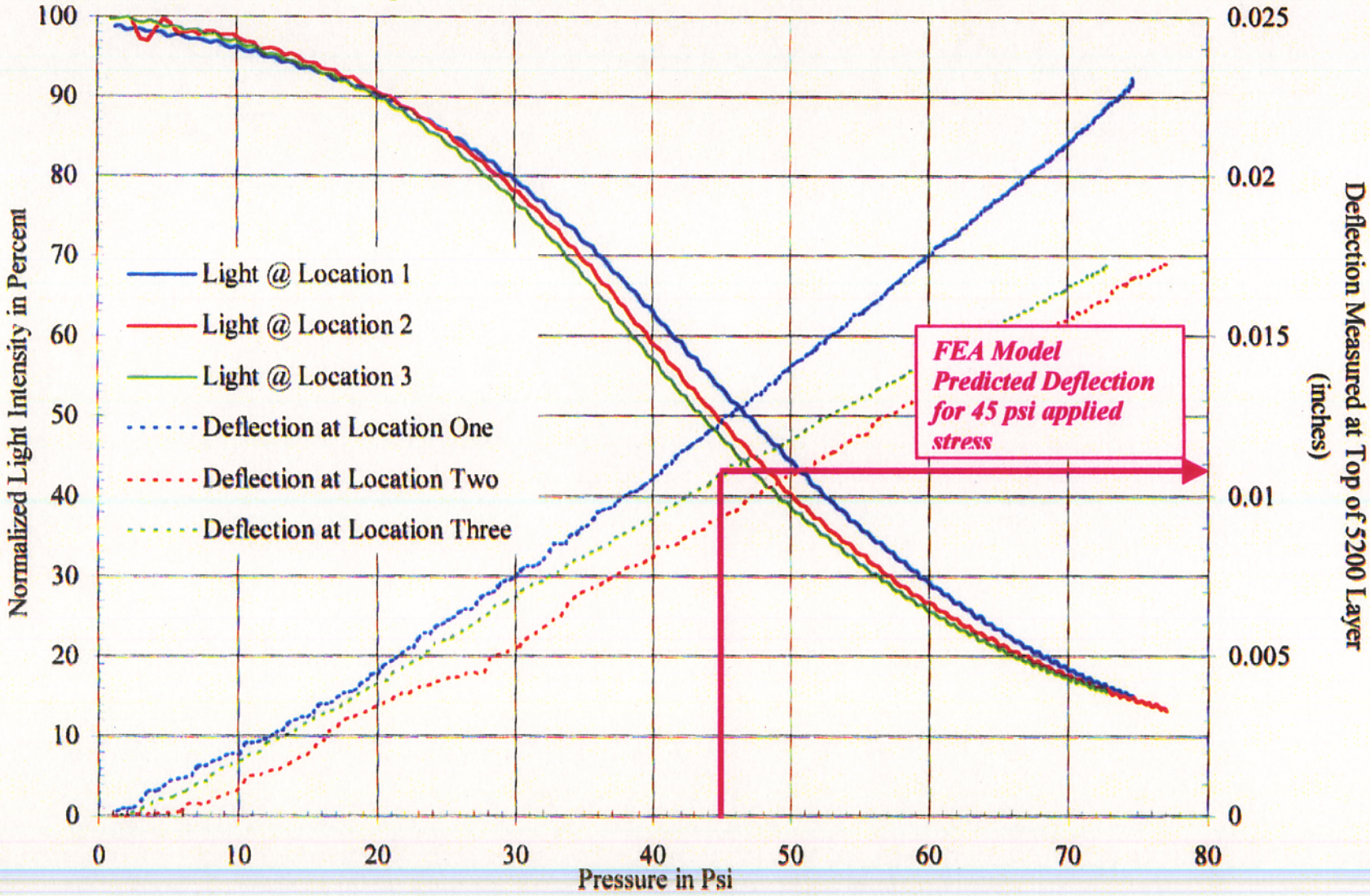

Figure 4.8 Sensor Overlaid with 5200 in a Channel

Table 4.5: Measured Stress and Deflection Values for Comparison to Channel/FOTS/5200 FEA Model

Surface deflection of the 5200 (corresponding FEA node 953)	0.011" ± 0.0015" (± 14%)
Surface deflection in the sensor (corresponding FEA node 1401)	0.0011" ± 0.00015" (± 14%)
Stress at the center top of the sensor (corresponding FEA element 594)	-11.6 psi ± 0.7 psi (± 6%)

Table 4.6 presents fourteen iterations of the model in the order in which they were performed. The analysis began with the 5200 having an input for Poisson's ratio of 0.47 (assuming it was an ideal rubber) [Horhorta, 1998] and an elastic modulus of 600 psi. A Poisson's ratio of 0.3 was assumed for the FOTS, while a value of 700 psi for the elastic modulus was calculated from the data given in Figure 4.7. Again, recall that the measured surface deflection was 0.011-inches and the measured deflection of the sensor was 0.0011-inches, while the measured stress to cause 50 percent light loss was 11.6 psi.

Referring to Table 4.6, iteration 1, the 13.5-mil deflection calculated at the top of the 5200 layer was 2 mils greater than the measured value of 11 mils. The modeled sensor deflections were 0.79 mils larger than the target value of 1.1 mils. The elastic modulus of the sensor and 5200 was increased during iterations 2 and 3 and the corresponding sensor and 5200 deflections decreased. However, the stresses on the sensor became larger than 15 psi.

Table 4.6: FEA Sensitivity Analysis Results

Iteration Number	Complaint Bonding-Agent		Fiber Optic Sensor		FEA Deflections (Mils)		Predicted Stress at Top-Center of FOTS
	Elastic Modulus (psi)	Poisson's Ratio	Elastic Modulus (psi)	Poisson's Ratio	Surface of Bonding Agent	Surface of the Sensor	
1	600	0.47	700	0.30	13.50	1.49	-14.10
2	700	0.47	1100	0.30	11.47	1.09	-15.20
3	700	0.47	1300	0.30	11.42	0.97	-15.70
4	700	0.47	1300	0.15	11.43	1.00	-15.50
5	700	0.47	1300	0.40	11.40	0.92	-15.90
6	700	0.35	1300	0.30	11.99	0.86	-13.60
7	700	0.35	900	0.30	12.08	1.10	-12.70
8	750	0.35	900	0.30	11.28	1.10	-12.50
9	750	0.30	900	0.30	11.43	1.05	-11.87
10	750	0.30	750	0.30	11.45	1.18	-11.34
11	750	0.30	800	0.30	11.43	1.10	-11.50
12	750	0.35	800	0.30	11.31	1.19	-12.20
13	750	0.35	750	0.30	11.33	1.24	-12.00
14	750	0.35	750	0.35	11.32	1.22	-12.10

To bring the deflection and stress values within proximity of the target values, Poisson's ratio of the 5200 was lowered to 0.35. Iteration 10 incorporated the same elastic properties for both materials. The predicted compressive stress of 11.34 psi at the sensor surface was lower than desired. Further iterations brought the value closer to the 11.6-psi target. If the properties of the FOTS/5200 were equivalent, then both materials could be modeled congruently in the third model. The final iteration for the FOTS/5200 system was modeled using an elastic modulus of 750 psi and a Poisson's ratio of 0.35.

The Table 4.7 is a comparison of the experimentally measured deflections with those predicted by the finite element analysis. Values predicted by the model fall within the measured range of values for all three parameters: The elastic modulus of each material had the greatest affect on the predicted deflections for that material, while Poisson's ratio for both materials had the greatest affect on the predicted stress at the top of the sensor.

The 5200 elastic modulus predicted by the model was 25 percent larger than the value determined by the unconfined compression test performed (750 psi versus 600 psi,

respectively). This was attributed to the top corner of the aluminum channel deflecting inward 0.0006-inches in the model. This inward channel deflection would increase the confining stresses on the 5200 in the channel and cause the elastic modulus to increase.

Table 4.7: Comparison of Critical Measured and Predicted stresses and Deflections for the FOTS Encapsulated in a Rigid Channel

	Experimentally Measured (Table 4.8)	FEA Predicted (Table 4.9)
Deflection at Top of the 5200 Layer	0.011" ± 0.0015" (± 14%)	0.01132"
Deflection at Top of the Sensor	0.0011" ± 0.00015" (± 14%)	0.00122"
Stress at Sensor Top	-11.6 psi ± 0.7 psi (± 6%)	-12/1 psi

The relatively low Poisson's ratio value that the FEA model predicts, may be a result of the copious number of CO_2 bubbles that formed during the 5200 curing process. The material could have changed volume as the bubbles compressed therefore, leading to a lower than anticipated Poisson's ratio.

4.4. FEA Model and Result for FOTS Installed Vertically in Flexible Pavement

The 29" by 28" *plane-strain 3-D* model simulating the FOTS installed in flexible pavement was comprised of 1398 nodes and 595 elements and is presented as Figure 4.9. The hot-mix asphalt layer was 4-inches thick; the lime rock base 8-inches; the subgrade sand was modeled as 16-inches. The nodes along the base of the model were fixed while the nodes along each vertical edge of the model were free to translate in the Y-direction (load direction). This allowed the material within the model to deflect and behave as though confined within an infinite half-space. Two enlarged images show the largest

model dimension was 30 inches, while the smallest element was 0.030" square (1000:1). This model was designed so that all nodes were coincident. The mesh systematically became finer, near the vertical groove so that nodal deflections were able to be determined with a high degree of confidence. The zone near the vertical groove or kerf is enlarged (Figures 4.10 and 4.11) with the latter figure showing the position of nodes that provided FOTS deflections.

The following assumptions were made for the third model:

- A diamond blade of thickness 0.090" was used to cut the two grooves for installing the two sensors. The actual width of the cut was wider than the blade and was measured at 0.125". Within this width, the 0.075" ± 0.004" thick sensor and the encapsulant were placed. The model used a width of 0.120" with four elements each 0.030" square, to model the groove filled with 5200 and FOTS (Figure 4.10), an overall difference of about 4 percent. The channeled FOTS/5200 system model (i.e., the second FEA model) showed that these two materials could be modeled congruently. It was therefore assumed that the models' additional stiffness, which would be provided by the extra HMA surrounding the kerf, would be negligible.

- The FOTS was designed as the two central elements in a groove, four elements wide (Figure 4.11). In reality, the FOTS could be situated anywhere in the groove because the installation could not be precisely controlled. Deflections of the nodes to either side of the centerline were used to determine a predicted movement of the FOTS. The sum of these two deflections was the predicted deflection in the FOTS. Based on the assumption that the materials being modeled were linear-elastic and the fact that the actual sensor was 0.075" ± 0.004" thick; not 0.060" per the model, this value was multiplied by 1.25.

- All materials were modeled as linearly elastic, homogenous and isotropic.

- Vehicles traveled at relatively low speeds simulated static loading.

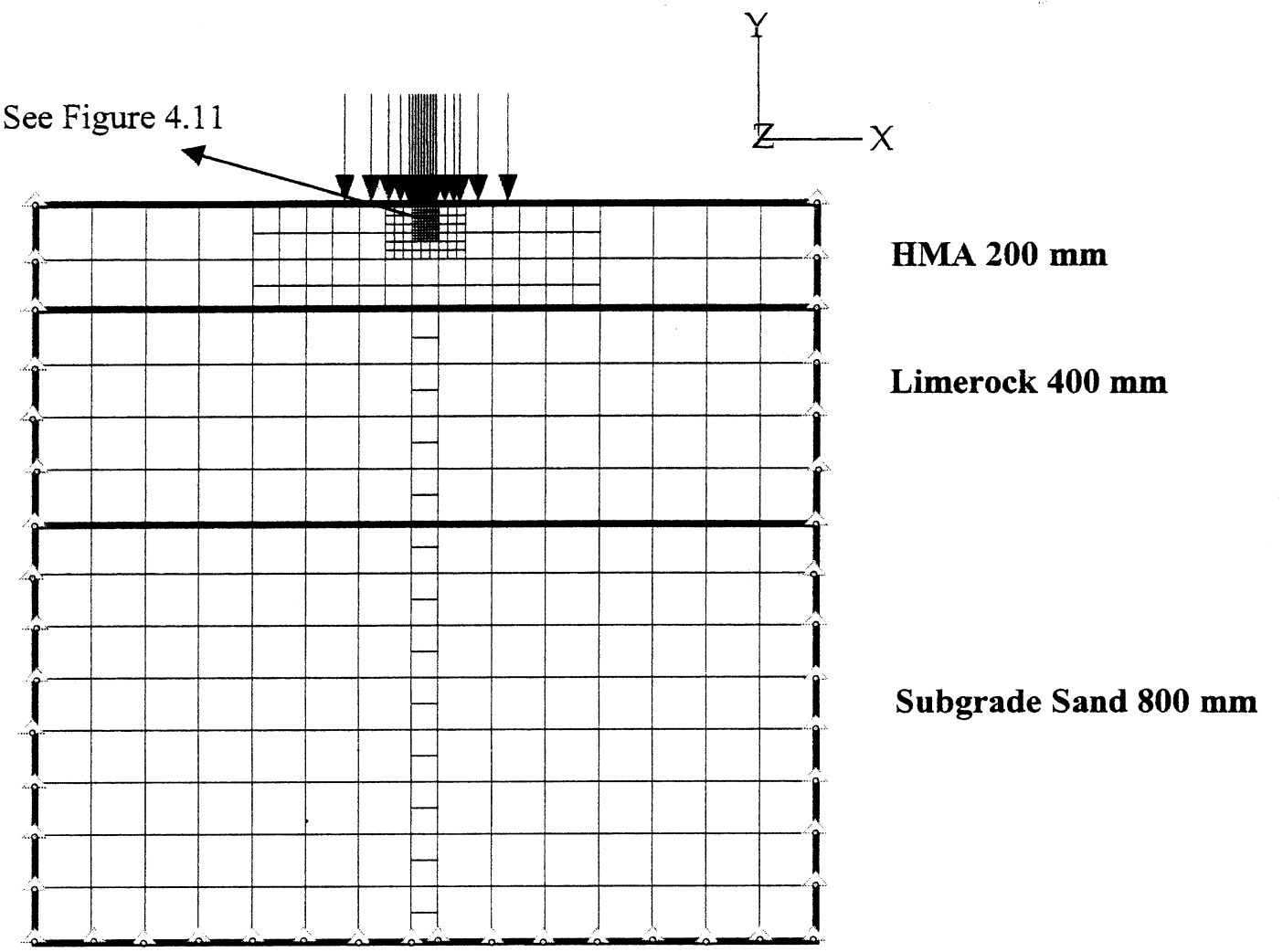

Figure 4.9 FEA Model 3 simulating a FOS installed in a vertical groove in flexible pavement

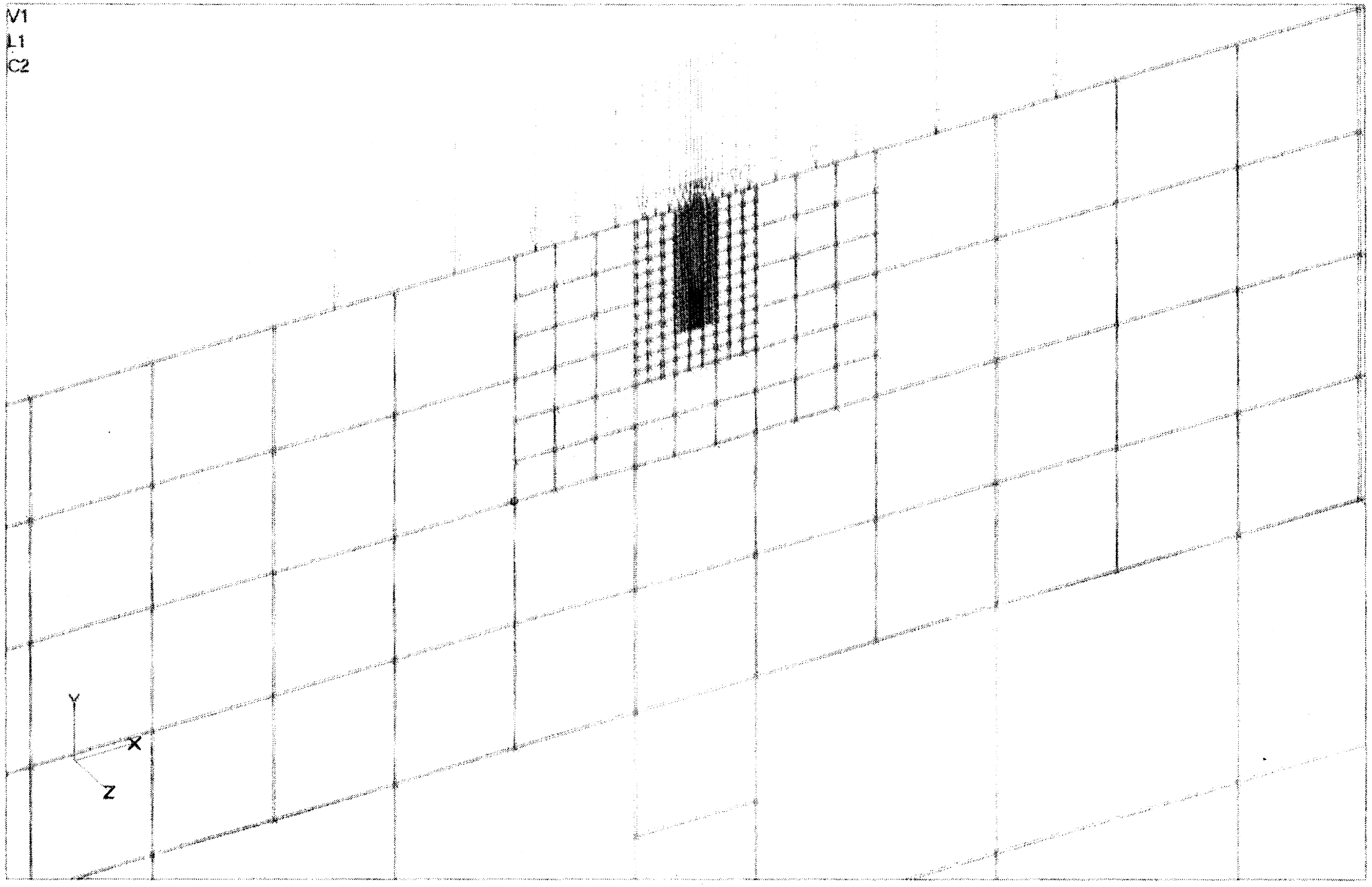

Figure 4.10 FOS Installed in a Vertical Pavement Groove

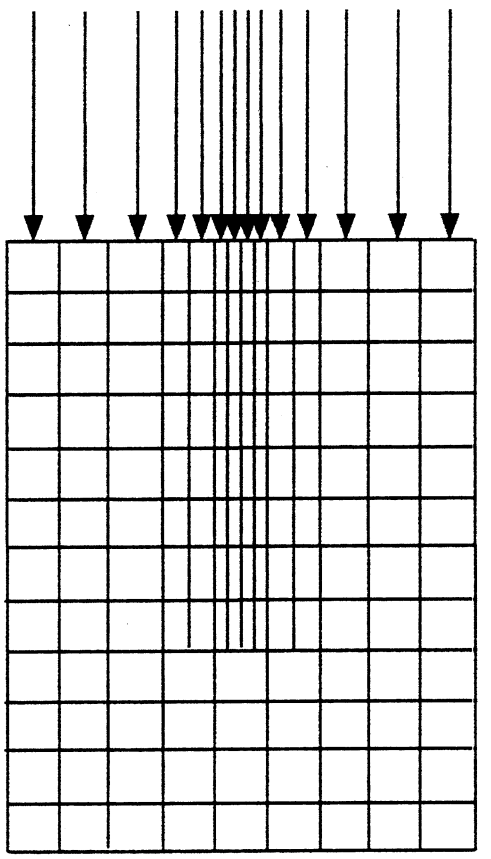

Figure 4.11 Close – up of FEA mesh in zone near sensor

The design of the model included the following increments of tire contact lengths to be modeled. They correlated to discrete dimensions in the element mesh: 3.24", 5.40", 7.56", and 9.72". Contact pressures used in the model to simulate automotive tires were 35 psi and 110 psi to simulate truck tires.

Data acquired during this study indicated that as the weight on a radial tire increased, the length of the footprint increased, while the width remained constant. Table 4.8 provided the necessary data for determining the weight distribution of the truck used for acquiring FOTS field data. A fully loaded well-designed truck equally distributed the load to all three axles. All six tires on the trucks were identical having 12.5"widths. If the contact area was assumed circular with the internal tire pressure equaling the contact stress, the empty truck's front tire contact length was estimated to be 4.4", while the rear tire contact length was calculated to be 2.6". Because these values were observed to be much too small, a test was performed to determine contact lengths.

Table 4.8: Weight Distributions in an International Class 6 Concrete Truck (Suddath Van Lines, Melbourne, Florida, Feb. 5,1997)

Axle	Empty Class 6 Concrete Truck Weight (lb.)	% Wt.	Truck Loaded With 25 kips of Gravel (lb.)	% Wt.
Front Axle	12,640	45	18,100	34
First Rear Axle	7,720	28	17,580	33
Second Rear Axle	7,320	27	17,240	33
Total Weights	27,680	100	52,920	100

Note: Empty ready-mix truck had full fuel tank plus 100 gallons of water.

Two sheets of paper were inserted between the pavement and the front and rear treads of a tire. The tire footprint dimensions were measured from the imprint on the paper and the data presented in Table 4.9. The truck tire contact lengths ranged from 7.7 to 10.3 inches while the Ford Pickup contact lengths ranged 5.4 inches. Figure 4.12 shows a typical high-pressure tire's contact pressure rose to 80 percent of its nominal value within the first inch of contact length [Ford and Charles, 1988]. Examination of this figure shows

that the maximum contact pressure occurs approximately 1-inch inform the edge along the tire length. It was therefore, assumed that two-inches should be subtracted from the measured values presented in Table 4.9 to acquire a reasonable value for the maximum contact length. The FEM contact length should have been equal to the measured contact length, minus two-inches, (e.g., for the Concrete Truck, 10.3 – 2.0 = 8.3 inches) however, the discrete increments of elements used in the model were smaller than the measured values because the mesh was developed based on the layer geometry (Table 4.9).

Table 4.9: Comparison of FEM and Measured Tire Contact Lengths

Axle	Measured Contact Length for Concrete Truck tire: 445/65R22.5	FEM Contact Length	Measured Contact Length for F-150 Pickup tire: P215/75R15	FEM Contact Length
Front	10.3"	7.6"	7.5"	5.4"
Rear	7.7"	5.4"	7.5"	5.4"

Note: Desired contact length should have been 2-inches less than measured lengths, however, FEM element sizes were controlled by layer geometry.

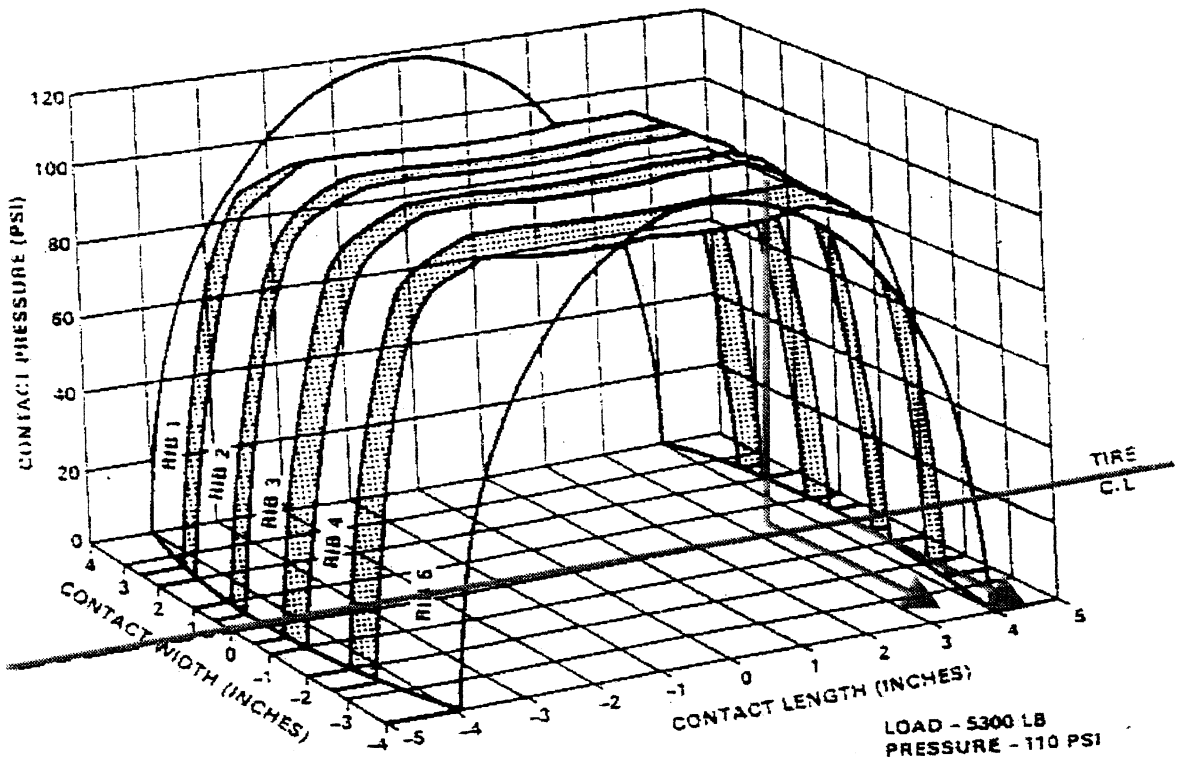

Figure 4.12 Contact Pressures for a Typical High Pressure Tire [Ford and Charles, 1988]

A sample FOTS deflection calculation is presented in Table 4.10. Figure 4.13 shows the groove mesh of the model on the right side. The graph on the left will be discussed later. The five, circled nodes within the mesh exhibit negative X-deflections and were utilized for this calculation. The nodal deflections were read in descending order of depth into the pavement. These deflections were for the right half of the sensor:

Table 4.10 Sample FOTS Deflection Calculation

Node Number	Deflection
84	-0.000151 inches
86	-0.000151 inches
88	-0.000146 inches
90	-0.000139 inches
92	-0.000132 inches
Average = -0.000144" *2 (to obtain total FOTS deflection)= -0.000288" = -0.000288" * 0.075"/0.060" (correction for sensor thickness) = -0.000360" (answer)	

The last value, 0.000360 inches, was the calculated deflection in the sensor. Entering Figure 4.7 from the right, a pressure of 6 psi caused this deformation. Examining the transmissivity curve at 6 psi shows that approximately 15 percent of the light was lost. FOTS waveforms acquired from a small truck and a large truck will be correlated to this transmissivity loss. Data acquired in the laboratory (Figure 3.10) has shown that transmissivity losses were insensitive to the sensor actuation length (for L> 4.5"). If this were not the case, then the example just presented would have to be worked on the appropriate graph for the width of tire that actuated the sensor. It was assumed that tires wider than 4.5 inches all had the same transmissivity and deflection curves. Therefore, this figure was used for all calculations performed in this chapter.

The field data used for comparison to the FEA predictions were acquired two months after the sensors were installed. These waveforms were from the first three inbound concrete trucks. It was assumed that inbound trucks were empty —that all the concrete was delivered to the site. Subsequently, it was learned that this was an incorrect assumption. Many trucks return with a few cubic yards. In addition to the large concrete trucks a small F-150 pickup truck was also used to actuate the two sensors. These same sensors were installed with 5200 on Sept. 12, 1998. The sensitivities of these strapping-tape sensors were close. They were installed in two grooves cut to different depths – 0.62" and 0.82".

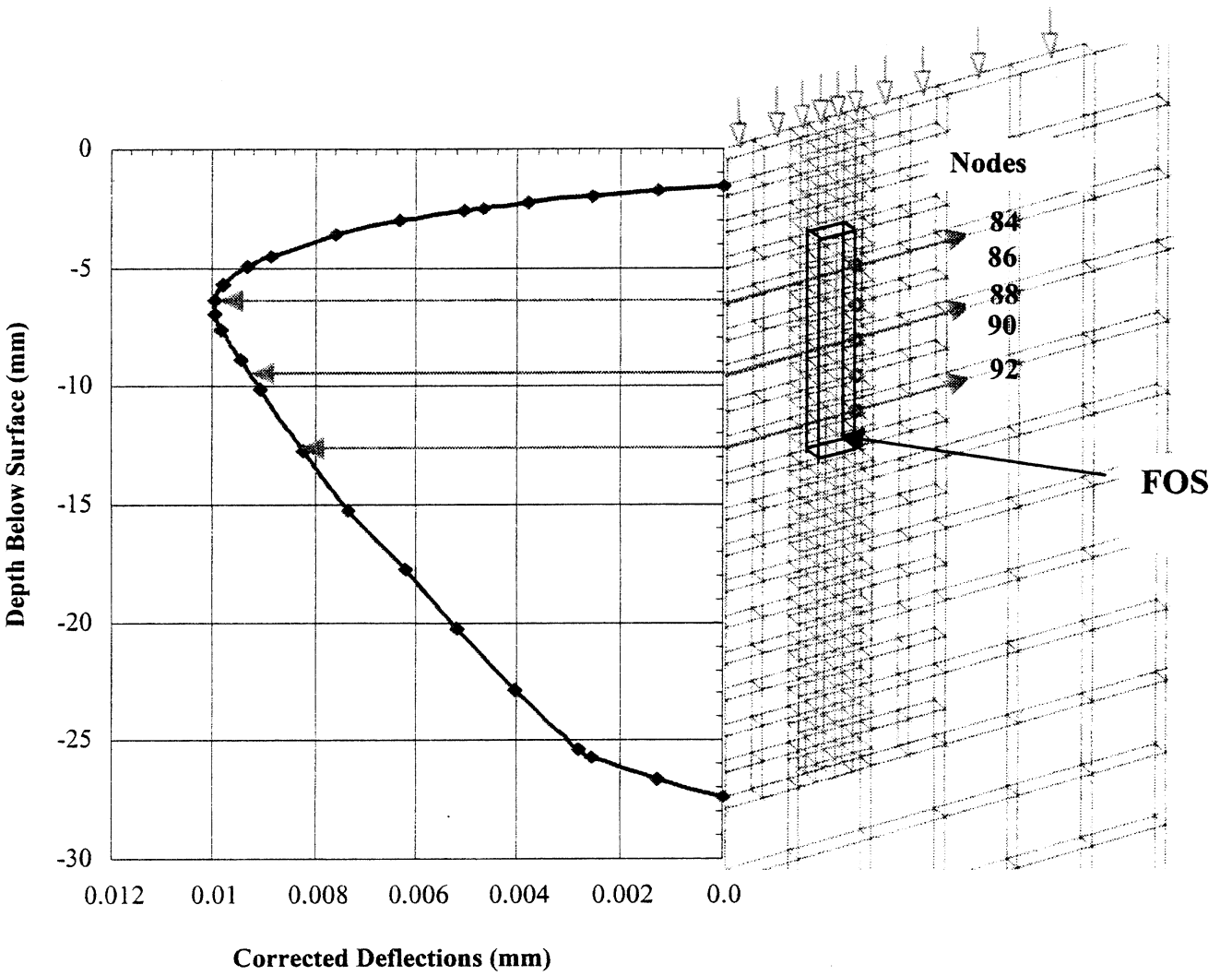

Figure 4.13 Model 3 FEA deflections versus depth for 245 kPa (35 psi) tire pressure simulation

The finite element analysis was performed assuming static loading whereas the field data were acquired dynamically. However, if the vehicle was rolling very slowly it was assumed to be a quasi-static waveform. Figure 4.14 shows the waveform data as the pickup traveling at 7-mph actuated the sensors. The sensor installed near the surface of a 0.62" deep groove lost between eight and ten percent light. The sensor installed near the surface of a 0.82" deep groove lost approximately 18 percent light. The signal to noise ratio was extremely high at nearly one. When the test was repeated by manually pushing the truck over the sensors, the waveforms were very similar to those acquired at 7-mph.

When the concrete truck traveling at approximately 7-mph actuated the sensor installed in a 0.62" deep groove, light losses averaged 51 percent for the front axle and 36 percent for the rear axle (Figure 4.15). The waveforms for the 0.82" deep groove showed that the front axle of a concrete truck produced a 72 percent light loss, whereas the lighter rear axle produced a 51 percent light loss (Figure 4.16).

Table 4.11 shows a comparison of the predicted light losses from the finite element model with the light losses measured in the field. Comparisons were made for two types of vehicles for two sensors embedded in different groove geometries. Because excellent correlations exist between predicted and measured losses, for several cases, it was concluded that the modeling was performed correctly.

Table 4.11: FEA Sensor Deflections from Eleven Iterations of Model 3 (Eckroth, 1999)

Iter. No.	Groove Depth (in)	Groove Width (in)	Elastic Moduli (ksi)			Contact Pressure (psi)	FOS Deflections (μin) for various tire contact lengths*				Optimal Depth to FOS **(in)
			HMA	Base	Subgrade		3.2"	5.4"	7.6"	9.7"	
1a	0.72	0.12	310	75	30	100	--	573	626	--	0.21
1b						35	142	183	--	--	0.21
2a	0.72	0.12	200	75	30	110	--	747	797	808	0.21
2b						35	195	238	--	--	0.21
3a	0.72	0.24.	200	75	30	110	--	286	316	--	0.30
3b						35	66	--	--	--	0.30
4a	1.08	0.12	200	75	30	110	--	1130	1220	1237	0.18
4b						35	291	360	--	--	0.18
5a	1.08	0.24	200	75	30	110	--	590	645	--	0.30
5b						35	142	188	--	--	0.30
6a	1.2	0.12	200	75	30	110	--	1250	1350	--	0.15
6b						35	320	399	--	--	0.15
7a	1.2	0.12	3000	75	30	110	--	216	--	--	0.24
7b						35	--	69	--	--	0.24
8a	1.2	0.12	200	30	30	110	--	1730	--	--	0.15
8b						35	--	551	--	--	0.15
9a	1.08	0.12	200	75	30	110	--		--	--	0.06
9b						35	--	393	--	--	0.06
10a	0.63	0.12	200	60	30	110	--	722	777	--	0.15
10b						35	185	230	--	--	0.15
11a	0.84	0.12	200	60	30	110	--	986	1067	--	0.15
11b						35	251	314	--	--	0.15

* Tire contact lengths correlate to discrete dimensions in the finite element mesh; not to measured lengths

-- Implies values not calculated ** depth to top of sensor

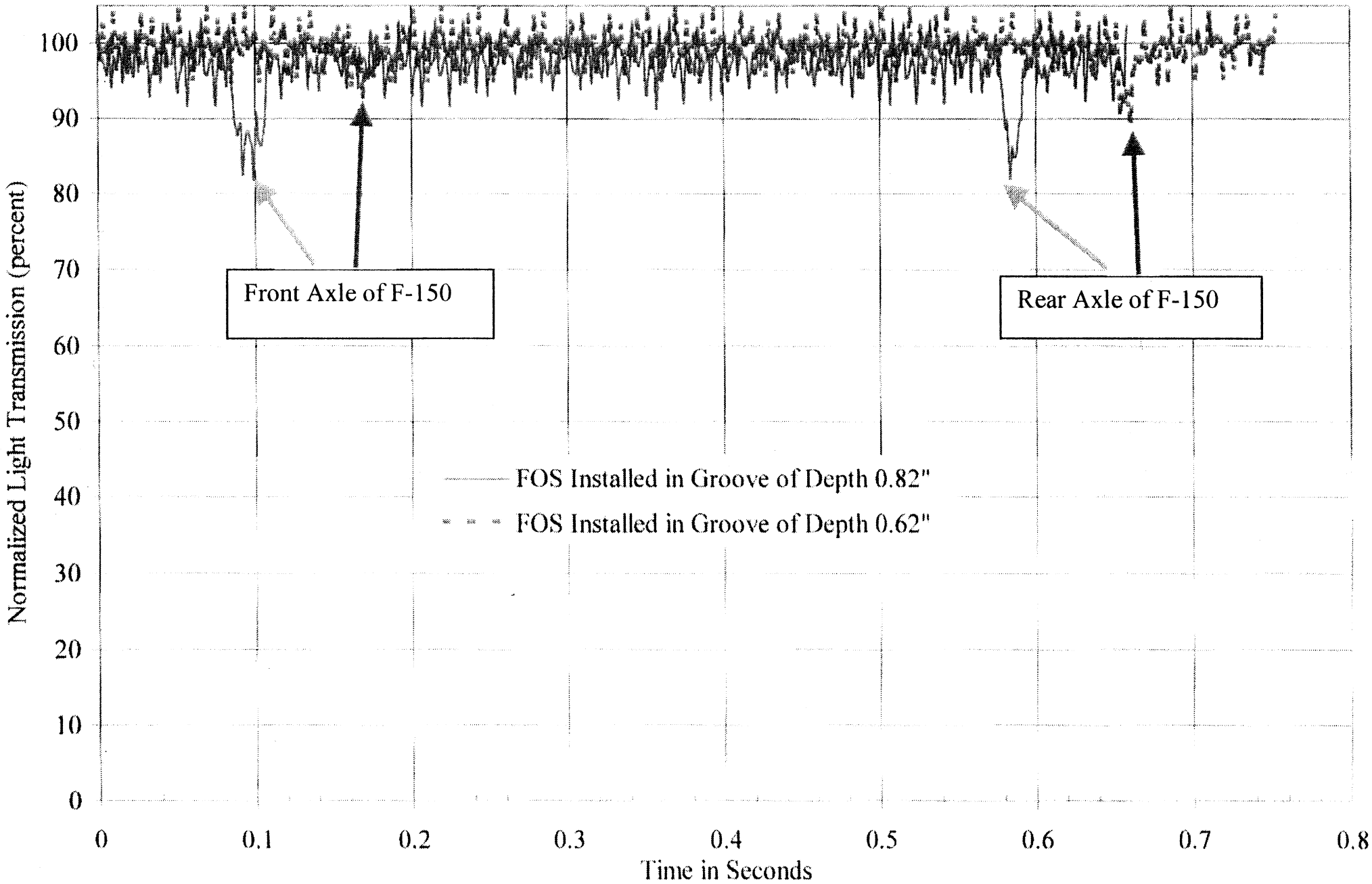

Figure 4.14 F-150 Pickup Truck Actuating Sensors Installed Vertically with 5200

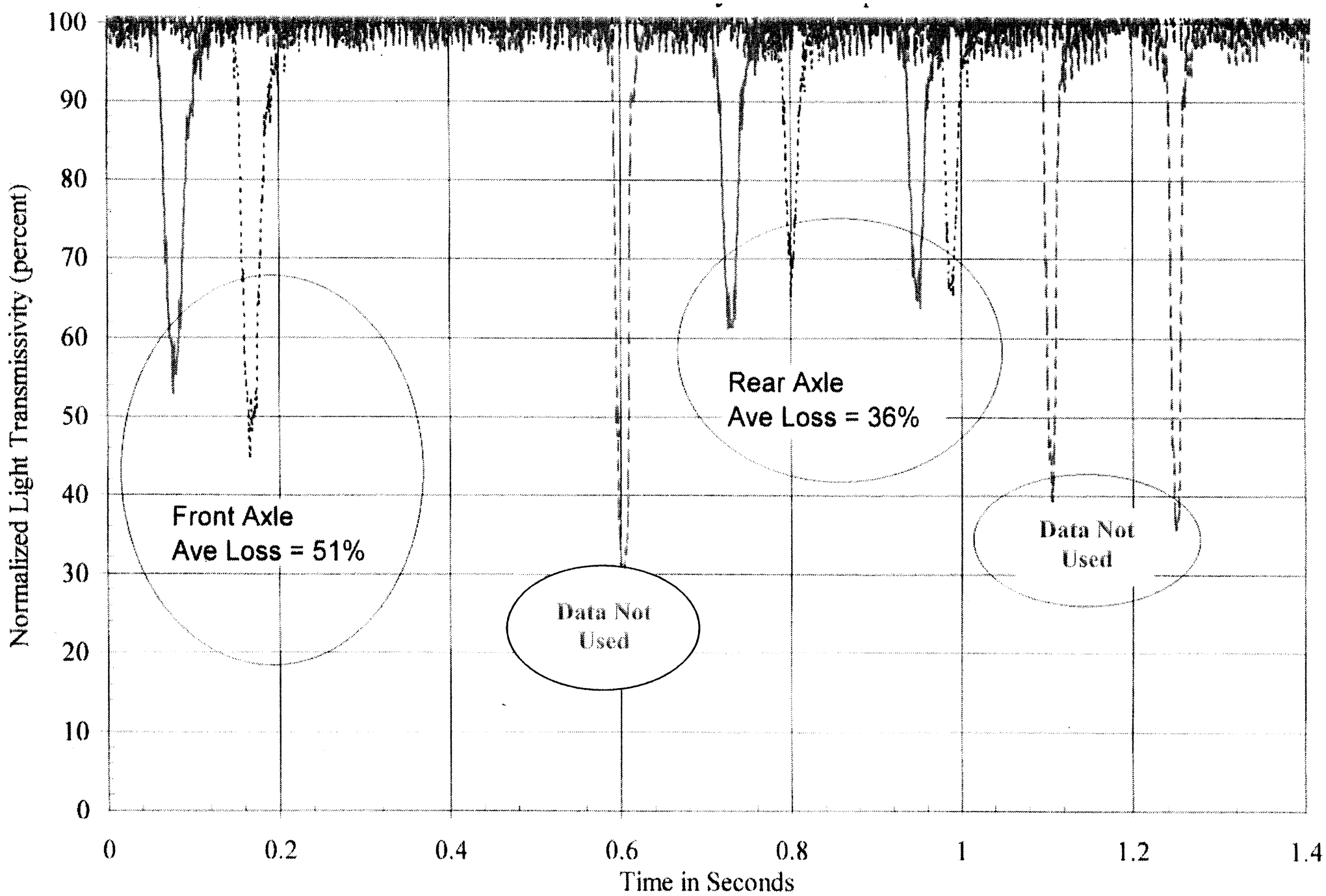

Figure 4.15 Concrete Trucks Actuating a Vertically Installed FOS (Groove was 0.12" Wide by 0.62" Deep)

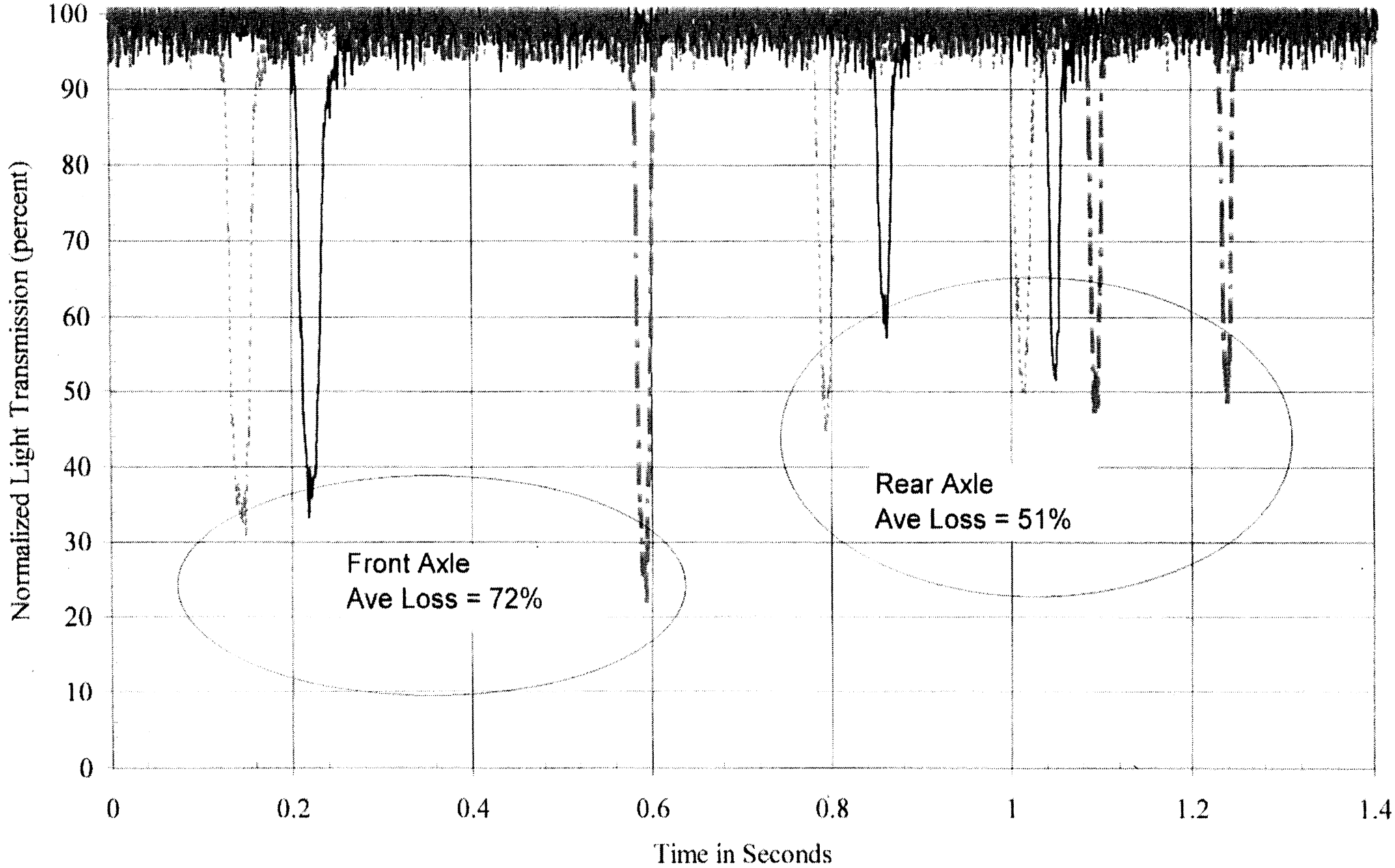

Figure 4.16 Concrete Trucks Actuating a Vertically Installed FOS (Groove was 0.12" Wide by 0.82" Deep)

Table 4.11 presents deflection data from the FEA for factors that have an affect on the deflection of the FOTS embedded in the groove. These factors were:

1. Groove depth
2. Groove width
3. Pavement type (rigid versus flexible)
4. Elastic Modulus of the base/subgrade
5. Vertical location of the FOTS in the groove

Before each of these items is discussed in detail, comments regarding the iterative process of changing the groove geometry and material properties are made. The first iterations in Table 4.11 used a groove depth of 0.72" – between the actual dimensions of 0.62" and 0.82". When this model was designed the investigator did not think that such close agreement between the model and empirical data (Table 4.12) were possible. The pavement model used 310-75 30 ksi for the elastic moduli of the pavement layers because these values provided close correlation to the measured deflection bowl obtained from FWD tests. MODULUS 5.0 calculated the elastic modulus of the limerock base at 60,000 psi. It was assumed that this value was too low in light of the very high moduli values presented in the literature search and the lack of confidence other engineers and scientists had expressed with regard to back-calculated stiffness values [Nazarian, *et.al*, 1988; Horhorta, 1998]. The limerock stiffness was changed to 75,000 psi and used in the first model presented in this chapter. The objective of that model was to establish stiffness values for the three pavement layers. Consequently, initial iterations of this third FEA model used a modulus of 75,000 psi for the limerock base. After nine modeling iterations it was decided to default to the 60,000 psi FWD value and rebuild the model to duplicate the two groove depths as closely as possible.

1). Affect of Groove Depth Both the model and the field data supported the conclusion that the deeper the groove the greater the sensor deflection. Iterations two and four as well as iterations ten and eleven supported this conclusion. The groove depth assumed in iteration two was less than that in four as was the groove depth assumed in ten less than that in eleven. In both comparisons, the sensor deflections in the shorter groove were less than those in the deeper groove. For iterations two and four, the shorter

groove was 66% shallower than the deeper groove and the FOTS deflections show that same percent difference between the two. For iterations ten and eleven, the shorter groove was 74% of the longer groove, while the corresponding FOTS deflections for the shorter groove were also 74% of those for the deeper groove. An analogy to this mechanism is found in a kerf cut in a wooden plank. The deeper the cut, the smaller the gap becomes at the top of the kerf when the plank is placed in bending (under the same loads).

2). Affect of Groove Width The material properties in one column of elements on either side of the groove were changed to reflect the properties of the 3M 5200 bonding-agent. The groove was modeled using four columns of elements 0.03" wide. The elements on either side of the groove were 0.06" square. This change formed a groove 0.24" wide (twice the actual size) and 0.72" deep (iteration three). If the F-150 pickup truck actuated a sensor installed in this wide groove, 91 microinches of FOTS deformation was predicted. Referring to Figure 4.7, expected light losses were calculated at less than three percent. When compared to iteration two, the predicted light loss for this same contact length and pressure (238 μin) was eight percent. When the groove geometry was changed to 1.08" deep by 0.24" wide (iteration five), the simulated F-150 pickup would cause a sensor deformation of 188 microinches. The calculated light loss for this deflection was five percent. Compare this value to the deflection of 360 microinches predicted in iteration four. The calculated light loss for this deflection was 15 percent. It was concluded that a wider groove transferred less force to the sensor.

3). Affect of Pavement Type The HMA was assigned an elastic modulus of 310,000 psi, as shown in iteration one. Using this value, the calculated light losses, based on the FOTS deflections being used in Figure 4.7,were about half those values being measured in the field for both vehicles (Figures 4.14 and 4.15). The stiffness of the HMA was then changed to 200,000 psi. This lower value was still within the range measured by the unconfined compression test. The room temperature stiffness value for the HMA in this test was 260 ksi. The second iteration predicted a light loss from the 35 psi pickup truck tire at ten percent, much closer to the 5 – 15 percent losses observed (Figure 4.14).

Changing the elastic modulus of the top four inches of pavement to 3,000,000 psi (iteration seven) simulated a rigid concrete pavement. It was predicted that the rear wheels of the concrete truck would cause a deformation of 216 microinches in the sensor. This equates to a loss in transmissivity of seven percent. The 69 microinch deflection predicted for the pickup truck could be lost in the electrical signal noise. It was concluded that an automobile may not actuate the FOTS if the sensor were installed vertically in rigid pavement.

4). Elastic Modulus of the base/subgrade A two-layer system was simulated by changing the elastic modulus of the base to 30,000 psi so that its stiffness was equal to the subgrade (iteration eight). The affect upon the FOTS output was significant. When installed in a groove of width 0.12" and depth 1.2", FOTS deformations were predicted to increase from 399 microinches (iteration 6) to 551 microinches when actuated by the 35 psi F-150 pickup tire. These deformations equate to calculated transmissivity losses of 12 percent and 26 percent, respectively. It was concluded that the FOTS output was sensitive to the stiffnesses of all the pavement subgrade.

5). Vertical location of the FOTS in the groove Installing the sensor close to the surface of the pavement was the normal installation procedure. This made sense because the bottom of the groove could not close. Referring to Figure 4.13 the dashed line represents deflections found in the sensor nodes with respect to depth. This dashed curve was for the loading case where all the bonding-agent surface elements were loaded. When the bonding-agent was flush with the surface of the pavement, groove deflections described by the dashed line were predicted. This line shows that the sensors should be installed at least 0.25" below the surface to overcome the surface affects. The surface effect could be considered the spreading of the groove as the bonding-agent was loaded. The last column of Table 4.11 shows the depth to the FOTS necessary to obtain the deflections predicted in that table. All eleven iterations were analyzed for optimum FOTS placement in the groove. If the load applied through the bonding-agent was removed (iteration nine), then the groove was predicted to close in a linear manner to the top of the pavement. Sensor nodal deformations were presented as the solid line in Figure 4.13 for this load case. When the bonding-agent was assumed to be convex with

the surface of the pavement, sensor deflections described by the solid line in Figure 4.13 were predicted. This condition was assumed possible due to the irregularities encountered along the pavement surface near the sensors.

Table 4.12: Comparison of Measured and Predicted Transmissivity Losses for Two Embedded FOTS

Vehicle Model	F-150 Pickup – 35 psi		Concrete Truck (Class 6) – 110 psi			
Contact Length	Either Axle 5.4"		Front Axle 7.6"		Rear Axles 5.4"	
Groove Depth	0.62"	0.82"	0.62"	0.82"	0.62"	0.82"
Measured loss	-10%	-15%	-51%	-72%	-36%	-51%
Predicted loss	-10%	-15%	-41%	-55%	-35%	-52%
Difference (%)	0%	0%	-20%	-24%	-2.8%	+2%

Sensor deflection results from iterations 10 and 11 presented in Table 4.11 were converted to sensor transmissivity losses using the curves in Figure 4.7. The calculated transmissivity losses were compared to transmissivity losses measured in the field in Table 4.12. The modeled groove depth was slightly different from the actual pavement groove. The 0.62" deep groove was modeled as 0.63" while the 0.82" deep groove was modeled as 0.84".

Referring to Table 4.12, excellent correlations exist between the model and measured light losses for the F-150 pickup. The model and field data for the lighter rear axle of the concrete truck correlate within two or three percent. The heavier from axle of the concrete truck caused more deflection in both grooves than predicted by the linear analysis performed in the finite element model. The difference between the measured loss and predicted losses was about 20 to 25 percent for the front axle of the concrete truck. A possible explanation for the difference between the model and measured values was that the tire contact length used in the model was about 10 percent smaller than the measured value. Increasing the contact area would increase the deflections and corresponding light losses and could account for a significant portion of the variation between measured and predicted value

Chapter 5

Field Program Results

5.1 Pre-Site Testing

Prior to sensor installation and monitoring, a strategy was developed so that the multiple variable combinations could be examined in a manner that fit into a time schedule for data collection. Availability and capacity of testing equipment and rapid surface temperature changes controlled the scope of data collection.

5.1.1 FOTS Telemetry Site Evaluation

On December 7, 1998, a fiber optic traffic sensor site was constructed on A1A in Melbourne Beach, Florida, at telemetry site #284. Ten sensors were installed with different encapsulants, sensor orientations and sensor depths. The intent was to determine which sensor configurations detected vehicle axles when connected to a Diamond® Traffic Classifier. This field site provided insight to which types of encapsulants protect the fiber optic traffic sensor, while producing a strong signal output. The testing performed at telemetry site #284 evaluated the role of the sensor for axle detection and vehicle classification, focusing on the accuracy of the on/off signal generation produced by the sensor. This test site also confirmed that vertically installed sensors produced consistently accurate signal generation and excellent longevity in flexible pavement. In addition, certain horizontally installed sensors, although highly sensitive to traffic detection, received too

much stress, produced 100 percent light loss, and failed within two months [Cosentino and Grossman, 1999].

Results from the A1A site revealed the benefits of vertical ProSeal 6006EX® for sensor longevity. This newer polyester resin was used for the installation of the last two fiber optic sensor installation projects performed by FOTS research staff.

5.1.2 Selected Encapsulants

In order to see effect changes due to different encapsulants, it was assumed that the materials must have significantly different elastic moduli. This was achieved by choosing ProSeal 6006EX® and 3M 5200® Fast Cure Polyurethane. Information on each material is shown in Table 5.1.

The first encapsulant was ProSeal 6006EX®, that had an elastic modulus of 1168 psi and was over 200 percent softer than its predecessor ProSeal 6006®, with an elastic modulus of 2700 psi. Although both ProSeal products were completely activated in 10 to 15 minutes, 6006® was also very easy to mix and pour, making it an excellent candidate for field use.

A marine sealant, 3M 5200® Fast Cure Polyurethane was the second selection. It had an elastic modulus of 600 psi at 32 degrees and 140 degrees Fahrenheit. This product, sold in ready-to-use tubes, was also very easy to apply. It dried tack-free in about one hour, and it cured completely in 24 hours [Eckroth, 1999]. Both products bonded well with the flexible and rigid pavements.

Table 5.1 Final Candidates for Encapsulation Materials Used at Field Sites

Product	Source	Elastic Modulus
ProSeal 6006EX® 2-Part Polyester Resin	RAI Products (Santa Fe Technologies, Gainesville, FL)	8200 kPa (1168 psi)
3M 5200® Fast Cure Polyurethane	3M; Minneapolis, MN (West Marine, Melbourne, FL)	4200 kPa (600 psi)

5.1.3 Pavement Temperature Collection

Before any site construction began, temperature data was collected in the field. Collection took place during the months of August and September 1999. Information was collected on the temperature ranges for rigid (concrete) and flexible (asphalt) pavements. To do this, a surface thermometer with a temperature range from 0° to 300° Fahrenheit was placed on the road surface for approximately 3-minute intervals, and the temperature recorded. If the thermometer remained in the sun any longer, the air temperature inside the thermometer would rise, causing the dial reading to indicate a value higher than the actual pavement surface temperature [Pacific Transducer Corporation, 1999].

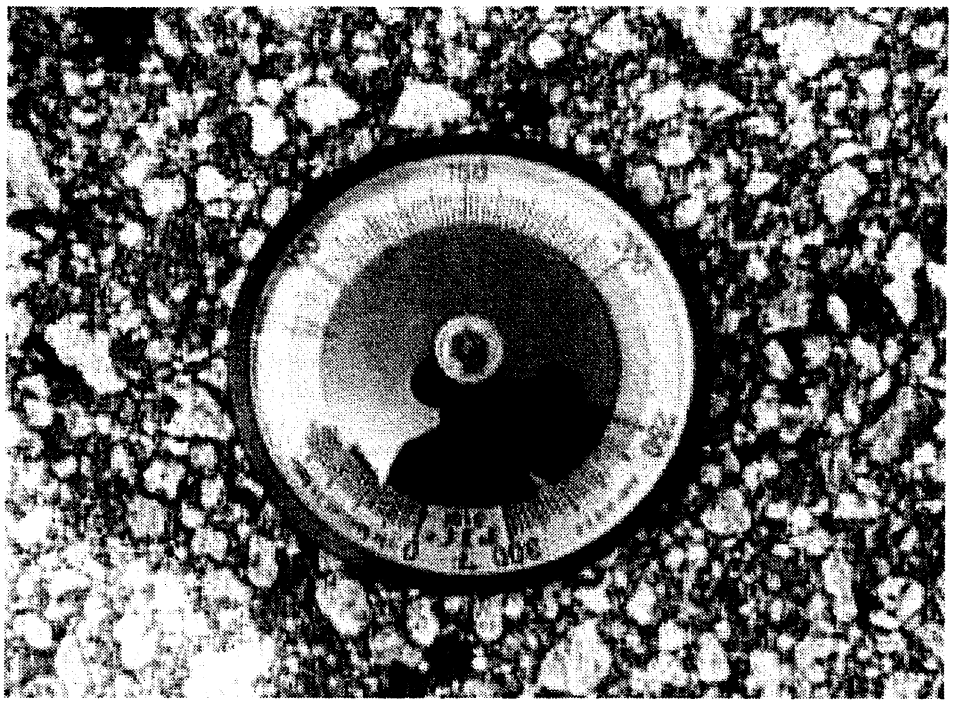

Figure 5.1 Surface Thermometer Reading Pavement Temperature

Temperature readings were collected from sunrise to midday, and again from the afternoon until dusk. These collection periods determined how rapidly temperatures rose and fell on the pavement surface. The surface thermometer was placed on both, rigid and flexible pavements in order to see the temperature rate change and maximum obtainable temperature differences between the two materials. Values were also collected after sundown, to determine what might be the lowest expected pavement temperature.

The most important information collected during this phase of pre-site testing was how quickly surface temperatures changed, and how weather conditions affected changes in surface temperatures. These tests showed that temperatures rose quickly with exposure to direct sunlight. Figure 5.2 showed how pavement surface temperatures change rapidly with time.

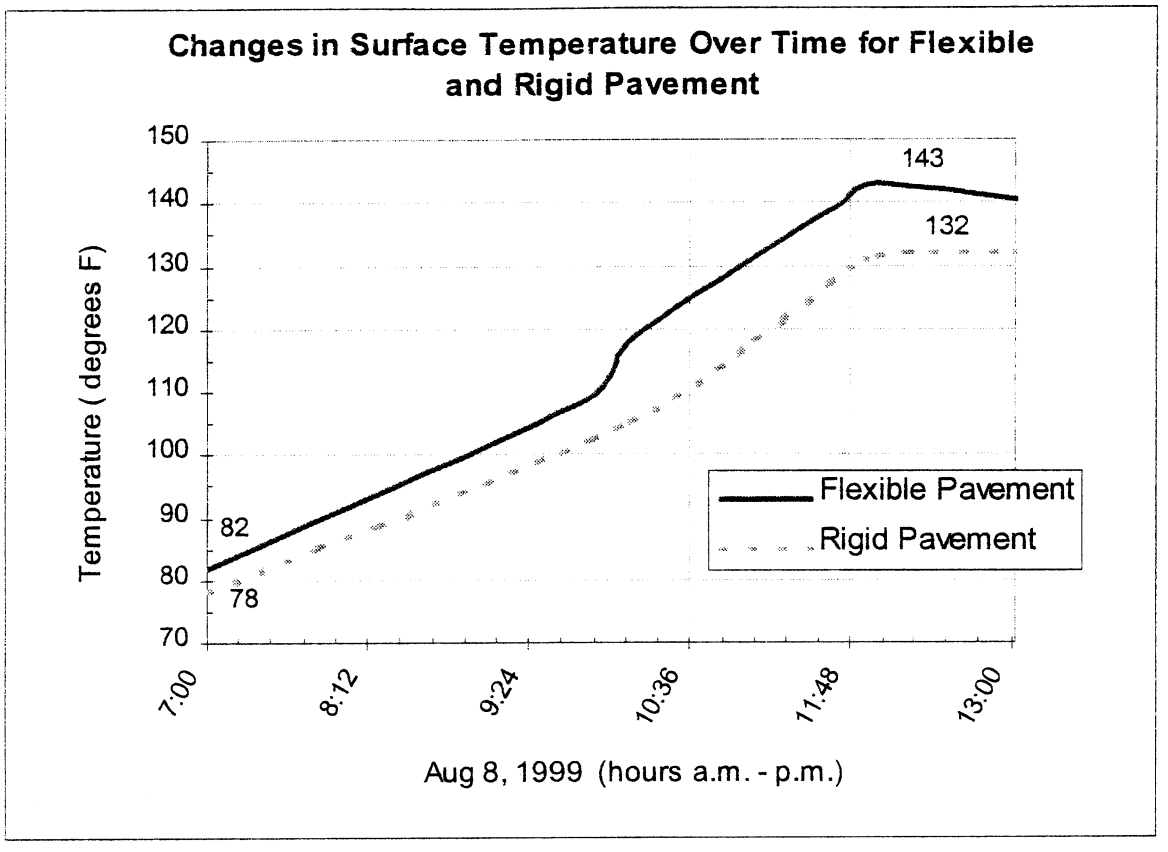

Figure 5.2 Temperature Changes in Pavement Surface

Surface temperatures for both pavement types rose steadily from sunrise until midday, with only slight differences in starting and finishing temperatures. Both pavement surface temperatures rose as much at 10°F within a 30-minute period. These findings indicated that in order to collect sensor response data for a variety of configurations within a specific temperature range, the testing procedure had to be performed rapidly. Therefore, the site layout had to be constructed in a manner to allow the testing equipment to relocate quickly from sensor to sensor. Also, testing repetition on the same sensor configuration was limited, to allow for testing on every sensor configuration within that specific temperature range.

5.1.4 Field Sensor Construction

Two strips, 1.8 m (6 ft) long by 7.6 mm (0.3 in.) wide, of G-10 fiberglass served as the plates for the body of each sensor. Pieces of G-10 fiberglass were cut to construct the loop ends (flags). The protective loop end for a horizontal sensor, without the top cover plate is shown in Figure 5.3.

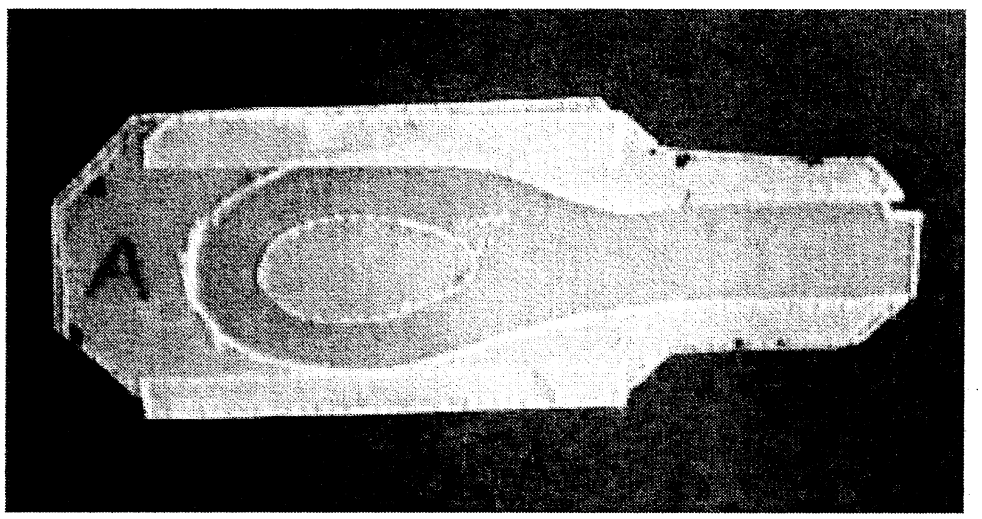

Figure 5.3 Protective Loop End Constructed of G-10 for Horizontal Sensor

A two-part quickset epoxy was used to construct and affix the flag to the end of the fiberglass plate. A razor blade was used to cut a strip of Tefzel® mesh the width of the G-10 plate. The mesh contained five rows of microbenders, called "tracks". The Tefzel® mesh was adhered to the bottom G-10 plate using spray adhesive. Care was taken to keep the mesh tracks in a straight line. The center of an appropriate length of 50/125/250 multimode fiber was folded into a loop and glued into the protective flag. The Tefzel® was also sprayed with adhesive and the fiber strands were affixed to tracks two and four (Figure 5.4).

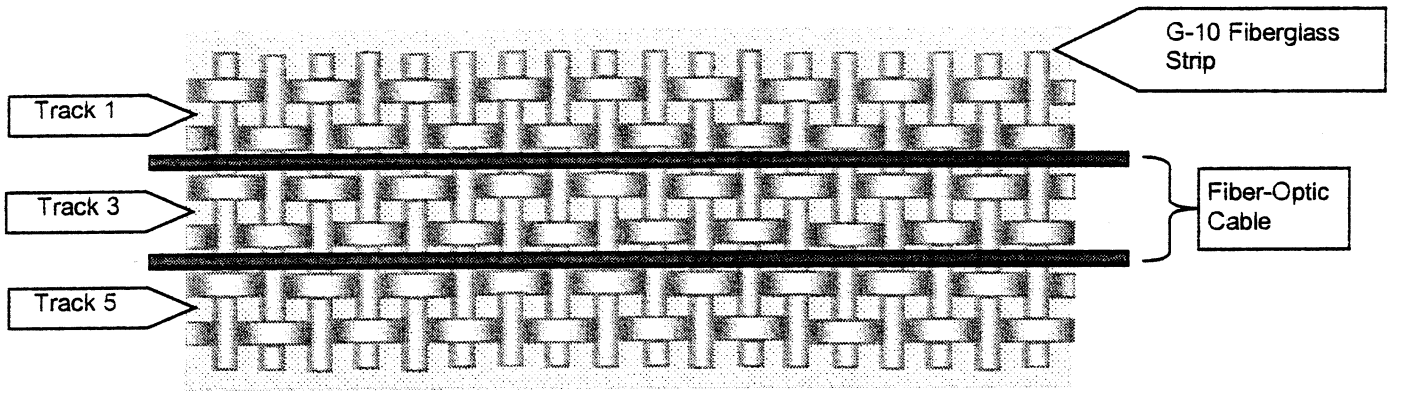

Figure 5.4 Sketch of Fiber-Optic Cable Lying in Tefzel® Tracks 2 and 4

Once again, a thin coating of adhesive was applied to the fibers and covered with the top strip, while compressing the plate against the fiber. The center of the one-inch wide strapping tape was then adhered, without forming any creases, to the sensor's top plate. One side of the tape was folded onto the edge of the sensor and the procedure repeated for the opposite edge. The bare fiber ends were then fed into the protective, orange bifurcation tubing. A 3.1 cm (2 in.) strip of heat shrink was cut and drawn over the point where the bifurcation tubing meets the fiberglass end of the sensor. A heat gun was used to constrict the heat shrink in place. The heat shrink was coated in 5-minute epoxy and covered with a second piece of heat shrink. Each bare fiber end was stripped of the protective coating, coated with epoxy and secured into a ceramic ST-connector. After the bead of epoxy on the end of the connector dried, the end of the ST-connector was wet-polished for optimal coupling of light into the fiber.

5.1.5 Sensor Calibration

Prior to installing a sensor into the road surface, each bare sensor was performance-tested. During calibration of the bare sensor, data was collected every 15.2 cm (6 in.) along the sensor's length. At each location a 3.1 cm (2 in.) platen was placed on the sensor for calibration. The sensor was placed on a compression-testing device. Care was taken to place the sensor on a level surface, such that the sensor rested flat between the compression surface and the platen.

The calibration device was a hand-operated compression-testing machine with digital transducer readout. The bare sensor was connected to an opto-electronics box with a numeric display. The opto-electronics voltage output was adjusted to 3.0. Next, pressure was applied to the platen by turning the handle to the compression-testing device at a moderately slow and steady rate. As the platen slowly compressed the bare sensor, values from the transducer and the opto-electronics box were noted. When the light loss through the sensor dropped to 50 percent, or 1.5 volts, the applied load to the sensor was recorded into a spreadsheet. The sensor was immediately unloaded, and the test was repeated for consistency at least three times. The average stress was calculated for the area over which the load was applied. This testing procedure was repeated at each calibration location along the sensor's length.

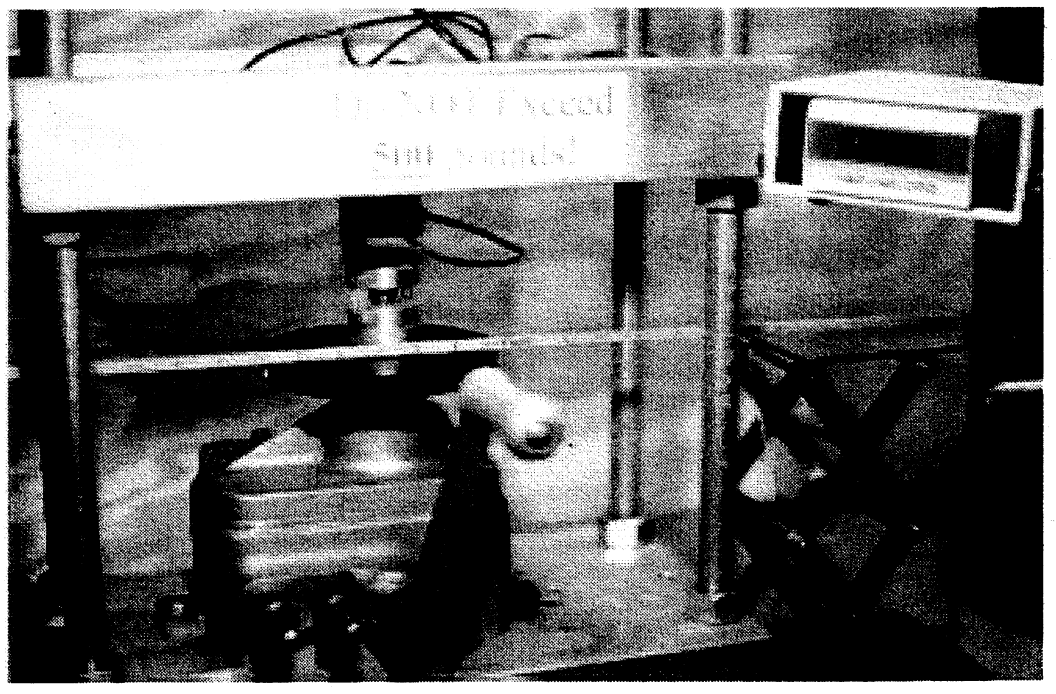

Figure 5.5 Compression Testing Machine

Once all calibration locations were tested, the average pressure sensitivity was determined. If the sensor's average sensitivity was too low or if the sensitivity deviated too much along its length, the sensor was not used at a test site.

Figure 5.6 shows the results from a typical bare sensor calibration test. The figure indicates the sensor's higher sensitivity near the ends. This sensitivity change has yet to be fully investigated. The calibration results of each sensor used in the field tests are included in Appendix B.

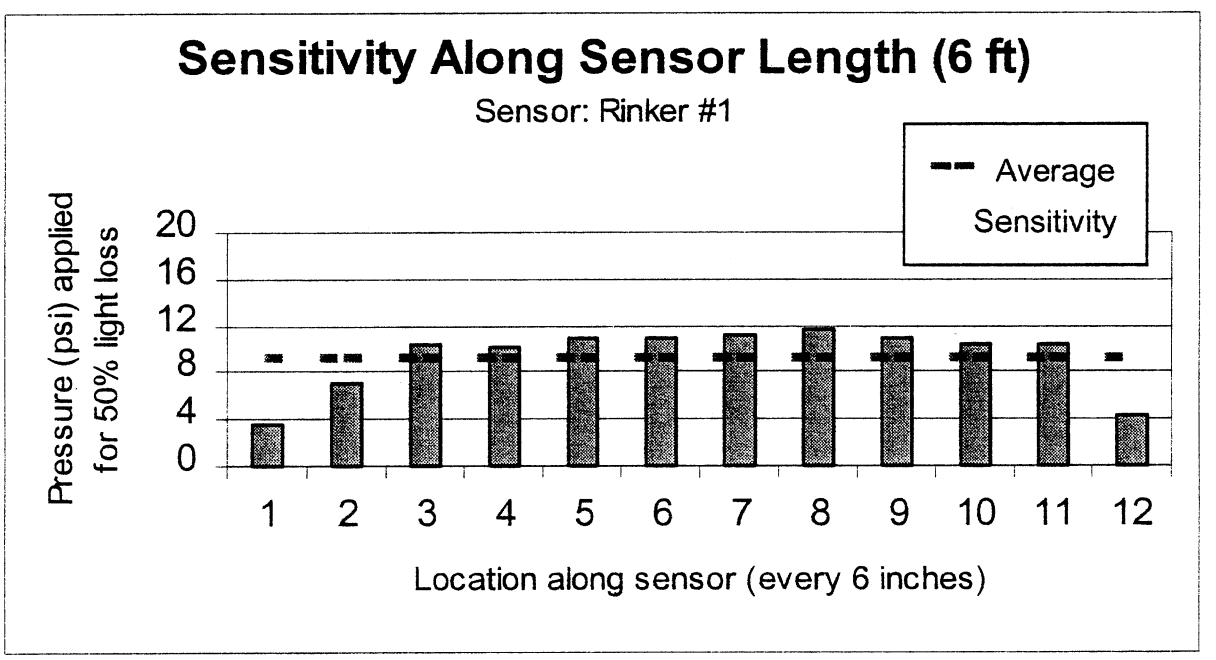

Figure 5.6 Typical Bare Sensor Calibration Graph for Sensor Used at Test Site

5.1.6 Site Layout and Testing Procedure

Several factors contributed to the design and testing procedure for the fiber-optic field test sites. First, a site design had to be created in such a manner that the variables being studied could be controlled. This required that different sensor orientations be placed within each encapsulant and in each pavement type. In order to examine all variables, each different sensor configuration was tested over a variety of loads at a range of different temperatures. Duplicate sensor configurations were also incorporated into the site layout for data comparison.

The next step was to determine what testing method would be used at the field sites. A repeatable testing sequence had to be performed rapidly over a variety of loading conditions. The testing procedure required four different load values to be dropped on the sensor. Therefore, FWD was selected as the preferred testing device. The FWD is a standard piece of equipment used by state transportation departments to evaluate pavement characteristics. Using this piece of testing equipment, sensor data and pavement information could be collected at the same time.

The FWD collected deflection data by using a series of geophones mounted to a beam that was lowered to the pavement surface. The distance from the drop location to the farthest geophone was just less than 1.8 m (6 ft). Therefore, each sensor at the test site was spaced six feet apart (Figure 5.7). Although the only deflection value required for evaluating the fiber-optic sensor's performance was at the sensor's immediate location, undisturbed pavement sections would be expected to produce more accurate pavement evaluation results.

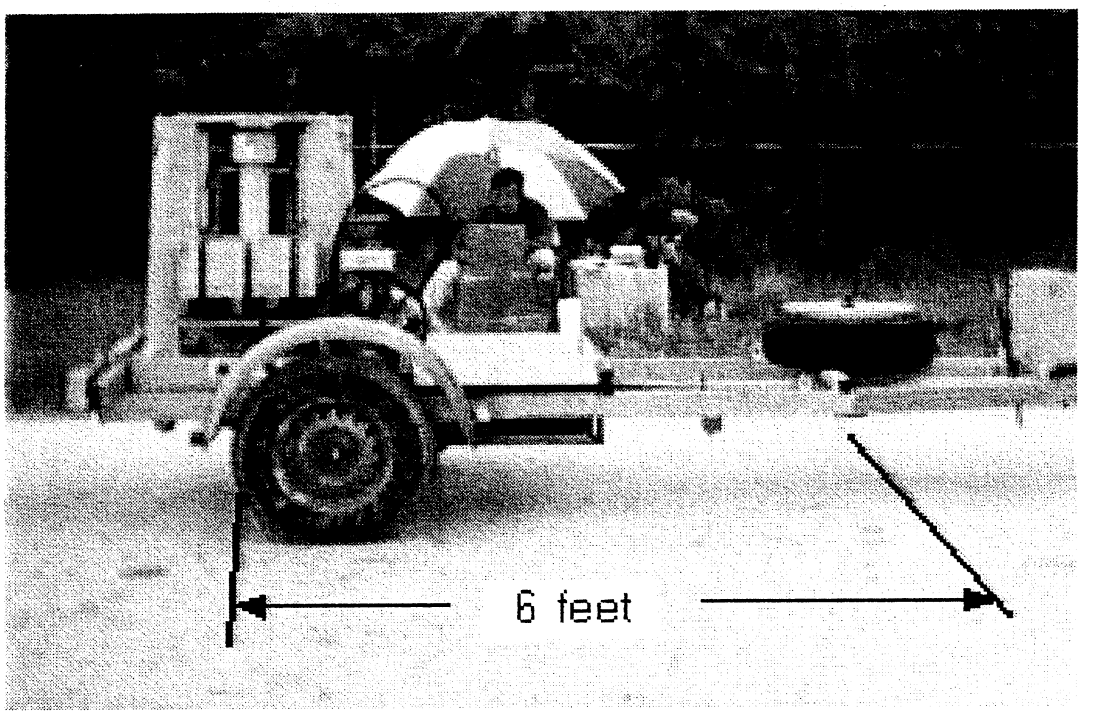

Figure 5.7 Sensor Separation at Field Site

Several items governed the number of sensors that could be tested. Primarily, the increasing surface pavement temperature controlled the time duration for sensor testing. This reduced the number of sensors that could be tested while the pavement remained within a certain temperature range. Because the FWD testing cycle for each sensor location was just under two minutes, surface pavement temperatures were likely to change from one range of values to another before the drop test were repeated three times on each sensor. For this reason, only duplicate configurations for some sensors were installed.

Research on Florida Institute of Technology's FOTS, performed by Wulf von Eckroth, showed that a sensor of any length over two inches produced nearly identical signal responses. Variation in sensor sensitivity along the length of the sensor produced, in effect, a separate signal response for a given length, as long as the test locations on the sensor did not overlap [Eckroth, 1999]. Therefore, three trials on one sensor in three separate, non-overlapping locations produced the same results as performing one trial on three separate sensors.

Information collected at the site on A1A in Melbourne Beach, telemetry site #284, also provided insight to what sensor configurations performed very poorly. Horizontal sensors encapsulated with Flexane®, a hard encapsulant used only at the A1A site, and ProSeal 6006® were unable to handle light vehicle traffic for an extended period, and failed. For this reason, horizontal sensors with ProSeal were not installed at the flexible pavement field site

Layouts were constructed for each field site, based on the sensor configurations, spacing required for testing equipment, and the number of sensors to be tested. These layouts were used to ensure each site was constructed properly (Figure 5.8 and Figure 5.9). The site layouts were also given to the FWD equipment operators prior to testing.

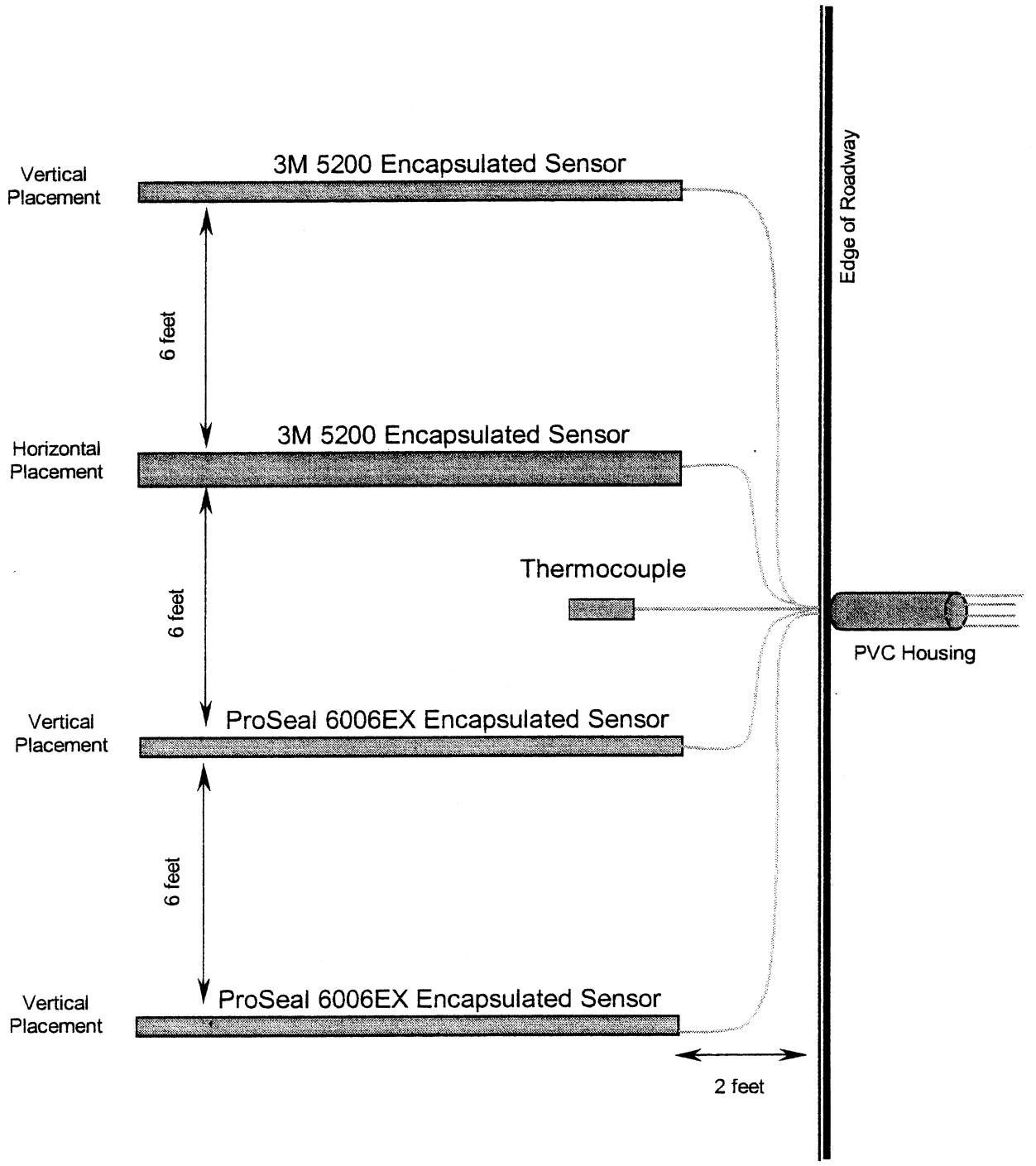

Figure 5.8 Site Layout for the Flexible Pavement Test Site

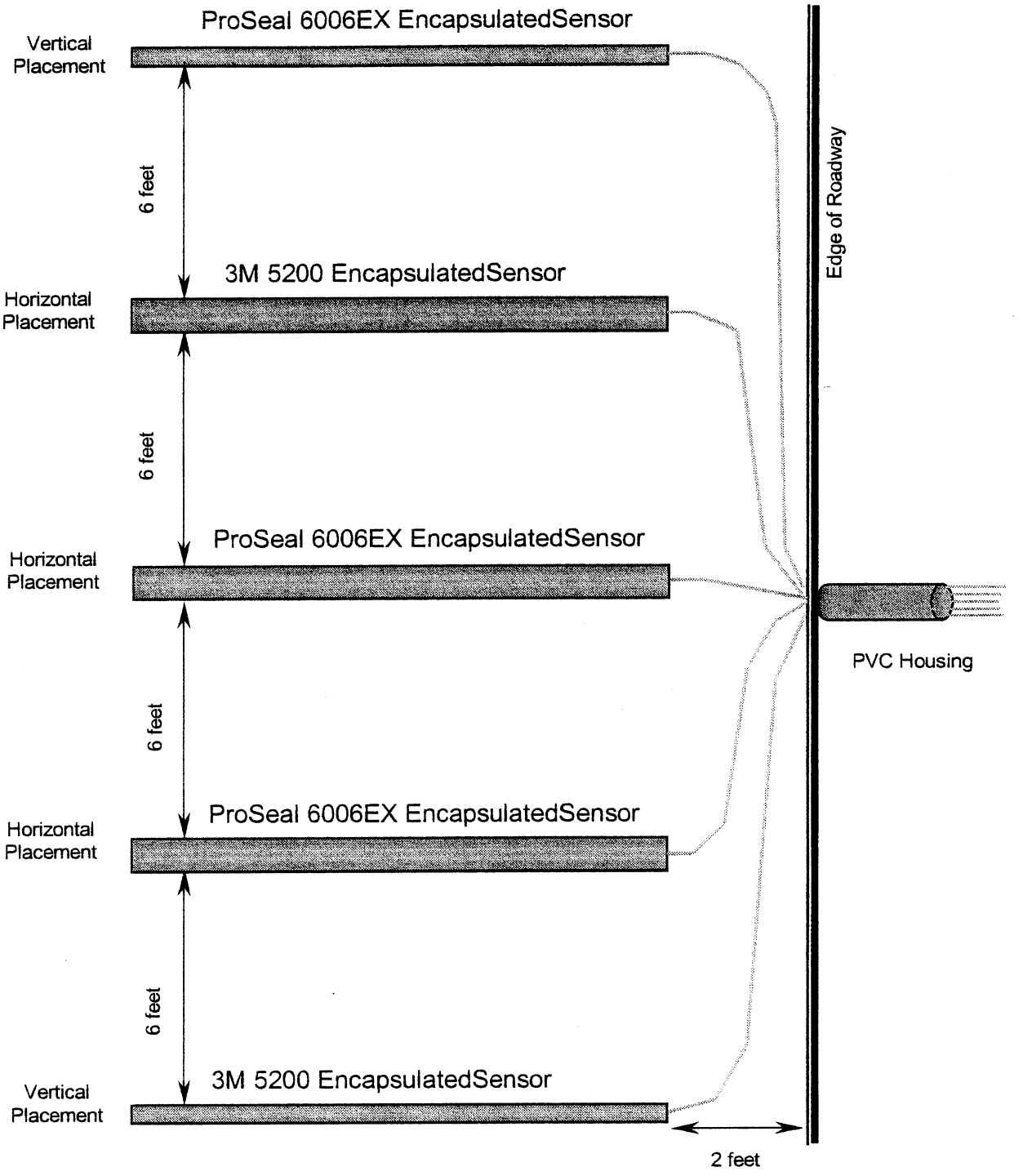

Figure 5.9 Site Layout for Rigid Pavement Test Site

5.2 Field Installation

Two test sites were selected based upon pavement type and road location. The flexible pavement test site was constructed on the access road to APAC-Florida, Inc. (Figure 5.8). Previous fiber-optic sensor testing had been performed along this same roadway. APAC-Florida, Inc., is located near U.S.1 in Melbourne, Florida, approximately 20 minutes north of the university, which made the mix plant an excellent test site. The CSR Rinker batch plant was selected as the rigid pavement test site (Figure 5.9). This test site is located off U.S.1 in Palm Bay, Florida, approximately 10 minutes southeast of the university. The long, wide concrete access road made for excellent test-equipment access. Prior fiber-optic sensor testing had also been performed at this location.

5.2.1 Site Installation

Fiber-optic sensor installation began with cleaning loose sand, gravel and other debris from the road surface. Washing the surface was unnecessary because dust was not a factor at this point in the sensor installation. The sensor locations were then marked on the road surface using a tape measure, a rope and spray paint. Measuring 61 cm (2 ft) from the shoulder of the road, a reference point was marked. The rope was then held down tightly atop the road, perpendicular to the shoulder. The rope was sprayed with paint, and then removed. A straight line created from the paint over-spray remaining on the road surface. The next sensor location was selected six feet away. This marking procedure was repeated for each sensor location.

Cutting procedures varied between the flexible and rigid pavement sites. At the flexible pavement site, a single pass of the circular saw equipped with a carborundum masonry blade was used to cut the vertical grooves. Multiple passes were used to create the wider grooves for the horizontal sensors. The circular saw was also used to cut the smooth curved homeruns.

The rigid concrete pavement was a harder, denser material than the flexible asphalt pavement and was a more difficult material to cut. Although cuts could be made into the concrete with a circular saw, it was not recommended. A walk-behind street saw was used for cutting into this road surface. A water hose is normally attached to this saw allowing water to flow onto the cutting area, thus lubricating and cooling the saw blade while eliminating large amounts of concrete dust. Due to the site location, a water hose was not available. The same cutting procedures were performed using the street saw as with the circular saw. In order to prevent binding the street saw blade while trying to make a smooth, curved cut, the grooves for the sensors' leads were made using a series of short, overlapping facet cuts.

Figure 5.10 Cutting Homeruns in Rigid Pavement with Street Saw

Four key areas were important during the cutting process, straight direction, correct depth, uniform depth and smooth groove bottoms. Straight cuts help to eliminate light loss within the sensor. If the sensor was placed within a wavy groove, micro-bends would be created and optimal light transmissivity would be reduced. Second, care was taken to create grooves to the proper depth. Vertical sensor depth must be made so that the top of the vertical sensor

rested immediately below the wearing surface of the road. Prior research on horizontally placed sensors revealed an optimal groove depth between 1.27 cm (0.5 in) and 2.54 cm (1 in.) [Criss, 1998]. Therefore, horizontal grooves were cut to a depth of 1.93 cm (0.74 in). Third, sensor depths needed to remain constant so that pressure transferred to the sensor would not be affected by changes in groove depth along the sensor's length. Lastly, because multiple saw passes were used to create the horizontal grooves, the bottom of each groove tended to be irregular. The irregularity, caused by thin shards of pavement protruding up from the bottom of the groove, was remedied by moving the saw blade from side-to-side along the groove length. This sawing motion removed any irregularities and unevenness from the bottom of the groove.

A PVC pipe with a 90° elbow was used to house the fiber-optic cable ends. To achieve this, a hole was dug in the shoulder of the road where the homeruns converge at the edge of the roadway. The PVC housing was placed in the hole.

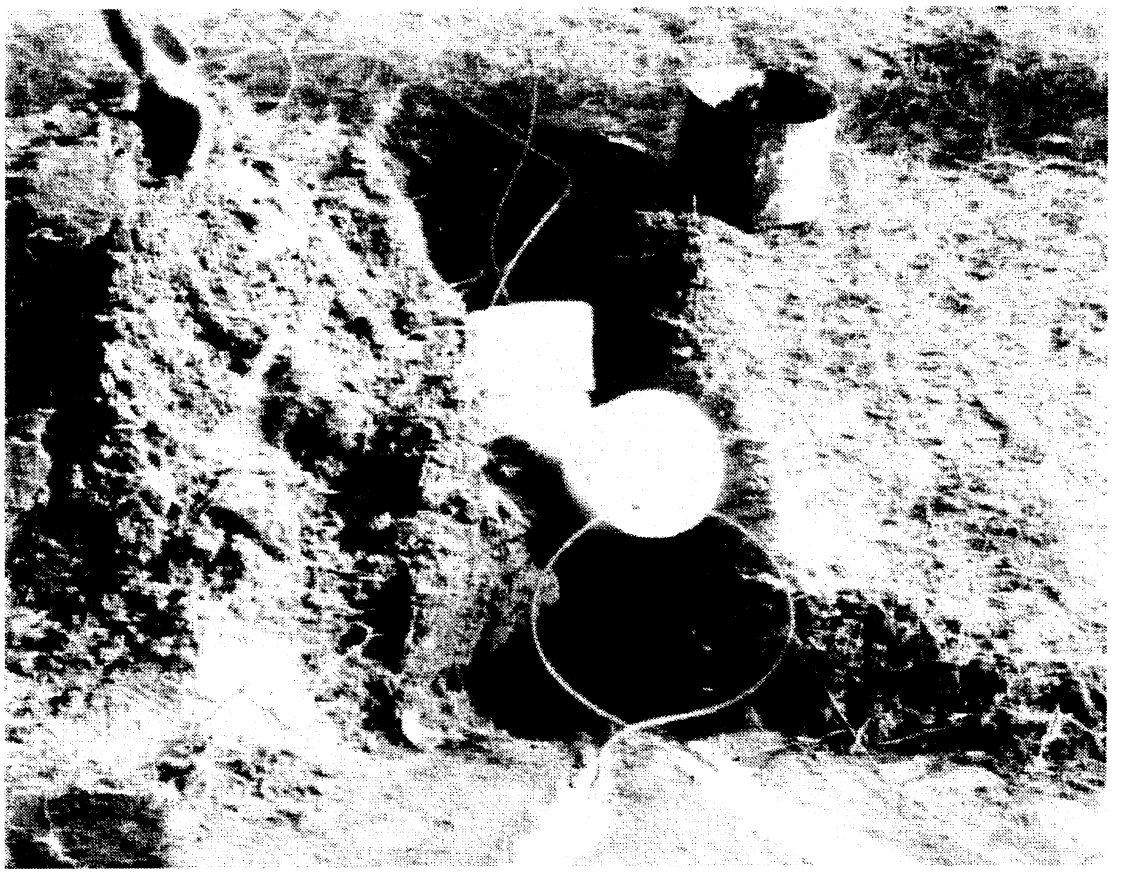

Figure 5.11 Protective PVC Housing for Sensor Leads

At this point, the site was ready for dry-fitting the sensors into their grooves, which were cleaned of dust and debris. Sensors were placed in the grooves to assess proper fit. The cable leads were laid in the homeruns and the ends were fed into the protective PVC piping.

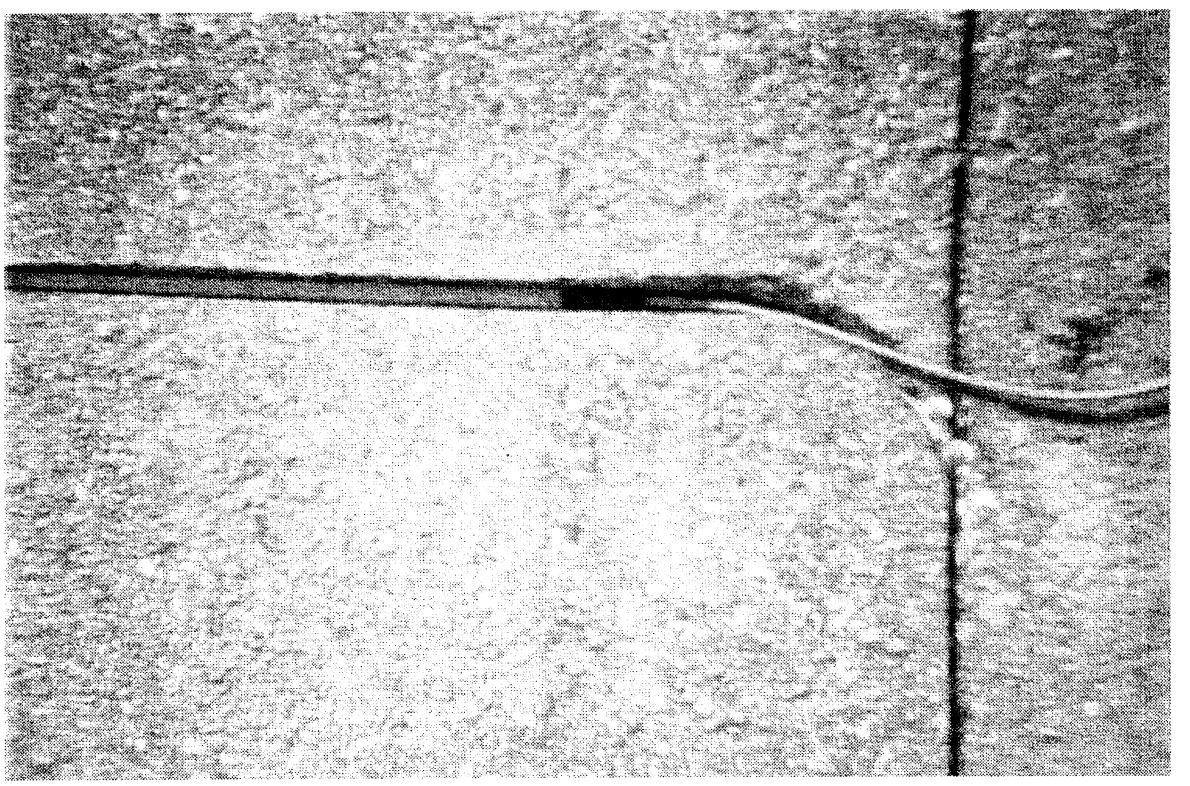

Figure 5.12 Dry Fit of Sensor in Groove Cut into Flexible Pavement

In addition to installing fiber-optic traffic sensors in the road, a second piece of equipment was installed at the flexible pavement test site. Grooves were cut into the pavement to the depth that allowed a pencil-shaped thermocouple to rest immediately below the wearing surface of the road. During testing, the thermocouple was first installed at only the flexible pavement site. Before placing a thermocouple in the rigid pavement field site, the thermocouple's performance was evaluated.

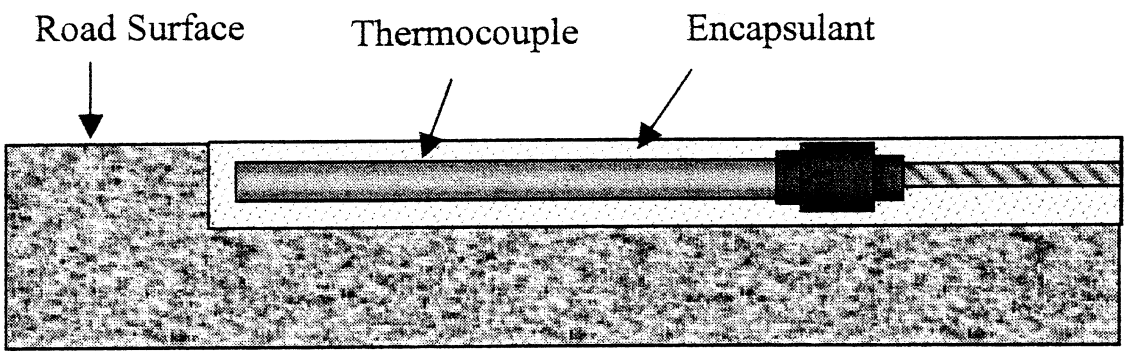

Figure 5.13 Profile of Thermocouple Encapsulated in Roadway

5.2.2 Encapsulation

Once each sensor was placed in its groove for a "dry fit," they were removed from the roadway. Any remaining dust was blown out from the grooves and homeruns. If water were available, the preferred cleaning process would be to wash and dry each sensor groove prior to encapsulation. The use of disposable latex gloves is recommended during sensor encapsulation. In order to avoid tearing the gloves on the rough road surface, wooden tongue depressors, or similar devices, were used for spreading the encapsulants and manipulating the sensors within the encapsulant filled grooves.

The encapsulation process varied slightly depending upon material. At each site, the sensors to be placed in the 3M 5200® were installed first. The caulking tube was cut open and placed in a manually operated caulking gun. Next, the entire length of the vertical groove was filled with 3M-sealant to a level even with the road surface. The vertical sensor was slowly pressed into the sealant filled groove. This process forced the excess encapsulant to extrude out the top of the groove. When the sensor was completely pushed below the road surface, the excess sealant was smoothed atop the vertical groove. Care was taken to apply an even layer of sealant above the sensor.

Installing the horizontal sensor required a thin bead of 3M-sealant to be placed in the bottom of the wide groove. The sensor was then pressed into the bead of sealant. It was very important to completely press the sensor to the bottom of the groove. The thin sealant bead only served to stick the sensor to the bottom while the remaining sealant was applied in the

rest of the open groove. 3M-sealant was then squeezed into the groove, filling from the bottom to the top. By placing the tip of the tube nozzle in the bottom of the groove and allowing the sealant to expand upward to fill the groove, air pockets did not form between the embedded sensor and the encapsulant. As with the vertical sensor, the entire sensor length was encased within the 3M 5200®, and the top of the groove worked smooth.

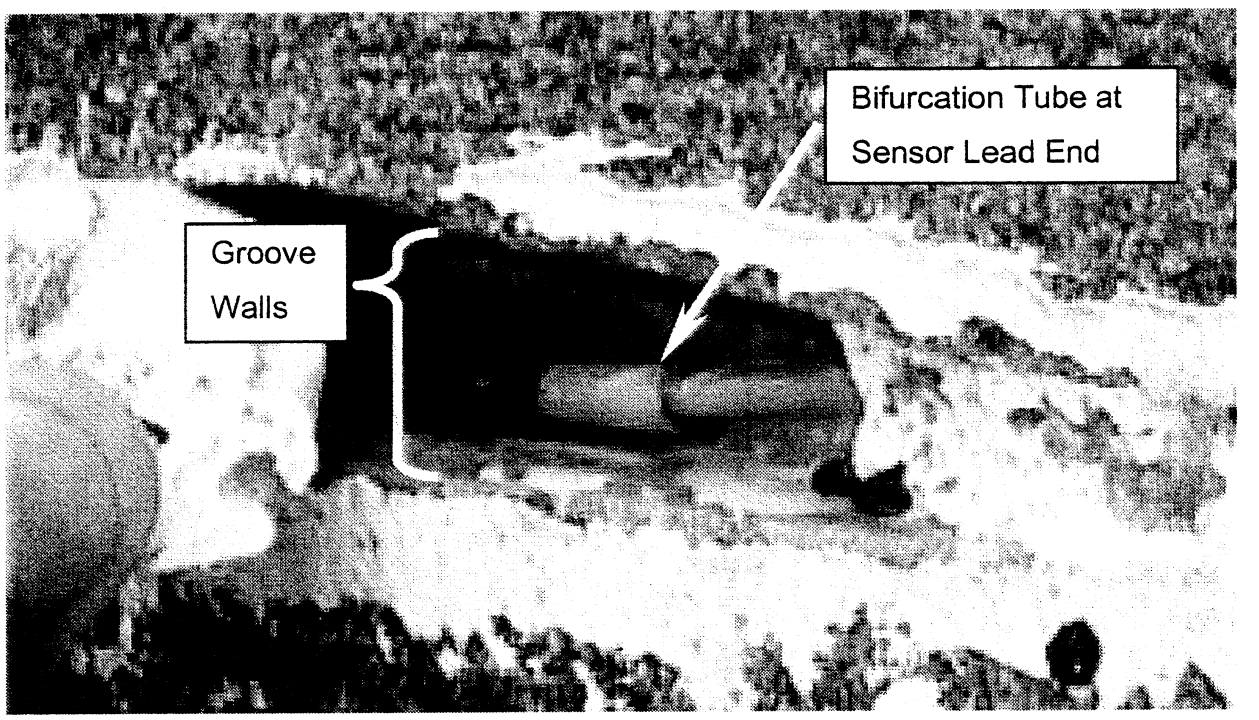

Figure 5.14 3M 5200 Shown Pulled Out of Channel to Reveal Sensor Resting in Bottom of Horizontal Groove Beneath Encapsulant

Installing sensors using ProSeal 6006EX® was a similar process. Unlike 3M 5200®, ProSeal 6006EX® was more fluid, and therefore naturally flowed into a smooth top surface. After the activator was stirred into the polyester resin base, the material was applied into the grooves by pouring the substance out of two punctured openings in the canister's lid. Horizontal sensor installation required placing the sensor in the open channel, and pouring the material into the groove. Due to the viscosity of the material, trapping air within the encapsulant was not a concern. Because the material easily flowed into openings, it was used to encapsulate

all bifurcation cable leads in the homeruns. The thermocouple placed in the road surface at the flexible pavement site was also encapsulated using ProSeal 6006EX®.

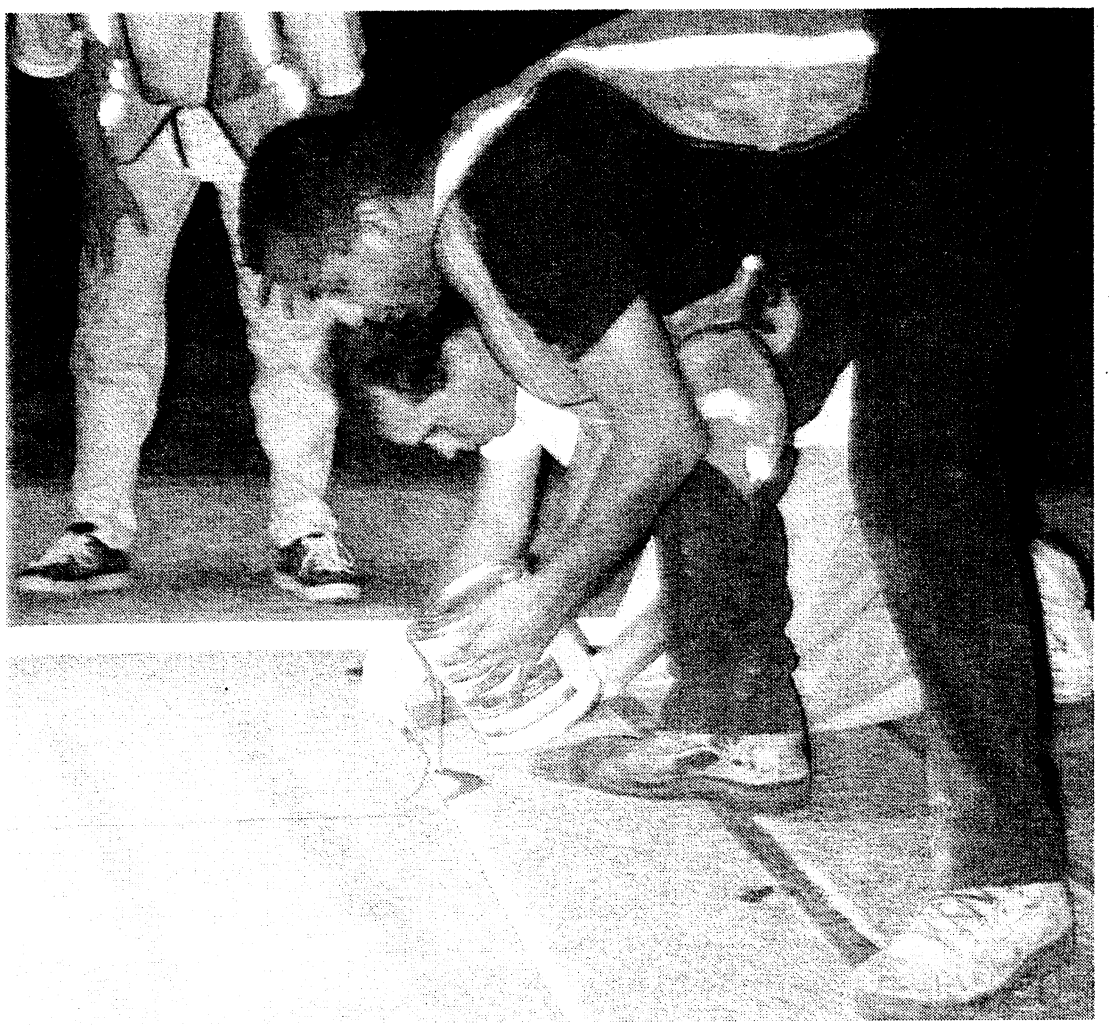

Figure 5.15 Pouring ProSeal 6006EX into Sensor Groove

Vertical sensors were placed into ProSeal in the same manner as the 3M product. ProSeal flowed freely, so if the road surface was at too great an angle, wood tongue depressors were used to smooth the material and keep it in place until the encapsulant began to activate. Once the material became jelly-like, care was taken not to manipulate the material any longer. Overworking the ProSeal once it began to harden resulted in an irregular, lumpy surface.

The curing period varied for each material. While ProSeal 6006EX® cured to a tacky surface within a few minutes, the 3M 5200® took several hours to cure at the surface. The 3M

encapsulant took 24 to 48 hours before it was fully cured. Because of the site locations, traffic cones were placed around the field sites while the encapsulants cured.

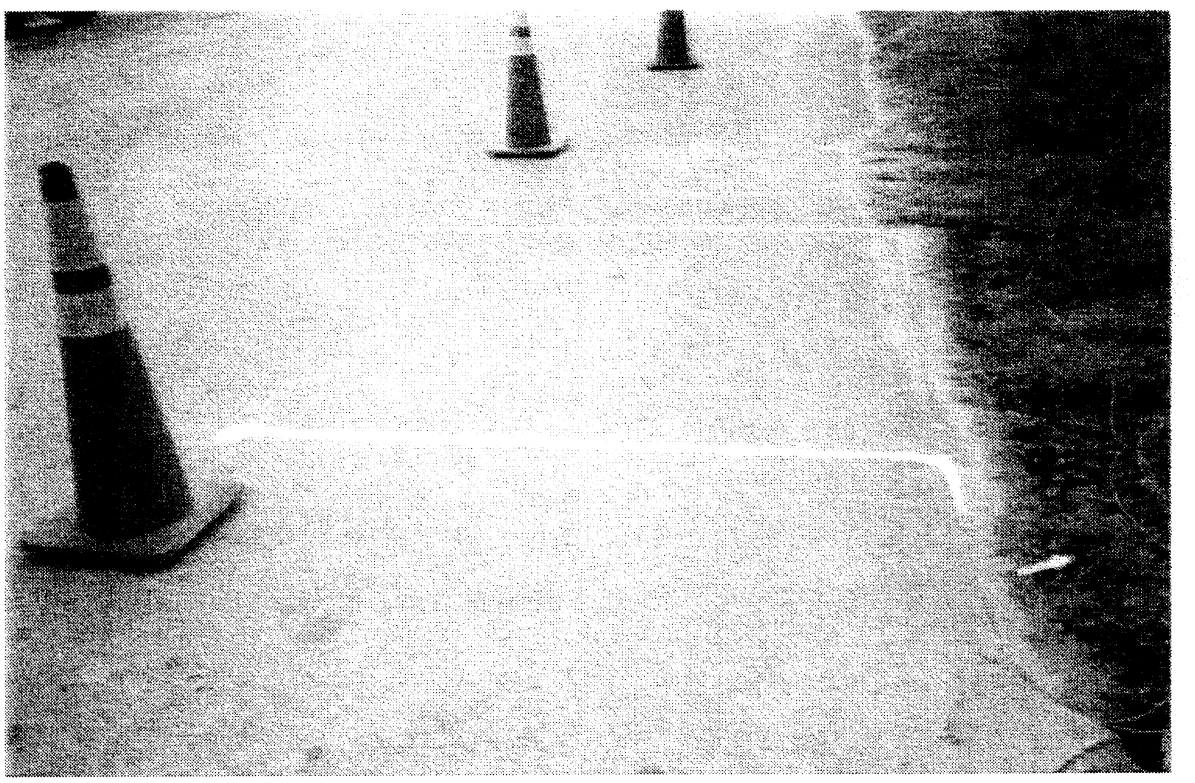

Figure 5.16 Traffic Cones Are Used to Keep Vehicles from Driving on Test Sensors While Encapsulation Material Cures

3M encapsulant expands while curing. Therefore, the smooth, flat surface on horizontally placed sensors would have an elevated bump when fully cured. This ridge of encapsulant was removed prior to FWD testing. A snap-blade razor knife could be used to slice the ridge off the top of the 3M 5200®. If the ridge remained in place, it would create stress concentrations immediately atop the horizontal sensor [Eckroth, 1999]. Although there was not enough 3M sealant in a vertical groove to create this effect, any irregularities atop the vertical 3M sensor were carefully removed.

5.3 Field Testing

The total time allotted for testing the fiber-optic traffic sensors was initially four days. The FDOT Pavement Evaluation Section performed the first two days of testing on Oct. 6, 1999 and Oct. 7, 1999. The following week of Oct. 12, 1999 and Oct. 13, 1999, Dynatest Consulting, Inc., performed FWD testing at both field sites. After the first two weeks of FWD data was analyzed, a determination was made to perform additional testing using lower pressure ranges on the fiber-optic sensors. Therefore, arrangements were made to have FDOT Pavement Evaluation Section return to the field sites on Dec. 6, 1999. On this date, FWD testing was performed at both test sites. The testing procedure consisted of monitoring surface pavement temperature while recording signal response data from the sensors. At the same time the FWD machine applied a load to the sensor, it recorded pavement deflection information. Both signal response data and pavement response data were recorded. The different data groups were combined and analyzed after the field-testing was completed.

5.3.1 FWD Procedures

Prior to the arrival of the FWD test equipment, three marks were placed on each traffic sensor. Using fluorescent spray paint, the locations for the FWD drop plate were painted on the sensor: one mark in the center of the sensor, and marks 45.7 cm (1.5 ft) to the left and to the right of the sensor's center. These marks served as reference points so that each series of FWD tests were performed at the same location along the sensor. As discussed in section 5.1.5 Sensor Calibration, the lead end and the flag end of the fiber-optic traffic sensor are extra sensitive. Because these sensitive ends would create irregular results, testing was not performed near the ends of the sensor (Figure 5.17). By placing marks 45.7 cm (1.5 ft) in from the ends of the sensor, the outermost edge of the circular drop plate remained about 30.4 cm (1 ft) from the sensor's end, sufficiently far enough away from the end to eliminate irregular test results.

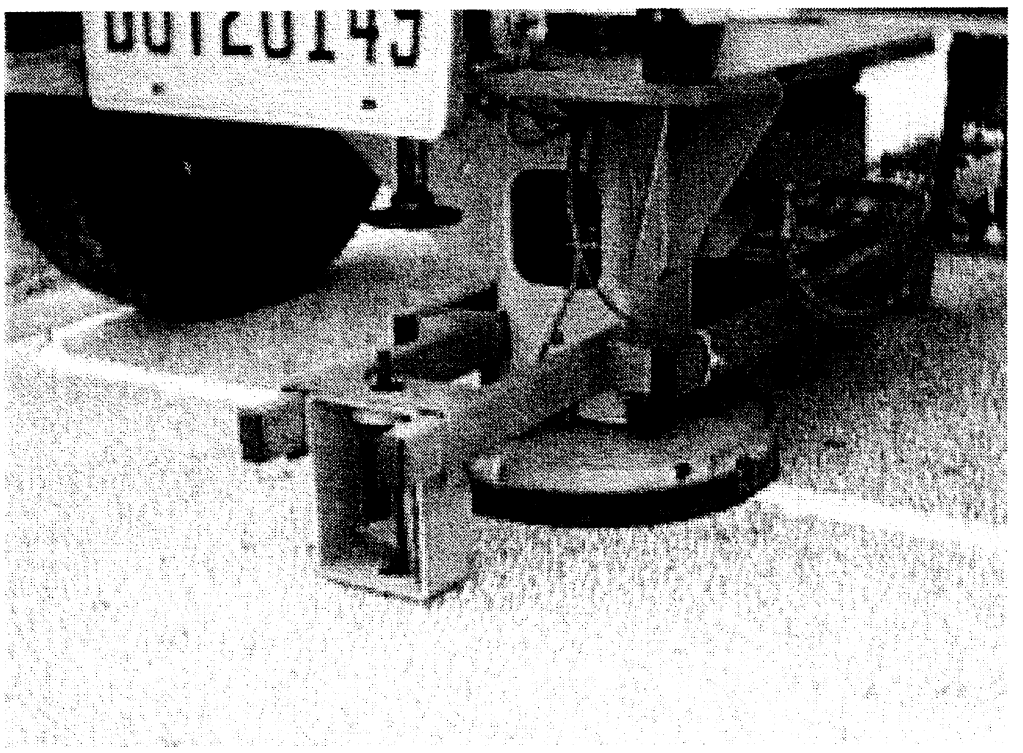

Figure 5.17 FWD Drop Platen Avoiding Sensor Ends by Performing Tests on the Middle Region of the Sensor

When the FWD testing equipment arrived at the site, a testing sequence was given to the FWD operator. The test sequence was designed so that each sensor configuration could be tested while the pavement temperature remained reasonably constant. The test pattern shown in Figure 5.18 was used for both the flexible and the rigid pavement field sites.

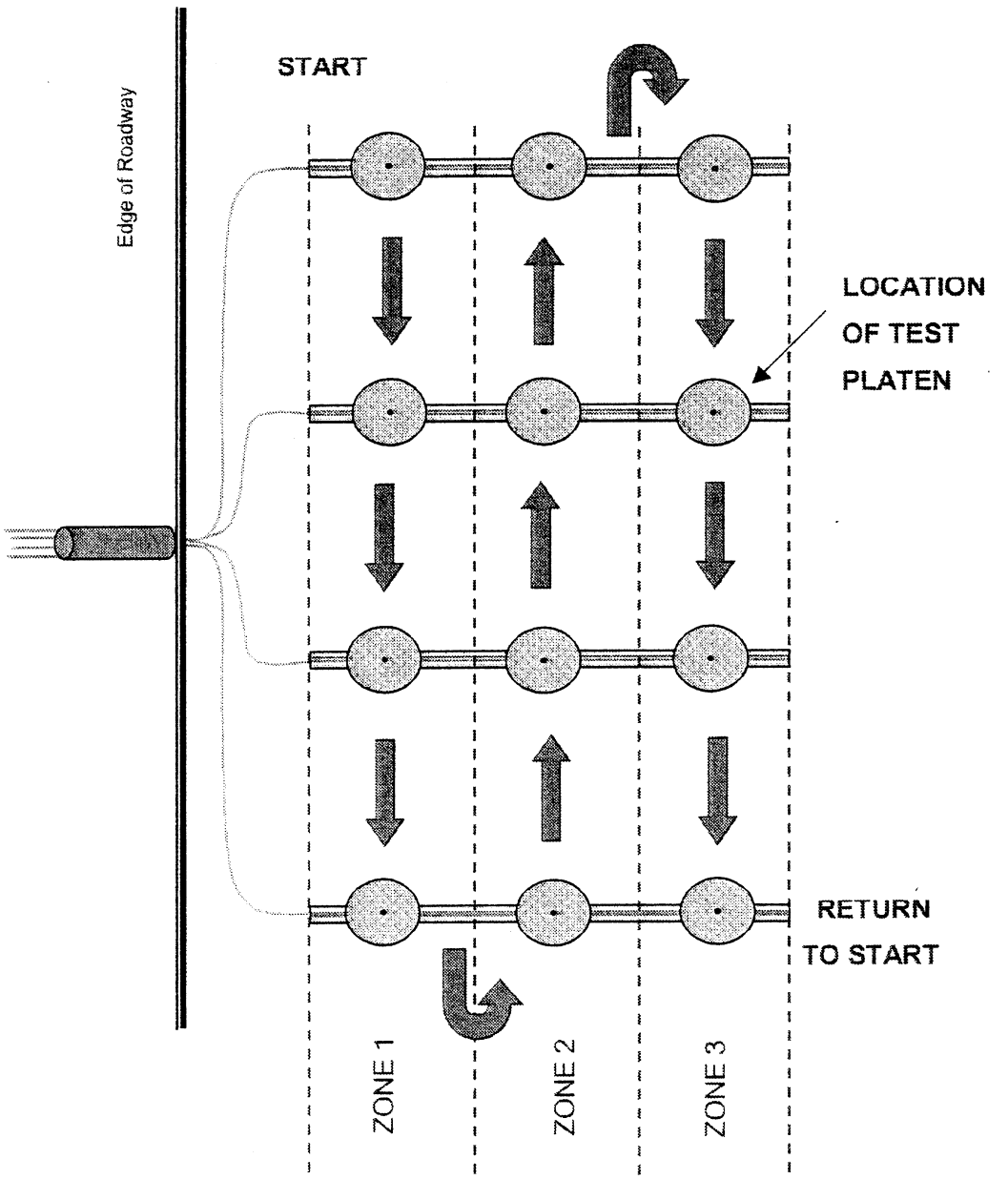

Figure 5.18 FWD Drop Pattern for Field Testing on Traffic Sensors

FWD testing began by aligning the drop platen over the center of the spray paint mark on the sensor in *Zone 1*. A drop sequence of 6,000 lbs, 9,000 lbs, 12,000 lbs, and 15,000 lbs was selected. A range of heavy loads was used during testing in order to simulate the higher stresses produced from heavy truck traffic [ERES, 1987]. To determine the duration of four drops, a trial run was performed prior to the first data collection set. A duration of 25 seconds was entered into the data acquisition software. The FWD test started the moment the data acquisition software was activated. The loading cycle was completed just short of 25 seconds. The FWD operators waited for confirmation that the data collection was complete before aligning the drop platen over the mark in *Zone 1* for the next sensor. One trial of FWD tests was performed on each sensor within *Zone 1* before performing the tests in *Zone 2* and *Zone 3*.

During each test run, FDOT computer software recorded the information collected from the geophones. This data was compiled into tables showing the applied load, equivalent pressure and pavement deflection for each geophone location. Paper copies of these results were mailed to research assistants at Florida Institute of Technology for pavement analysis and sensor deflection calculations immediately following the field-testing.

5.3.2 LabView® Collection

A data collection station was set up along the shoulder of the road. A table was placed beside the protective PVC housing. On the table, the laptop computer was connected to the opto-electronics box through a data acquisition card (DAC) interface. The sensor's bifurcation tubes were removed from the PVC housing and secured to the table. Then, the lead ends of the sensor were exposed; the fiber-optic cables were cleaned and joined into ST-connectors. The ST-connectors were wiped free of any possible dust and inserted into the opto-box.

Figure 5.19 Electronics Equipment Prepared for Data Collection at Field Site

Using the LabView® data acquisition software, an initial test was performed to show the sensor signal response. This test assured the sensor was transmitting adequate light, and that the data collection software was functioning properly. The sensor was not actuated during the trial test, to that the ascertain voltage output was uniform and at the desired level.

As stated in section 5.3.1 FWD Procedures, the time duration for one set of FWD drops was 25 seconds. This value was entered into the LabView® software. Specific data regarding sensor type, test number and pavement temperature were also entered into a field in the data acquisition software. This additional data served to help collate the multiple signal response output files with the FWD deflection data.

The LabView® was started the moment prior to releasing the weights on the FWD. Releasing an electromagnetic sensor dropped the weights. Because the trigger made a distinctive noise prior to release, the start button for data collection was actuated upon hearing that noise.

For the 25 seconds of data collection, LabView® captured a series of events. The software's time duration was set to record fiber-optic sensor signals from the moment the weights were dropped until the drop platen was removed from the sensor. The high sampling rate (1000 scans per second) produced a detailed signal response graph, not just a recording of maximum and minimum signal response output. These detailed graphs were analyzed to critique the different performance for each sensor configuration.

Once the output file was saved, the LabView® software was reset for the next sensor to be tested. During the brief time required for resetting the software, the FWD drop platen was realigned over the next sensor.

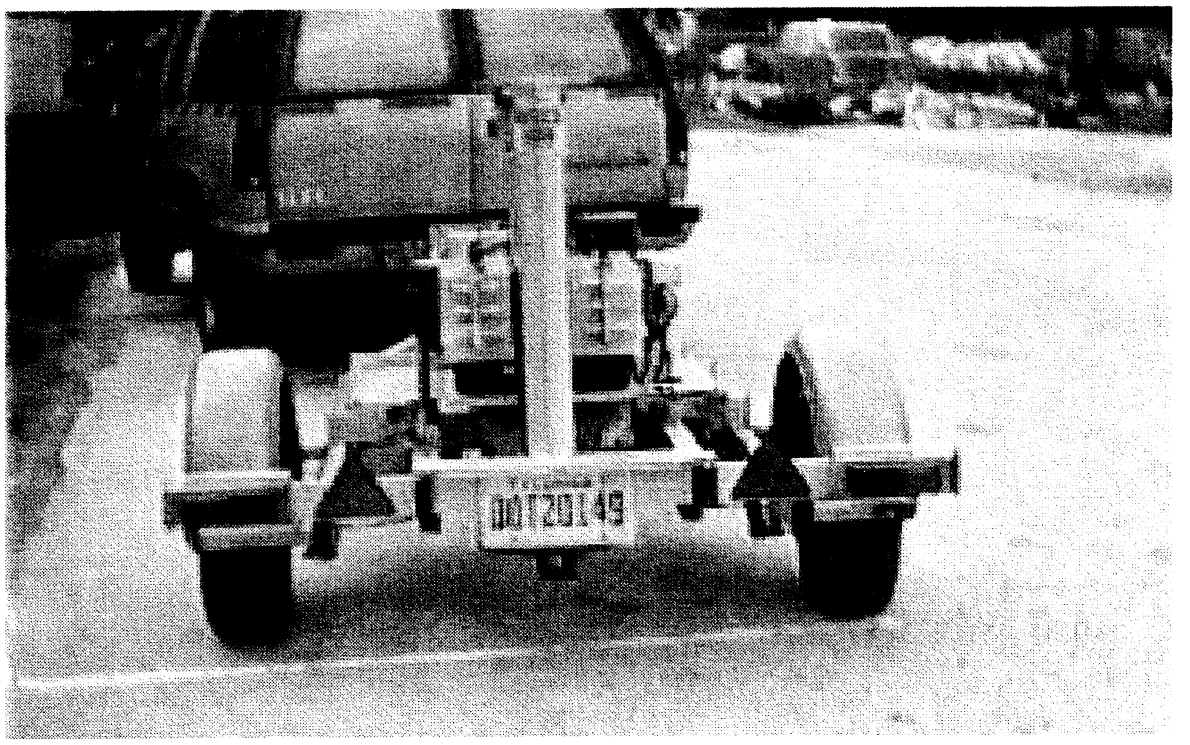

Figure 5.20 FWD Equipment Realigning Over Test Sensor

5.3.3 Pavement Temperature Collection

Changes in pavement surface temperature required constant monitoring during the FWD testing. On the first day of testing, three temperature collection devices were used. The surface thermometer was placed next to, but not in the shadow of, the FWD machine. The

four different loads were dropped on the sensor, and the value off the surface temperature was recorded into the data collection software.

Second, a hand-held temperature gauge was connected to the thermocouple. Unfortunately, the temperature readings from the thermocouple were highly sporadic, and did not compare to the values obtained from the surface thermometer. Temperatures fluctuating well above what was expected made the thermocouple reading unusable.

The final thermometer was a hand-held laser thermometer. This device was held 15.2 - 20.3 cm (6-8 in.) above the road surface. When the trigger was depressed, a digital screen displayed the recorded temperature. The values collected after several test runs were compared to the values collected from the surface dial thermometer. The difference in value was only 1°F. Because of the ease of use and the least possibility of error, the laser thermometer was used for the remainder of the field tests.

5.4 Data Reduction

After field-testing was completed, three major tasks remained with regard to data reduction: FWD pavement deflection data was interpreted, FOTS responses to FWD load pulses were analyzed, and multi-variant design matrices for statistical analysis were generated. These data reduction processes are discussed below.

5.4.1 Reduction of Raw FWD Deflection Data

Raw FWD field data was analyzed to determine pavement characteristics. As Cunagin stated, "the pavement profile strongly influences the random error of the sensor" [1988]. Therefore, data reduction began with the FWD load-deflection test information. The raw output files were converted to a spreadsheet format that contained load values and the corresponding pavement deflection. It was essential to know how the pavement was performing precisely at the sensor location, because previous field-testing showed low-level pavement deflections generated only a few inches away from the sensor produced negligible signal responses. Therefore, only the deflection values from directly beneath the FWD load plate were used.

This information was used to determine which sensor trials, if any, yielded errors due to irregular pavement deflection at the sensor. However, the statistical analysis program was not designed to incorporate random error in the pavement. If the pavement deflections for a particular trial appeared irregular, the sensor signal response was noted as a potential statistical outlier for that series of tests. If the pavement deflection differed only slightly from one trial to another, the sensor's change in signal response was considered an acceptable effect due to pavement characteristics, not the result of a poorly executed test trial.

5.4.2 Graphical Interpretation of FWD Testing on FOTS

The actual load pulses from the FWD on the fiber-optic traffic sensors were interpreted to determine the magnitude of light loss for each sensor trial (Appendix B). In order to collect this information from the plots generated from the LabView® software, the FWD load pulses had to be properly interpreted. To do this, a typical load pulse produced by a FWD was broken down into its components (Figure 5.21).

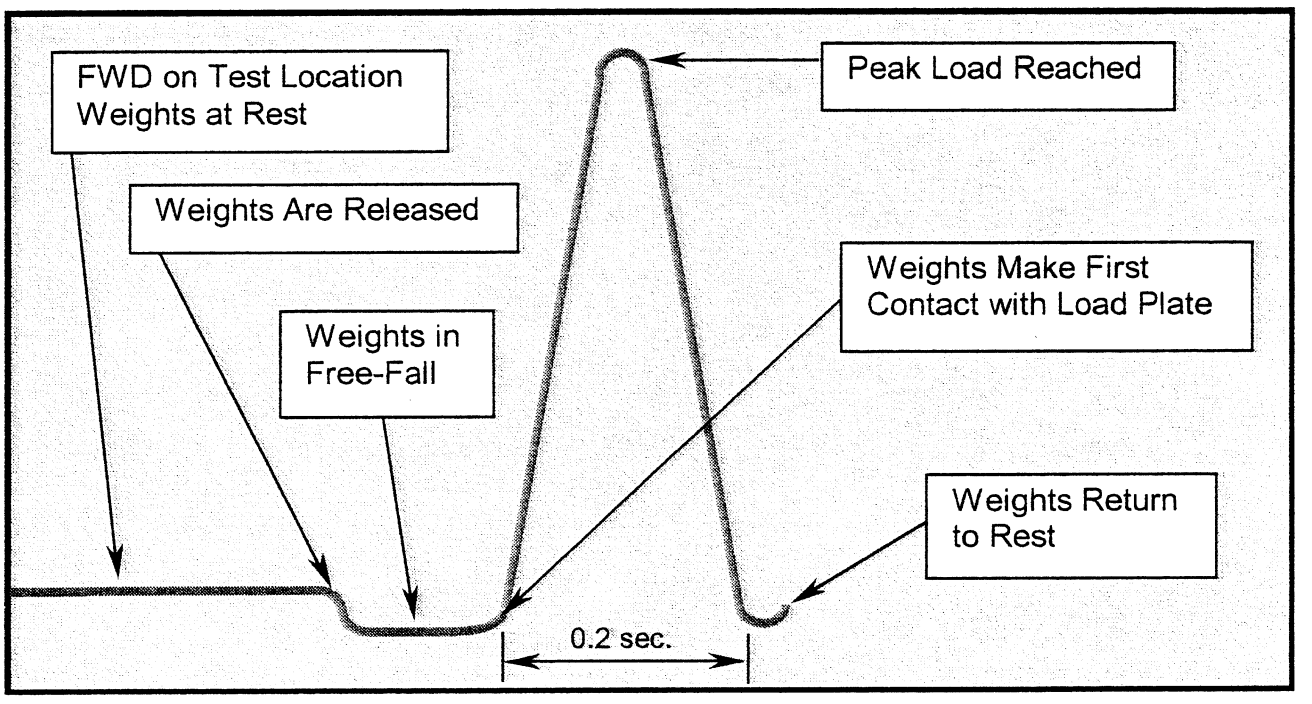

Figure 5.21 Typical Load Pulse Produced by FWD [Call, 2000]

Once the FWD lowered the drop plate on the test location, the weight of the at-rest test device produced a slight surcharge on the pavement. At this point, the pavement response was constant, as indicated by the initial horizontal portion of the curve. The moment the weights were released, the load on the pavement was lessened because the weights were free falling. The moment the weights contacted the load plate, stress was transferred to the pavement. In less than 0.2 seconds, the entire load was transferred to the pavement, creating a spike in the curve. As the

weights bounced from impacting the load plate, the load pulse rebounded. Once the drop weights returned to a state of rest, the stresses in the pavement returned to equilibrium, indicated by the load pulse returning to the original position [ERES, 1987].

These six key locations were required for interpreting the FOTS signal response plots. Although the signals were inverted and slightly more complex than the load pulse shown in Figure 5.22, the two plots were interpreted in the same manner.

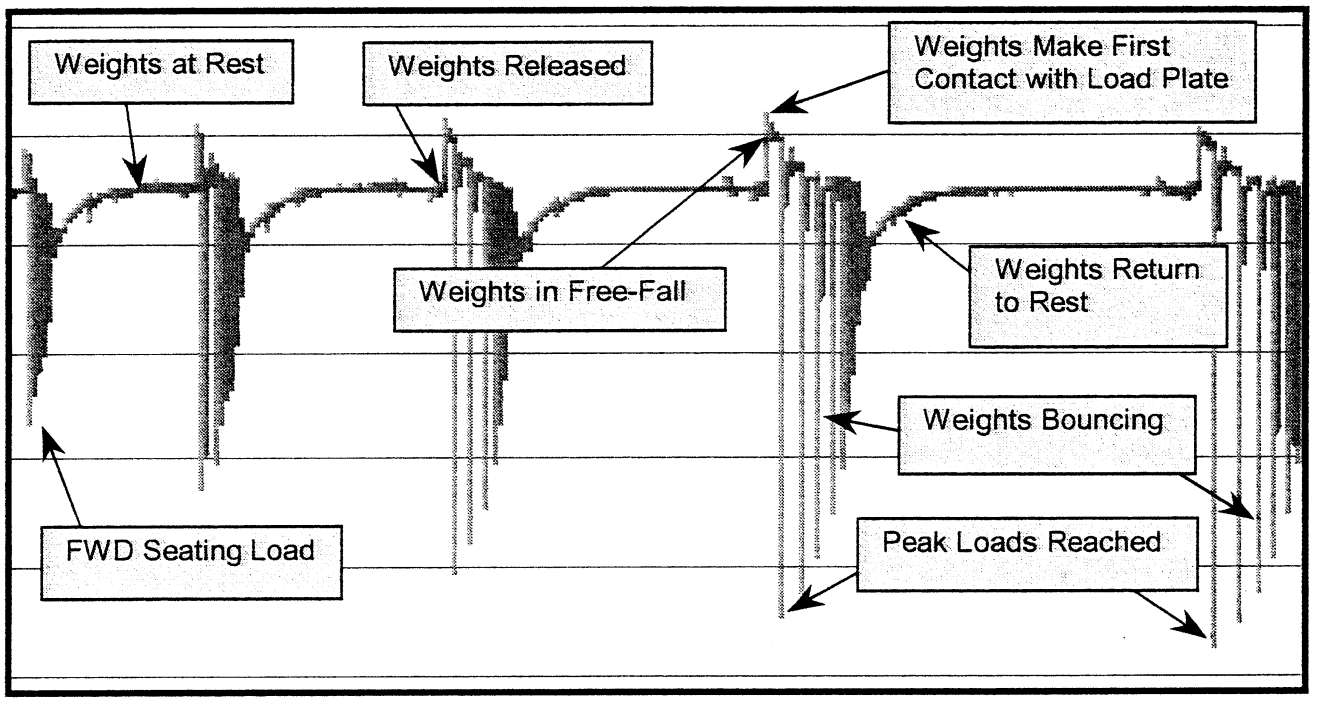

Figure 5.22 Actual Load Pulse from FWD on Fiber Optic Traffic Sensor [Call, 2000]

Each FWD field test on the FOTS produced a graph similar to the above figure. The LabView® plots from field trials for each sensor test run are included in Appendix E. The first spike in the LabView® plot was the seating load. Prior to every series of drops, the FWD equipment applied this seating load. After that, the FOTS signal response plot showed the change in light loss for each of the four progressively increasing drop loads. The maximum load applied to the sensor was selected as the first thin spike in the grouping of spikes for each of the different

load ranges. The grouping of decreasing spikes were the result of the drop load bouncing and settling back to rest. Between loads, the signal response returned to a constant level, which was controlled by the opto-electronics equipment. The difference between the constant signal response (at rest position) and the peak spike (maximum load transfer) from each drop load was used to determine the percent light loss for each different drop weight applied to the sensor. The percent light loss was tabulated for each sensor, trial and load. These values were then used to produce the findings reported in *Chapter 6: Results*.

5.4.3 Statistical Analysis Using ANOVA

Last, the LabView® signal response data was tabulated for use with statistical analysis. Data from the field-testing was input into an ANOVA program to evaluate the effects site-specific field variables have on FOTS signal response. A full factorial design was created for all variables to be evaluated at once. Separate full factorial designs were also created for each field test site. The benefit of the full factorial design was the ability to evaluate the main effects and the two-factor interactions [Rekab, 1999].

The results from each field trial were sorted into different categories, based upon sensor orientation, encapsulant, temperature, load value and pavement type. The design variables were the site-specific field variables, and design yield was the percent light loss from the FOTS. Additionally, the yield values from the multiple trials were converted into a dispersion value. This dispersion value, or deviation of the individual trial value from the average value for the trial set, was then assigned to each of the different trial configuration.

The light loss yield values for each similar trial were examined for outliers. If the yield differed more than 50 percent from the average value for that group of tests, the particular test trial was reviewed further. Examination revealed that outlier

results were lower than the average yield. If the difference in light loss could be attributed to a slightly lower pavement deflection from the average, the trial was not considered an outlier, because the resulting sensor performance could be attributed to the pavement characteristics. If pavement deflections were 200 percent lower than prior trials in the same location, that particular trial was marked as an outlier. If the pavement deflection values for the particular trial were normal, a signal response with a 50 percent decrease from the norm was assumed to be the result of poor loading on the sensor. If the FWD load plate rested unevenly on the pavement surface, the resulting drop load might have been applied several inches to either side the sensor. The result would be a pavement deflection that may not have fully actuated the sensor, causing decreased light loss.

The FWD testing performed in October 1999 was used for input into the ANOVA design. Testing that occurred in December 1999 was not used in the analysis for several reasons. Analysis of the field data indicated that the overall pavement stiffness for the flexible pavement system had increased during those two months. When FWD data from October was compared with FWD data from December, the pavement response to the same loading tests were significantly different. Additionally, the data collection system appeared to be performing poorly, which resulted in abnormal signal response plots. Because sufficient data was collected in October to perform replicated design analysis, it was decided to not incorporate the light-load drop test results into the ANOVA design.

Chapter 6

Presentation of FWD Results

6.1 Pavement Stiffness Evaluation

Surface pavement deflection profiles were created for both pavement types, using light and heavy weight drop tests (Appendix B). Findings in the literature confirmed the deflection results from the FWD testing would yield higher deflection values near the shoulder of the road, and in the wheel path, than in the middle of the roadway [ERES, 1987].

In addition, FWD research revealed that, within a single project, the coefficient of variation for deflection was typically around 20 percent, due to random variation in pavement construction [ERES, 1987]. When the four load levels were plotted with respect to their pavement deflections in Figure 6.1, the percent error fell within the expected range for the FWD on flexible pavement. For each load group, the deflections (plotted on the y-axis) ranged between 11 percent and 15 percent. The applied load (plotted on the x-axis) varied 2 percent to 7 percent from the target value.

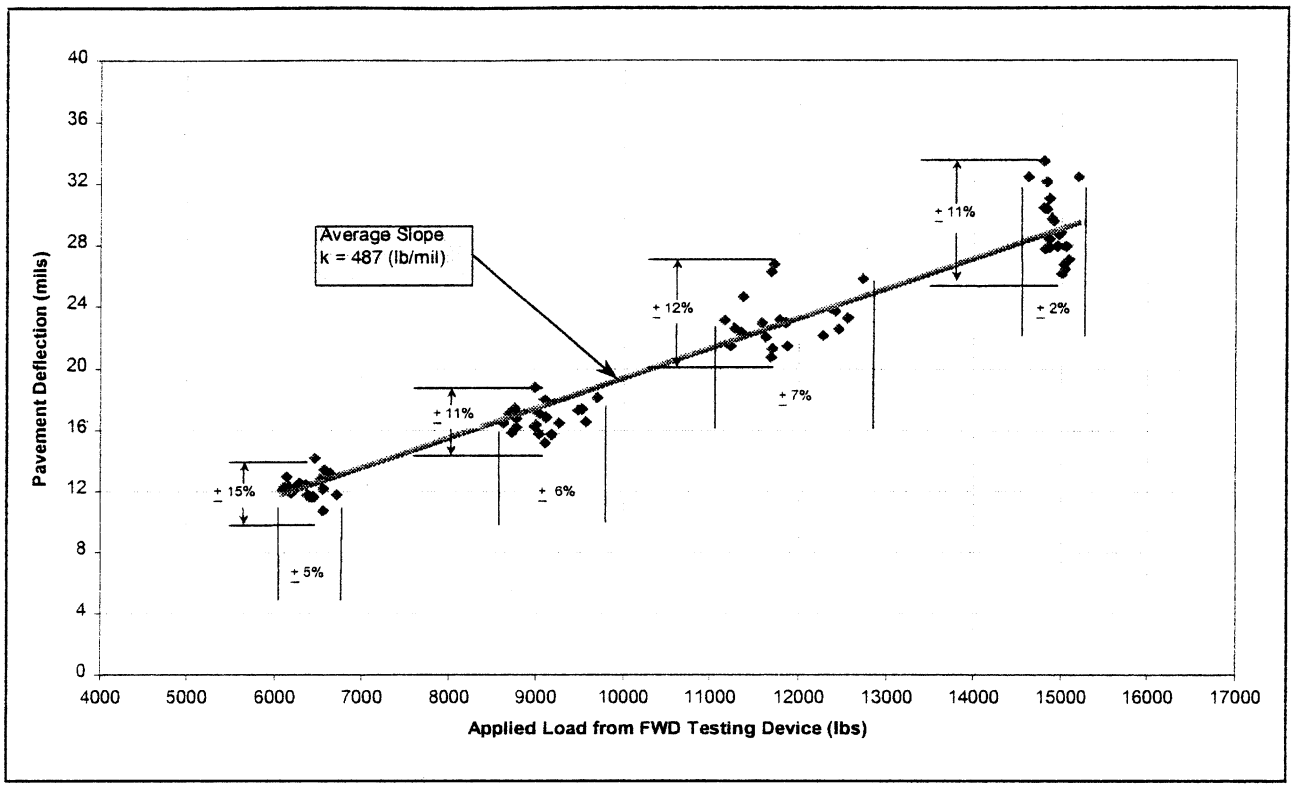

Figure 6.1 Stiffness of Flexible Pavement System Using Heavy Drop Weights

The data collected from FWD tests performed on the rigid pavement was also plotted (Figure 6.2). Because of the FWD drop plate's proximity to pavement joints, and warping/curling effects on the rigid pavement sections, the percent error for the rigid pavement system was slightly higher that the expected performance range for the FWD. The pavement deflections for the loading groups averaged 25 percent and reached as high as 29 percent.

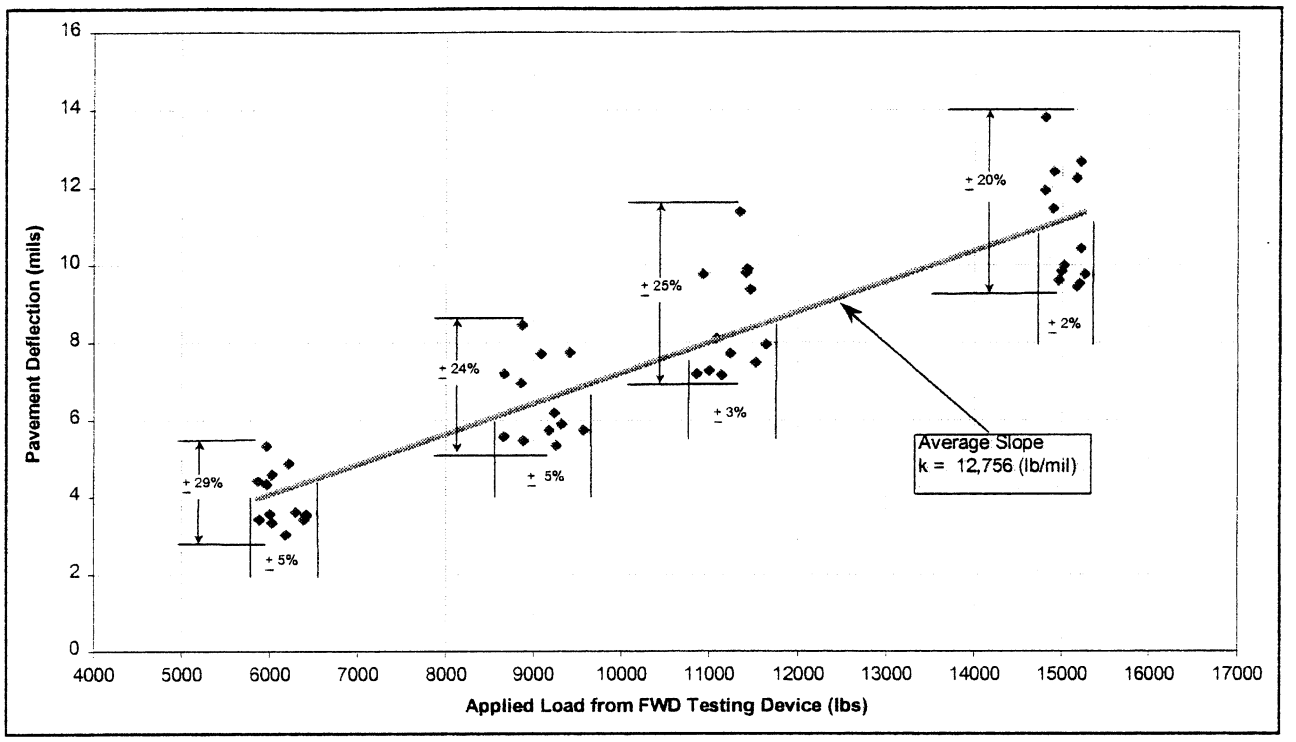

Figure 6.2 Stiffness of Rigid Pavement System Using Heavy Drop Weights

A linear relationship was found for the pavement systems when the load versus deflection information was graphed. The pavement system stiffness was determined by finding the average slope for that system. The stiffness value for the flexible pavement system was 487 lb/mil. The rigid pavement system stiffness was 12,758 lb/mil. These two systems, because of their different stiffness values, were used for comparing the effects of pavement type on FOTS signal performance. The nature of the pavement systems (i.e. response to surface temperature), not just the system stiffness, defined the difference between these two variables.

6.2 ANOVA Results

The FWD loads, deflections, and sensor response data was compiled and entered into the ANOVA statistical design. Because multiple FWD testing trials were performed for each sensor, an average value for the light loss, denoted *Y-bar*, was determined and entered into the design. By imputing *Y-bar* for each possible configuration a full-factorial design was

developed. This was beneficial because multiple trials resulted in more accurate results and the replicated design allowed for investigation into the sensor configurations' effect on dispersion, denoted *S*.

A full factorial design with multiple trials was constructed for examining the field test data. An example design, shown as Table 6.1, demonstrates how results from test trials, containing variables (A and B), would be configured for the ANOVA design. *Y1* and *Y2* were yield values for two trials, *Y-bar* was the average for the trials, and *S* was the deviation from the average for the trials. This matrix could then be used to evaluate the main effects and interaction effects.

Table 6.1 Sample Full Factorial Design: Main Effects and 2-Factor Interaction

Run	A	B	AB	Y1	Y2	Y-bar	S
1	+	+	+	30	40	35	5
2	+	-	-	18	20	19	1
3	-	+	-	33	39	36	3
4	-	-	+	22	26	24	2

6.2.1 Full Variable Evaluation

Constructing a full factorial design required assigning a high setting and a low setting to each variable, where the high setting represented one variable option, and the low settling represented another variable option. Rather than evaluate all five variables at once, the design was constructed such that the FWD load was held constant, while the other variables were varied to produce a yield value for the different test runs. Holding the applied load constant, the four remaining variables were assigned a high/low designation, as defined in Table 6.2.

Table 6.2 ANOVA Design of 4 Variables, Assignment of High /Low Conditions

Variable:	Pavement Type	Encapsulant Material	Sensor Orientation	Surface Temperature
Designation:	A	B	C	D
Low (-1)	Rigid Low Deflections	3M5200 E = 600psi	Horizontal	78 - 88°F
High (1)	Flexible High Deflections	ProSeal6006EX E = 1168psi	Vertical	90 - 110°F

6.2.1.1 Effects on Sensor Yield

Table 6.3 was constructed to examine the effects of the field variables on the average light loss of the sensor. Because horizontal ProSeal sensors in flexible pavement historically produced 100 percent light loss over the range of pressures used in other field tests, that specific configuration was not deployed for field-testing. However, to include it in the analysis, the average yield value for that configuration was reported as 100 percent light loss. This was based upon the assumption that the historical trends were acceptable. All possible combinations were used as input to the design matrix.

Table 6.3 Full Variable ANOVA Design Matrix for Yield

Evaluation of Field Variables Affecting FOTS Average Signal Response											
	Pavement Type	Encapsulant Material	Sensor Orientation	Surface Temperature	Percent Light Loss	Inter-action	Inter-action	Inter-action	Inter-action	Inter-action	Inter-action
Row	A	B	C	D	Y-bar	AB	AC	AD	BC	BD	CD
1	-1	-1	-1	-1	65.60	1	1	1	1	1	1
2	-1	-1	-1	1	23.50	1	1	-1	1	-1	-1
3	-1	-1	1	-1	87.00	1	-1	1	-1	1	-1
4	-1	-1	1	1	83.00	1	-1	-1	-1	-1	1
5	-1	1	-1	-1	81.86	-1	1	1	-1	-1	1
6	-1	1	-1	1	81.50	-1	1	-1	-1	1	-1
7	-1	1	1	-1	1.25	-1	-1	1	1	-1	-1
8	-1	1	1	1	2.00	-1	-1	-1	1	1	1
9	1	-1	-1	-1	92.88	-1	-1	-1	1	1	1
10	1	-1	-1	1	81.71	-1	-1	1	1	-1	-1
11	1	-1	1	-1	63.24	-1	1	-1	-1	1	-1
12	1	-1	1	1	52.29	-1	1	1	-1	-1	1
13	1	1	-1	-1	100.00	1	-1	-1	-1	-1	1
14	1	1	-1	1	100.00	1	-1	1	-1	1	-1
15	1	1	1	-1	70.18	1	1	-1	1	-1	-1
16	1	1	1	1	76.00	1	1	1	1	1	1

The result of the ANOVA design produced a value for the effect from each variable on yield (Table 6.4). The sign of the effect indicated which of the two options caused the greatest light loss, and the magnitude of the effect indicated the level of influence of the effect on light loss. Pareto charts were used as basic analysis tools for obtaining explanations to the ANOVA design results in a summarized format. In order to graph the effects on a Pareto chart, the effects were divided in half and the signs were removed by taking their absolute value. The absolute values of the half effects were plotted for main effects and two-factor interactions (Figure 6.3).

Table 6.4 Full Variable ANOVA Design: Effects Influencing Yield

	Main Effects				Interaction Effects					
	A	**B**	**C**	**D**	**AB**	**AC**	**AD**	**BC**	**BD**	**CD**
Δ	26.3	-4.5	-24.0	-7.7	18.6	-4.2	3.6	-27.5	9.3	5.6
|Δ/2|	13.2	2.3	12.0	3.9	9.3	2.1	1.8	14.7	4.6	2.8

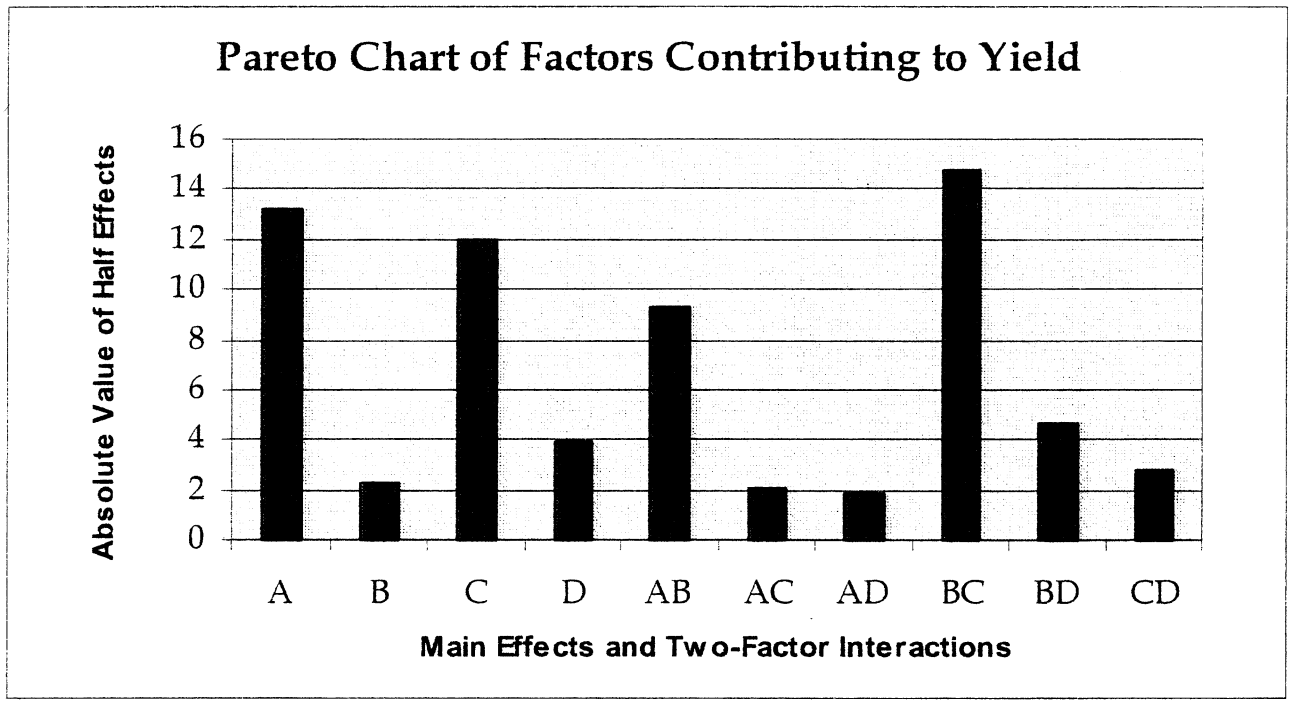

Figure 6.3 Contributions of Main Effects and Two-Factor Interactions on FOTS Light Loss Percentage

Similar procedures were repeated for the 6k, 9k, 12k, and 15k loading conditions, and Pareto charts were generated for each condition (Appendix B). Each load level produced similar results, identifying variables BC, A, C, and AB as the influential variables in FOTS light loss, respectively.

The Pareto charts from the constant load tests revealed the interaction between the type of encapsulant and the sensor orientation caused the greatest change in signal response, (BC= -27.5). Immediately following, the pavement type (A= 26.3) and the sensor orientation (C= -24.0) affected signal response. As well, the interaction between pavement type and encapsulant material (AB= 18.6) contributed to sensor light loss. The Pareto chart revealed the magnitude of temperature as a contributing factor to signal response was negligible as compared to the influential main effects and interaction effects.

Because the ANOVA design used the percent light loss for yield, the sign notation for the *influential* main effects and interaction effects indicated which setting, high or low, produced the most light loss. Flexible pavement should be selected, because it was the positive setting, and the main effect for pavement type was positive. The effect from sensor orientation was negative; therefore the negative setting, (horizontal orientation) should be selected to give the highest signal response.

The sign notations for interaction effects were determined by multiplying the signs of the individual main effects. Consider the predominant two-factor interaction, BC. The sign notation for BC was negative, as was the effect of C, yet the effect of B was also negative. If the setting for C were changed to the positive setting, the outcome on sensor yield would be altered, because C strongly affected yield. On the other hand, B had little or no effect on yield; therefore the setting for encapsulant material could be changed to the positive setting. By keeping C negative and selecting the positive setting for B, the interaction BC remained negative, which indicated the preferred encapsulant to be ProSeal (the positive setting). Also, the positive B setting kept the interaction AB positive, which it should, because this two-factor interaction also affected signal response. Like those main effects whose

contributions to yield were negligible, evaluation of two-factor interactions with little effect was not needed.

With the proper settings selected for the four main effects so that the sign notation for the effects that influenced yield did not change, that combination should produce the system with the greatest light loss. Field-testing and the ANOVA design both revealed that within flexible pavement, a horizontal sensor encapsulated with ProSeal 6006EX® should produce a sensor with the greatest light loss, regardless of surface temperatures.

6.2.1.2 Effects on Sensor Dispersion

Table 6.5 was constructed to examine the effects of the field variables on sensor response dispersion. The dispersion, of the signal is useful for evaluating WIM. In general, the lower the signal dispersion the better the WIM results would be. However, an exception would result from the 100 percent light loss for each trial of a horizontal ProSeal sensor in flexible pavement. This would produce zero dispersion, yet the signal response was 100 percent regardless of axle weight, which indicated a poor WIM configuration.

Table 6.5 Full Variable ANOVA Design Matrix for Dispersion

Evaluation of Field Variables Affecting FOTS Signal Response Dispersion											
	Pavement Type	Encapsulant Material	Sensor Orientation	Surface Temperature	Dispersion	Inter-action	Inter-action	Inter-action	Inter-action	Inter-action	Inter-action
Row	A	B	C	D	S	AB	AC	AD	BC	BD	CD
1	-1	-1	-1	-1	19.96	1	1	1	1	1	1
2	-1	-1	-1	1	9.50	1	1	-1	1	-1	-1
3	-1	-1	1	-1	7.28	1	-1	1	-1	1	-1
4	-1	-1	1	1	8.00	1	-1	-1	-1	-1	1
5	-1	1	-1	-1	30.52	-1	1	1	-1	-1	1
6	-1	1	-1	1	16.90	-1	1	-1	-1	1	-1
7	-1	1	1	-1	0.61	-1	-1	1	1	-1	-1
8	-1	1	1	1	0.00	-1	-1	-1	1	1	1
9	1	-1	-1	-1	9.82	-1	-1	-1	1	1	1
10	1	-1	-1	1	17.85	-1	-1	1	1	-1	-1
11	1	-1	1	-1	93.50	-1	1	-1	-1	1	-1
12	1	-1	1	1	49.25	-1	1	1	-1	-1	1
13	1	1	-1	-1	0.00	1	-1	-1	-1	-1	1
14	1	1	-1	1	0.00	1	-1	1	-1	1	-1
15	1	1	1	-1	51.33	1	1	-1	1	-1	-1
16	1	1	1	1	25.61	1	1	1	1	1	1

The ANOVA design produced values for the effects on dispersion (Table 6.6). The absolute value of the half effects were taken and plotted for both main effects and two-factor interactions (Figure 6.4).

Table 6.6 Full Variable ANOVA Design: Effects Influencing Dispersion

	Main Effects				Interaction Effects					
	A	**B**	**C**	**D**	**AB**	**AC**	**AD**	**BC**	**BD**	**CD**
Δ	19.3	-11.3	16.4	-10.7	-12.1	31.6	-4.7	-8.8	0.8	-6.7
|Δ/2|	9.7	5.6	8.2	5.4	6.0	15.8	2.4	4.4	0.4	3.4

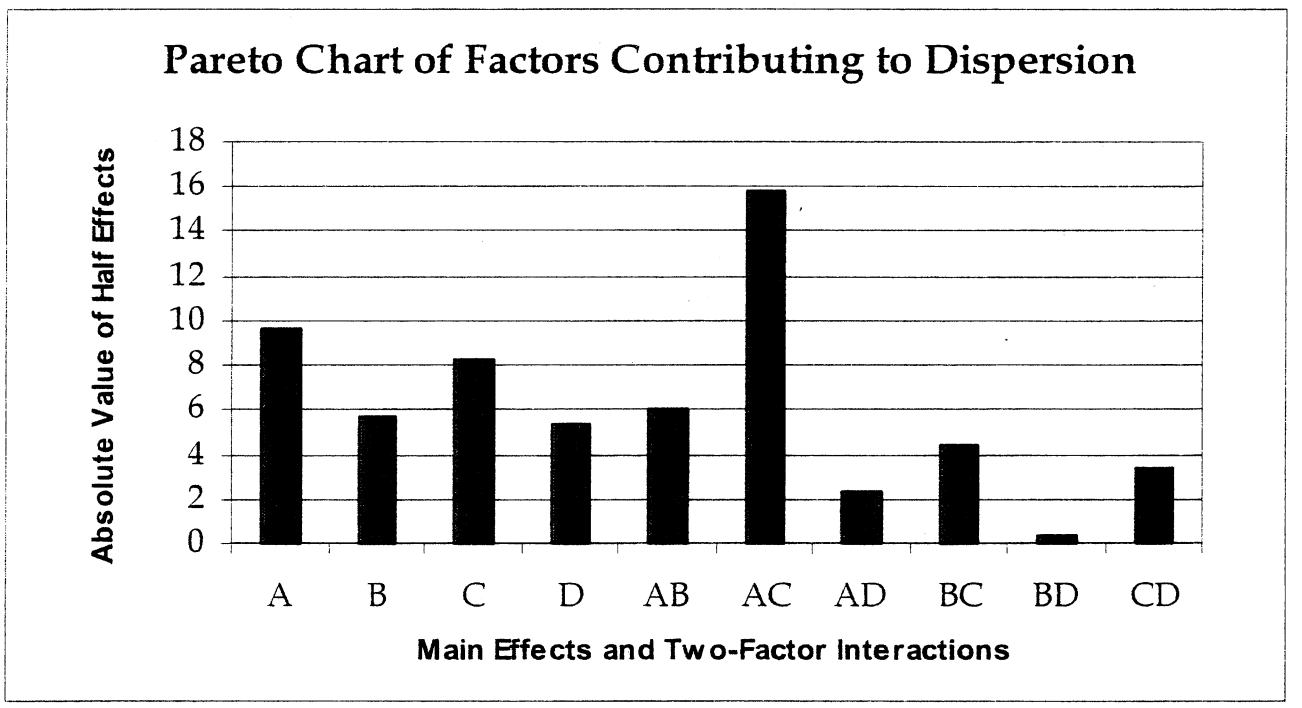

Figure 6.4 Contributions of Main Effects and Two-Factor Interactions on FOTS Dispersion.

The Pareto charts from the constant load tests revealed the pavement type/sensor orientation interaction caused the greatest dispersion (AC= 31.6). Next, the pavement type (A= 19.3) and the sensor orientation (C= 16.4) affected dispersion. The Pareto chart revealed the other main effects and two-factor interactions were negligible when compared to interaction AC.

The ANOVA design was used to examine the dispersion due to the different design variables. The sign notation for each main effect and two-factor interaction recorded in Table 6.6 revealed which setting, high or low, was responsible for producing the *greatest* dispersion. Therefore, in order to produce the *lowest* dispersion, an objective in WIM, the reverse settings for each variable should be selected from the configuration shown in Table 6.6. For this reason, rigid pavement should be selected, because the main effect for pavement type should be switched to a negative value. Additionally, the negative setting, (horizontal orientation) should be selected for C. The other main effects should have their settings reversed to keep the matrix valid. This would not significantly affect the result, because variables B and D were not influential main effects for dispersion. The negative setting for variables A and C still resulted in a positive value for the interaction effect AC, which validated the ANOVA design.

If the settings were selected so that dispersion was minimized, the proper combinations of main effects should produce a sensor that produced a repeatable signal under a constant load. If a sensor configuration was selected that maximized light loss, the low dispersion could result from 100 percent light loss, regardless of load level, which would be unacceptable for WIM. Therefore, the best configuration for a FOTS used for WIM applications would be a sensor placed horizontally rigid pavement with 3M 5200® encapsulant.

6.2.2 Flexible Pavement Site Evaluation

To clarify the findings on the site-specific variables' effects on fiber optic sensor performance, each field site was examined independently. The smaller design matrix was generated from the larger four-variable design by selecting only those trial runs that had the flexible pavement setting. By having the same pavement type setting for every trial,

pavement type was essentially removed from the ANOVA matrix. With this configuration, the applied load was held constant so that the ANOVA design examined only the effects of encapsulant type, sensor orientation and surface temperature, as defined in Table 6.7.

Table 6.7 ANOVA Design of 3 Variables, Assignment of High /Low Conditions

Variable:	Encapsulant Material	Sensor Orientation	Surface Temperature
Designation:	A	B	C
Low (--):	3M5200 E = 600 psi	Horizontal	78 - 88°F
High (+):	ProSeal6006EX E = 1168 psi	Vertical	90 - 110°F

6.2.2.1 Effects on Sensor Yield at a Flexible Pavement Site

Table 6.8 was constructed to examine the effects of the field variables on the average light loss of the sensor, without incorporating the effect of pavement type. All flexible pavement combinations were input to the design matrix.

Table 6.8 Flexible Pavement ANOVA Design Matrix for Yield

Full Factorial Design of Main Effects and Two-Factor Interactions for Flexible Pavement							
	Encapsulant Material	Sensor Orientation	Surface Temperature	Percent Light Loss	Inter-action	Inter-action	Inter-action
Row	A	B	C	Y-bar	AB	AC	BC
1	--	--	--	92.88	+	+	+
2	+	--	--	100.00	--	--	+
3	--	+	--	63.24	--	+	--
4	+	+	--	70.18	+	--	--
5	--	--	+	81.71	+	--	--
6	+	--	+	100.00	--	+	--
7	--	+	+	52.29	--	--	+
8	+	+	+	76.00	+	+	+

The result of the ANOVA design produced a value for the effect of each variable on yield (Table 6.9). The absolute values were determined for the half effects, and plotted for both main effects and two-factor interactions (Figure 6.5).

The numeric values for the effects on yield were shown to have changed from the four-variable ANOVA design to the three-variable ANOVA design. Because the sum of the yield values generated during the ANOVA analysis changes from test to test, the values of the effects also change. These values cannot be used as a means of comparing magnitude of influence between separate ANOVA designs.

Table 6.9 Flexible Pavement ANOVA Design: Effects Influencing Yield

	Main Effects			Interaction Effects		
	A	**B**	**C**	**AB**	**AC**	**BC**
Δ	14.0	-28.2	-4.0	1.3	7.0	1.5
|Δ/2|	7.0	14.1	2.0	0.6	3.5	0.7

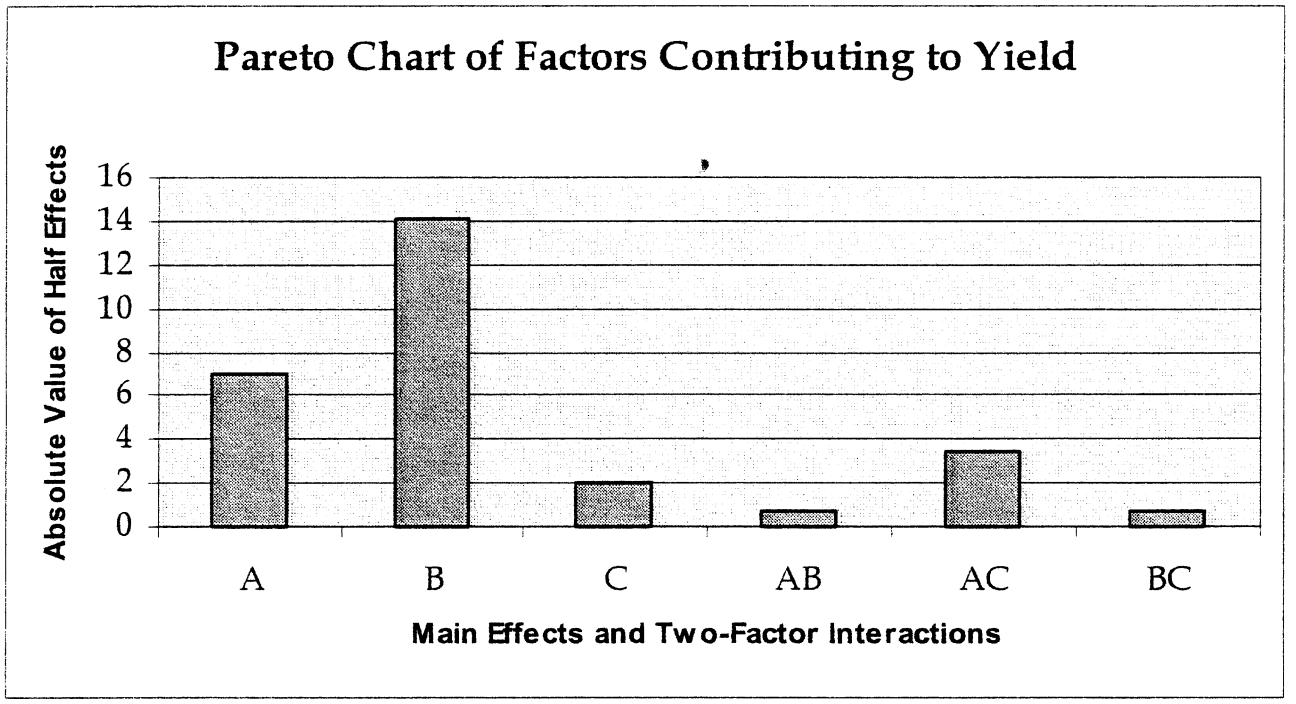

Figure 6.5 Contributions of Main Effects and Two-Factor Interactions on FOTS Light Loss Percentage at Flexible Pavement Site

Table 6.9 showed that within flexible pavement the sensor orientation produced the greatest effect on signal response (B= -28.2). As in the case with the full variable ANOVA design, the horizontal sensor configuration (low setting) resulted in the greatest signal response. Comparatively, the encapsulant material had only a slight effect, while the temperature and the two-factor interactions had negligible effects on the response of fiber-optic sensors installed in flexible pavement.

The influence level for site-specific variables changed when examining only one field site. For example, because pavement was not being directly examined, the ANOVA design could not present findings regarding pavement/encapsulant interaction because the ANOVA design did not have input for comparing two different pavement types. Importance of variables shown in both analyses remained constant from one test to the next. If orientation were shown to be important in the four-variable analysis for yield, then orientation would also appear to be important in the three-variable analysis for yield.

6.2.2.2 Effects on Sensor Dispersion at a Flexible Pavement Site

Table 6.10 was constructed to examine the effects of the field variables on sensor response dispersion. Like the three-variable trial created to examine effects on sensor yield, Table 6.10 was generated directly from the larger four-variable design matrix for dispersion.

Table 6.10 Flexible Pavement ANOVA Design Matrix for Dispersion

Full Factorial Design of Main Effects and Two-Factor Interactions for Flexible Pavement							
	Encapsulant Material	Sensor Orientation	Surface Temperature	Dispersion	Inter-action	Inter-action	Inter-action
Row	A	B	C	S	AB	AC	BC
1	--	--	--	9.82	+	+	+
2	+	--	--	17.85	--	--	+
3	--	+	--	53.95	--	+	--
4	+	+	--	49.25	+	--	--
5	--	--	+	0.00	+	--	--
6	+	--	+	0.00	--	+	--
7	--	+	+	35.04	--	--	+
8	+	+	+	22.75	+	+	+

The result of the ANOVA design produced a value for the effect on yield (Table 6.11). The absolute value of the half effects were calculated and plotted for both main effects and two-factor interactions (Figure 6.6).

Table 6.11 Flexible Pavement ANOVA Design: Effects Influencing Dispersion

	Main Effects			Interaction Effects		
	A	**B**	**C**	**AB**	**AC**	**BC**
Δ	-2.2	33.3	-18.2	-6.2	-3.9	4.4
|Δ/2|	1.1	16.7	9.1	3.1	1.9	2.2

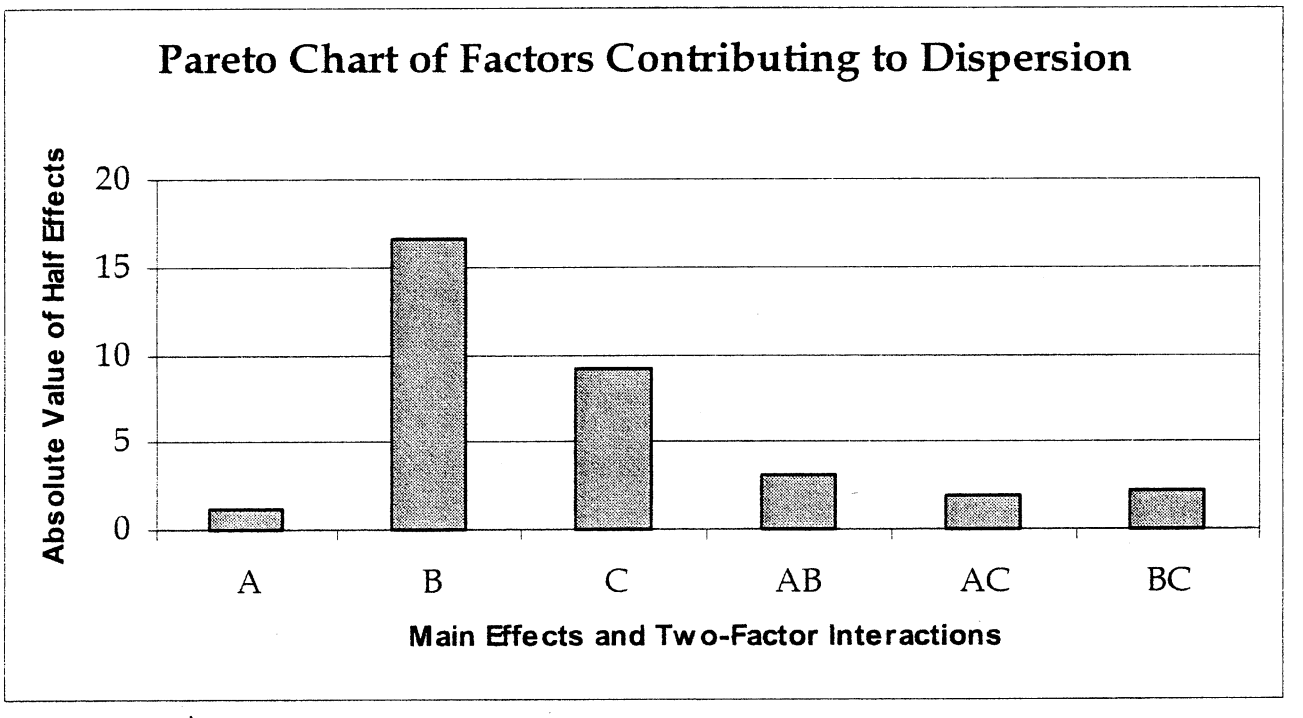

Figure 6.6 Contributions of Main Effects and Two-Factor Interactions on FOTS Signal Dispersion at Flexible Pavement Site

The Pareto charts from the constant load tests at the flexible pavement site revealed that sensor orientation dominated the effect on dispersion (B= 33.3). The positive sign of the effect revealed it was again the vertically placed sensor configuration that resulted in the greatest sensor response dispersion. In the flexible pavement, temperature was shown to

have had a small effect on dispersion, although it was negligible. Signal response dispersion from encapsulant material selection and two-factor interactions were negligible compared to the effects from sensor orientation.

6.2.2.3 Load Effects on Sensor Yield at a Flexible Pavement Site

To show the effect applied load had on FOTS signal response, a varied load was applied to the test runs, where the low setting represented a 6k drop load and the high setting represented a 15k drop load. The three remaining variables and their settings were not changed, only their designation letter, shown in Table 6.12.

Table 6.12 ANOVA Design of 4 Variables, Assignment of High /Low Conditions

Variable:	Applied Load	Encapsulant Material	Sensor Orientation	Surface Temperature
Designation:	A	B	C	D
Low (-1):	6k	3M5200	Horizontal	78 - 88°F
High (1):	15k	ProSeal	Vertical	90 - 110°F

The value for *Y-bar* in Table 6.13 represented the average value for the percent light loss of that specific trial. The first eight runs represented the 6k drop load on the sensors in flexible pavement, and the second eight runs represented the 15k drop loads on the same sensors. As discussed previously, the horizontal ProSeal sensor produced 100 percent light loss for both conditions.

Table 6.13 Flexible Pavement ANOVA Design Including Load Effects on Yield

Full Factorial Design of Main Effects and Two-Factor Interactions - Flexible Pavement

Row	Applied Load A	Encapsulant Material B	Sensor Orientation C	Surface Temperature D	Percent Light Loss Y-bar	Inter-action AB	Inter-action AC	Inter-action AD	Inter-action BC	Inter-action BD	Inter-action CD
1	-1	-1	-1	-1	74.25	1	1	1	1	1	1
2	-1	-1	-1	1	71.14	1	1	-1	1	-1	-1
3	-1	-1	1	-1	52.86	1	-1	1	-1	1	-1
4	-1	-1	1	1	47.17	1	-1	-1	-1	-1	1
5	-1	1	-1	-1	100.00	-1	1	1	-1	-1	1
6	-1	1	-1	1	100.00	-1	1	-1	-1	1	-1
7	-1	1	1	-1	50.63	-1	-1	1	1	-1	-1
8	-1	1	1	1	61.58	-1	-1	-1	1	1	1
9	1	-1	-1	-1	87.63	-1	-1	-1	1	1	1
10	1	-1	-1	1	91.43	-1	-1	1	1	-1	-1
11	1	-1	1	-1	87.57	-1	1	-1	-1	1	-1
12	1	-1	1	1	78.43	-1	1	1	-1	-1	1
13	1	1	-1	-1	100.00	1	-1	-1	-1	-1	1
14	1	1	-1	1	100.00	1	-1	1	-1	1	-1
15	1	1	1	-1	88.42	1	1	-1	1	-1	-1
16	1	1	1	1	90.92	1	1	1	1	1	1

The result of the ANOVA design produced a value for the effect on yield (Table 6.14). The absolute values of the half effects were also plotted (Figure 6.7).

Table 6.14 Flexible Pavement Design: Effects Including Load on Yield

	Main Effects				Interaction Effects					
	A	**B**	**C**	**D**	**AB**	**AC**	**AD**	**BC**	**BD**	**CD**
Δ	20.8	12.6	-20.9	-0.1	-4.1	12.4	-0.6	-6.3	3.4	-0.3
$\lvert\Delta/2\rvert$	10.4	6.3	10.4	0.05	2.0	6.2	0.3	3.2	1.7	0.1

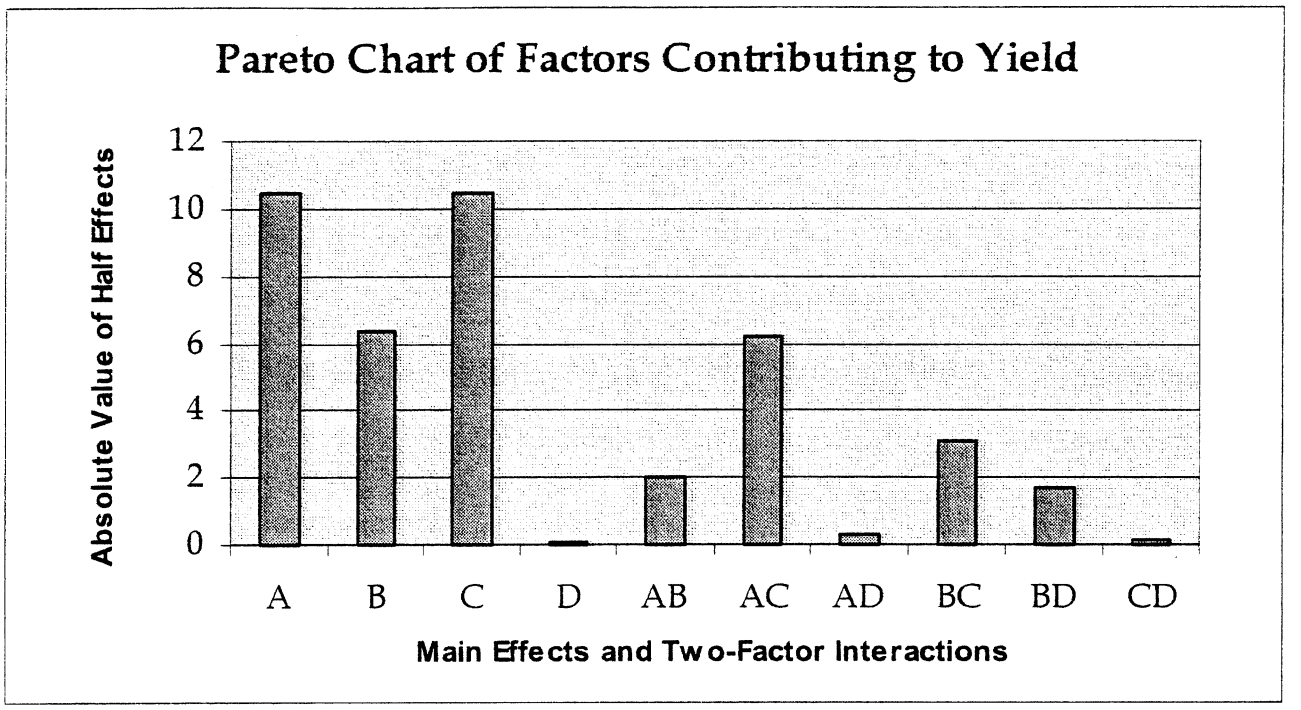

Figure 6.7 Contributions of Main Effects and two-Factor Interactions on Yield when Applied Load was Varied at Flexible Pavement Site

The resulting analysis reported that loading conditions caused effects on sensor yield. Sign notation on the main effects indicated increasing loads caused increased signal response. The Pareto chart clearly showed the reduced effects of temperature and interactions with varied loads. Because of their strong effects, the combination of high loads on horizontal ProSeal sensors should be avoided for WIM.

6.2.3 Rigid Pavement Site Evaluation

To clarify the findings on the site-specific variables' effects on fiber optic sensor performance, the rigid pavement field site was examined independently. The smaller design matrix was generated from the larger four-variable design by selecting only those trial runs that had the rigid pavement setting. By having the same pavement setting for every trial, pavement type was essentially removed from the ANOVA matrix. With this configuration, the applied load was again held constant such that the ANOVA design examined only the effects of encapsulant type, sensor orientation and surface temperature, as defined in Table 6.15.

The temperature ranges used at the rigid pavement site were slightly different than the temperature ranges used at the flexible pavement site. Although the low temperature settings were the same at both sites, the high setting for the rigid pavement did not extend above 100°F.

Table 6.15 ANOVA Design of 3 Variables, Assignment of High /Low Conditions

Variable:	Encapsulant Material	Sensor Orientation	Surface Temperature
Designation:	A	B	C
Low (--):	3M5200 E = 600 psi	Horizontal	78 - 88°F
High (+):	ProSeal6006EX E = 1168 psi	Vertical	> 90°F

6.2.3.1 Effects on Sensor Yield at a Rigid Pavement Site

Table 6.16 was constructed to examine the effects of the field variables on the average light loss of the sensor. Because the performance of the different configurations was not known at the time of testing, each of the four sensor configurations were placed within the rigid pavement and tested to obtain sensor response data for the ANOVA design.

Table 6.16 Rigid Pavement ANOVA Design Matrix for Yield

Full Factorial Design of Main Effects and Two-Factor Interactions for Rigid Pavement							
	Encapsulant Material	Sensor Orientation	Surface Temperature	Percent Light Loss	Inter-action	Inter-action	Inter-action
Row	A	B	C	Y-bar	AB	AC	BC
1	–	–	–	65.60	+	+	+
2	+	–	–	81.86	–	–	+
3	–	+	–	87.00	–	+	–
4	+	+	–	1.25	+	–	–
5	–	–	+	23.50	+	–	–
6	+	–	+	81.50	–	+	–
7	–	+	+	83.00	–	–	+
8	+	+	+	2.00	+	+	+

The result of the ANOVA design produced a value for the effect of each variable on yield (Table 6.17). The absolute value of the half effects were calculated and plotted for both main effects and two-factor interactions (Figure 6.8). Since the rigid pavement was stiffer than the flexible pavement, a change in influence from the main effects and two-factor interactions was seen between the two sites.

Table 6.17 Rigid Pavement ANOVA Design: Effects Influencing Yield

	Main Effects			Interaction Effects		
	A	B	C	AB	AC	BC
Δ	-23.1	-19.8	-11.4	-60.2	11.6	9.8
$\lvert \Delta/2 \rvert$	11.6	9.9	5.7	30.1	5.8	4.9

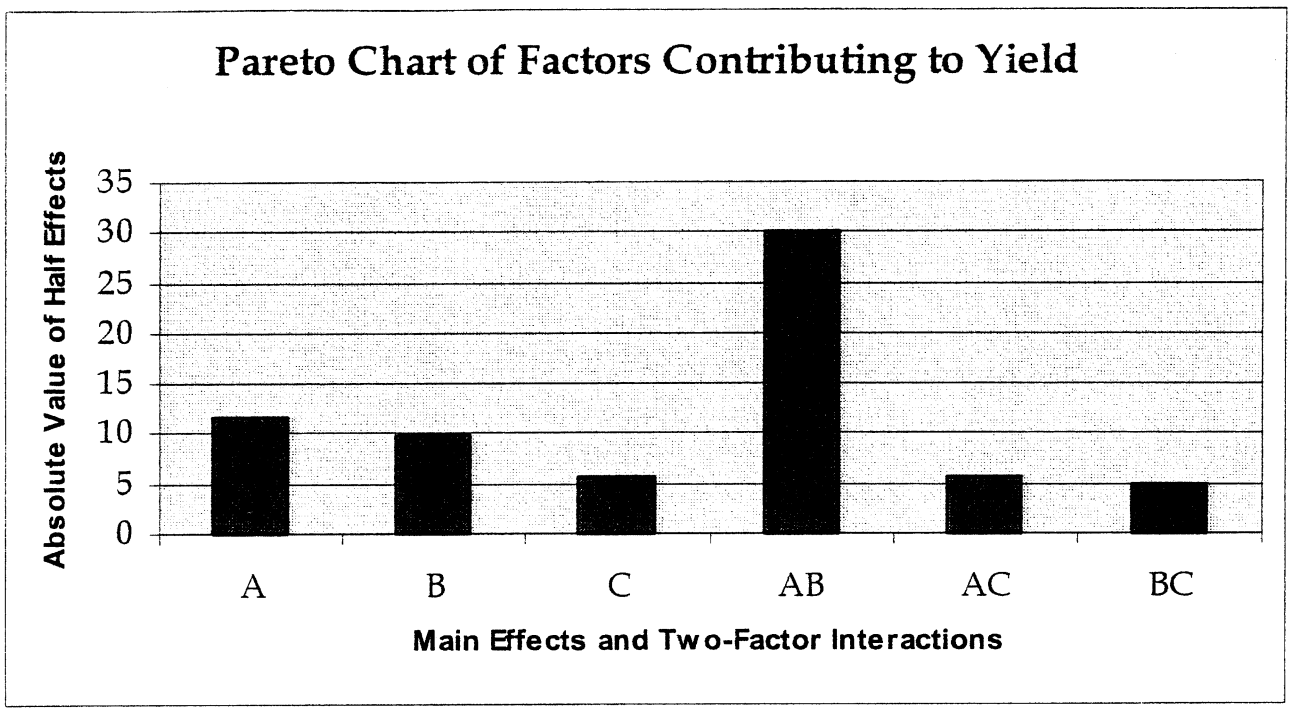

Figure 6.8 Contributions of Main Effects and Two-Factor Interactions on FOTS Light Loss Percentage at Rigid Pavement Site

The Pareto chart from the constant load test revealed that within a rigid pavement site it was the interaction between the encapsulant type and the pavement orientation that produced the greatest effect on signal response (AB= -60.2). As in the case with the full variable ANOVA design, it was an interaction that had the greatest effect. If a partial analysis had been performed in which only main effects were examined, the true controlling factor would have been missed.

Because no specific encapsulant or orientation main effect dominated signal response, the highest yield would be achieved by taking the setting combination that kept the sign of interaction AB negative. It would not be advised to select the same setting for both the encapsulant and the orientation at a rigid pavement site. Because there were two theoretical combinations to make this case true, the proper setting combination was revealed by examining the design matrix, previously shown in Table 6.16. The yield values, *Y-bar*, for the rows with a vertically placed 3M5200® sensor were consistently higher than the rows with the horizontally placed ProSeal6006EX®. Therefore, it can be reported that the vertical

sensors encapsulated in 3M5200® produced the greatest signal response. Once again, the temperature had a negligible contribution to FOTS performance.

6.2.3.2 Effects on Sensor Dispersion at a Rigid Pavement Site

Table 6.18 was constructed to analyze the effects of the field variables on sensor response dispersion in rigid pavement. It is important to note that although the dispersion value for a sensor may be low, which would indicate a precise sensor response performance, it does not necessarily relate to accurate sensor responses. For example, the vertical ProSeal 6006EX® sensor repeatedly produced a light loss value of only 1 percent to 2 percent. This resulted in a low dispersion, yet the signal response was unvarying, which would indicate a poor configuration for weigh-in-motion.

Table 6.18 Rigid Pavement ANOVA Design Matrix for Dispersion

Full Factorial Design of Main Effects and Two-Factor Interactions for Rigid Pavement							
	Encapsulant Material	Sensor Orientation	Surface Temperature	Dispersion	Inter-action	Inter-action	Inter-action
Row	A	B	C	S	AB	AC	BC
1	--	--	--	19.96	+	+	+
2	+	--	--	9.50	--	--	+
3	--	+	--	7.28	--	+	--
4	+	+	--	8.00	+	--	--
5	--	--	+	30.52	+	--	--
6	+	--	+	16.90	--	+	--
7	--	+	+	0.61	--	--	+
8	+	+	+	0.00	+	+	+

The result of the ANOVA design produced a value for the effect on yield (Table 6.19). The absolute value of the half effects were calculated and plotted for both main effects and two-factor interactions (Figure 6.9).

Table 6.19 Rigid Pavement ANOVA Design: Effects Influencing Dispersion

	Main Effects			Interaction Effects		
	A	**B**	**C**	**AB**	**AC**	**BC**
Δ	-6.0	-15.2	0.8	6.0	-1.2	-8.1
|Δ/2|	3.0	7.6	0.4	3.0	0.6	4.0

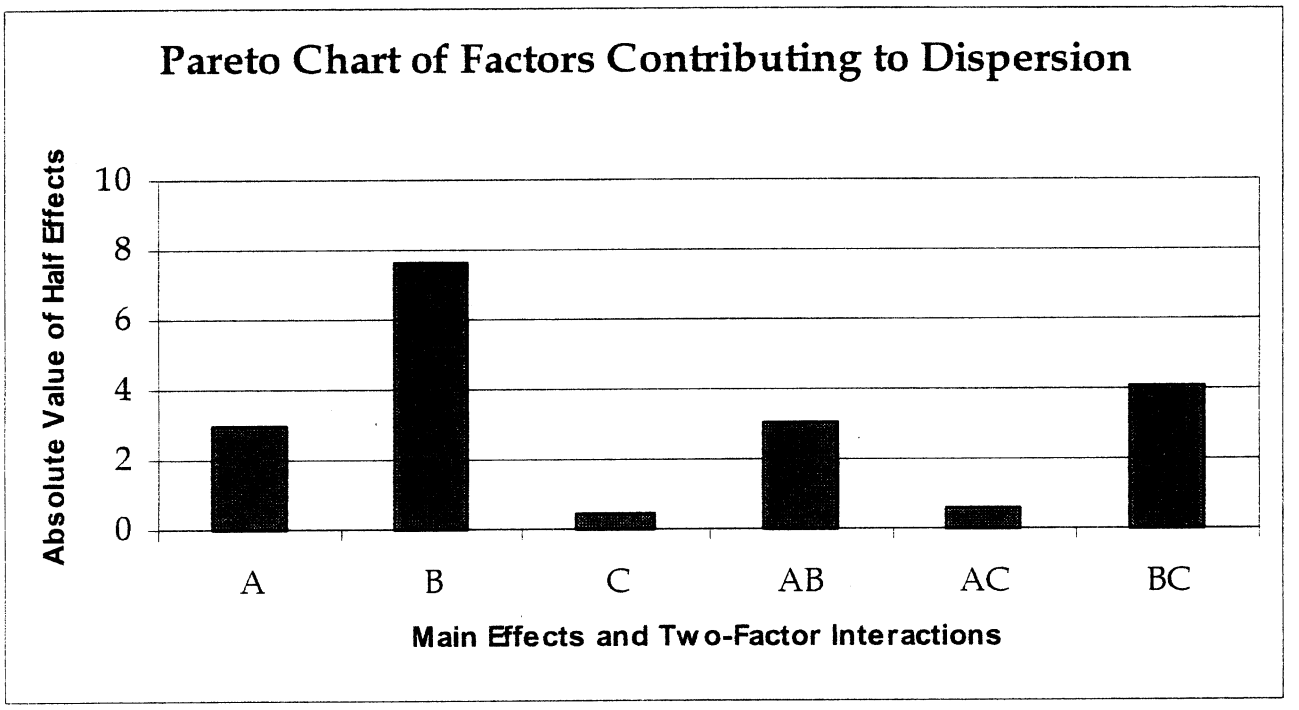

Figure 6.9 Contributions of Main Effects and Two-Factor Interactions on FOTS Signal Dispersion at Rigid Pavement Site

The Pareto charts from the constant load tests at a rigid pavement site revealed that it was the sensor orientation that dominated the effect on dispersion (B= -15.2). The negative sign of the main effect revealed it was the vertically placed sensor configuration that resulted in poor precision of the sensor response. In the full variable design, the positive setting for the orientation main effect could again be identified as the cause for FOTS signal response dispersion. This was the case for the flexible and the rigid pavement site. In the rigid pavement, temperature had no effect on dispersion. Signal response dispersion from encapsulant material selection and two-factor interactions was negligible when compared to the effects from sensor orientation.

6.2.3.3 Load Effects on Sensor Yield at a Rigid Pavement Site

To show the effect applied load had on FOTS signal response, a varied load was applied to the test runs, where the low setting represented a 6k drop load and the high setting represented a 15k drop load. The three additional variables and their settings were not changed, only their designation letter, shown in Table 6.20.

Table 6.20 ANOVA Design of 4 Variables, Assignment of High /Low Conditions

Variable:	Applied Load	Encapsulant Material	Sensor Orientation	Surface Temperature
Designation:	A	B	C	D
Low (-1):	6k	3M5200 E = 600 psi	Horizontal	78 - 88°F
High (1):	15k	ProSeal E = 1168 psi	Vertical	> 90°F

The values for *Y-bar* represented the average value for the percent light loss of that specific trial. The first eight runs were the averaged result of the 6k FWD drop load on the sensors in flexible pavement, and the second eight runs were the averaged results of the 15k FWD drop loads on the same sensors (Table 6.21).

Table 6.21 Rigid Pavement ANOVA Design Including Load Effects on Yield

Full Factorial Design of Main Effects and Two-Factor Interactions - Rigid Pavement

Row	Applied Load A	Encapsulant Material B	Sensor Orientation C	Surface Temperature D	Percent Light Loss Y-bar	Inter-action AB	Inter-action AC	Inter-action AD	Inter-action BC	Inter-action BD	Inter-action CD
1	-1	-1	-1	-1	48.40	1	1	1	1	1	1
2	-1	-1	-1	1	29.00	1	1	-1	1	-1	-1
3	-1	-1	1	-1	79.70	1	-1	1	-1	1	-1
4	-1	-1	1	1	66.50	1	-1	-1	-1	-1	1
5	-1	1	-1	-1	59.70	-1	1	1	-1	-1	1
6	-1	1	-1	1	60.25	-1	1	-1	-1	1	-1
7	-1	1	1	-1	1.00	-1	-1	1	1	-1	-1
8	-1	1	1	1	1.50	-1	-1	-1	1	1	1
9	1	-1	-1	-1	80.33	-1	-1	-1	1	1	1
10	1	-1	-1	1	43.00	-1	-1	1	1	-1	-1
11	1	-1	1	-1	92.40	-1	1	-1	-1	1	-1
12	1	-1	1	1	96.50	-1	1	1	-1	-1	1
13	1	1	-1	-1	87.33	1	-1	-1	-1	-1	1
14	1	1	-1	1	95.50	1	-1	1	-1	1	-1
15	1	1	1	-1	2.00	1	1	-1	1	-1	-1
16	1	1	1	1	3.50	1	1	1	1	1	1

The ANOVA design results produced values for the effects on yield (Table 6.22). The absolute values of the half effects were also plotted (Figure 6.10).

Table 6.22 Rigid Pavement Design: Effects Including Load on Yield

	Main Effects				Interaction Effects					
	A	**B**	**C**	**D**	**AB**	**AC**	**AD**	**BC**	**BD**	**CD**
Δ	19.3	-28.1	-20.1	-6.9	-2.8	-7.9	1.0	-53.6	9.6	5.1
|Δ/2|	9.7	14.1	10.0	3.4	1.4	3.9	0.5	26.8	4.8	2.6

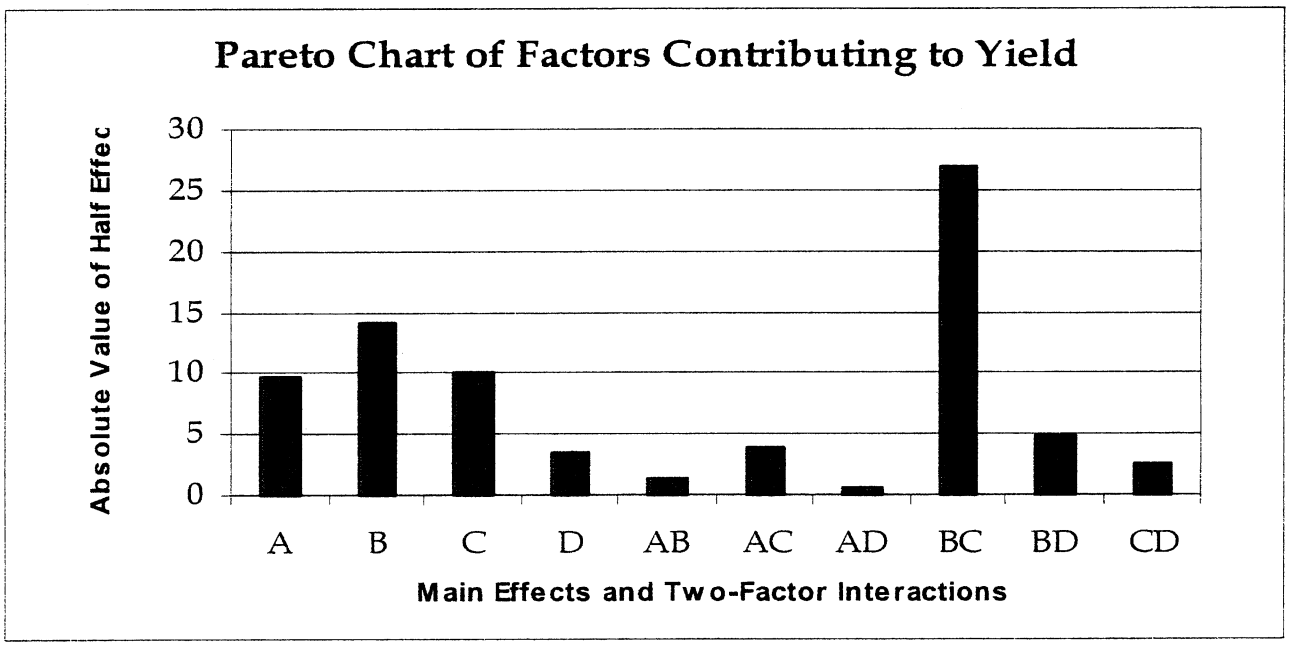

Figure 6.10 Contributions of Main Effects and Two-Factor Interactions on Yield when Applied Load was Varied at Rigid Pavement Site

The Pareto chart showed quite different results from those for the flexible pavement site. Sensors placed within rigid pavement did not appear to be effected by load variations. It was still the two-factor interaction effect of the encapsulant material and the sensor orientation that controlled FOTS signal response. This does not imply that the amount of light loss did not change with respect to applied load. The LabView® plots in Appendix B showed an increase in load resulted in an increase in light loss. The Pareto chart reported that changing the combination of encapsulant and sensor orientation would have a greater effect on altering the amount of light lost from the sensor than changing the applied load. This remained true as long as the sensor did not produce 100 percent light loss with each applied load.

Chapter 7

Conclusions

1. A microbend fiber-optic traffic classification and weigh-in-motion sensor was developed. It is based on the microbend fiber-optic sensor technology, the least expensive of the fiber-optic sensor technologies currently available. This sensor can be constructed with off-the-shelf materials for a cost similar to the piezoelectric sensors. It can be placed in a narrow groove in either flexible or rigid pavements. This embedment procedure would minimize pavement damage. An opto-electronics interface device has been developed that allows the light-intensity signals from the sensor to be converted to voltage. Various traffic classifiers and WIM computer control systems can read the voltage output from this box.

2. Five field sites have been instrumented with the fiber-optic traffic sensors. Four of the sites are flexible pavements while the fifth site is a rigid pavement. The sensors installed at all five sites have worked for sufficient time to indicate that this technology is marketable. There are nearly 50 sensors installed in these five sites. The ten sensors installed in Telemetry Site #284 (Melbourne Beach, Florida) have been working properly since installation on December 7, 1998. Sensors installed in the access roads of the APAC MacAsphalt site, Melbourne, Florida, and CSR Palm Bay Plant, have been functioning under heavy truck traffic. Four sensors installed in Telemetry Site #345 on SR 507, Melbourne Florida, have been functioning since installation September 10, 1999. Signals from these sensors are not as strong as desired for proper classification. Either sensor construction or field installation could have caused this problem.

3. Sensor installation procedures have been thoroughly documented. Sensors can be installed in any desired length by cutting a narrow groove, placing the sensor and the

appropriate encapsulant into the groove and running the sensors leads to the control cabinet at the side of the road. Sensors may be installed either vertically or horizontally, although vertical installation would cause less pavement damage and allow the sensors to last longer under vehicle loadings.

4. A thorough laboratory-testing program has been implemented that allows the sensors to be tested and calibrated prior to field installation. Both static and pneumatic loads were used to calibrate sensors. Sensors less than 60 cm (24 inches) long can be tested pneumatically at pressures up to 700 kPa (100 psi) in a testing chamber, while deflections along the sensor are recorded. Impulse pressures up to 700 kPa (100 psi) were successfully applied to the sensor through various encapsulating materials, using a cylindrical pressure vessel testing system.

5. The failure stress-testing objective was achieved; determining the load at which the acrylate coat cracks was achieved. During microbending, the acrylate coat cracks occurs when subjected to a compressive load of around 896 N (200 lb) over a length of 1.04 cm (0.41 inches) as shown from testing procedure. This load corresponds to a compressive failure stress of about 700,000 kPa (100,000 psi). Secondly, the Hertz equation can be used to predict the length of the contact area at failure.

6. A relationship was determined between moduli of elasticity of different encapsulating materials and stress transmitted to the sensor, in the bottom of channels, under dynamic impulse load conditions.

7. From a plot of the Sensitivity Slope versus the modulus of elasticity it was demonstrated that as the modulus of elasticity increases from 0 kPa (0 psi) to approximately 10,500 kPa (1500 psi) there was a significant decrease in the Sensitivity Slope. This indicated that small variances in the modulus of elasticity within this range would have significant effects on the amount of load transmitted to the bottom of the groove. From 10,500 kPa (1500 psi) on, the plot demonstrated the exact opposite. Large changes in the modulus of elasticity would be required to create the same amount of load transferal, from 10,500 kPa (1500 psi) until the Sensitivity Slope reaches zero.

8. The material used to seal a sensor from its environment had an effect on the performance of the sensor. Prior to this research electrical conduit, heat shrink was used to seal the sensor. Due to many irregularities found, between both sensors and points tested along the length of the sensors, this material was discarded. Cellophane based, fiber embedded strapping tape was tested and yielded sensors with nearly identical sensitivities and a standard deviation of sensitivities along their length of less than 7 kPa (1 psi).

9. Due to problems encountered with Bondo 7084F, this material was determined a poor choice for sensor encapsulation. Congruency between pours, even between channels from the same mix could not be attained.

10. Field data from motorcycles to heavy trucks has been recorded on sensors in the flexible and rigid pavement sites. Additionally, FWD tests were conducted to document which parameters control the sensors output signal.

11. Finite element modeling of the sensor placed in a flexible pavement system similar to that present at the APAC MacAsphalt site, revealed that a linear elastic analysis could be used to predict the sensors response for tire pressures of 245 and 770 kPa (35 and 110 psi). The FEA model predicted light loss for the 245 kPa (35 psi) tires was exactly the same as the measured loss, while the predicted loss for the 770 kPa (110 psi) tire was 3 percent, when the tire contact length was modeled properly.

12. The variables affecting signal generation were identified and weighted, based upon magnitude of influence, from FWD tests performed at field sites. Of the variables investigated, the interaction between the encapsulant material and the sensor orientation had the greatest effect on fiber optic traffic sensor signal generation. This implied that changing the orientation from vertical to horizontal and/or the modulus of elasticity of the encapsulant from 4200 kPa (600 psi) to 8200 kPa (1168 psi) would significantly change the sensor performance.

13. Changing pavement surface temperatures, in the ranges evaluated, had minimal effect on signal response. This was true for both flexible and rigid pavement types.

14. Sensor orientation dominated signal response at the flexible pavement field site. Horizontally placed sensors generated the greatest light loss in the sensor, while vertically placed sensors produced the greatest dispersion. Either encapsulant choice, if placed within a horizontal groove, did little to affect signal response.

15. At the rigid pavement field site, interaction between sensor orientation and encapsulant material controlled signal response generation. Dispersion effects were attributed to sensor orientation. Vertically placed sensors resulted in high dispersion values, which was poor for WIM.

16. Vertical and horizontal sensors, encapsulated in materials with elastic moduli below 14,000 kPa (2,000 psi), generated 100 percent light loss from FWD pressures in excess of 980 kPa (140 psi).

17. FWD testing provided useful data for evaluating sensors under a variety of field conditions.

Chapter 8

Recommendations

1. For vehicle classification, install the fiber optic traffic sensors vertically in grooves in flexible pavements using encapsulation materials with elastic moduli less than 3000 psi that are not affected by temperature changes from 0° to 40 °C (32 to 140 °F).

2. When evaluating candidate fiber optic traffic sensors from various suppliers, check that they have been manufactured using the microbend fiber optic technologies to ensure that the lowest cost alternative has been implemented.

3. To calibrate fiber optic traffic sensors for WIM sites, use FWD tests with the weights dropped directly on various segments of the sensors. The FWD loads should range from approximately 3,000 to 15,000 lbs. Two sets of drops should be used to achieve this range.

4. Encapsulation materials that require large percentages of hardener to base should be avoided, due to the increased possibilities of mixing errors in the field. The two encapsulants recommended are Proseal 6006EX® and 3M 5200 Marine Sealant. The Proseal® is the easier of the two to use because it mixes and hardens quickly.

5. Rigid pavements should be investigated for WIM sites because the concrete stiffness is linear and controls the response of the pavement system. Flexible pavement system layers all behave in a nonlinear stress-strain manner, making calibration of these systems more complicated than rigid pavements.

6. Fiber optic traffic sensors should be calibrated in the lab using pneumatic testing in a chamber similar to the one developed for this research (Figure 4.1). The chamber should allow sensors to be tested at pressures reaching 700 kPa (100 psi) to simulate truck tire pressures. It should be large enough to enable LVDT's to be used to measure the sensor deflections during loading. A more complete knowledge of the sensors behavior is obtained if pressure versus light loss versus deflection data is collected and reduced to plots similar to Figure 3.10.

References

Ansari, F., editor. 1993. *Applications of Fiber Optic Sensors in Engineering Mechanics.* ASCE.

Askland, D.R. 1989. *The Science and Engineering of Materials.* 2nd Edition. PWS-Kent Publishing Company, Boston.

Berthod, J.W. 1995. "Historical Review of Microbend Fiber-Optic Sensors," *J. Lightwave Technol.*, vol. 13, no. 7, pp. 1193-1199.

Carrasquillo, R.L., Fowler, D.W., Ueber, E.J. 1994. "Investigation of Bonding Materials for Piezoelectric Traffic Monitoring Equipment," Center for Transportation Research, The University of Texas at Austin, Austin, TX.

Corning Glass Works Telecommunications Product Division. 1988. *At the Core.* Corning, NY.

Cosentino, P.J., Grossman, B.G. 1996. "Development and Implementation for a Fiber Optic Vehicle Detection and Counter System," Report FDOT, Agency Contract No. B-9213.

Cosentino, P.J., Grossman, B.G. 1997. "Development of Fiber Optic Dynamic Weigh-in-Motion Systems," Final Report FDOT, Agency Contract No. BA-021.

Cosentino, P.J., Grossman, B.G. 1999. "Optimization and Implementation of Fiber Optic Sensors for Traffic Classification and Weigh-in-Motion Systems (Phase 3)," Quarterly Report #6 FDOT, Agency Contract No. BB-038.

Criss, G.W. 1998. *Evaluation of Stress Transfer Characteristics of Encapsulating Materials for Fiber Optic Traffic Sensors*. Masters Thesis, Florida Institute of Technology, Melbourne, Florida.

Cunagin, W.D. 1988. "WIM System Accuracy," 3rd National Conference on Weigh-In-Motion. St. Paul, Minnesota, pp.24-27.

Eckroth, W. 1998. *Stress Distribution Surrounding Embedded Traffic Sensors*. Ph.D. Dissertation, Florida Institute of Technology, Melbourne, Florida.

ERES Consultants, Inc. 1987. "Techniques for Pavement Rehabilitation Training Course Participant's Notebook." U.S. Department of Transportation. Illinois.

Ford, Thomas L., and Charles, Fred S. 1988. *Heavy Duty Truck Tire Engineering*. Goodyear Tire and Rubber Company, SAE SP-729, p.29.

Horhorta, David. 1998. FDOT Personal communication.

Lambe, William T. and Whitman, Robert V. 1969. *Soil Mechanics*. John Wiley & Sons, Inc., New York.

Michalak, Chester H., and Scullion, Tom. 1995. "*Modulus 5.0*: User's Manual," Texas DOT, Research Report 1987-1, p. 96, November.

Nazarian, Soheil, *et.al.* 1988. "Determination of Pavement Layer Thicknesses and Moduli by SASW (Spectral Analysis of Surface Waves) Method." *Transportation Research Record 1196*, p133.

Pacific Transducer Corporation. 1999. "PTC® Fully Enclosed Surface Thermometer, Model 310F Operating Manual." California.

Peek Traffic, Inc. 1992 . "TraffiCOMP® III, Model 241 Operating Manual." Florida.

Powers, J.P. 1993. *An Introduction to Fiber Optic Systems*. Richard D. Irwin, Inc. and Askin Associates Inc. Illinois.

Rekab, Kamel. 1999. *Fundamentals of the Design of Experiments*. Melbourne, Florida.

Roak, R.J. and Young W.C. 1975. *Formulas for Stress and Strain*. 5th Edition. McGraw-Hill Book Company, Inc., New York.

Taylor, C.L. 1995. *Investigation of Fiber Optic Microbend Sensors for use in Traffic Applications*. Masters Thesis, Florida Institute of Technology, Melbourne, Florida.

Udd, E. 1995. *Fiber Optic Smart Structures*. John Wiley & Sons, Inc., New York, pp. 319-355.

USDOT and FHA, NHI Course No. 13127. February 1994. "Pavement Deflection Analysis Participant Workbook." National Highway Institute. Publication No. FHWA-HI-94-021.

U.S. Department of Transportation. October, 1992. *Traffic Monitoring Guide*, Office of Highway Information Management.

Appendix A

Determination of Modulus of Elasticity Test Procedure

Test specimens were cast in cardboard rolls approximately 4.1cm (1.6in) in diameter by 8.9 cm (3.5 in) in length. Manila envelope mold bottoms were attached by using "5-Minute" epoxy. Care was taken not to get epoxy on the bottom of the mold because it chemically degraded the cast materials in those areas and made for a rough bottom during compression testing.

The specimens were de-aired in a desiccating jar fitted with an aluminum top plate and hose bard for attaching the vacuum pump and gage. De-airing was accomplished under a vacuum of 66 cm (26 in) of mercury for 5 minutes. De-airing at these conditions is per-manufacturer recommendation.

Three temperatures were selected for thermally soaking the specimens (32°F, 72°F, and 140°F) because they represent a typical range of pavement temperatures. Internal specimen temperatures were not measured at the time of testing but are considered to be close to the soaking values because the materials tested have low thermal conductivity. The coldest temperature was obtained with a freezer in an overnight soak with the hottest temperature obtained in a laboratory oven, also overnight. The specimens were placed into an S-610 Brainard Kilman CBR/UCC testing machine, instrumented with an LVDT for measuring total deflection and a load cell for measuring total load. The rate of deformation (travel of the head) was 0.06 cm/min (0.025 in/min) for all materials.

Stress vs. Strain plots were created for each material at the three different temperatures. These following plots are presented by increasing modulus of elasticity.

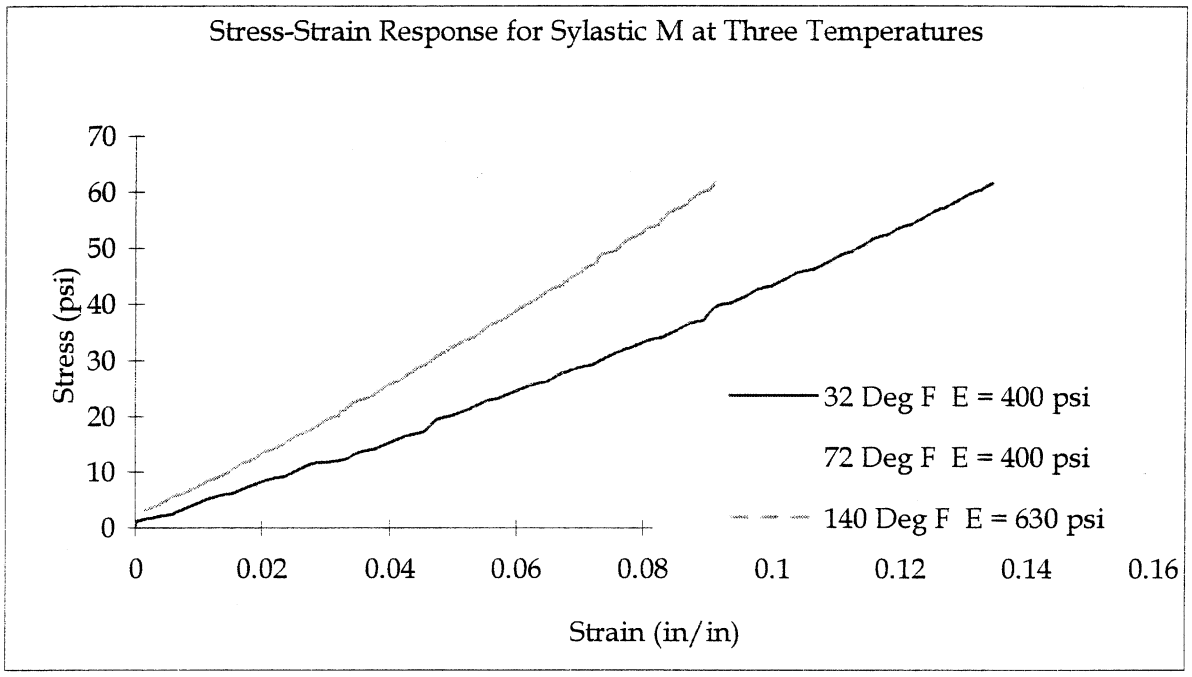
Stress-Strain Response for Sylastic M at Three Temperatures
Stress (psi)
70
60
50
40
30
20
10
0
0
0.02
0.04
0.06
0.08
0.1
0.12
0.14
0.16
Strain (in/in)
32 Deg F E = 400 psi
72 Deg F E = 400 psi
140 Deg F E = 630 psi

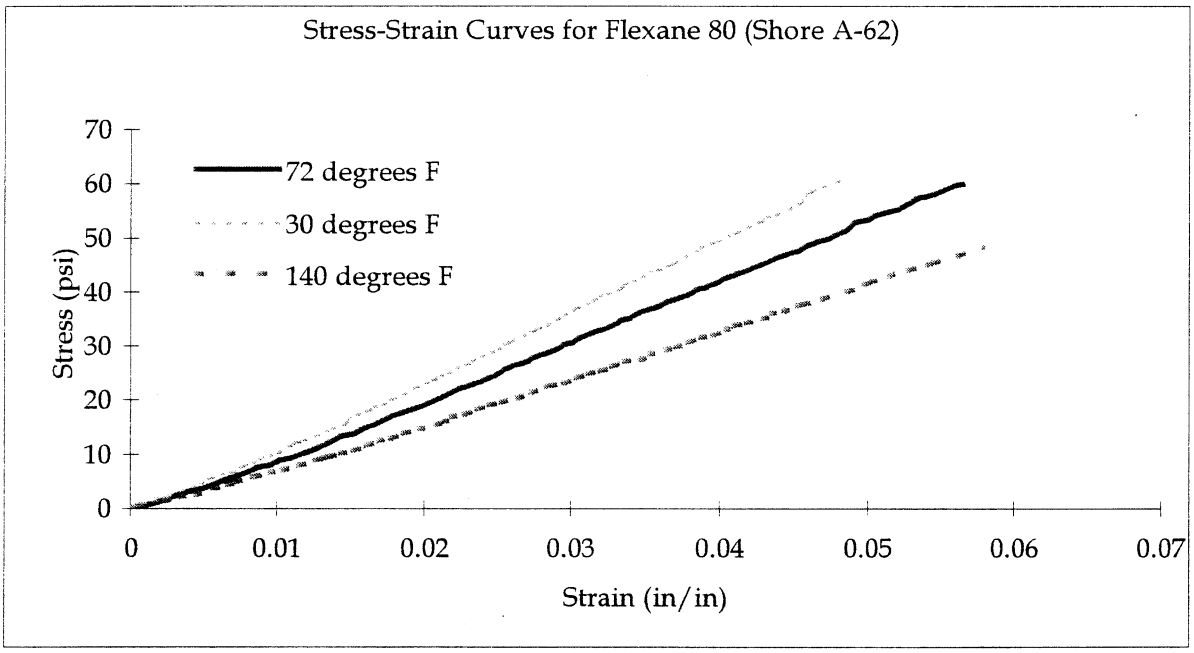
Stress-Strain Curves for Flexane 80 (Shore A-62)
Stress (psi)
70
60
50
40
30
20
10
0
0
0.01
0.02
0.03
0.04
0.05
0.06
0.07
Strain (in/in)
72 degrees F
30 degrees F
140 degrees F

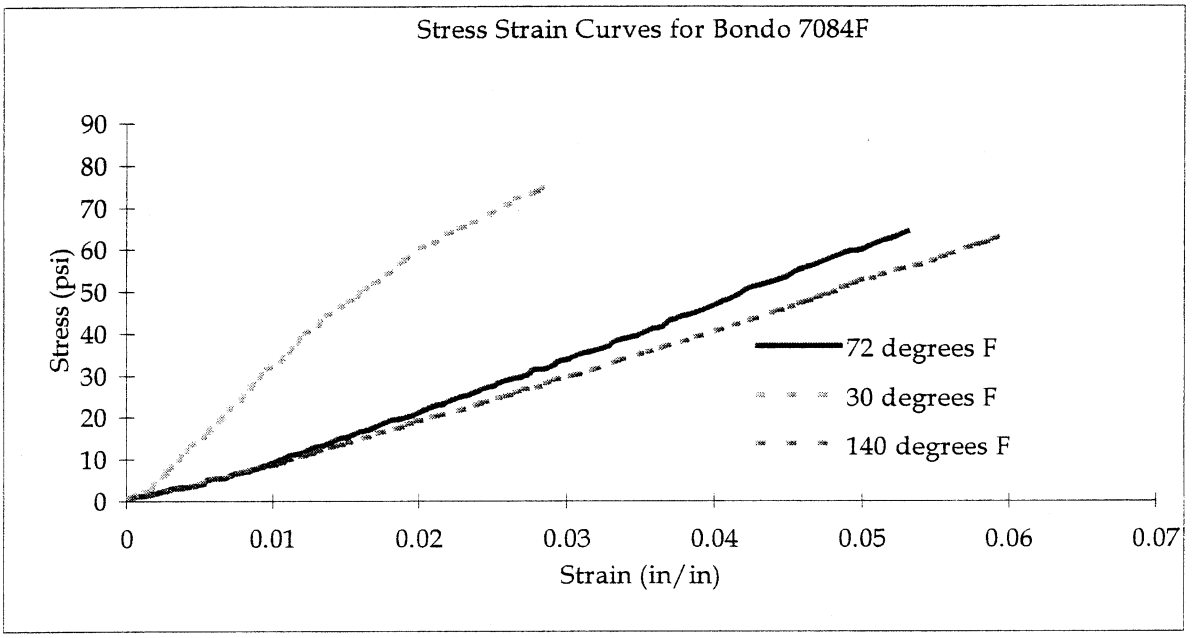
Stress Strain Curves for Bondo 7084F
Stress (psi)
90
80
70
60
50
40
30
20
10
0
0
0.01
0.02
0.03
0.04
0.05
0.06
0.07
Strain (in/in)
72 degrees F
30 degrees F
140 degrees F

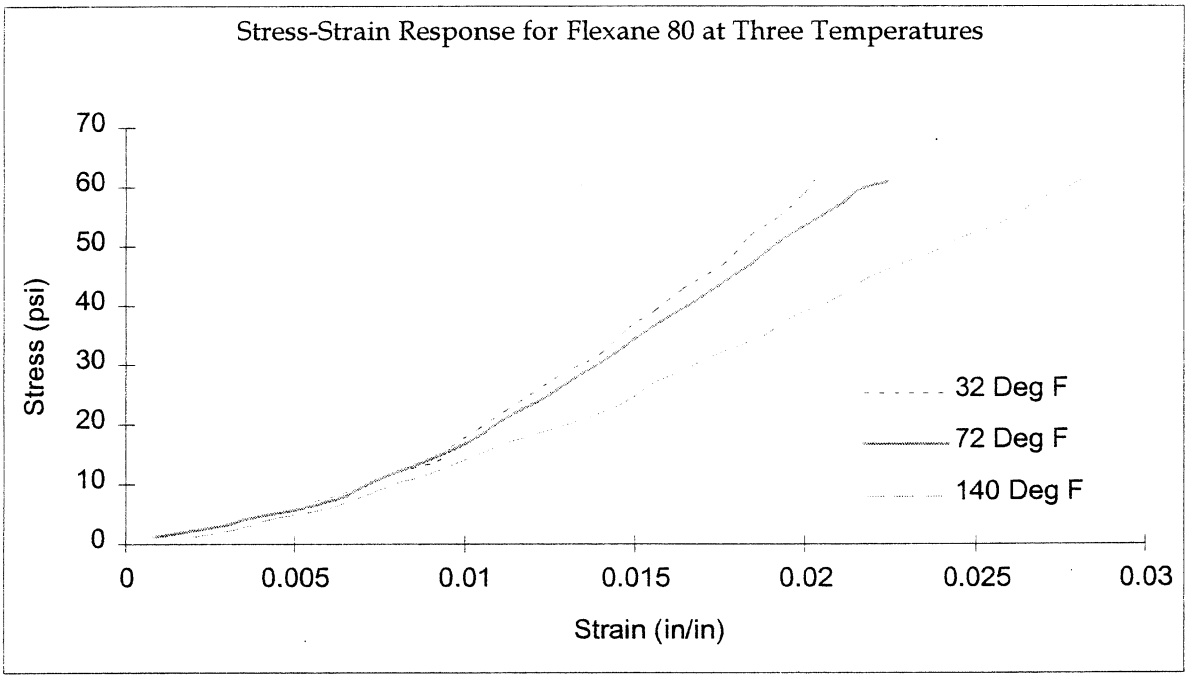
Stress-Strain Response for Flexane 80 at Three Temperatures
Stress (psi)
70
60
50
40
30
20
10
0
0
0.005
0.01
0.015
0.02
0.025
0.03
Strain (in/in)
32 Deg F
72 Deg F
140 Deg F

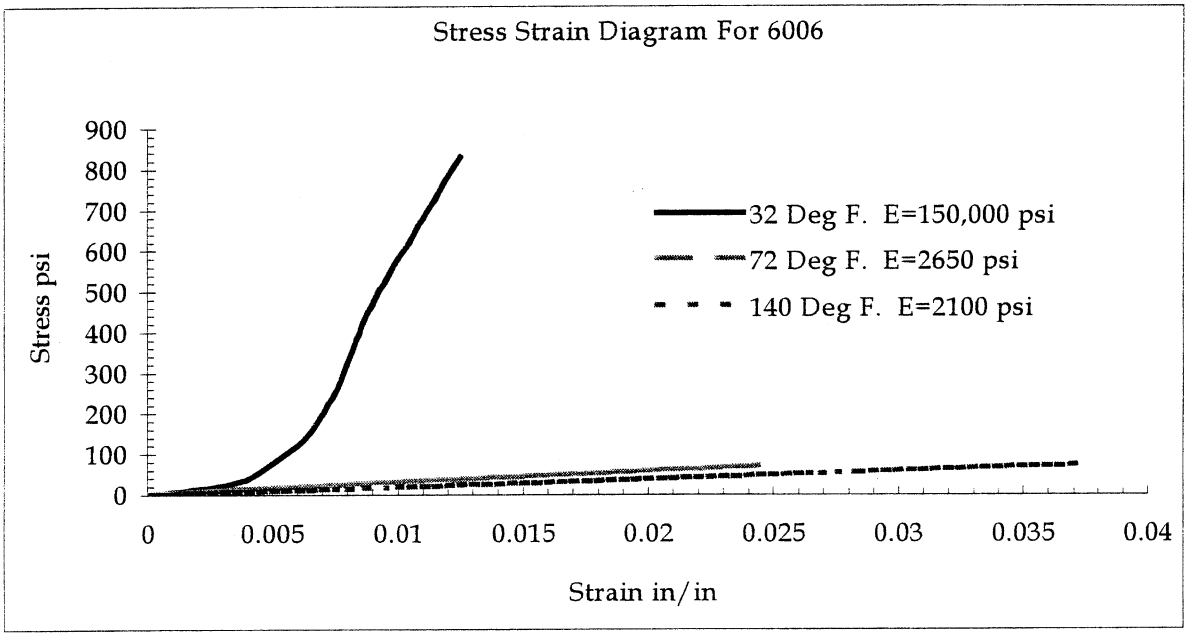
Stress Strain Diagram For 6006
Stress psi
900
800
700
600
500
400
300
200
100
0
0
0.005
0.01
0.015
0.02
0.025
0.03
0.035
0.04
Strain in/in
32 Deg F. E=150,000 psi
72 Deg F. E=2650 psi
140 Deg F. E=2100 psi

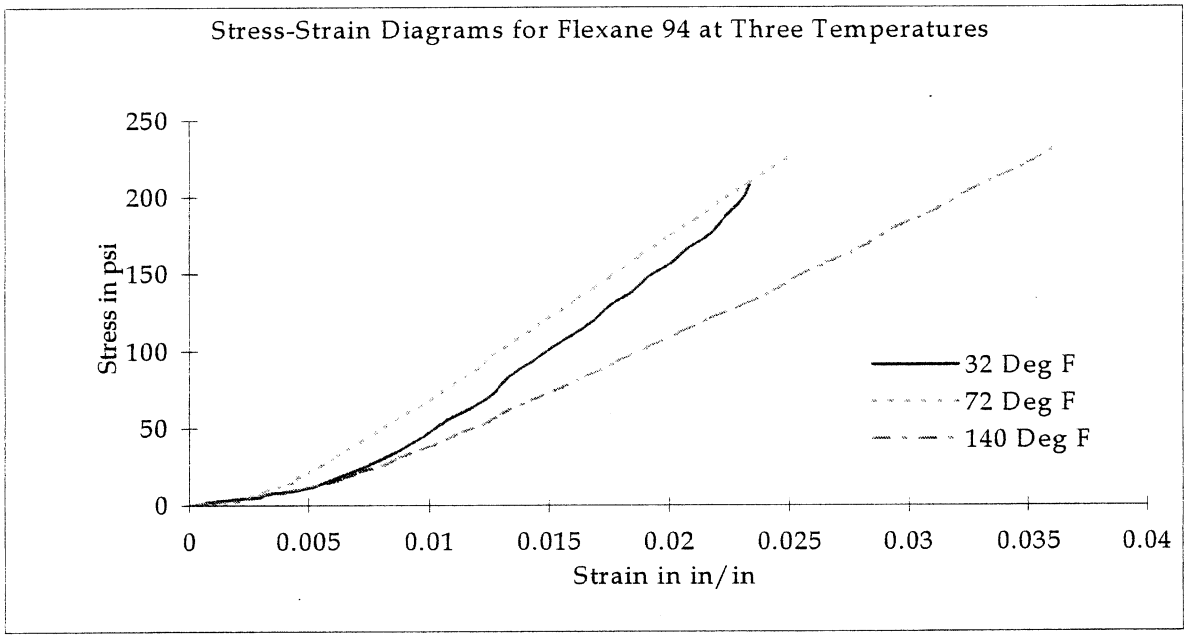
Stress-Strain Diagrams for Flexane 94 at Three Temperatures
Stress in psi
250
200
150
100
50
0
0
0.005
0.01
0.015
0.02
0.025
0.03
0.035
0.04
Strain in in/in
32 Deg F
72 Deg F
140 Deg F

Appendix B

Bare Sensor Calibration Graphs

LabView® Plots

Pavement Profiles

Pareto Charts

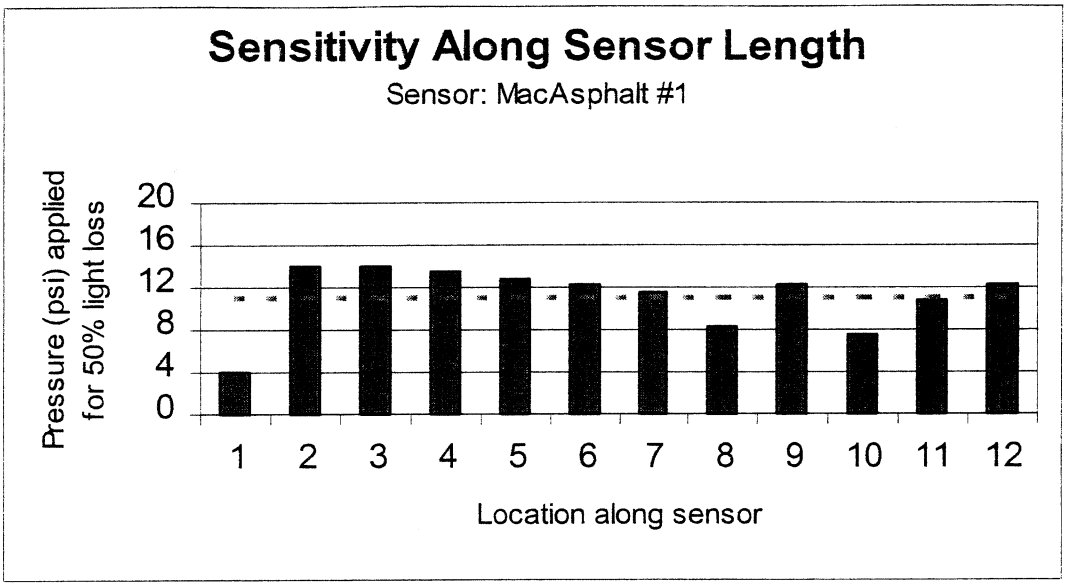

MacAsphalt Bare Sensor Calibration Graph (Sensor 1)

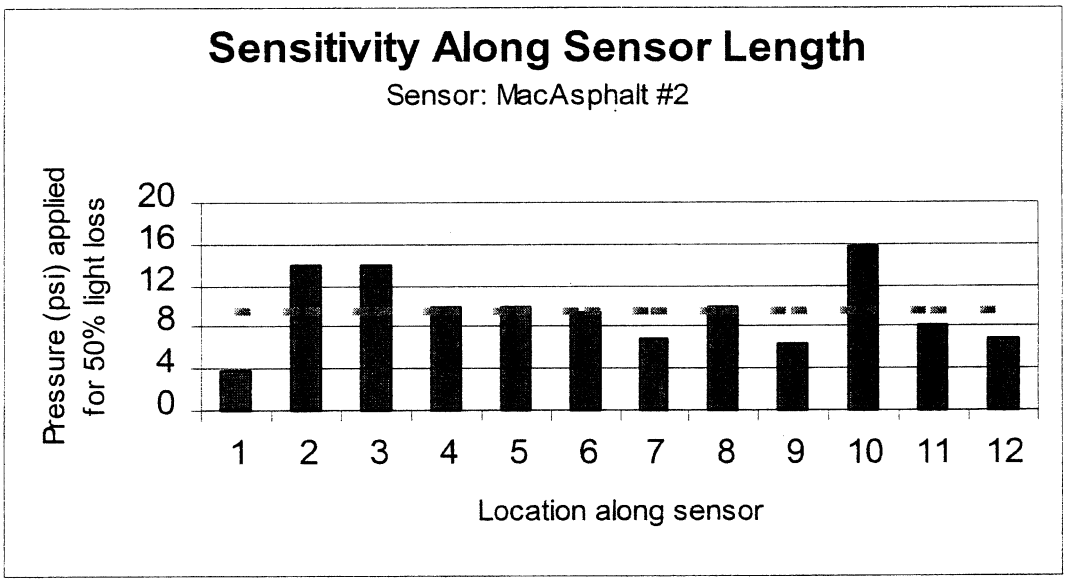

MacAsphalt Bare Sensor Calibration Graph (Sensor 2)

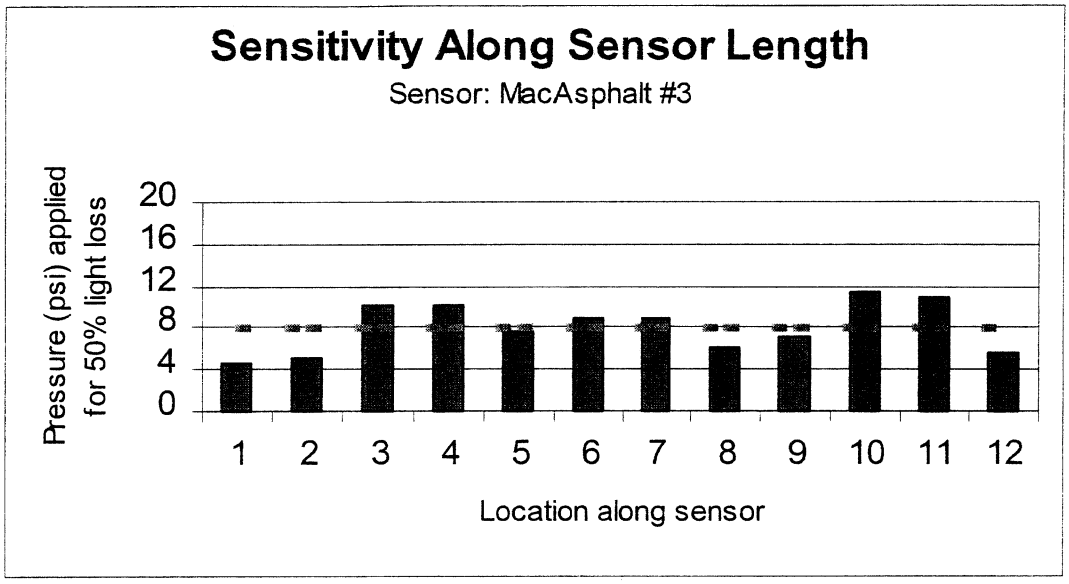

MacAsphalt Bare Sensor Calibration Graph (Sensor 3)

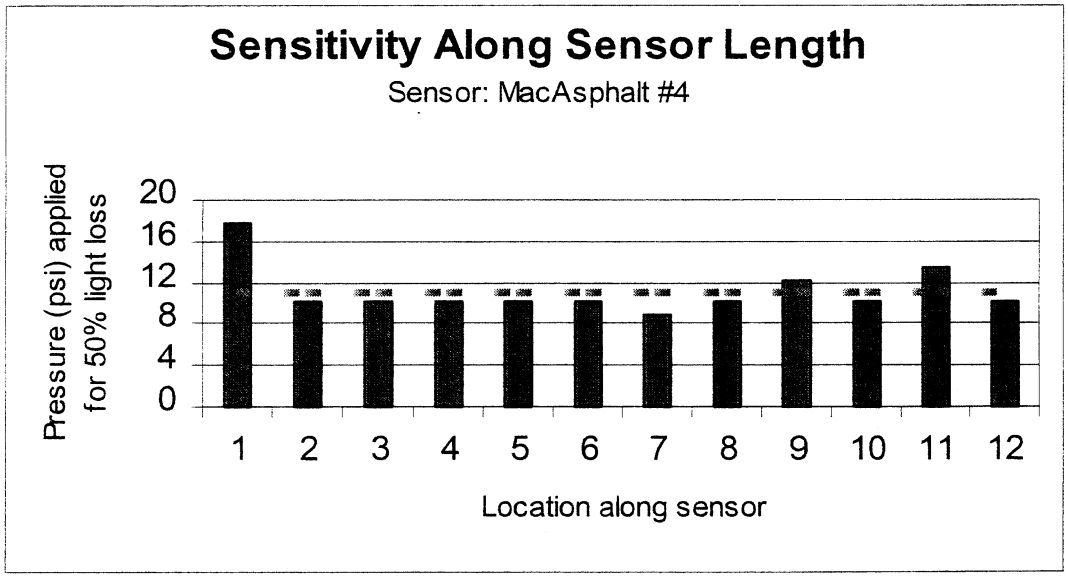

MacAsphalt Bare Sensor Calibration Graph (Sensor 4)

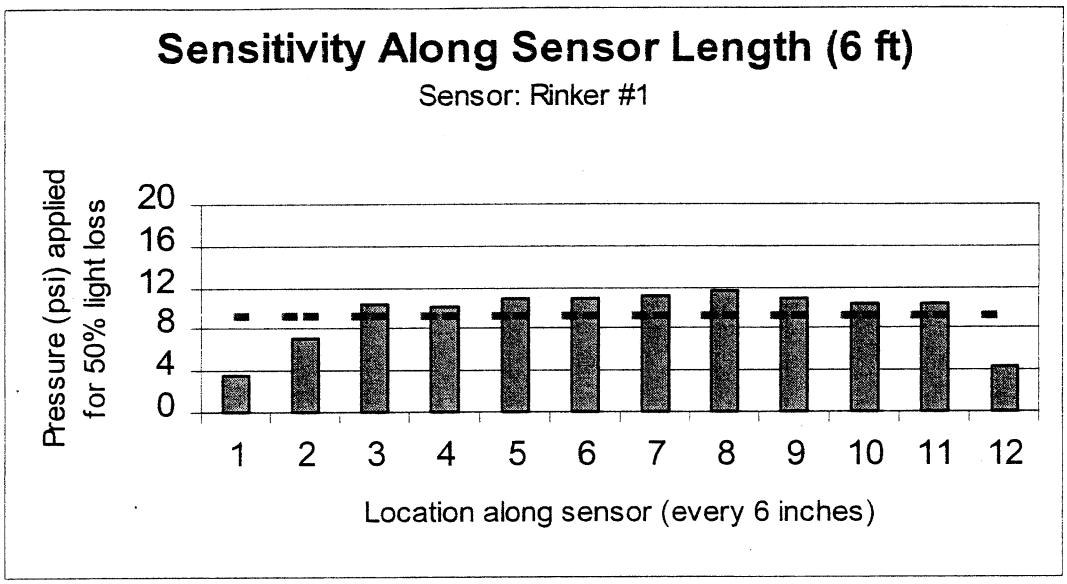

Rinker Bare Sensor Calibration Graph (Sensor 1)

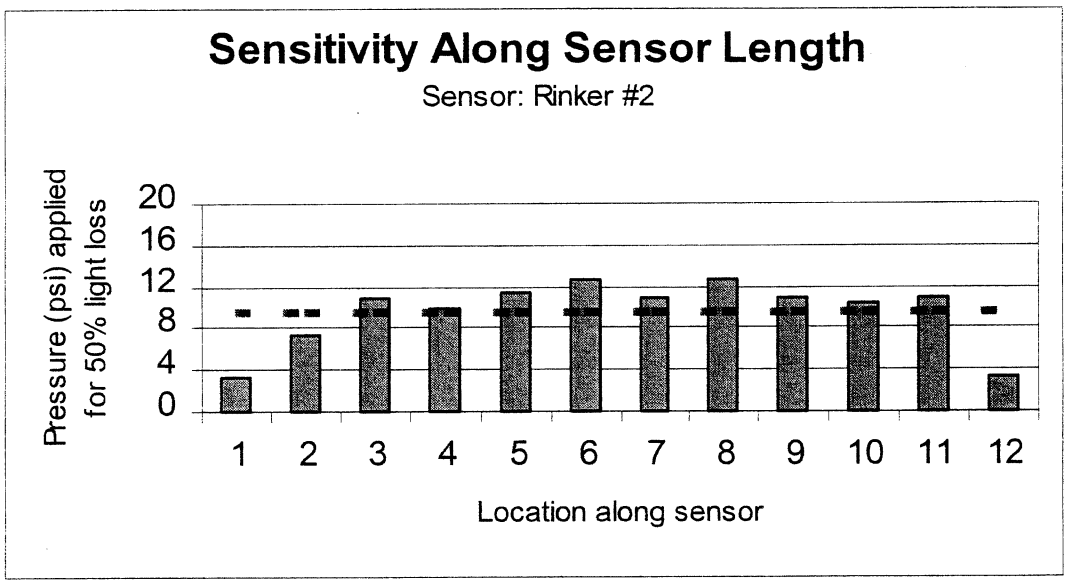

Rinker Bare Sensor Calibration Graph (Sensor 2)

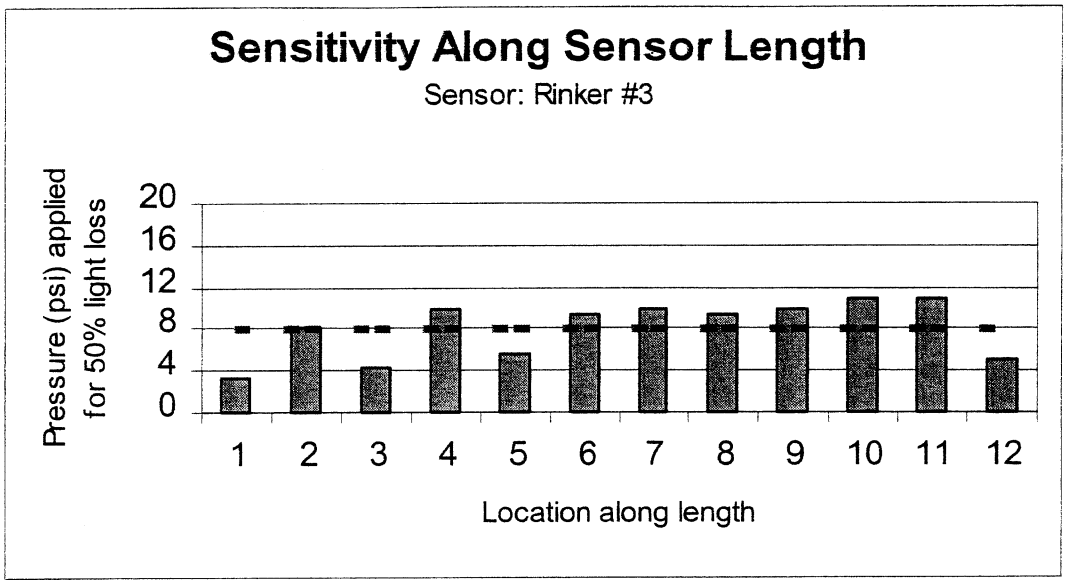

Rinker Bare Sensor Calibration Graph (Sensor 3)

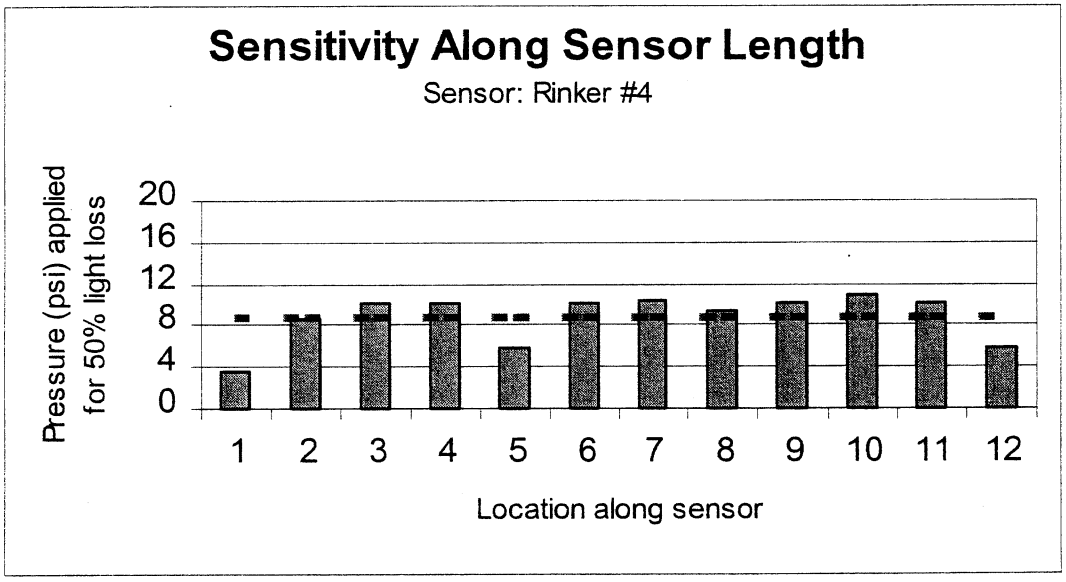

Rinker Bare Sensor Calibration Graph (Sensor 4)

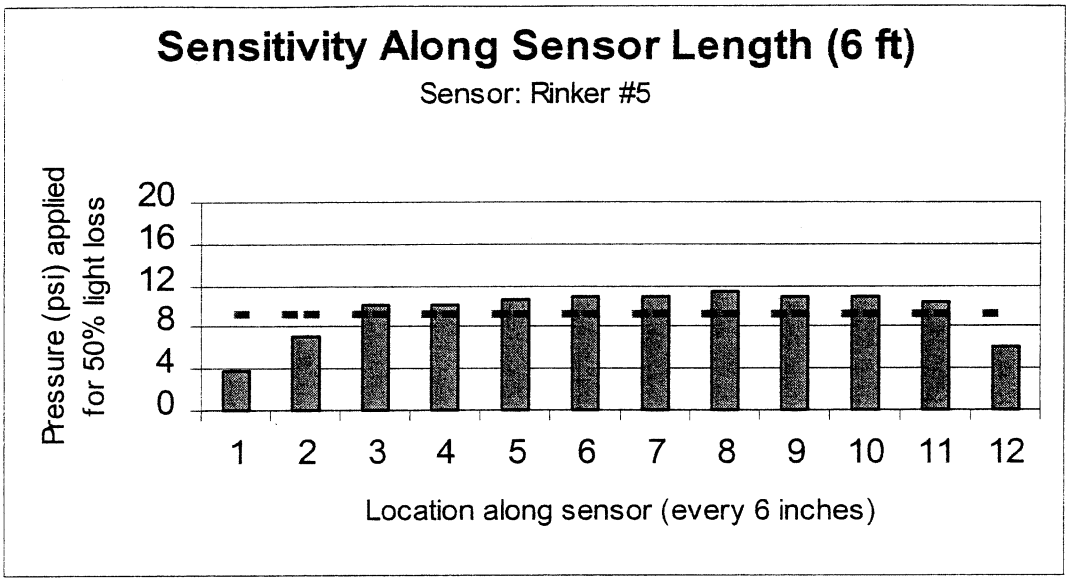

Rinker Bare Sensor Calibration Graph (Sensor 5)

October 05-06, 1999 FWD LabView Plots Taken at MacAsphalt Field Test Site

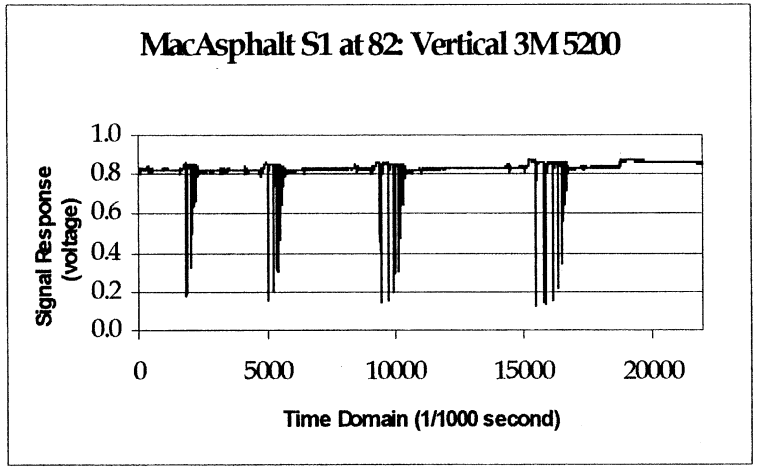

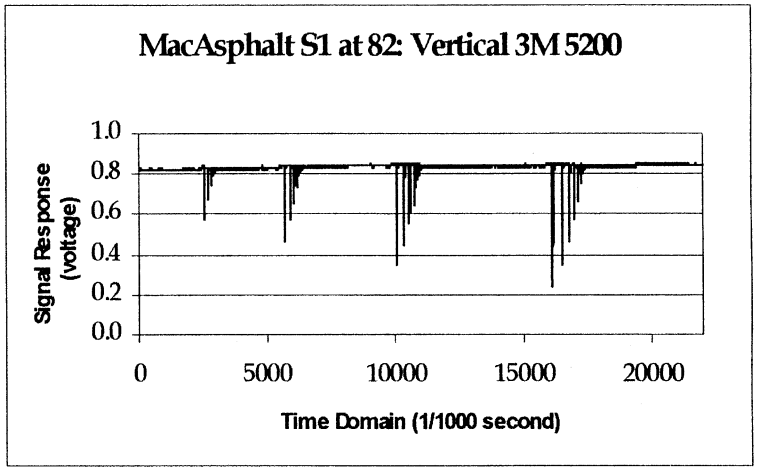

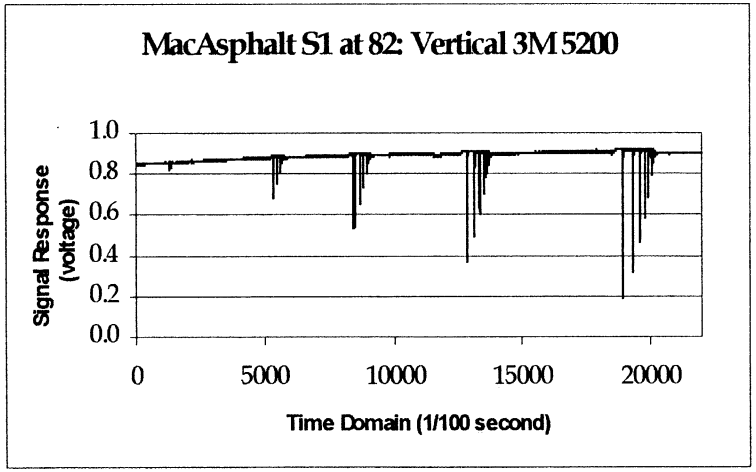

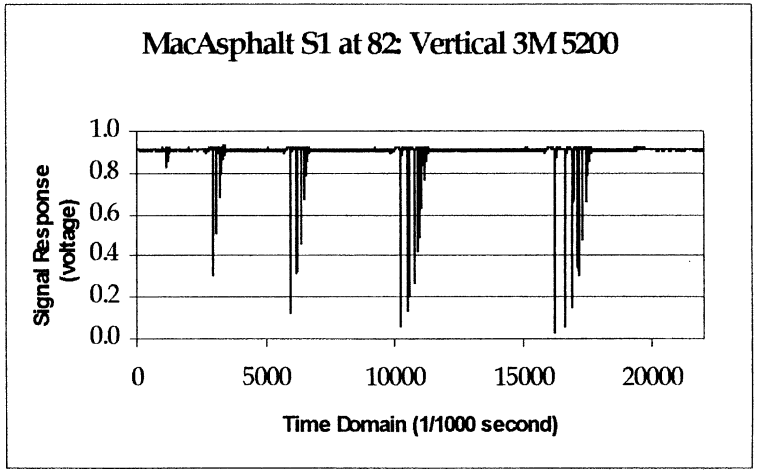

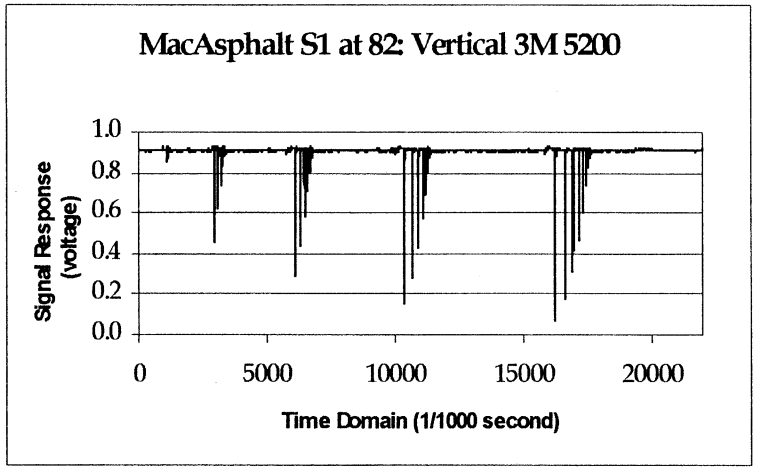
MacAsphalt S1 at 82: Vertical 3M 5200
Signal Response (voltage)
1.0
0.8
0.6
0.4
0.2
0.0
0
5000
10000
15000
20000
Time Domain (1/1000 second)

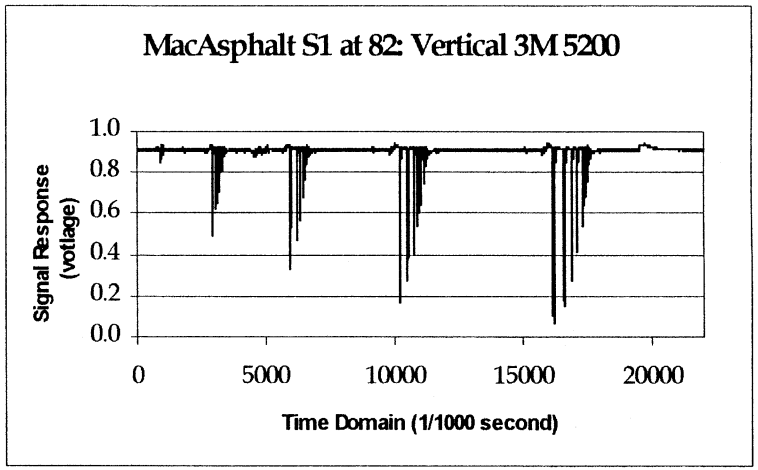
MacAsphalt S1 at 82: Vertical 3M 5200
Signal Response (voltage)
1.0
0.8
0.6
0.4
0.2
0.0
0
5000
10000
15000
20000
Time Domain (1/1000 second)

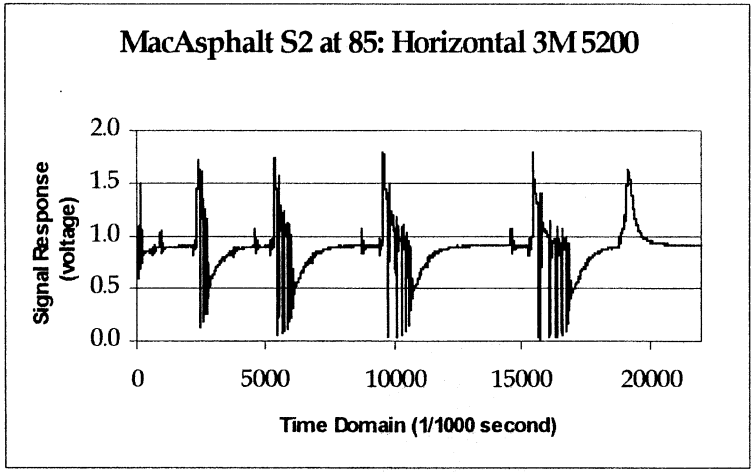
MacAsphalt S2 at 85: Horizontal 3M 5200
Signal Response (voltage)
2.0
1.5
1.0
0.5
0.0
0
5000
10000
15000
20000
Time Domain (1/1000 second)

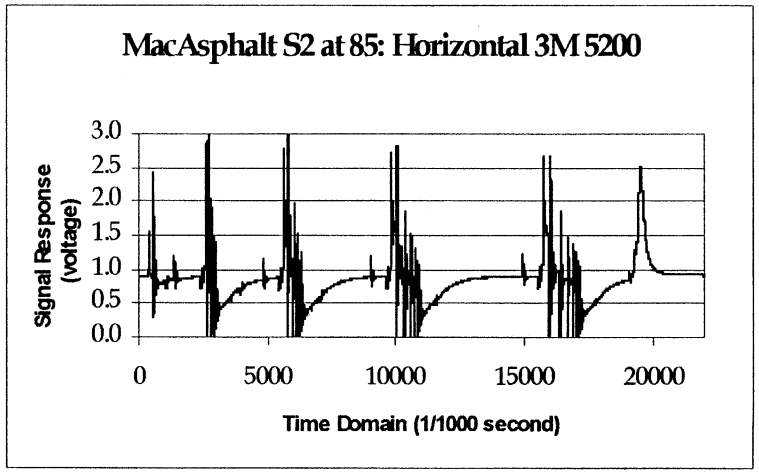
MacAsphalt S2 at 85: Horizontal 3M 5200
Signal Response (voltage)
3.0
2.5
2.0
1.5
1.0
0.5
0.0
0
5000
10000
15000
20000
Time Domain (1/1000 second)

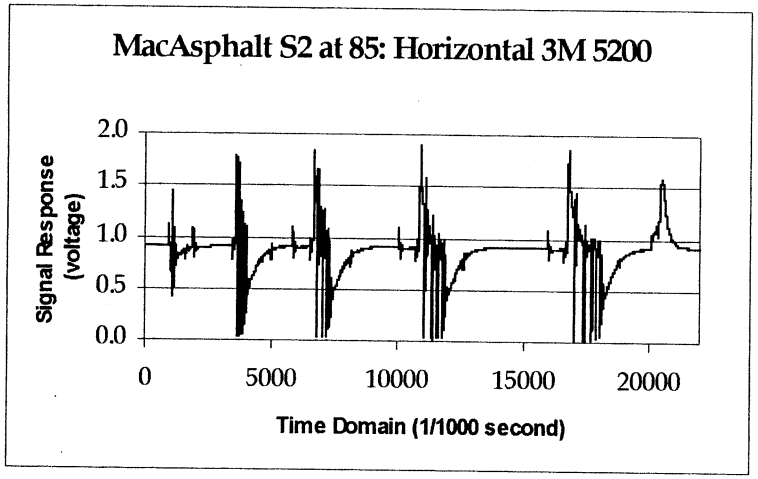
MacAsphalt S2 at 85: Horizontal 3M 5200
Signal Response (voltage)
2.0
1.5
1.0
0.5
0.0
0
5000
10000
15000
20000
Time Domain (1/1000 second)

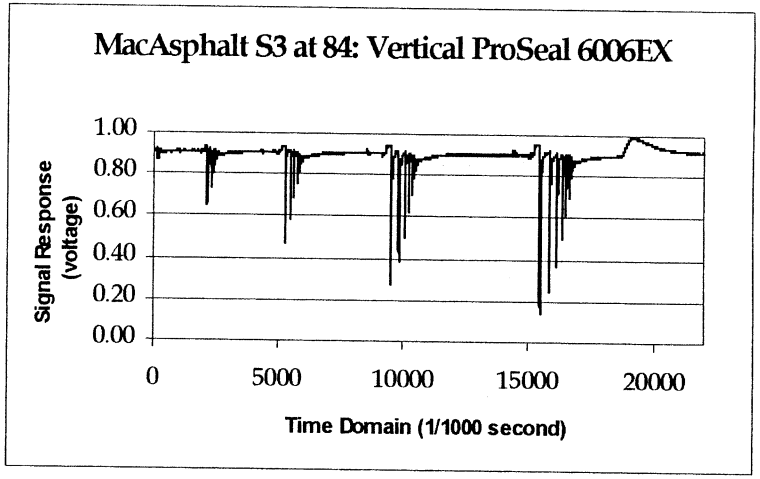
MacAsphalt S3 at 84: Vertical ProSeal 6006EX
Signal Response (voltage)
1.00
0.80
0.60
0.40
0.20
0.00
0
5000
10000
15000
20000
Time Domain (1/1000 second)

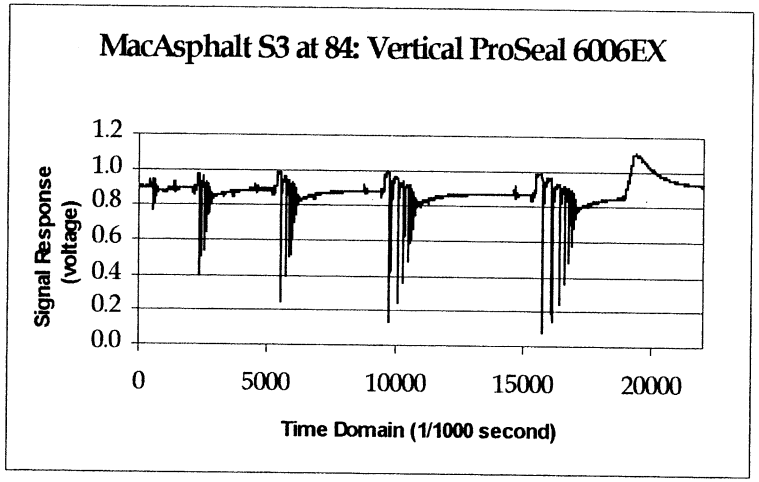
MacAsphalt S3 at 84: Vertical ProSeal 6006EX
Signal Response (voltage)
1.2
1.0
0.8
0.6
0.4
0.2
0.0
0
5000
10000
15000
20000
Time Domain (1/1000 second)

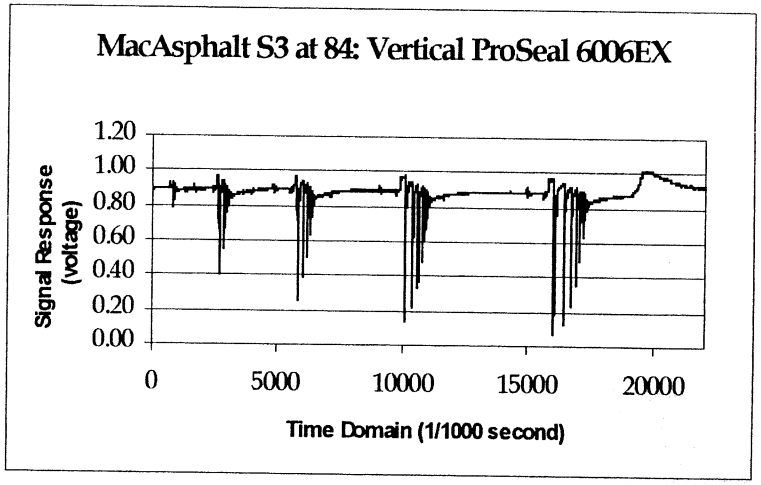
MacAsphalt S3 at 84: Vertical ProSeal 6006EX
Signal Response (voltage)
1.20
1.00
0.80
0.60
0.40
0.20
0.00
0
5000
10000
15000
20000
Time Domain (1/1000 second)

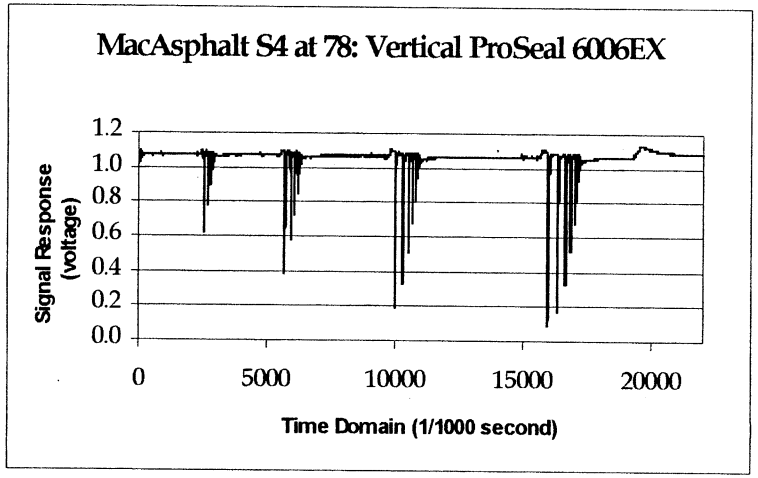
MacAsphalt S4 at 78: Vertical ProSeal 6006EX
Signal Response (voltage)
1.2
1.0
0.8
0.6
0.4
0.2
0.0
0
5000
10000
15000
20000
Time Domain (1/1000 second)

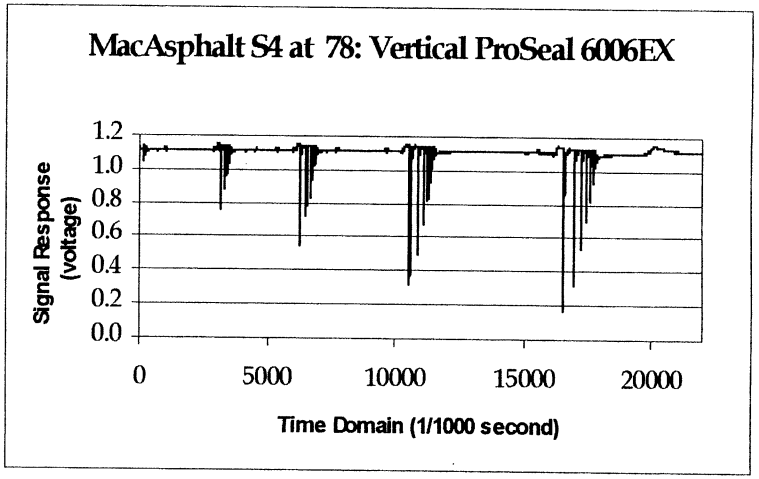
MacAsphalt S4 at 78: Vertical ProSeal 6006EX
Signal Response (voltage)
1.2
1.0
0.8
0.6
0.4
0.2
0.0
0
5000
10000
15000
20000
Time Domain (1/1000 second)

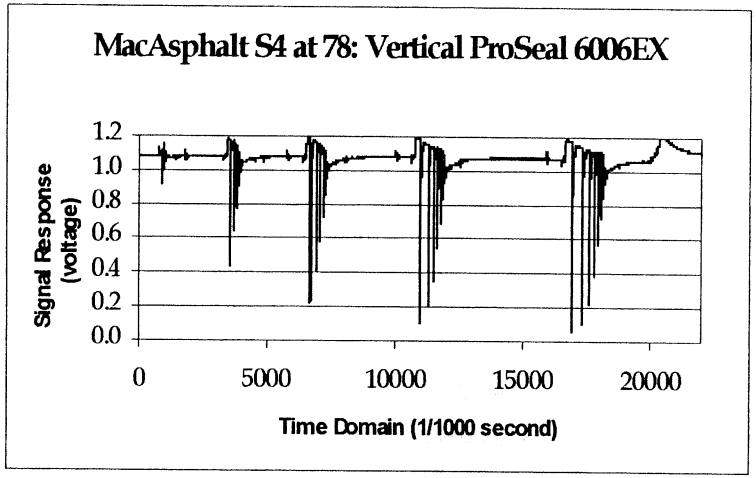
MacAsphalt S4 at 78: Vertical ProSeal 6006EX
Signal Response (voltage)
1.2
1.0
0.8
0.6
0.4
0.2
0.0
0
5000
10000
15000
20000
Time Domain (1/1000 second)

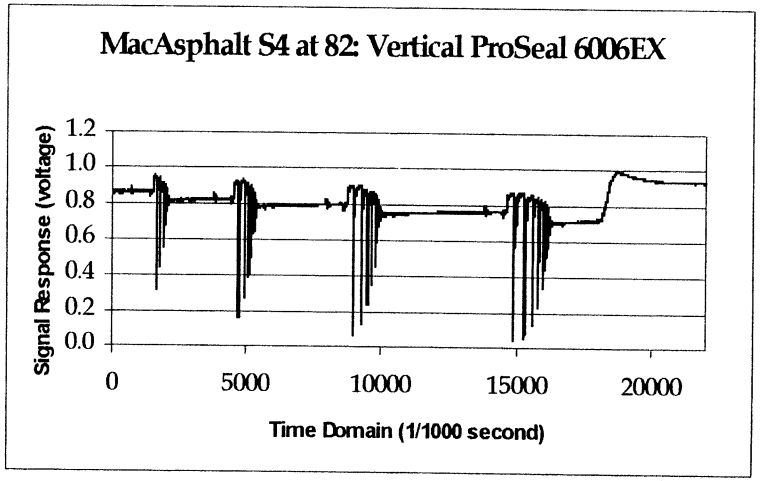
MacAsphalt S4 at 82: Vertical ProSeal 6006EX
Signal Response (voltage)
1.2
1.0
0.8
0.6
0.4
0.2
0.0
0
5000
10000
15000
20000
Time Domain (1/1000 second)

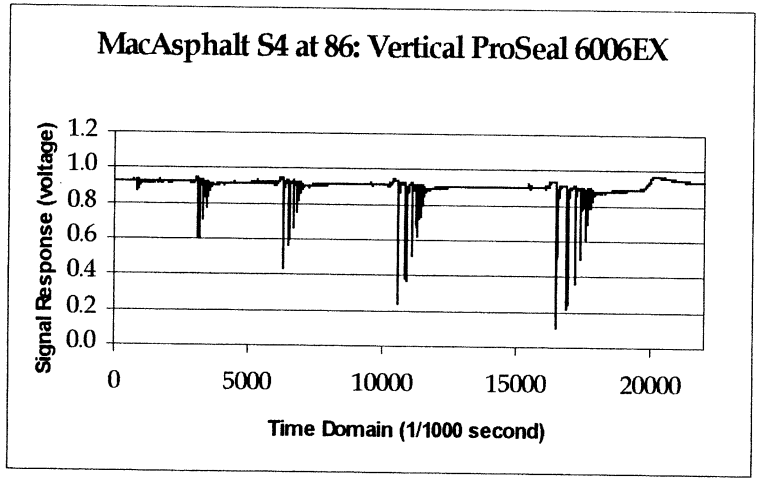
MacAsphalt S4 at 86: Vertical ProSeal 6006EX
Signal Response (voltage)
1.2
1.0
0.8
0.6
0.4
0.2
0.0
0
5000
10000
15000
20000
Time Domain (1/1000 second)

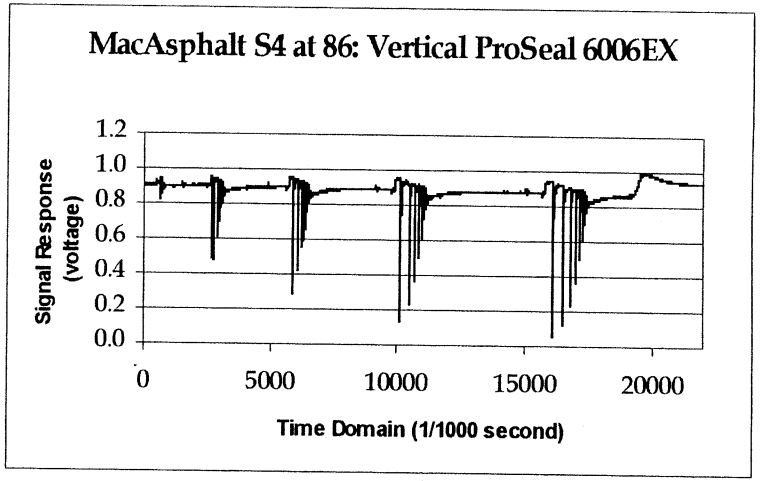
MacAsphalt S4 at 86: Vertical ProSeal 6006EX
Signal Response (voltage)
1.2
1.0
0.8
0.6
0.4
0.2
0.0
0
5000
10000
15000
20000
Time Domain (1/1000 second)

October 05-06, 1999 FWD LabView Plots Taken at CSR Rinker Field Test Site

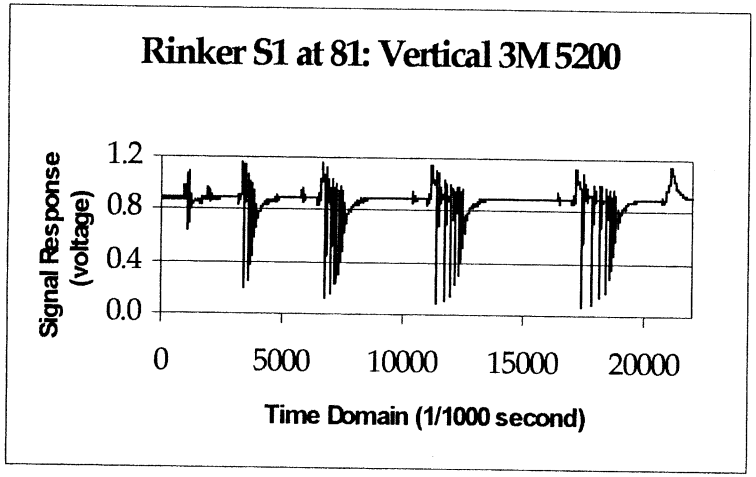

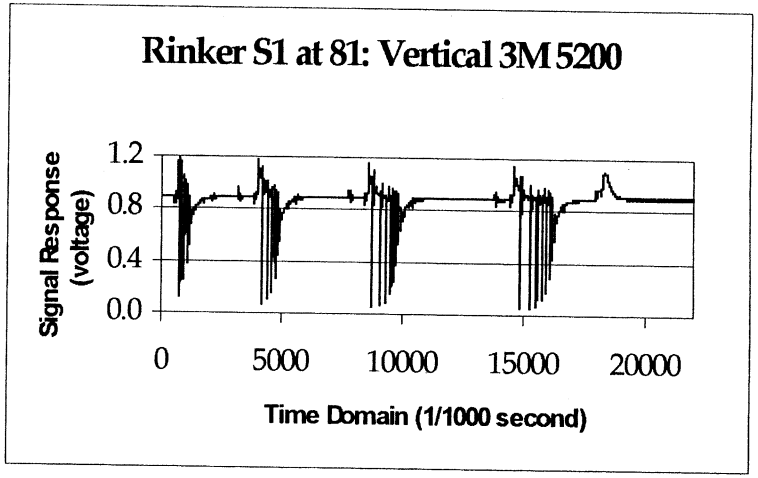

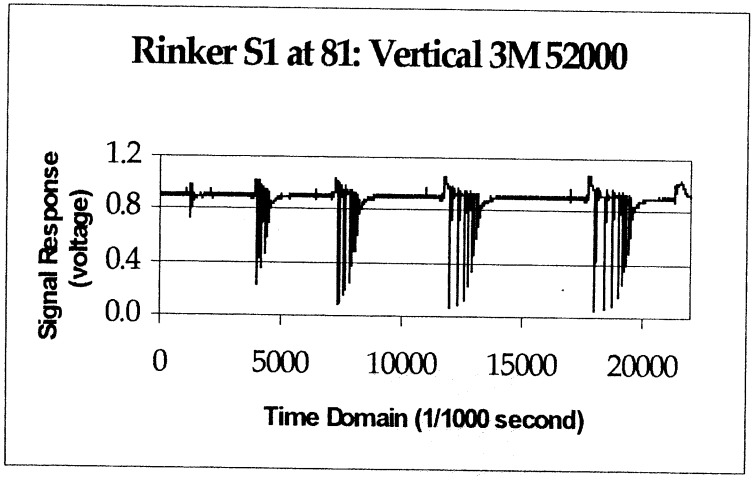

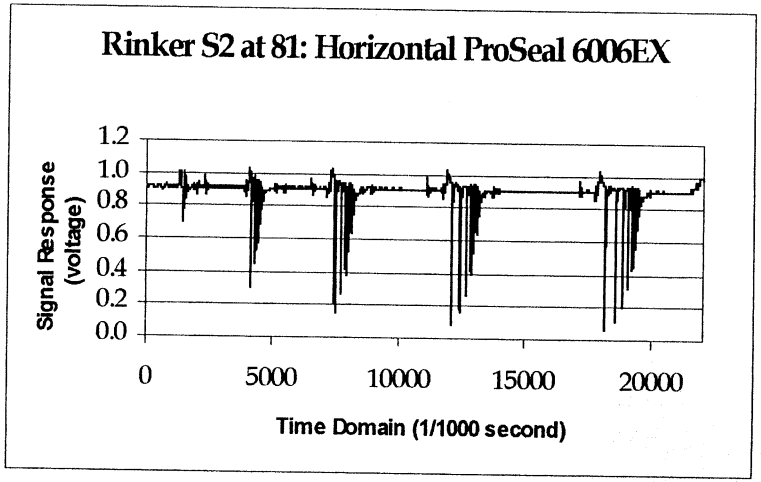

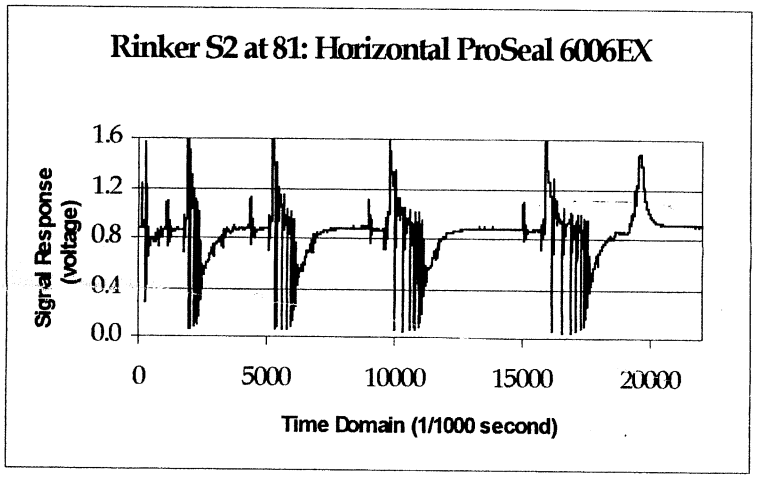
Rinker S2 at 81: Horizontal ProSeal 6006EX
Signal Response (voltage)
1.6
1.2
0.8
0.4
0.0
0
5000
10000
15000
20000
Time Domain (1/1000 second)

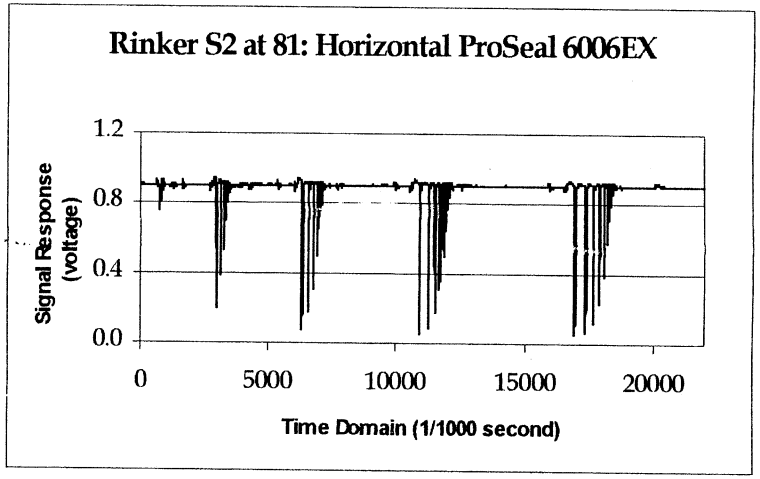
Rinker S2 at 81: Horizontal ProSeal 6006EX
Signal Response (voltage)
1.2
0.8
0.4
0.0
0
5000
10000
15000
20000
Time Domain (1/1000 second)

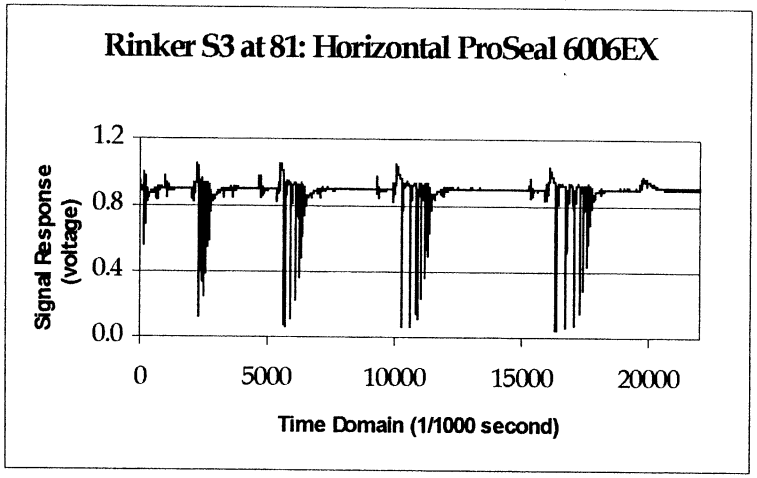
Rinker S3 at 81: Horizontal ProSeal 6006EX
Signal Response (voltage)
1.2
0.8
0.4
0.0
0
5000
10000
15000
20000
Time Domain (1/1000 second)

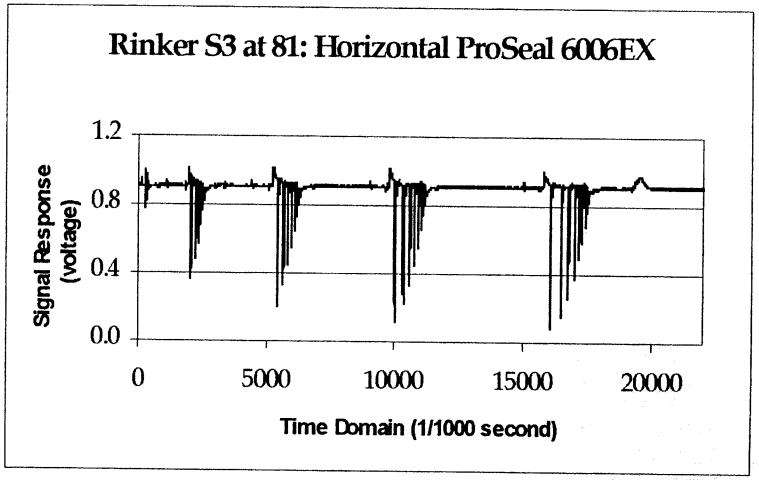
Rinker S3 at 81: Horizontal ProSeal 6006EX
Signal Response (voltage)
1.2
0.8
0.4
0.0
0
5000
10000
15000
20000
Time Domain (1/1000 second)

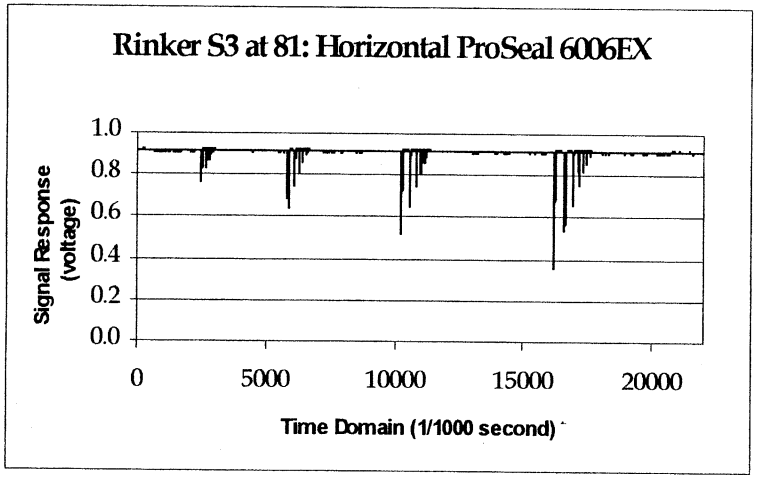
Rinker S3 at 81: Horizontal ProSeal 6006EX
Signal Response (voltage)
1.0
0.8
0.6
0.4
0.2
0.0
0
5000
10000
15000
20000
Time Domain (1/1000 second)

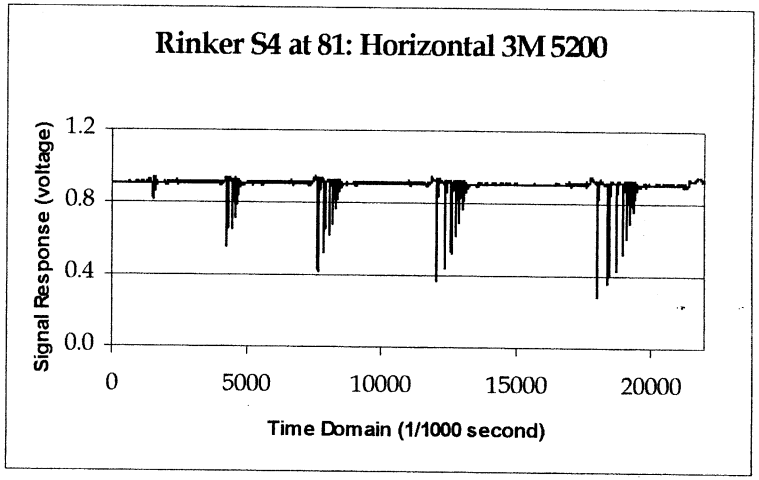
Rinker S4 at 81: Horizontal 3M 5200
Signal Response (voltage)
1.2
0.8
0.4
0.0
0
5000
10000
15000
20000
Time Domain (1/1000 second)

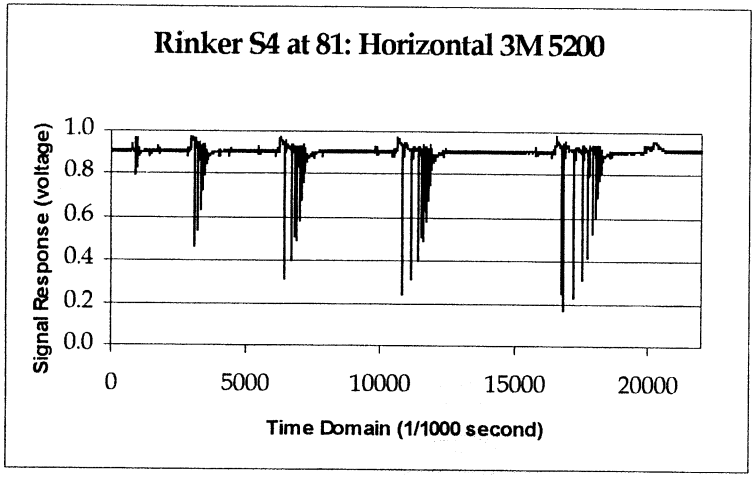
Rinker S4 at 81: Horizontal 3M 5200
Signal Response (voltage)
1.0
0.8
0.6
0.4
0.2
0.0
0
5000
10000
15000
20000
Time Domain (1/1000 second)

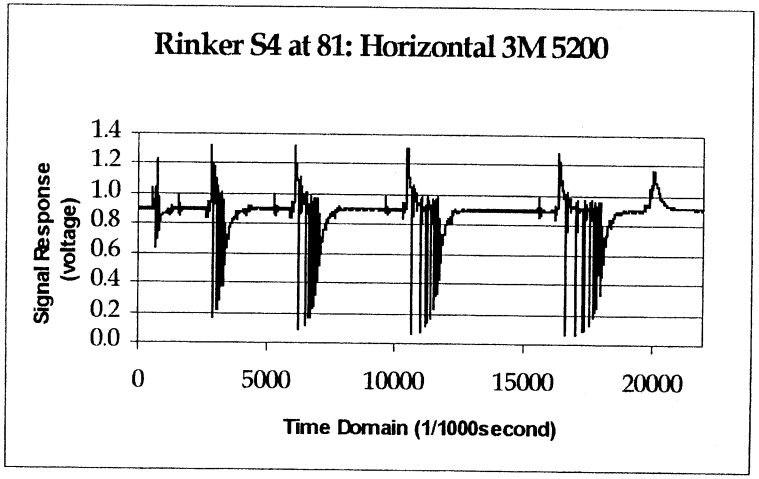
Rinker S4 at 81: Horizontal 3M 5200
Signal Response (voltage)
1.4
1.2
1.0
0.8
0.6
0.4
0.2
0.0
0
5000
10000
15000
20000
Time Domain (1/1000second)

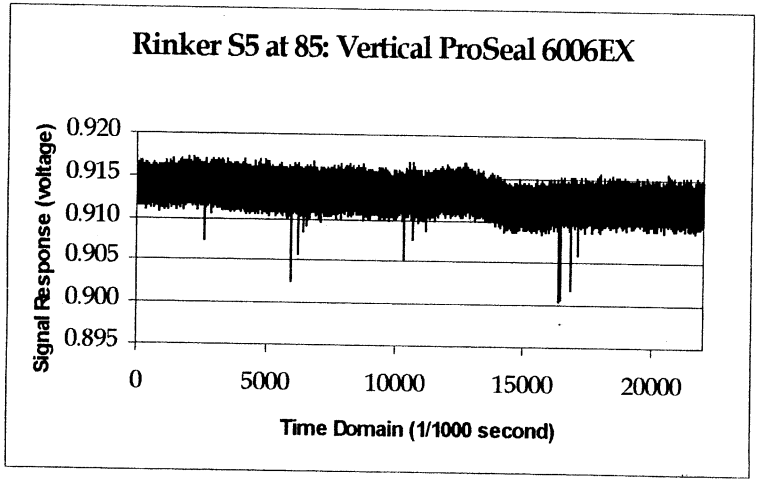
Rinker S5 at 85: Vertical ProSeal 6006EX
Signal Response (voltage)
0.920
0.915
0.910
0.905
0.900
0.895
0
5000
10000
15000
20000
Time Domain (1/1000 second)

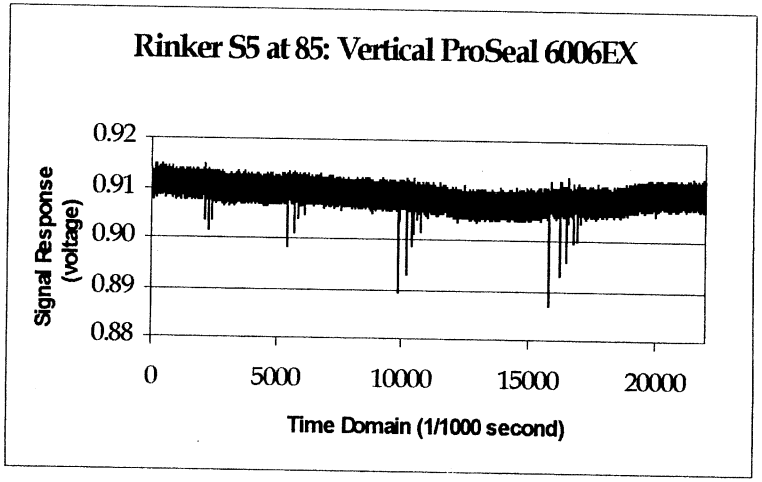
Rinker S5 at 85: Vertical ProSeal 6006EX
Signal Response (voltage)
0.92
0.91
0.90
0.89
0.88
0
5000
10000
15000
20000
Time Domain (1/1000 second)

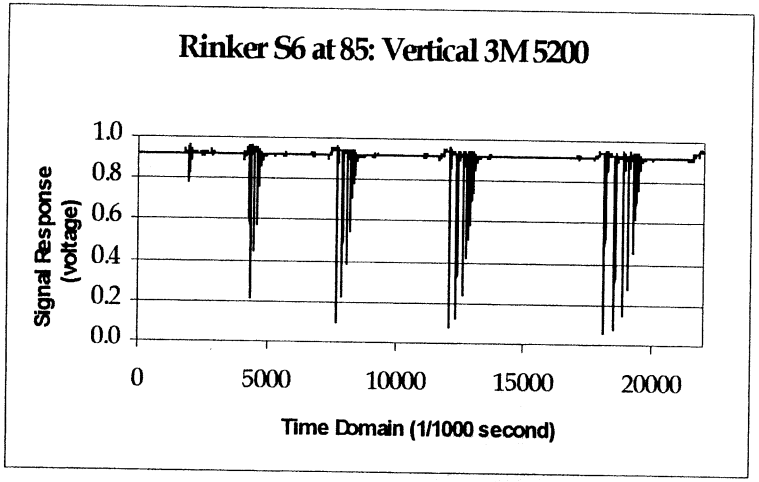
Rinker S6 at 85: Vertical 3M 5200
Signal Response (voltage)
1.0
0.8
0.6
0.4
0.2
0.0
0
5000
10000
15000
20000
Time Domain (1/1000 second)

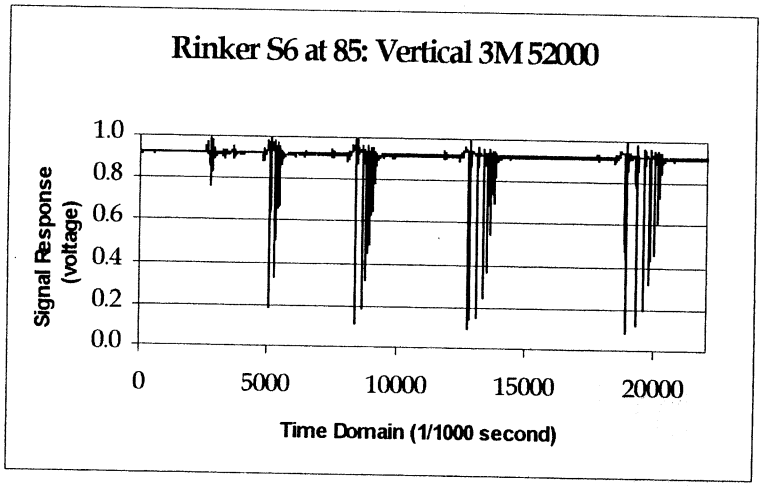
Rinker S6 at 85: Vertical 3M 52000
Signal Response (voltage)
1.0
0.8
0.6
0.4
0.2
0.0
0
5000
10000
15000
20000
Time Domain (1/1000 second)

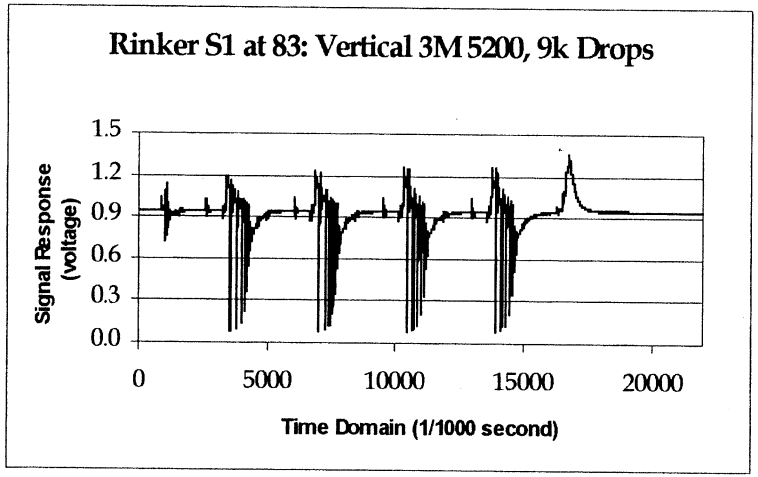
Rinker S1 at 83: Vertical 3M 5200, 9k Drops
Signal Response (voltage)
1.5
1.2
0.9
0.6
0.3
0.0
0
5000
10000
15000
20000
Time Domain (1/1000 second)

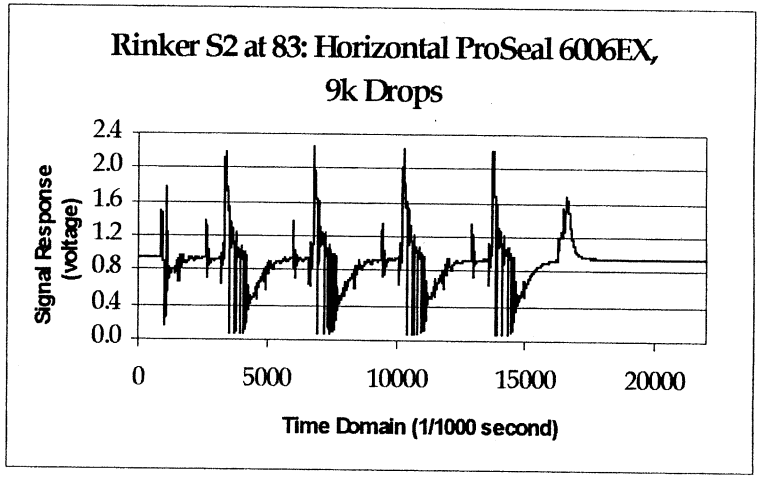
Rinker S2 at 83: Horizontal ProSeal 6006EX, 9k Drops
Signal Response (voltage)
2.4
2.0
1.6
1.2
0.8
0.4
0.0
0
5000
10000
15000
20000
Time Domain (1/1000 second)

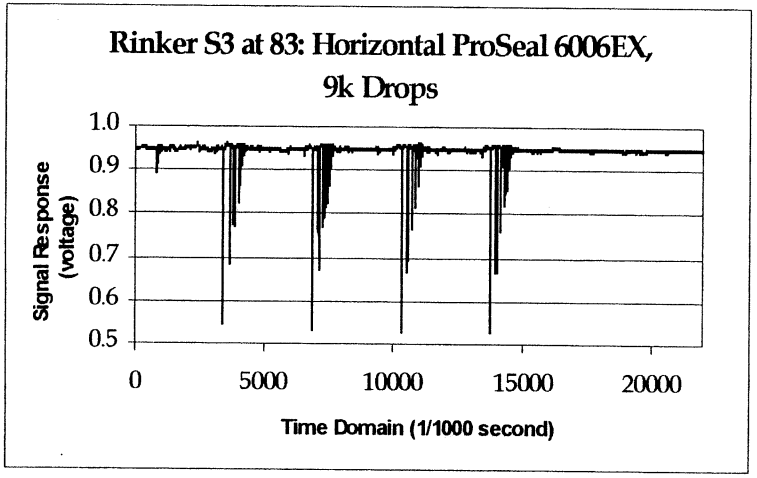
Rinker S3 at 83: Horizontal ProSeal 6006EX, 9k Drops
Signal Response (voltage)
1.0
0.9
0.8
0.7
0.6
0.5
0
5000
10000
15000
20000
Time Domain (1/1000 second)

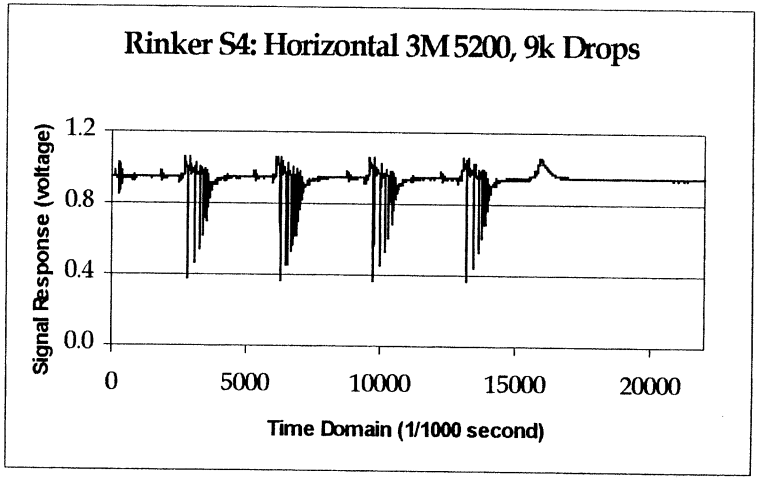
Rinker S4: Horizontal 3M 5200, 9k Drops
Signal Response (voltage)
1.2
0.8
0.4
0.0
0
5000
10000
15000
20000
Time Domain (1/1000 second)

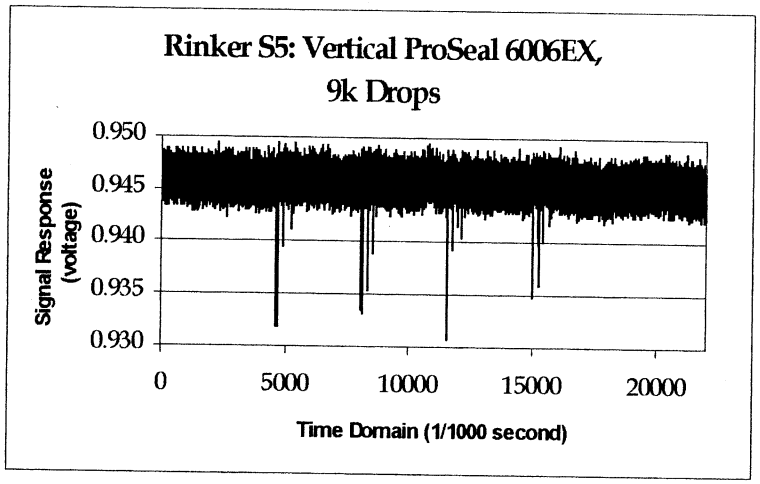
Rinker S5: Vertical ProSeal 6006EX, 9k Drops
Signal Response (voltage)
0.950
0.945
0.940
0.935
0.930
0
5000
10000
15000
20000
Time Domain (1/1000 second)

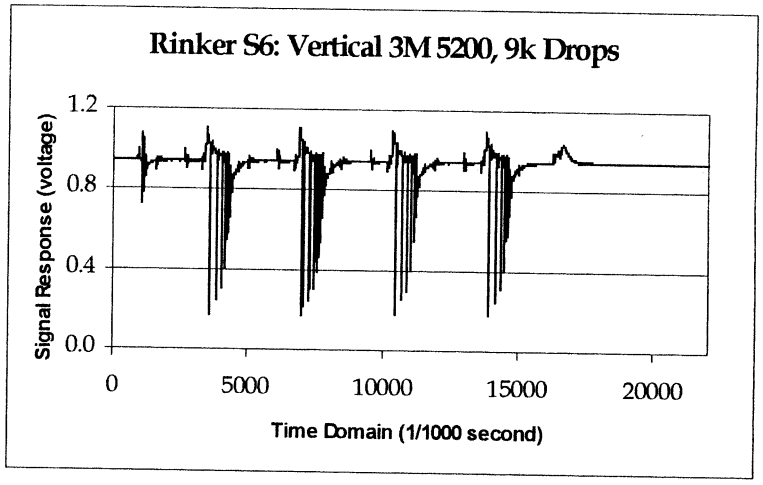
Rinker S6: Vertical 3M 5200, 9k Drops
Signal Response (voltage)
1.2
0.8
0.4
0.0
0
5000
10000
15000
20000
Time Domain (1/1000 second)

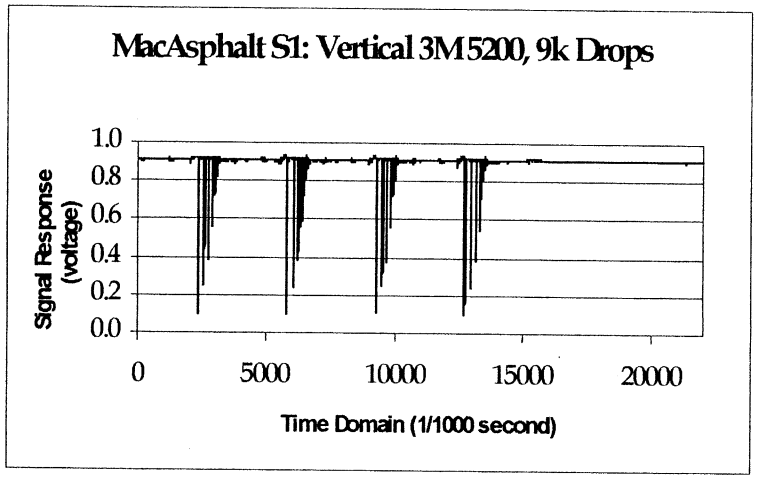
MacAsphalt S1: Vertical 3M 5200, 9k Drops
Signal Response (voltage)
1.0
0.8
0.6
0.4
0.2
0.0
0
5000
10000
15000
20000
Time Domain (1/1000 second)

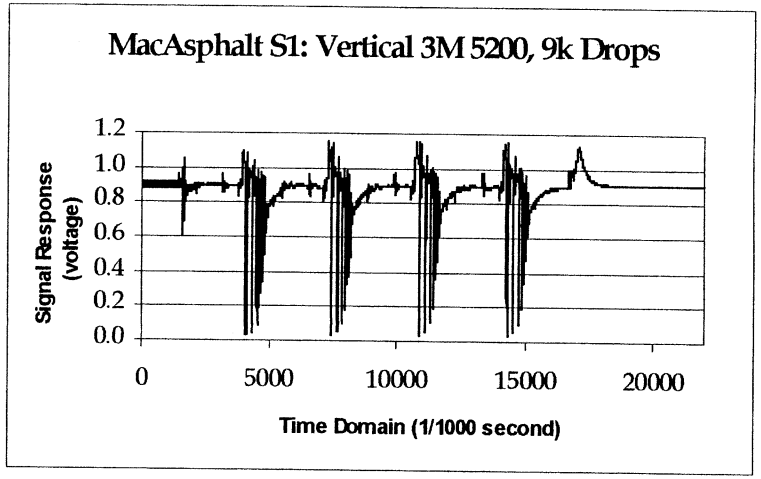
MacAsphalt S1: Vertical 3M 5200, 9k Drops
Signal Response (voltage)
1.2
1.0
0.8
0.6
0.4
0.2
0.0
0
5000
10000
15000
20000
Time Domain (1/1000 second)

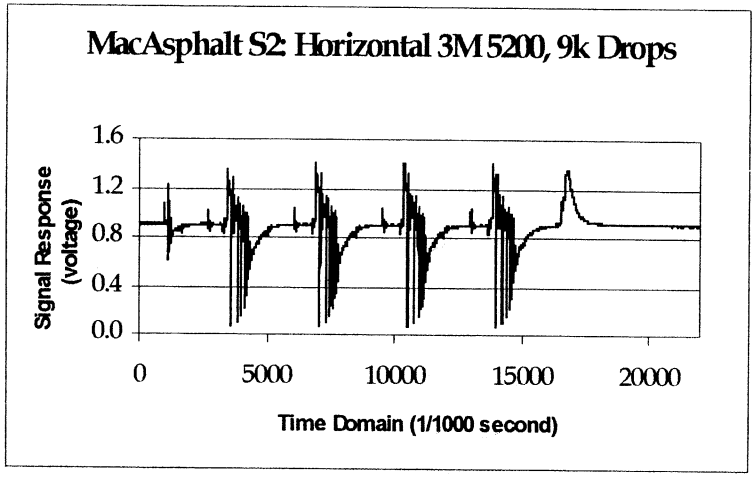
MacAsphalt S2: Horizontal 3M 5200, 9k Drops
Signal Response (voltage)
1.6
1.2
0.8
0.4
0.0
0
5000
10000
15000
20000
Time Domain (1/1000 second)

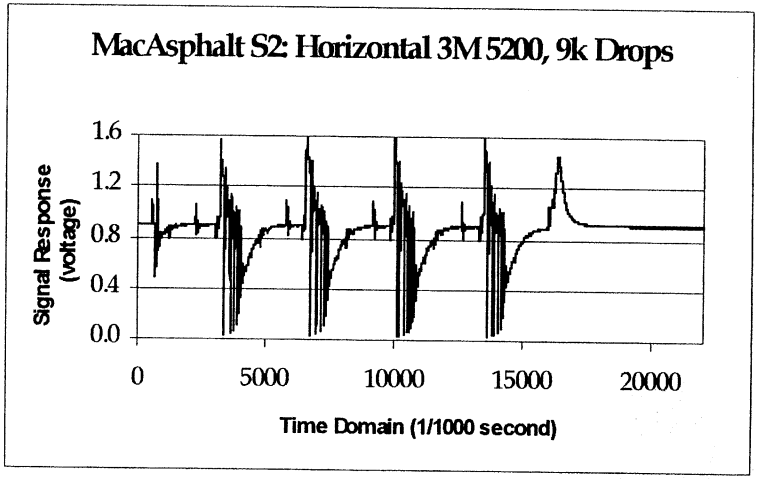
MacAsphalt S2: Horizontal 3M 5200, 9k Drops
Signal Response (voltage)
1.6
1.2
0.8
0.4
0.0
0
5000
10000
15000
20000
Time Domain (1/1000 second)

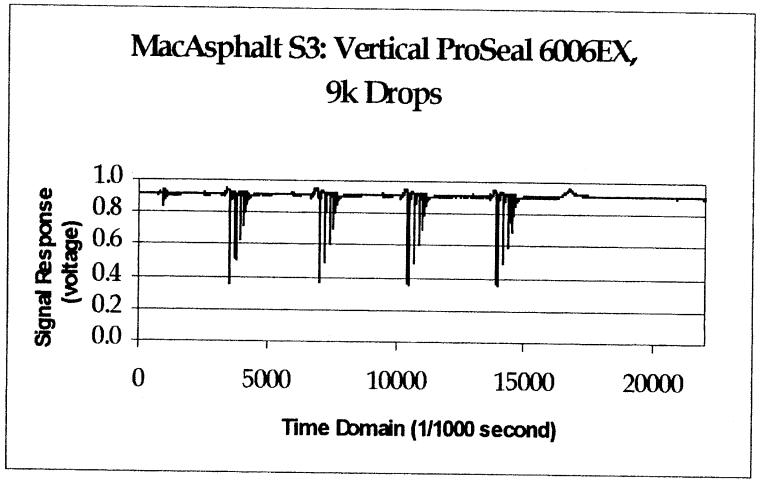
MacAsphalt S3: Vertical ProSeal 6006EX,
9k Drops
Signal Response (voltage)
1.0
0.8
0.6
0.4
0.2
0.0
0
5000
10000
15000
20000
Time Domain (1/1000 second)

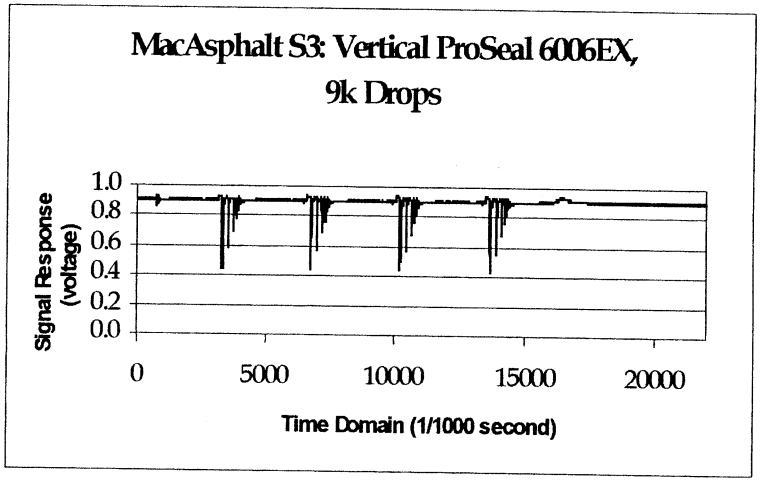
MacAsphalt S3: Vertical ProSeal 6006EX,
9k Drops
Signal Response (voltage)
1.0
0.8
0.6
0.4
0.2
0.0
0
5000
10000
15000
20000
Time Domain (1/1000 second)

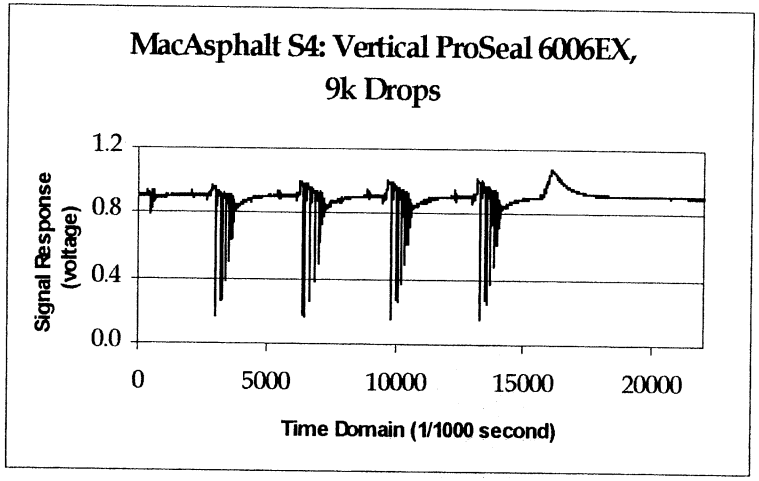
MacAsphalt S4: Vertical ProSeal 6006EX,
9k Drops
Signal Response (voltage)
1.2
0.8
0.4
0.0
0
5000
10000
15000
20000
Time Domain (1/1000 second)

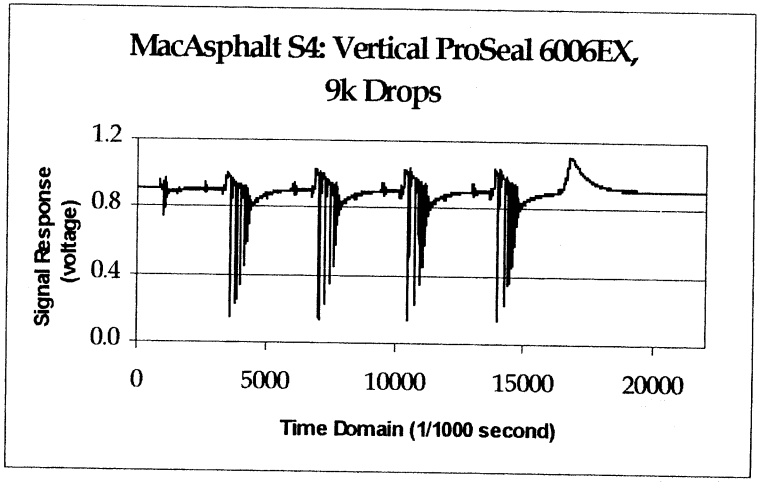
MacAsphalt S4: Vertical ProSeal 6006EX,
9k Drops
Signal Response (voltage)
1.2
0.8
0.4
0.0
0
5000
10000
15000
20000
Time Domain (1/1000 second)

October 12-13, 1999 FWD LabView Plots Taken at MacAsphalt Field Test Site

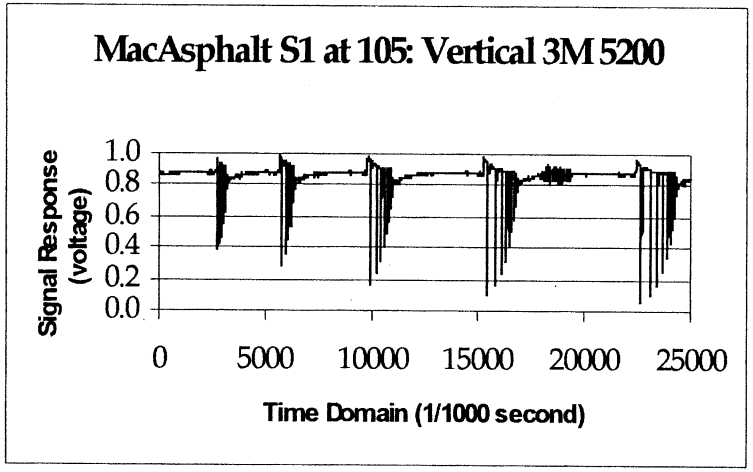

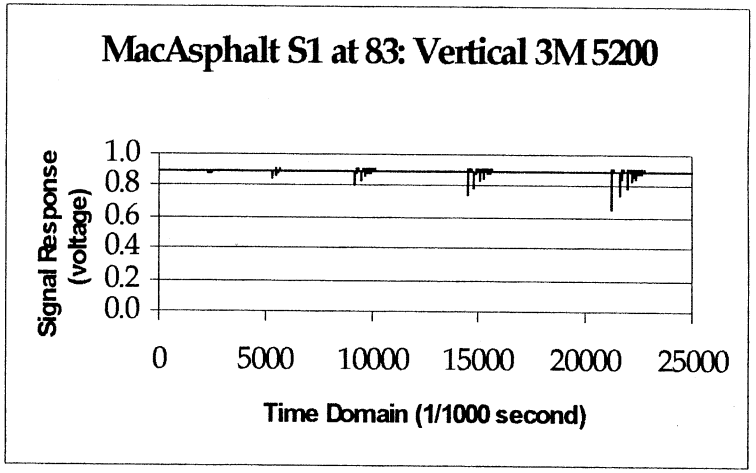

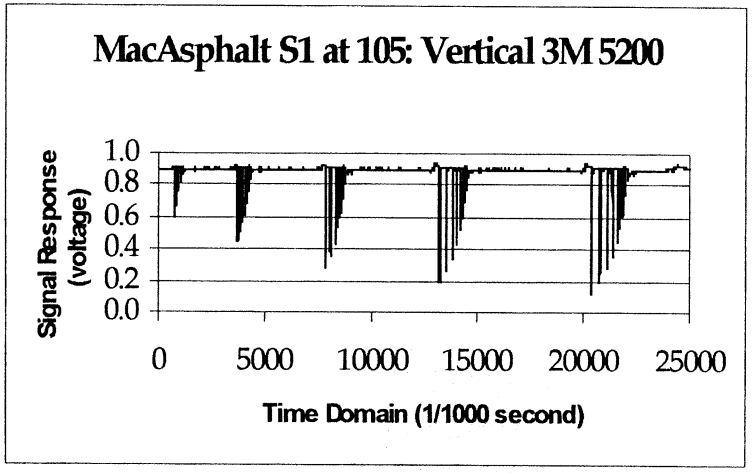

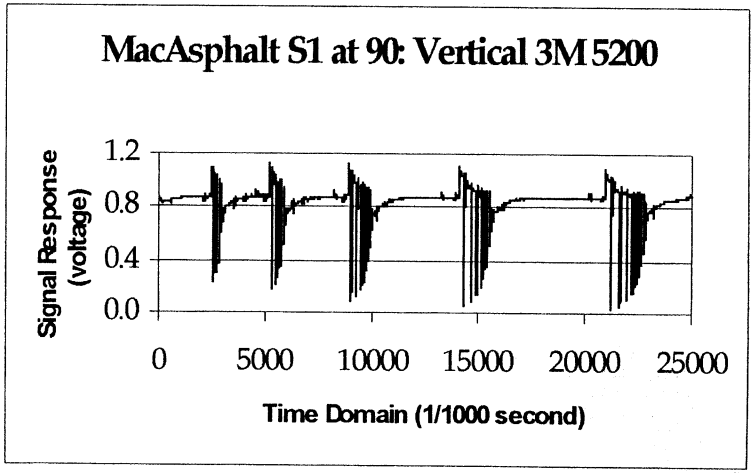

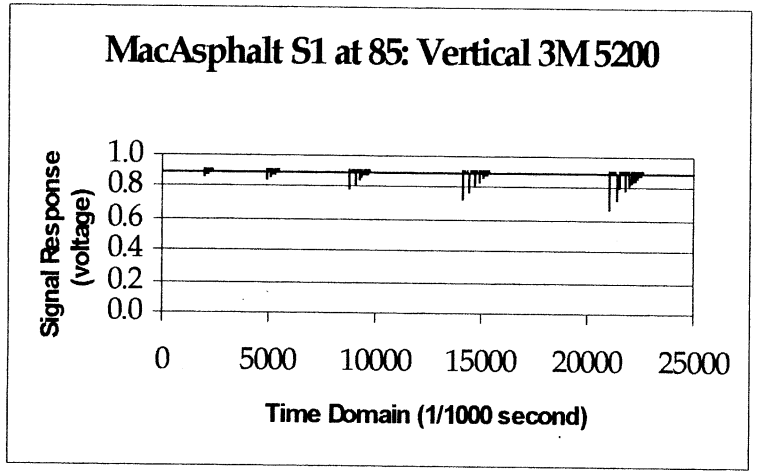
MacAsphalt S1 at 85: Vertical 3M 5200
Signal Response (voltage)
1.0
0.8
0.6
0.4
0.2
0.0
0
5000
10000
15000
20000
25000
Time Domain (1/1000 second)

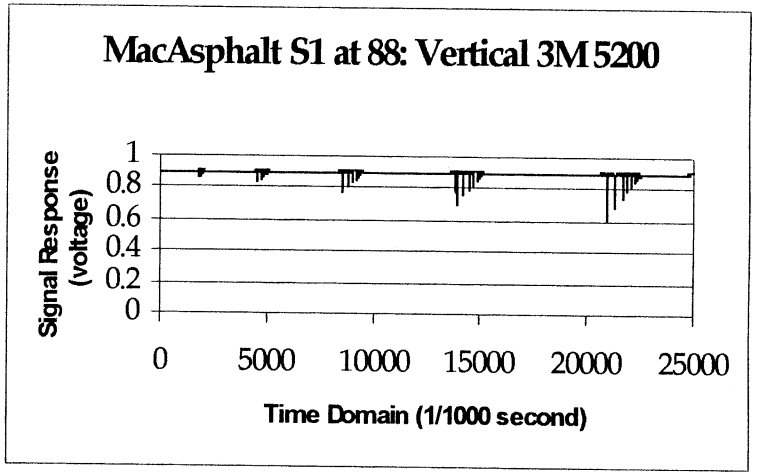
MacAsphalt S1 at 88: Vertical 3M 5200
Signal Response (voltage)
1
0.8
0.6
0.4
0.2
0
0
5000
10000
15000
20000
25000
Time Domain (1/1000 second)

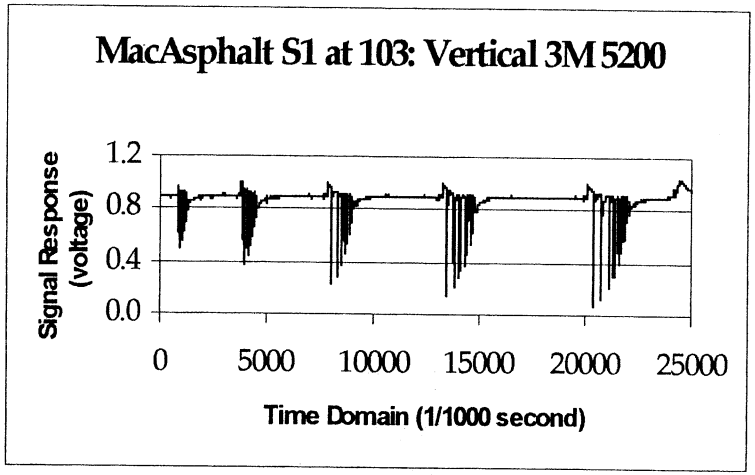
MacAsphalt S1 at 103: Vertical 3M 5200
Signal Response (voltage)
1.2
0.8
0.4
0.0
0
5000
10000
15000
20000
25000
Time Domain (1/1000 second)

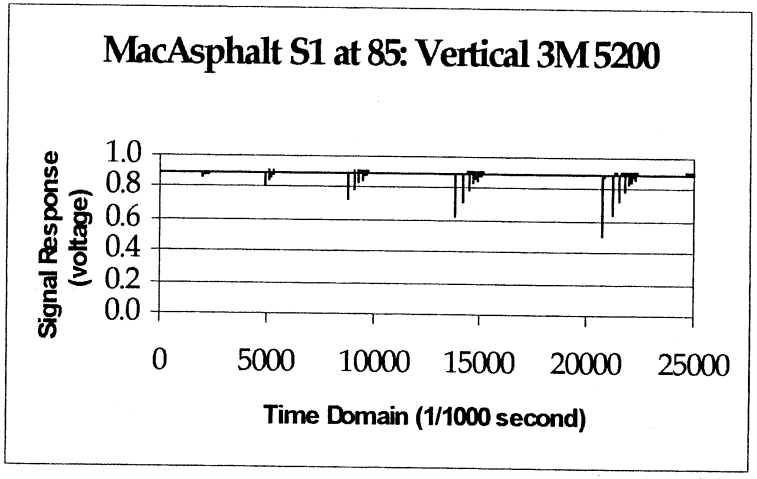
MacAsphalt S1 at 85: Vertical 3M 5200
Signal Response (voltage)
1.0
0.8
0.6
0.4
0.2
0.0
0
5000
10000
15000
20000
25000
Time Domain (1/1000 second)

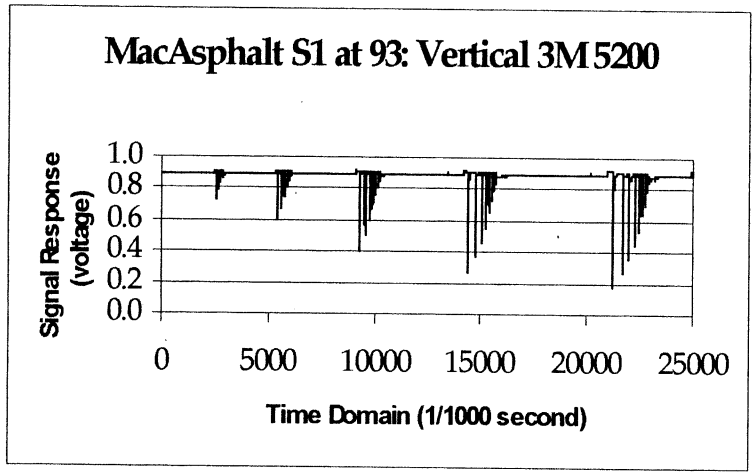
MacAsphalt S1 at 93: Vertical 3M 5200
Signal Response (voltage)
1.0
0.8
0.6
0.4
0.2
0.0
0
5000
10000
15000
20000
25000
Time Domain (1/1000 second)

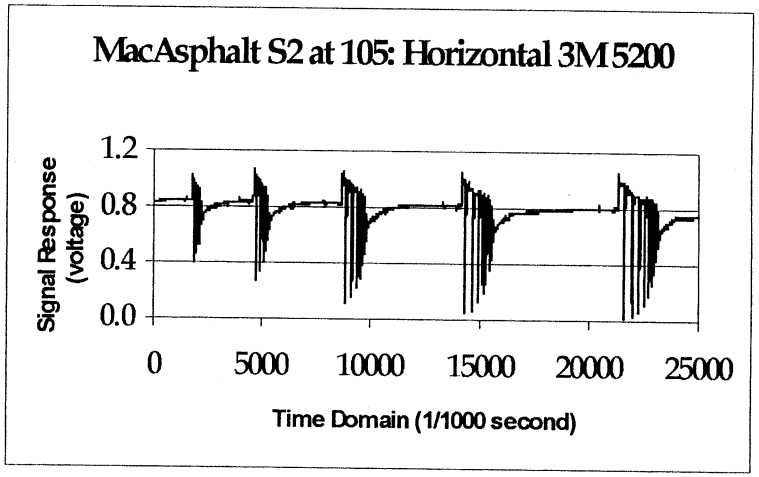
MacAsphalt S2 at 105: Horizontal 3M 5200
Signal Response (voltage)
1.2
0.8
0.4
0.0
0
5000
10000
15000
20000
25000
Time Domain (1/1000 second)

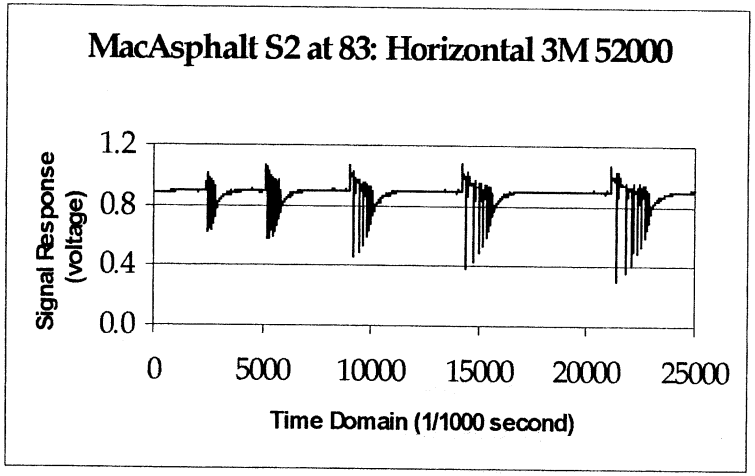
MacAsphalt S2 at 83: Horizontal 3M 52000
Signal Response (voltage)
1.2
0.8
0.4
0.0
0
5000
10000
15000
20000
25000
Time Domain (1/1000 second)

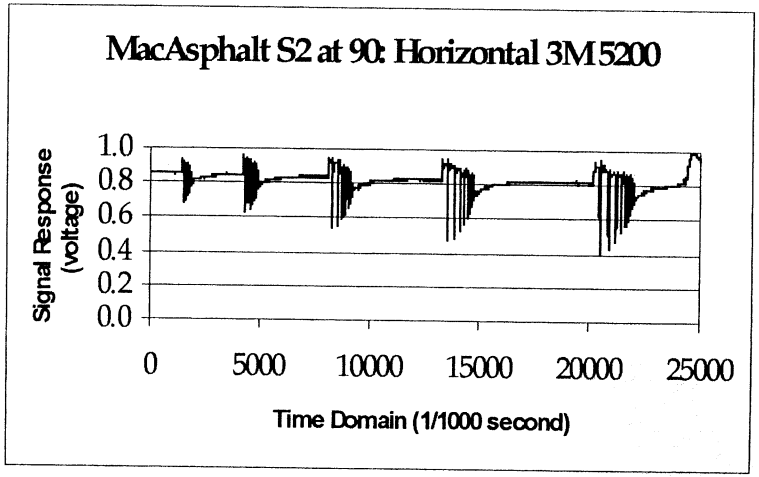
MacAsphalt S2 at 90: Horizontal 3M 5200
Signal Response (voltage)
1.0
0.8
0.6
0.4
0.2
0.0
0
5000
10000
15000
20000
25000
Time Domain (1/1000 second)

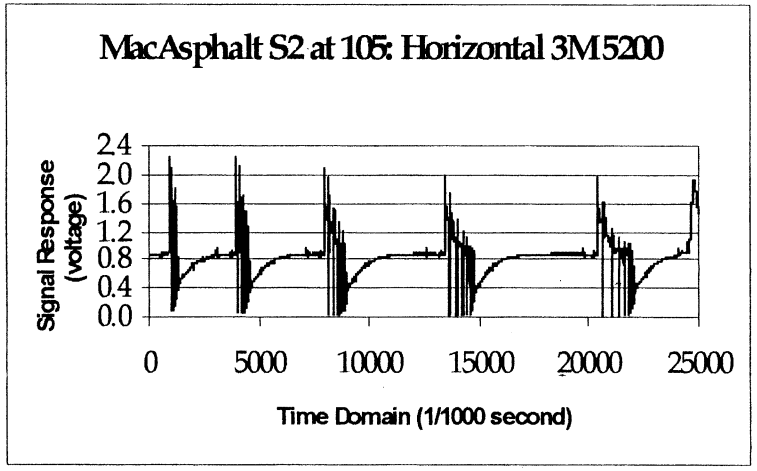
MacAsphalt S2 at 105: Horizontal 3M5200
Signal Response (voltage)
2.4
2.0
1.6
1.2
0.8
0.4
0.0
0
5000
10000
15000
20000
25000
Time Domain (1/1000 second)

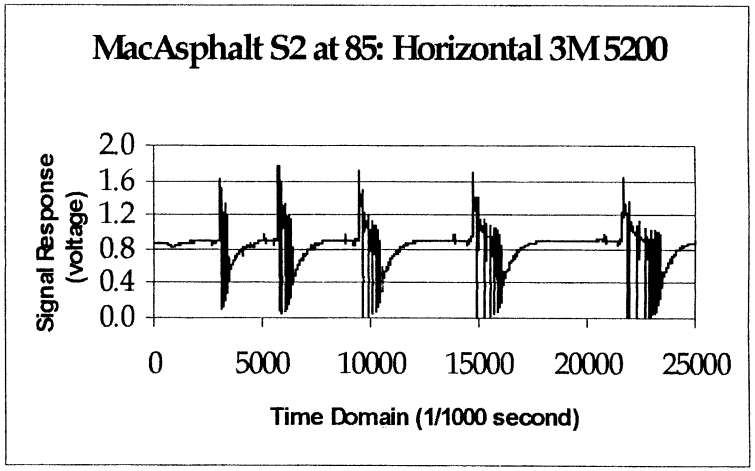
MacAsphalt S2 at 85: Horizontal 3M 5200
Signal Response (voltage)
2.0
1.6
1.2
0.8
0.4
0.0
0
5000
10000
15000
20000
25000
Time Domain (1/1000 second)

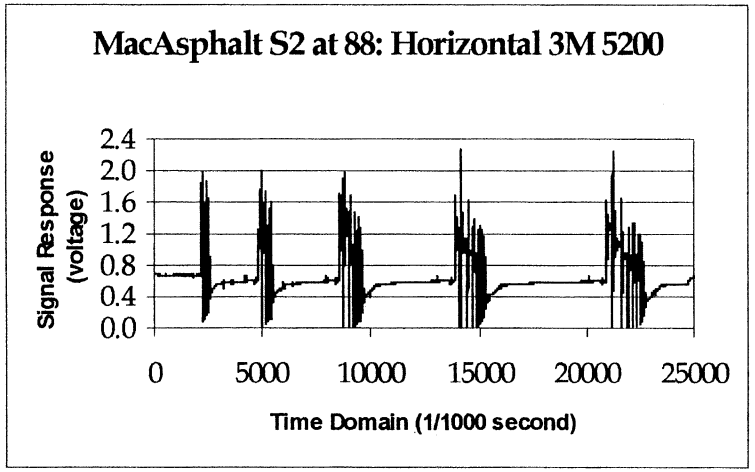
MacAsphalt S2 at 88: Horizontal 3M 5200
Signal Response (voltage)
2.4
2.0
1.6
1.2
0.8
0.4
0.0
0
5000
10000
15000
20000
25000
Time Domain (1/1000 second)

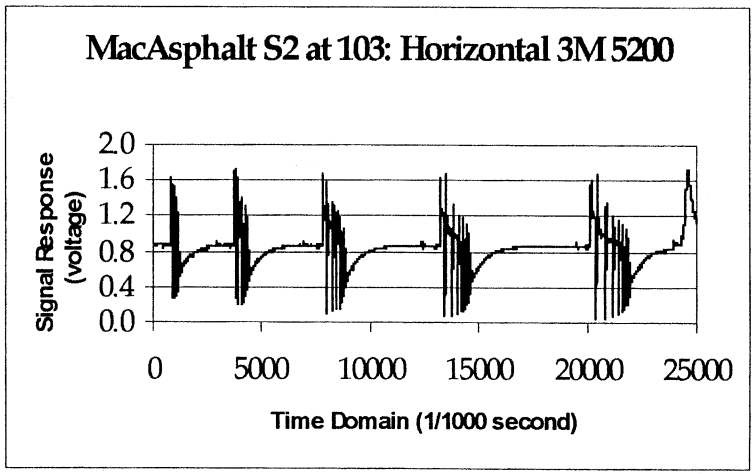
MacAsphalt S2 at 103: Horizontal 3M 5200
Signal Response (voltage)
2.0
1.6
1.2
0.8
0.4
0.0
0
5000
10000
15000
20000
25000
Time Domain (1/1000 second)

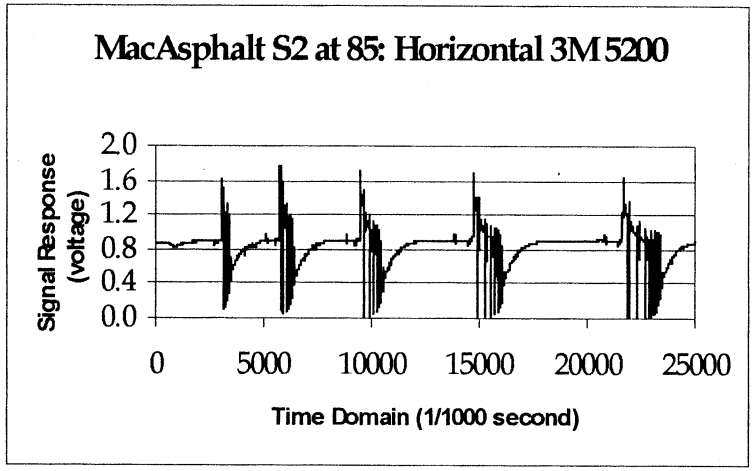
MacAsphalt S2 at 85: Horizontal 3M 5200
Signal Response (voltage)
2.0
1.6
1.2
0.8
0.4
0.0
0
5000
10000
15000
20000
25000
Time Domain (1/1000 second)

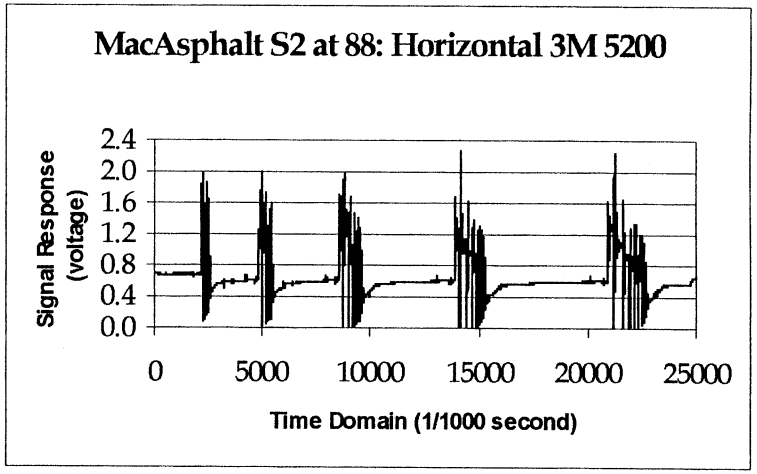
MacAsphalt S2 at 88: Horizontal 3M 5200
Signal Response (voltage)
2.4
2.0
1.6
1.2
0.8
0.4
0.0
0
5000
10000
15000
20000
25000
Time Domain (1/1000 second)

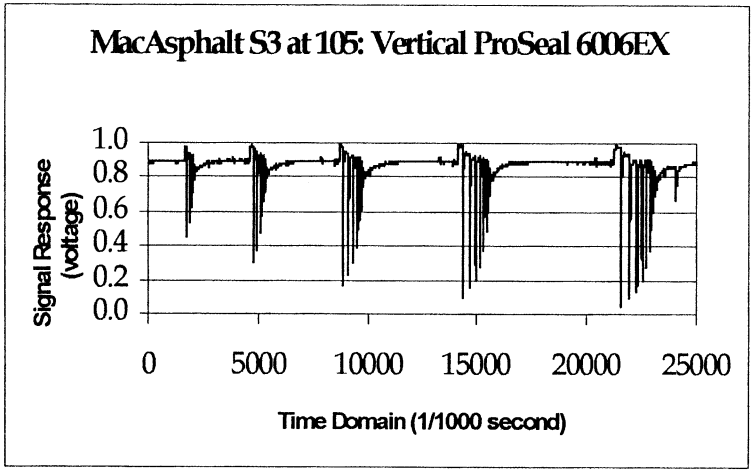
MacAsphalt S3 at 105: Vertical ProSeal 6006EX
Signal Response (voltage)
1.0
0.8
0.6
0.4
0.2
0.0
0
5000
10000
15000
20000
25000
Time Domain (1/1000 second)

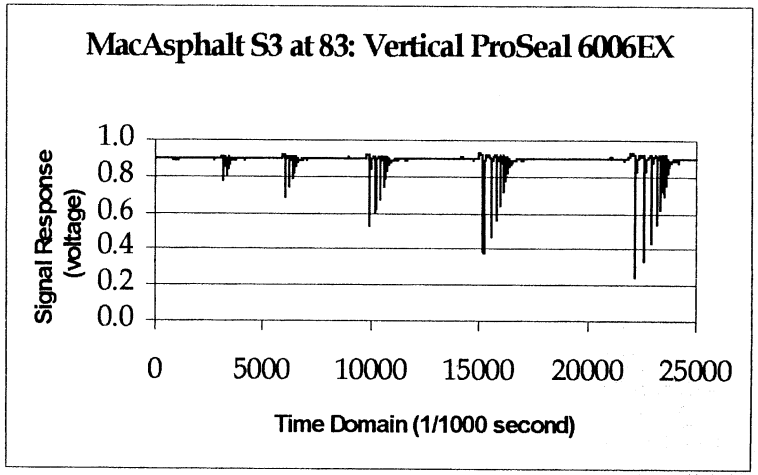
MacAsphalt S3 at 83: Vertical ProSeal 6006EX
Signal Response (voltage)
1.0
0.8
0.6
0.4
0.2
0.0
0
5000
10000
15000
20000
25000
Time Domain (1/1000 second)

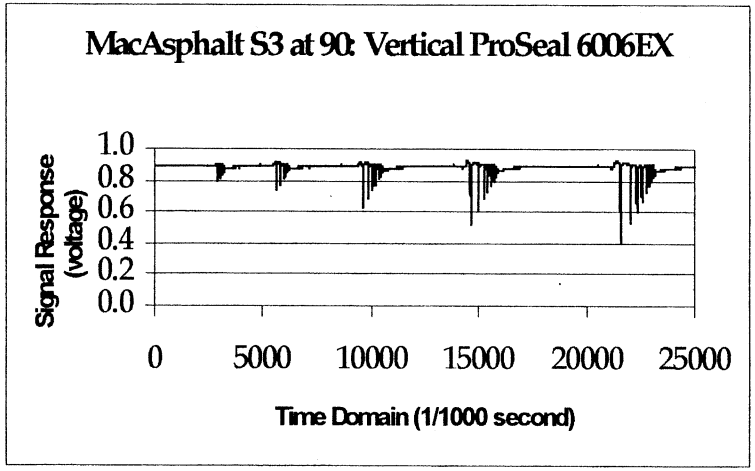
MacAsphalt S3 at 90: Vertical ProSeal 6006EX
Signal Response (voltage)
1.0
0.8
0.6
0.4
0.2
0.0
0
5000
10000
15000
20000
25000
Time Domain (1/1000 second)

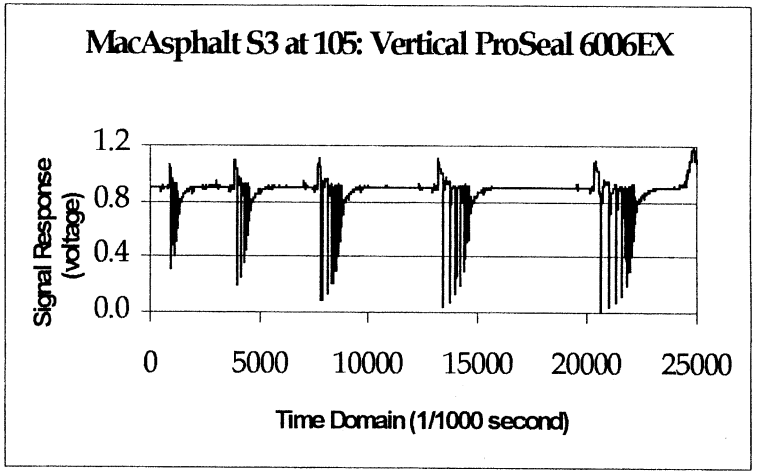
MacAsphalt S3 at 105: Vertical ProSeal 6006EX
Signal Response (voltage)
1.2
0.8
0.4
0.0
0
5000
10000
15000
20000
25000
Time Domain (1/1000 second)

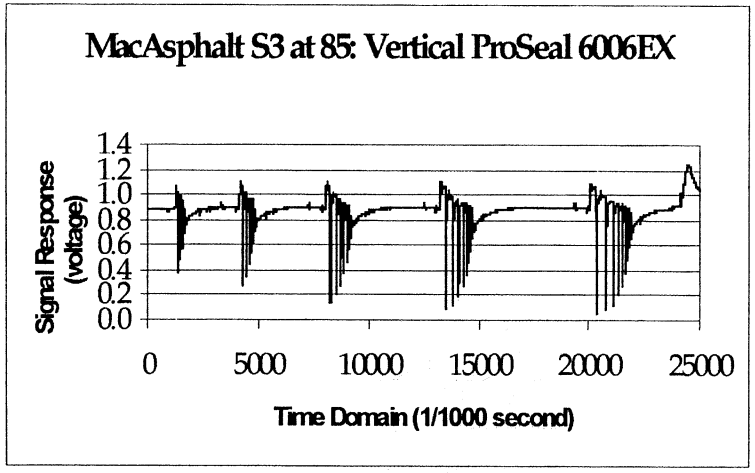
MacAsphalt S3 at 85: Vertical ProSeal 6006EX
Signal Response (voltage)
1.4
1.2
1.0
0.8
0.6
0.4
0.2
0.0
0
5000
10000
15000
20000
25000
Time Domain (1/1000 second)

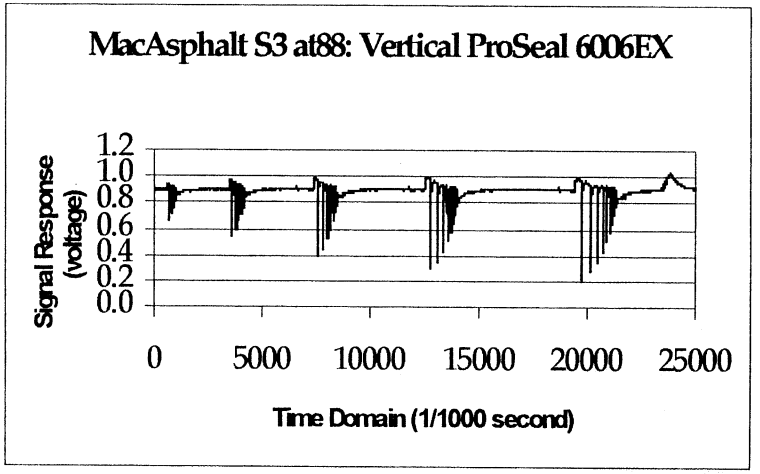
MacAsphalt S3 at88: Vertical ProSeal 6006EX
Signal Response (voltage)
1.2
1.0
0.8
0.6
0.4
0.2
0.0
0
5000
10000
15000
20000
25000
Time Domain (1/1000 second)

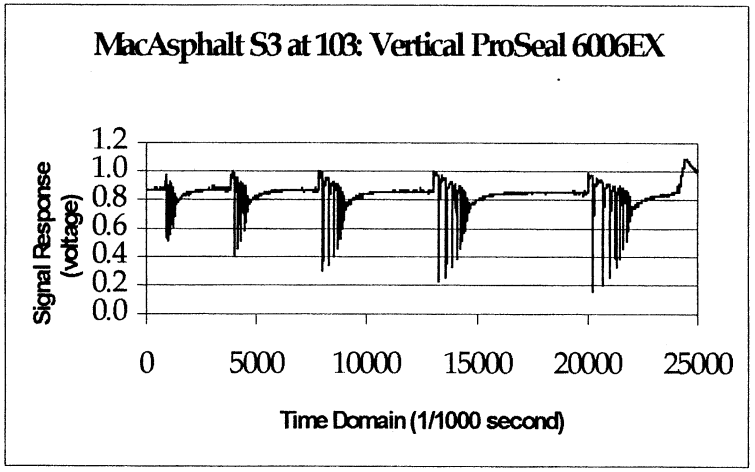
MacAsphalt S3 at 103: Vertical ProSeal 6006EX
Signal Response (voltage)
1.2
1.0
0.8
0.6
0.4
0.2
0.0
0
5000
10000
15000
20000
25000
Time Domain (1/1000 second)

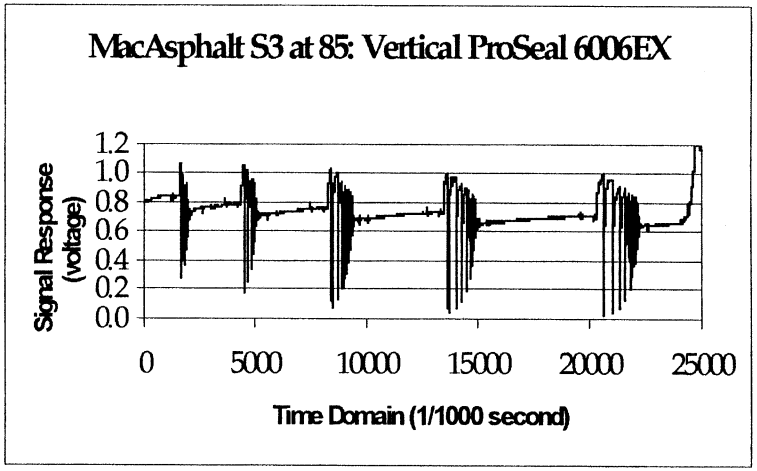
MacAsphalt S3 at 85: Vertical ProSeal 6006EX
Signal Response (voltage)
1.2
1.0
0.8
0.6
0.4
0.2
0.0
0
5000
10000
15000
20000
25000
Time Domain (1/1000 second)

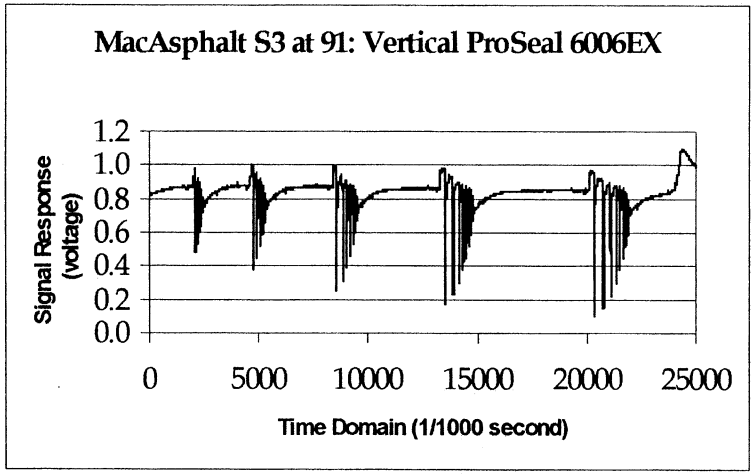
MacAsphalt S3 at 91: Vertical ProSeal 6006EX
Signal Response (voltage)
1.2
1.0
0.8
0.6
0.4
0.2
0.0
0
5000
10000
15000
20000
25000
Time Domain (1/1000 second)

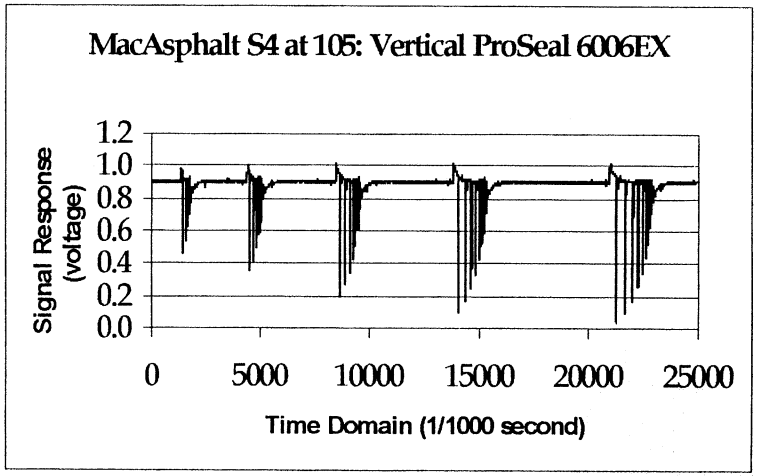
MacAsphalt S4 at 105: Vertical ProSeal 6006EX
Signal Response (voltage)
1.2
1.0
0.8
0.6
0.4
0.2
0.0
0
5000
10000
15000
20000
25000
Time Domain (1/1000 second)

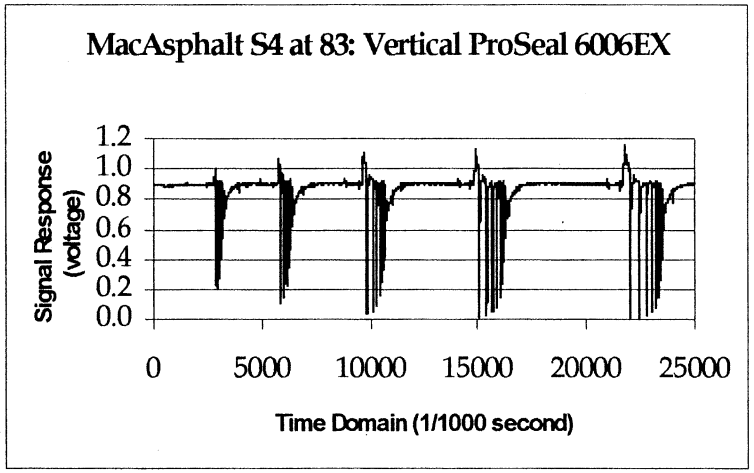
MacAsphalt S4 at 83: Vertical ProSeal 6006EX
Signal Response (voltage)
1.2
1.0
0.8
0.6
0.4
0.2
0.0
0
5000
10000
15000
20000
25000
Time Domain (1/1000 second)

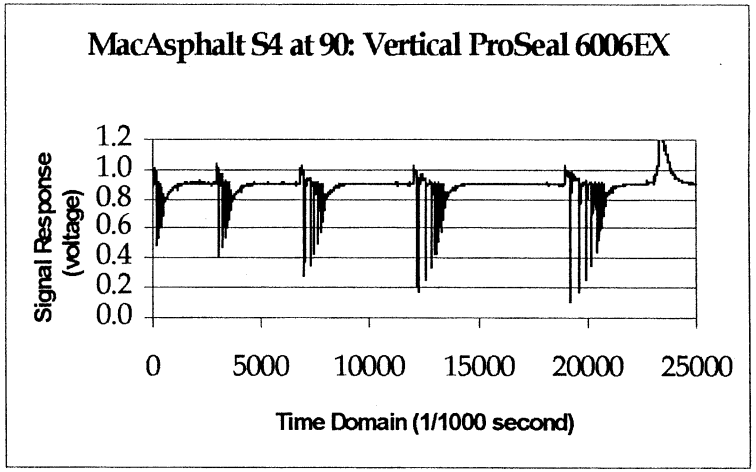
MacAsphalt S4 at 90: Vertical ProSeal 6006EX
Signal Response (voltage)
1.2
1.0
0.8
0.6
0.4
0.2
0.0
0
5000
10000
15000
20000
25000
Time Domain (1/1000 second)

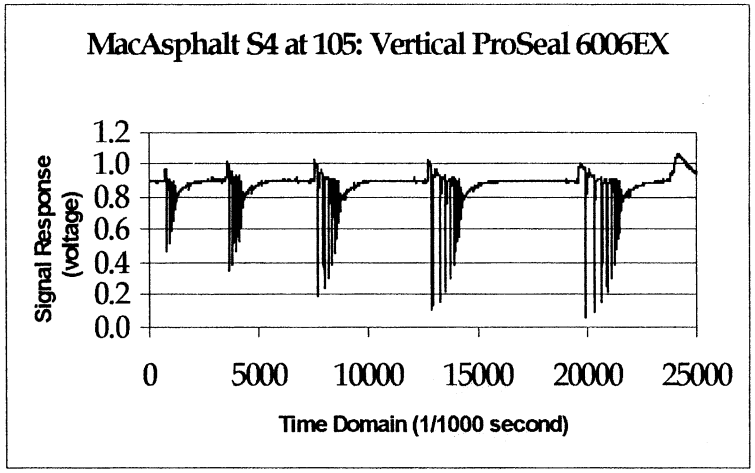
MacAsphalt S4 at 105: Vertical ProSeal 6006EX
Signal Response (voltage)
1.2
1.0
0.8
0.6
0.4
0.2
0.0
0
5000
10000
15000
20000
25000
Time Domain (1/1000 second)

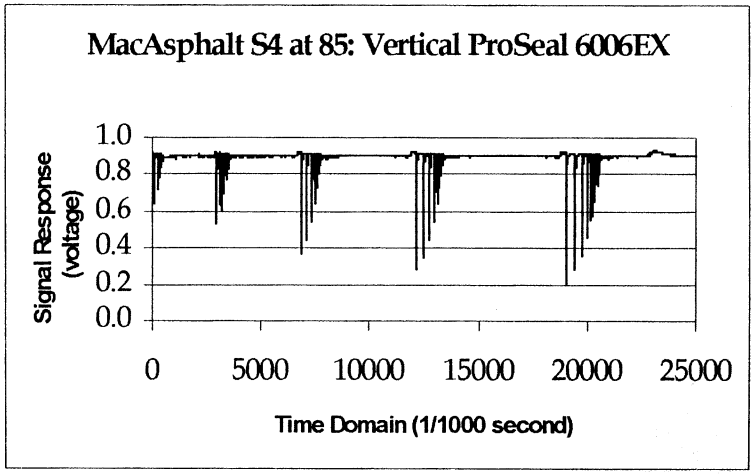
MacAsphalt S4 at 85: Vertical ProSeal 6006EX
Signal Response (voltage)
1.0
0.8
0.6
0.4
0.2
0.0
0
5000
10000
15000
20000
25000
Time Domain (1/1000 second)

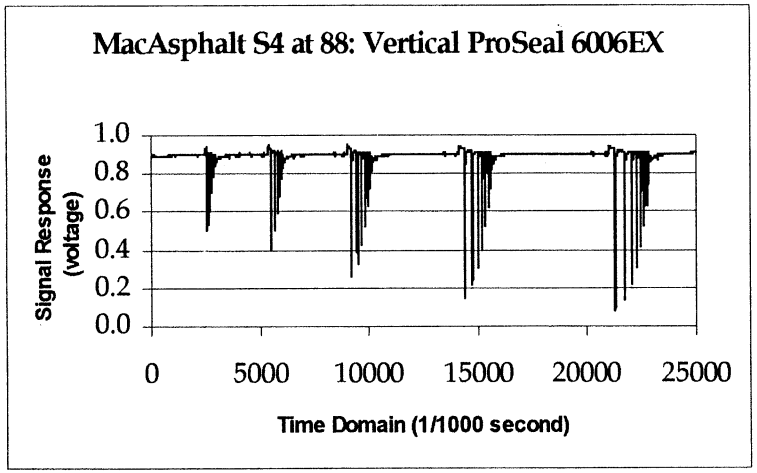
MacAsphalt S4 at 88: Vertical ProSeal 6006EX
Signal Response (voltage)
1.0
0.8
0.6
0.4
0.2
0.0
0
5000
10000
15000
20000
25000
Time Domain (1/1000 second)

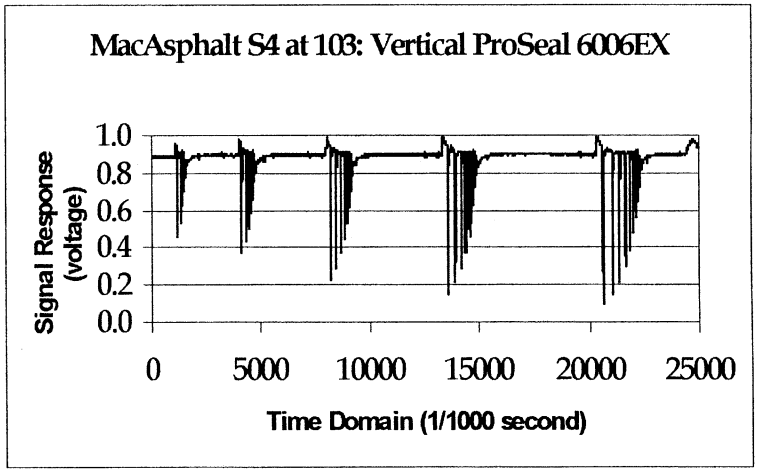
MacAsphalt S4 at 103: Vertical ProSeal 6006EX
Signal Response (voltage)
1.0
0.8
0.6
0.4
0.2
0.0
0
5000
10000
15000
20000
25000
Time Domain (1/1000 second)

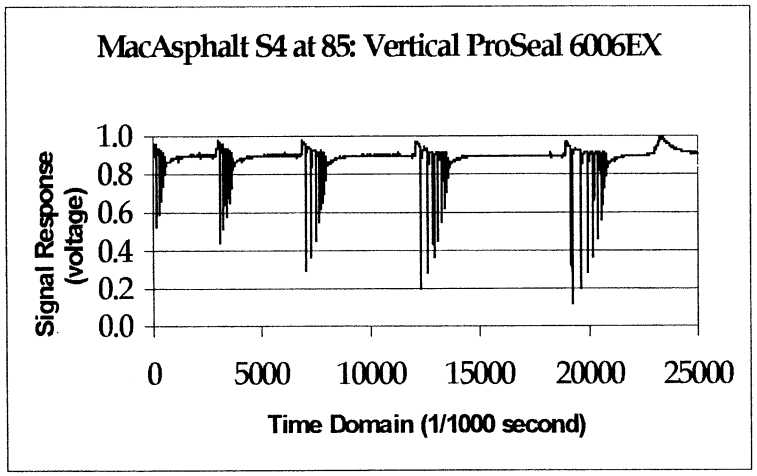
MacAsphalt S4 at 85: Vertical ProSeal 6006EX
Signal Response (voltage)
1.0
0.8
0.6
0.4
0.2
0.0
0
5000
10000
15000
20000
25000
Time Domain (1/1000 second)

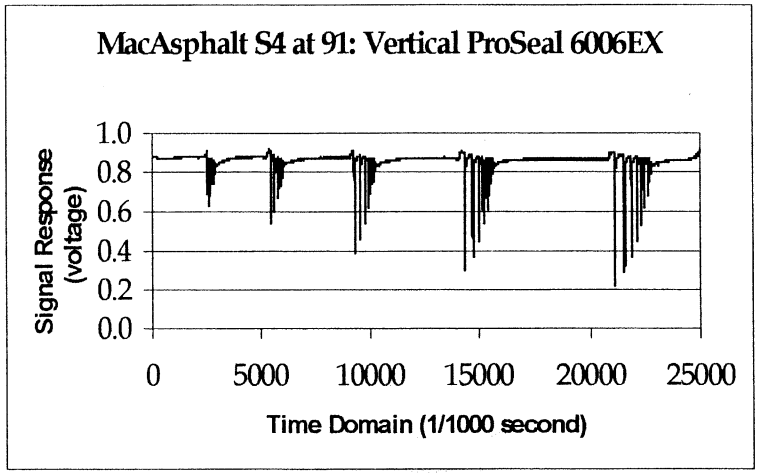
MacAsphalt S4 at 91: Vertical ProSeal 6006EX
Signal Response (voltage)
1.0
0.8
0.6
0.4
0.2
0.0
0
5000
10000
15000
20000
25000
Time Domain (1/1000 second)

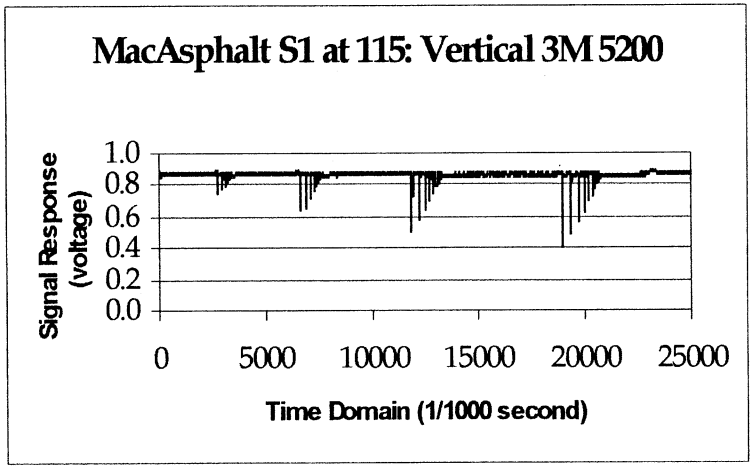
MacAsphalt S1 at 115: Vertical 3M 5200
Signal Response (voltage)
1.0
0.8
0.6
0.4
0.2
0.0
0
5000
10000
15000
20000
25000
Time Domain (1/1000 second)

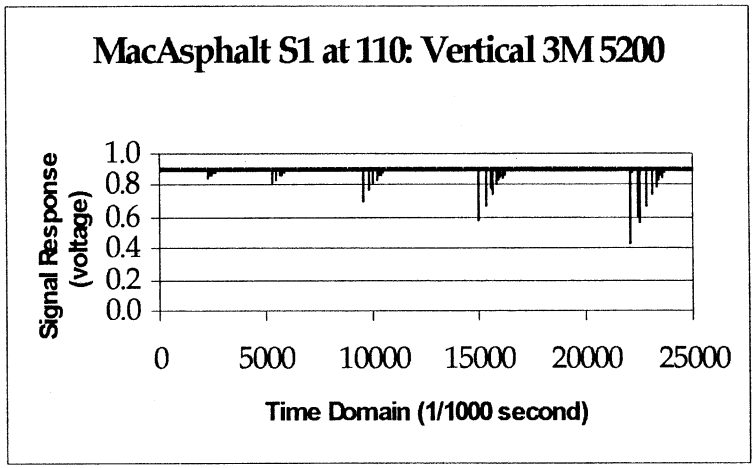
MacAsphalt S1 at 110: Vertical 3M 5200
Signal Response (voltage)
1.0
0.8
0.6
0.4
0.2
0.0
0
5000
10000
15000
20000
25000
Time Domain (1/1000 second)

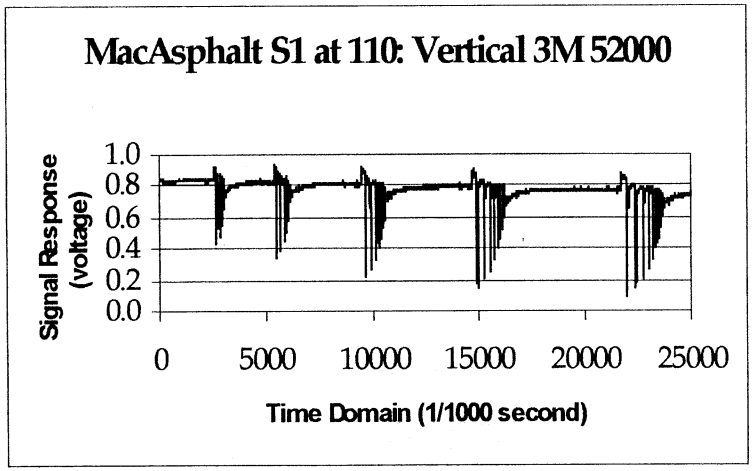
MacAsphalt S1 at 110: Vertical 3M 52000
Signal Response (voltage)
1.0
0.8
0.6
0.4
0.2
0.0
0
5000
10000
15000
20000
25000
Time Domain (1/1000 second)

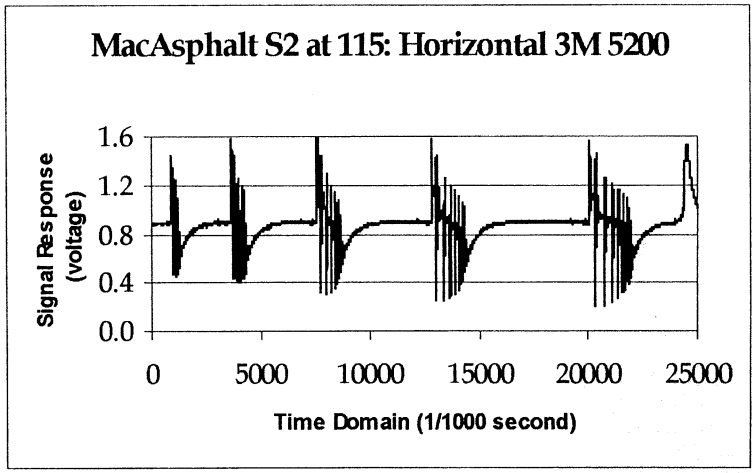
MacAsphalt S2 at 115: Horizontal 3M 5200
Signal Response (voltage)
1.6
1.2
0.8
0.4
0.0
0
5000
10000
15000
20000
25000
Time Domain (1/1000 second)

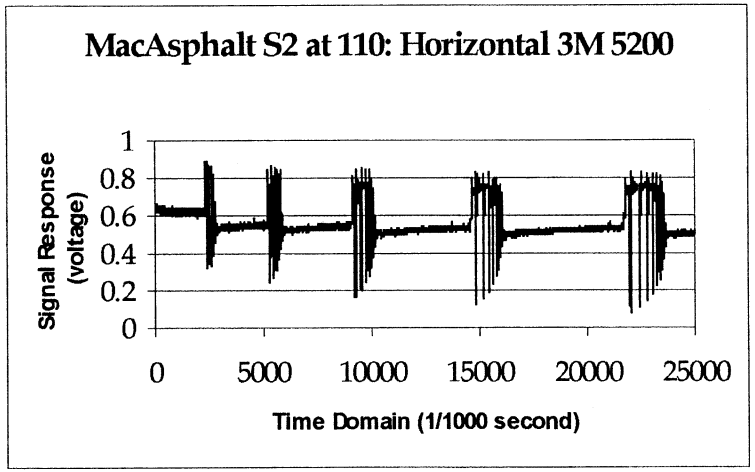
MacAsphalt S2 at 110: Horizontal 3M 5200
Signal Response (voltage)
1
0.8
0.6
0.4
0.2
0
0
5000
10000
15000
20000
25000
Time Domain (1/1000 second)

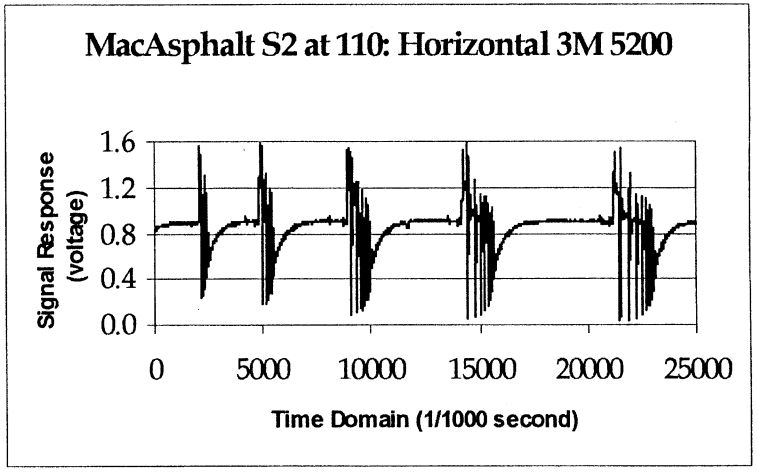
MacAsphalt S2 at 110: Horizontal 3M 5200
Signal Response (voltage)
1.6
1.2
0.8
0.4
0.0
0
5000
10000
15000
20000
25000
Time Domain (1/1000 second)

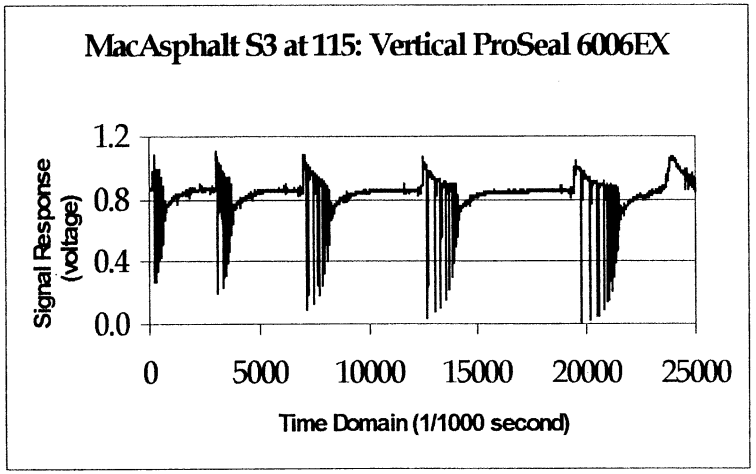
MacAsphalt S3 at 115: Vertical ProSeal 6006EX
Signal Response (voltage)
1.2
0.8
0.4
0.0
0
5000
10000
15000
20000
25000
Time Domain (1/1000 second)

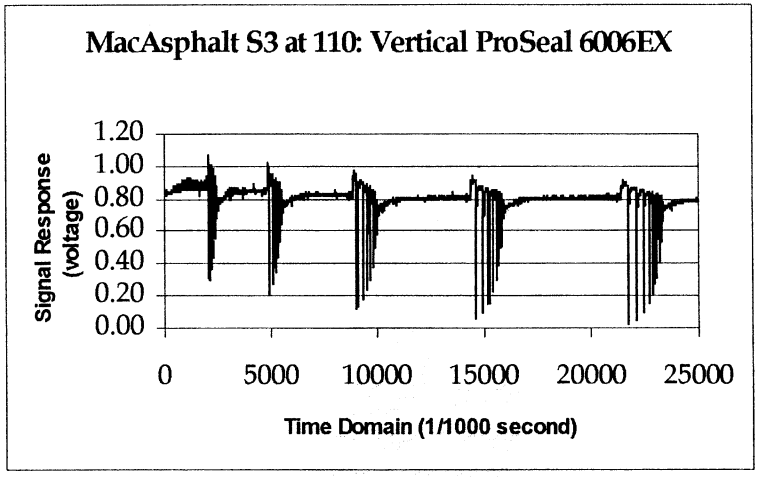
MacAsphalt S3 at 110: Vertical ProSeal 6006EX
Signal Response (voltage)
1.20
1.00
0.80
0.60
0.40
0.20
0.00
0
5000
10000
15000
20000
25000
Time Domain (1/1000 second)

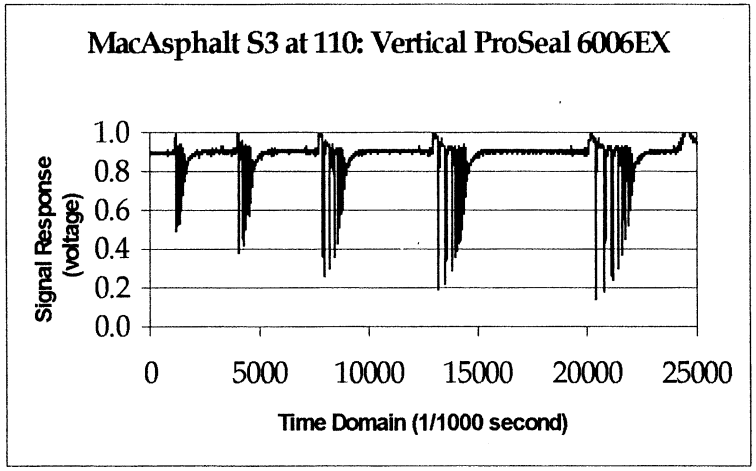
MacAsphalt S3 at 110: Vertical ProSeal 6006EX
Signal Response (voltage)
1.0
0.8
0.6
0.4
0.2
0.0
0
5000
10000
15000
20000
25000
Time Domain (1/1000 second)

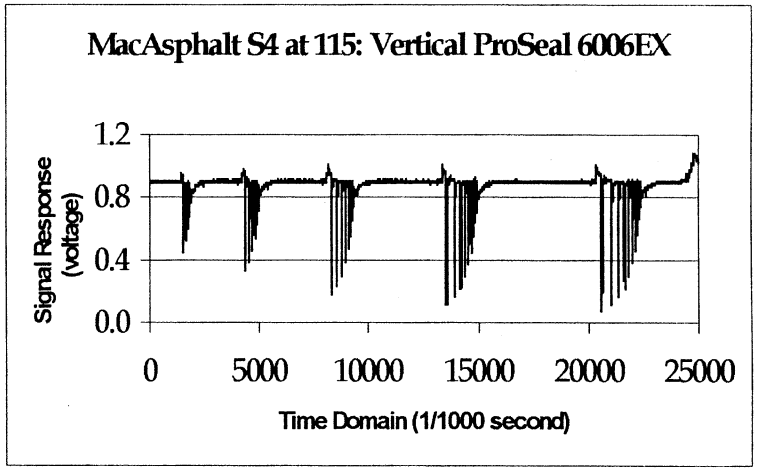
MacAsphalt S4 at 115: Vertical ProSeal 6006EX
Signal Response (voltage)
1.2
0.8
0.4
0.0
0
5000
10000
15000
20000
25000
Time Domain (1/1000 second)

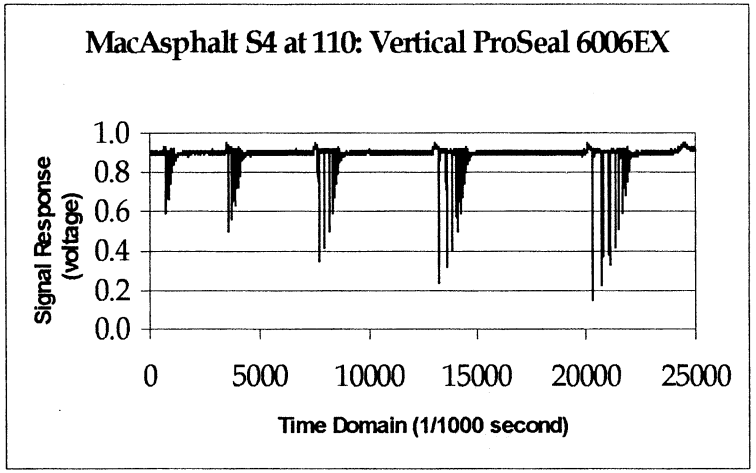
MacAsphalt S4 at 110: Vertical ProSeal 6006EX
Signal Response (voltage)
1.0
0.8
0.6
0.4
0.2
0.0
0
5000
10000
15000
20000
25000
Time Domain (1/1000 second)

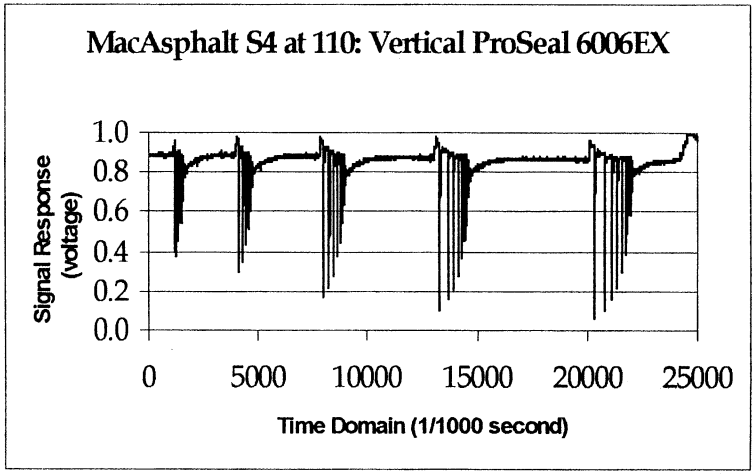
MacAsphalt S4 at 110: Vertical ProSeal 6006EX
Signal Response (voltage)
1.0
0.8
0.6
0.4
0.2
0.0
0
5000
10000
15000
20000
25000
Time Domain (1/1000 second)

October 12-13, 1999 FWD LabView Plots Taken at CSR Rinker Field Test Site

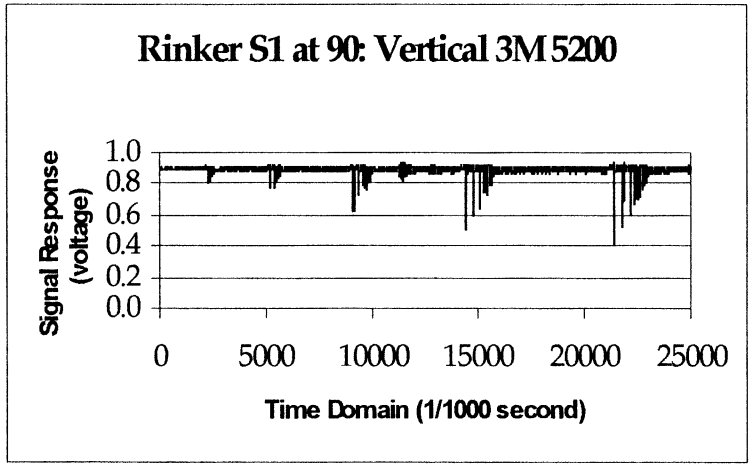

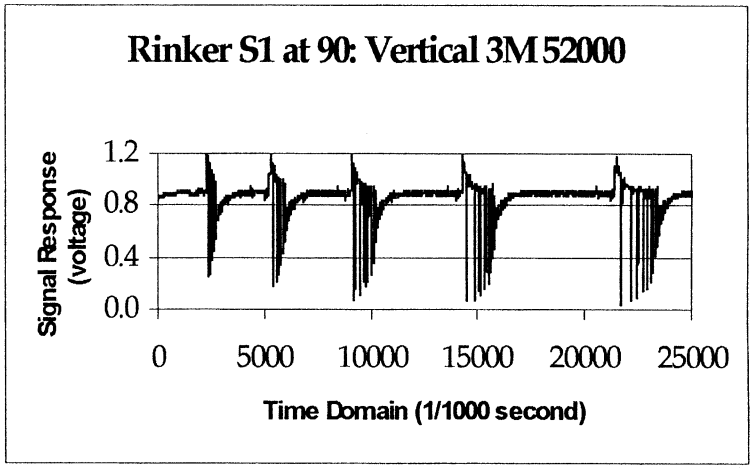

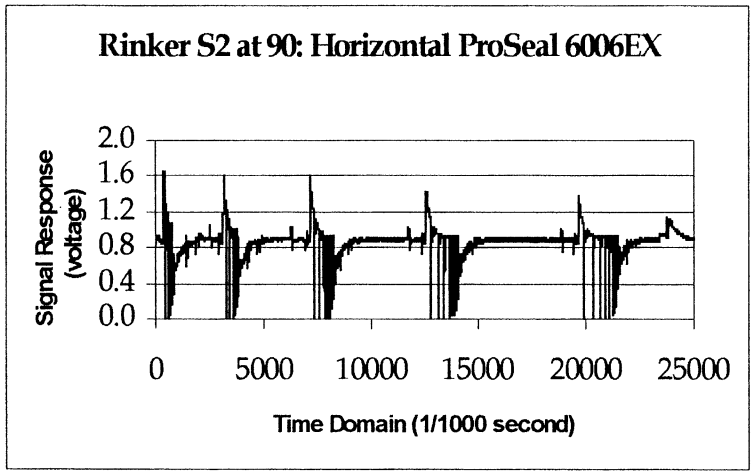

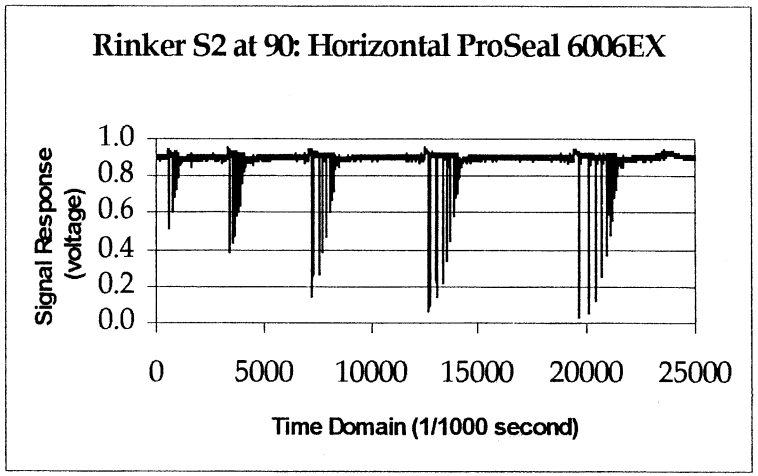

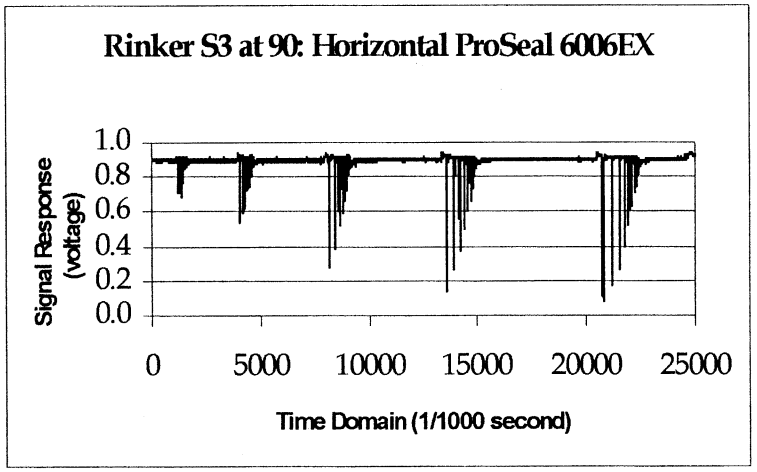
Rinker S3 at 90: Horizontal ProSeal 6006EX
Signal Response (voltage)
1.0
0.8
0.6
0.4
0.2
0.0
0
5000
10000
15000
20000
25000
Time Domain (1/1000 second)

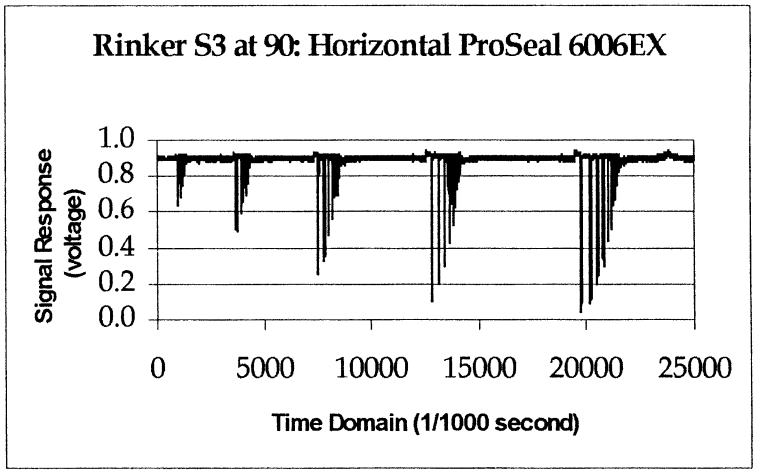
Rinker S3 at 90: Horizontal ProSeal 6006EX
Signal Response (voltage)
1.0
0.8
0.6
0.4
0.2
0.0
0
5000
10000
15000
20000
25000
Time Domain (1/1000 second)

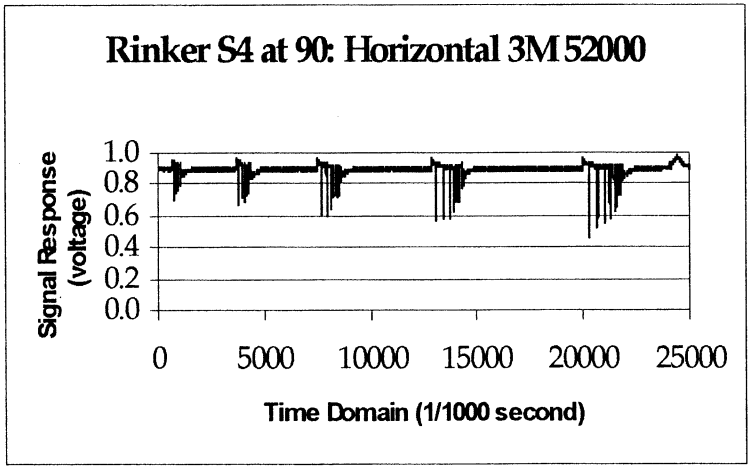
Rinker S4 at 90: Horizontal 3M 52000
Signal Response (voltage)
1.0
0.8
0.6
0.4
0.2
0.0
0
5000
10000
15000
20000
25000
Time Domain (1/1000 second)

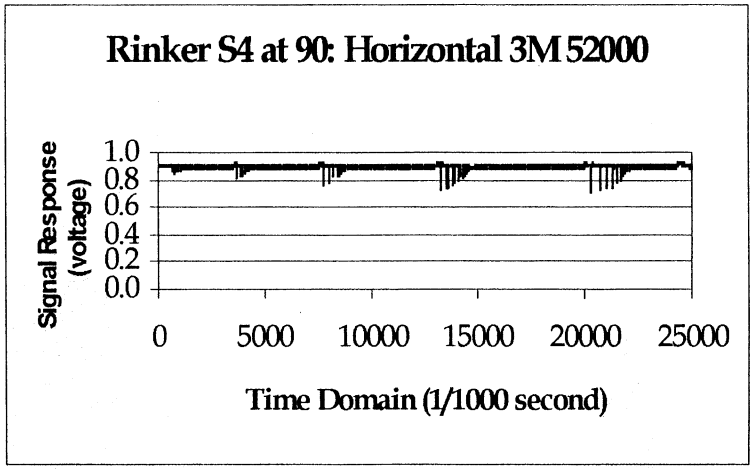
Rinker S4 at 90: Horizontal 3M 52000
Signal Response (voltage)
1.0
0.8
0.6
0.4
0.2
0.0
0
5000
10000
15000
20000
25000
Time Domain (1/1000 second)

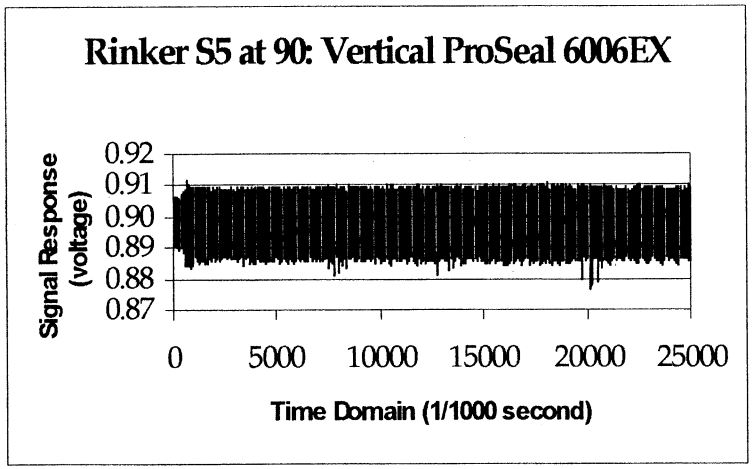
Rinker S5 at 90: Vertical ProSeal 6006EX
Signal Response (voltage)
0.92
0.91
0.90
0.89
0.88
0.87
0
5000
10000
15000
20000
25000
Time Domain (1/1000 second)

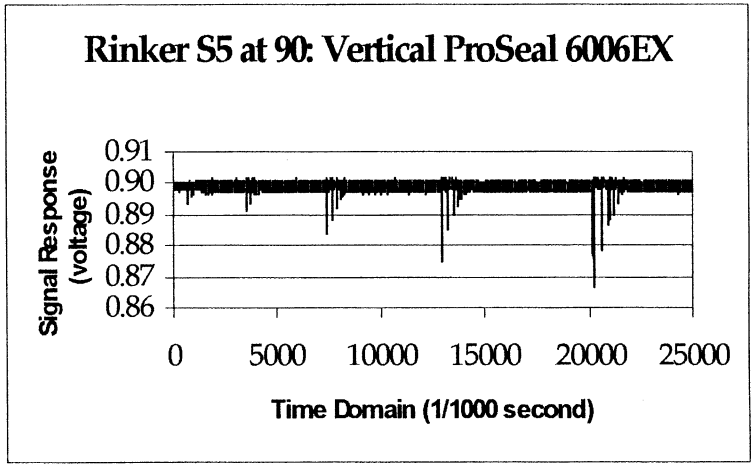
Rinker S5 at 90: Vertical ProSeal 6006EX
Signal Response (voltage)
0.91
0.90
0.89
0.88
0.87
0.86
0
5000
10000
15000
20000
25000
Time Domain (1/1000 second)

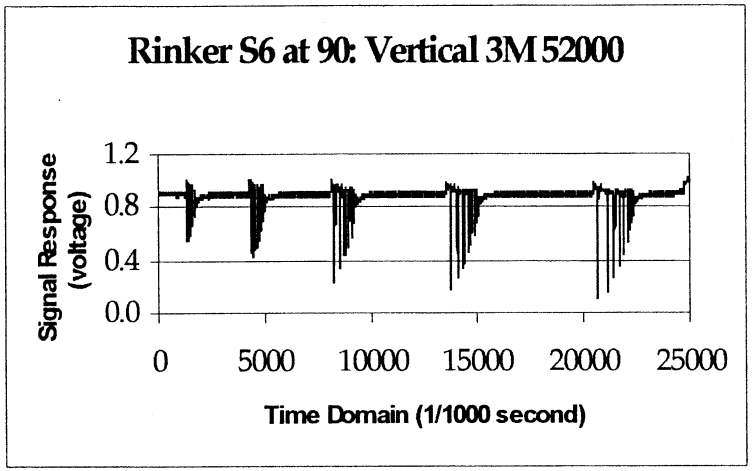
Rinker S6 at 90: Vertical 3M 52000
Signal Response (voltage)
1.2
0.8
0.4
0.0
0
5000
10000
15000
20000
25000
Time Domain (1/1000 second)

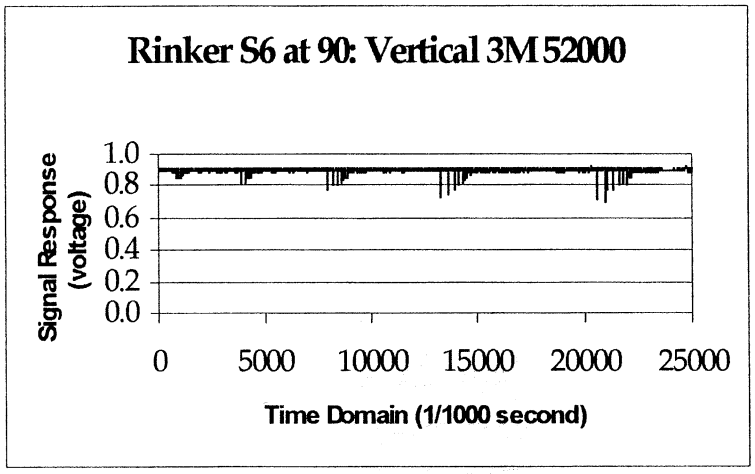
Rinker S6 at 90: Vertical 3M 52000
Signal Response (voltage)
1.0
0.8
0.6
0.4
0.2
0.0
0
5000
10000
15000
20000
25000
Time Domain (1/1000 second)

December 07, 1999 FWD LabView Plots Taken at MacAsphalt Field Test Site

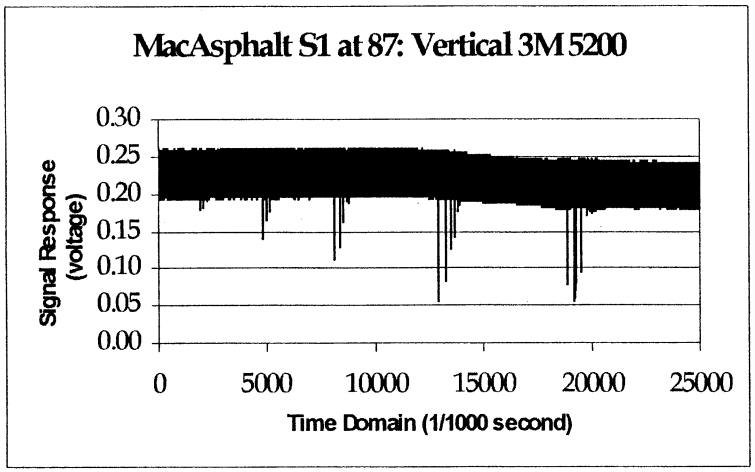

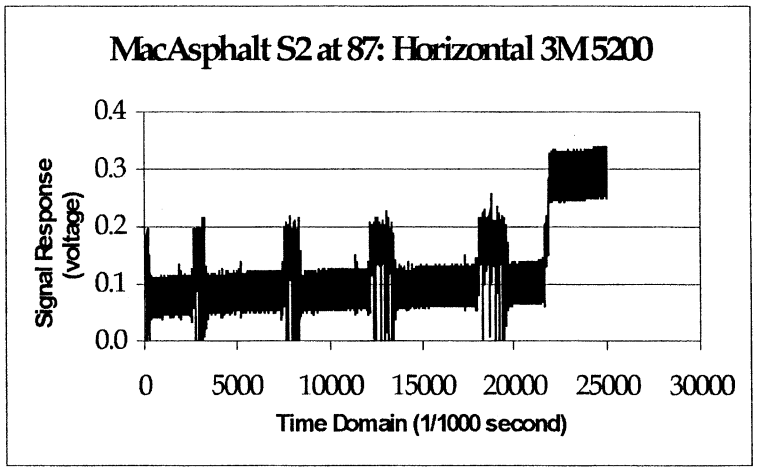

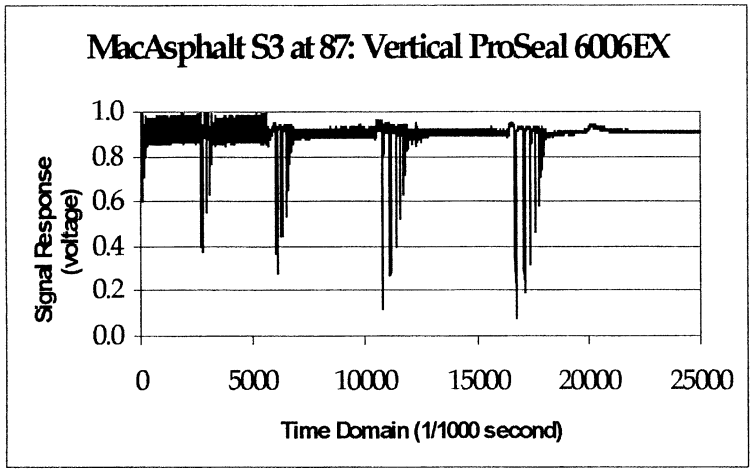

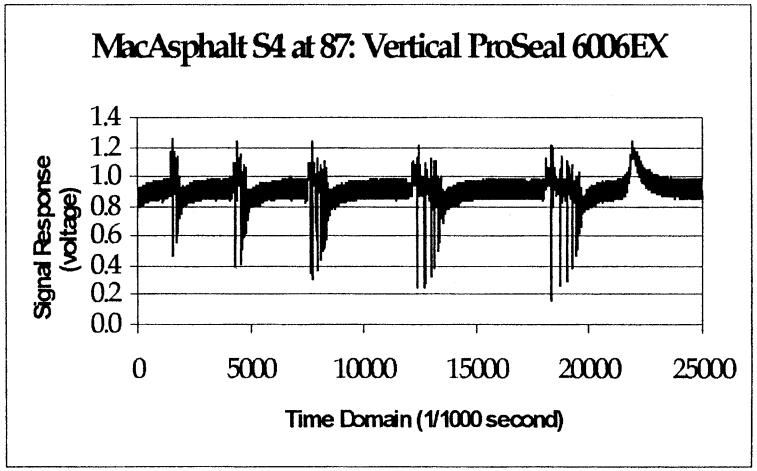

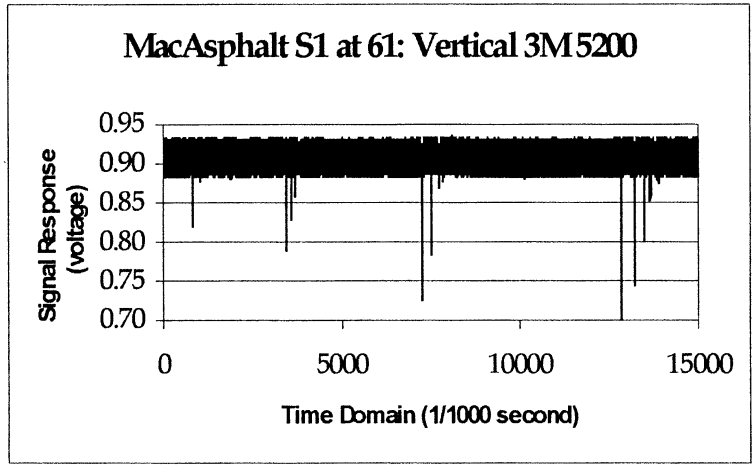
MacAsphalt S1 at 61: Vertical 3M 5200
Signal Response (voltage)
0.95
0.90
0.85
0.80
0.75
0.70
0
5000
10000
15000
Time Domain (1/1000 second)

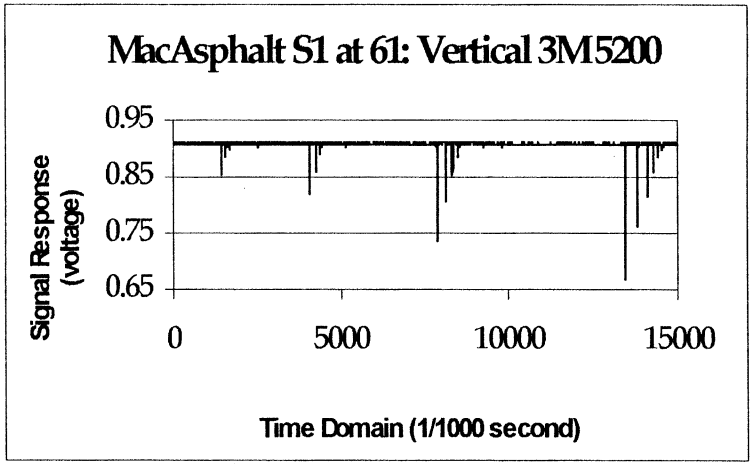
MacAsphalt S1 at 61: Vertical 3M 5200
Signal Response (voltage)
0.95
0.85
0.75
0.65
0
5000
10000
15000
Time Domain (1/1000 second)

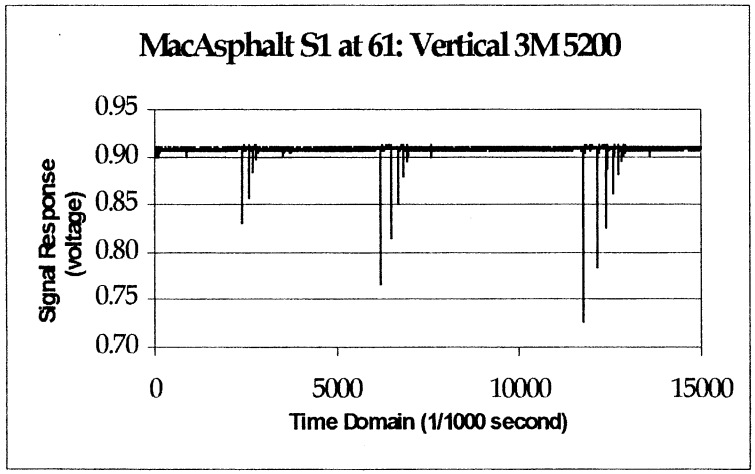
MacAsphalt S1 at 61: Vertical 3M 5200
Signal Response (voltage)
0.95
0.90
0.85
0.80
0.75
0.70
0
5000
10000
15000
Time Domain (1/1000 second)

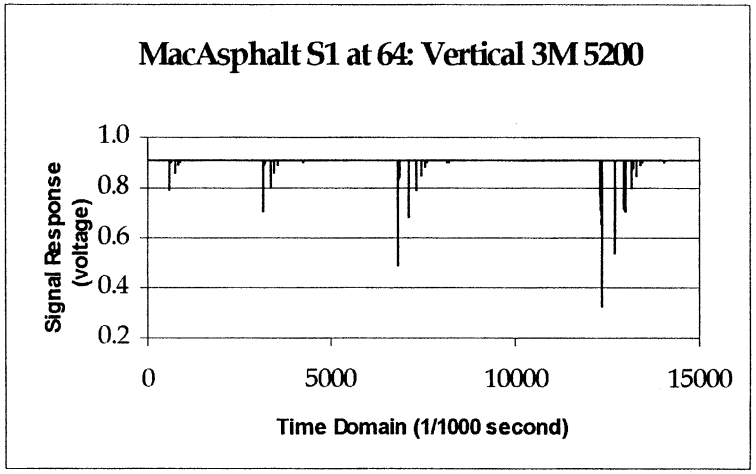
MacAsphalt S1 at 64: Vertical 3M 5200
Signal Response (voltage)
1.0
0.8
0.6
0.4
0.2
0
5000
10000
15000
Time Domain (1/1000 second)

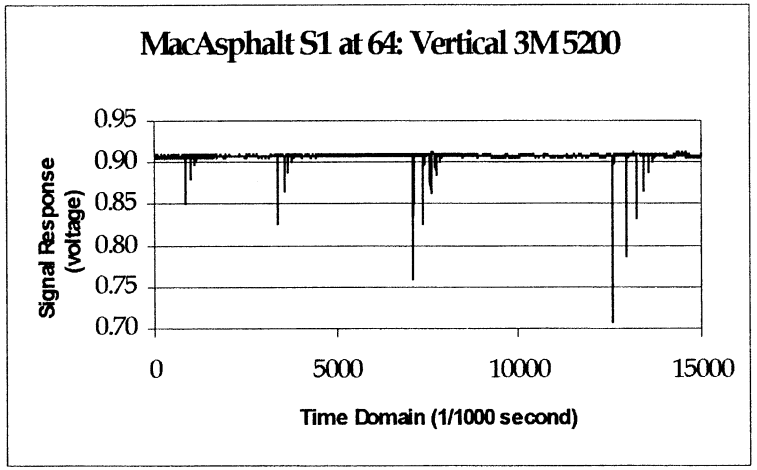
MacAsphalt S1 at 64: Vertical 3M 5200
Signal Response (voltage)
0.95
0.90
0.85
0.80
0.75
0.70
0
5000
10000
15000
Time Domain (1/1000 second)

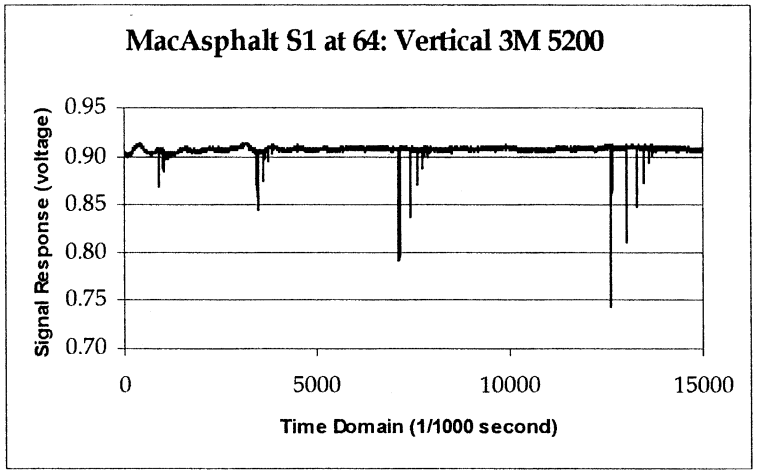
MacAsphalt S1 at 64: Vertical 3M 5200
Signal Response (voltage)
0.95
0.90
0.85
0.80
0.75
0.70
0
5000
10000
15000
Time Domain (1/1000 second)

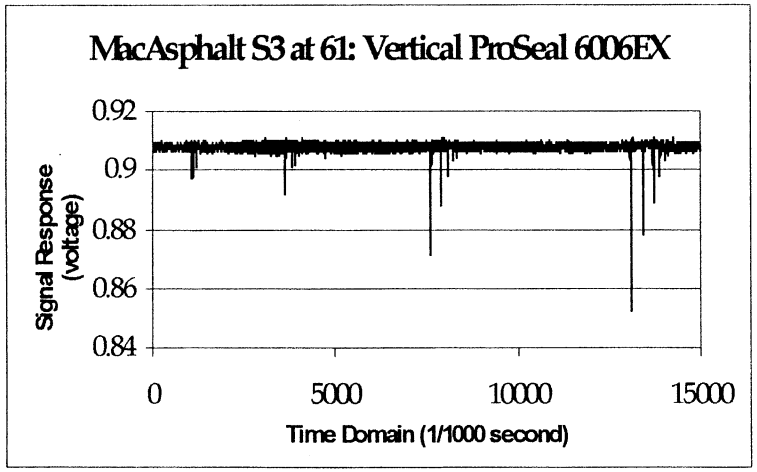
MacAsphalt S3 at 61: Vertical ProSeal 6006EX
Signal Response (voltage)
0.92
0.9
0.88
0.86
0.84
0
5000
10000
15000
Time Domain (1/1000 second)

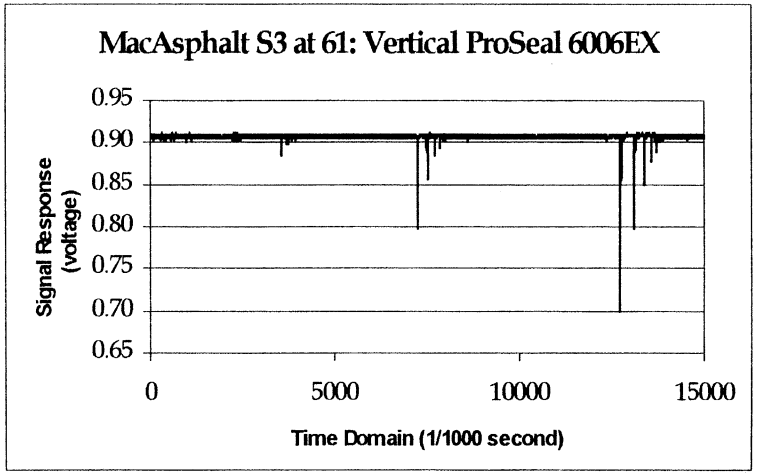
MacAsphalt S3 at 61: Vertical ProSeal 6006EX
Signal Response (voltage)
0.95
0.90
0.85
0.80
0.75
0.70
0.65
0
5000
10000
15000
Time Domain (1/1000 second)

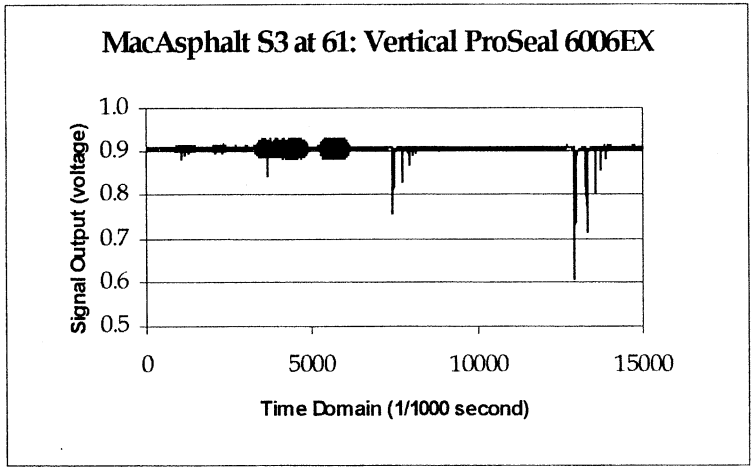
MacAsphalt S3 at 61: Vertical ProSeal 6006EX
Signal Output (voltage)
1.0
0.9
0.8
0.7
0.6
0.5
0
5000
10000
15000
Time Domain (1/1000 second)

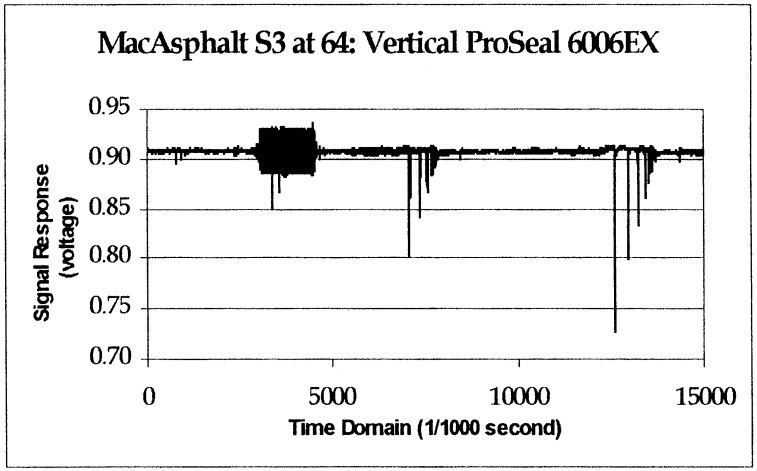
MacAsphalt S3 at 64: Vertical ProSeal 6006EX
Signal Response (voltage)
0.95
0.90
0.85
0.80
0.75
0.70
0
5000
10000
15000
Time Domain (1/1000 second)

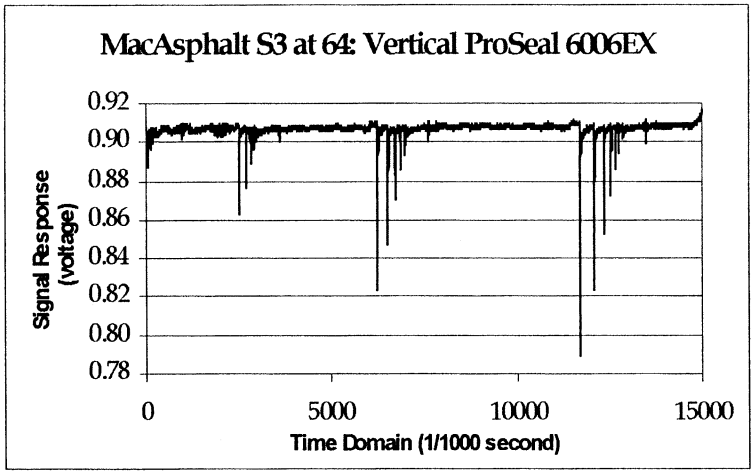
MacAsphalt S3 at 64: Vertical ProSeal 6006EX
Signal Response (voltage)
0.92
0.90
0.88
0.86
0.84
0.82
0.80
0.78
0
5000
10000
15000
Time Domain (1/1000 second)

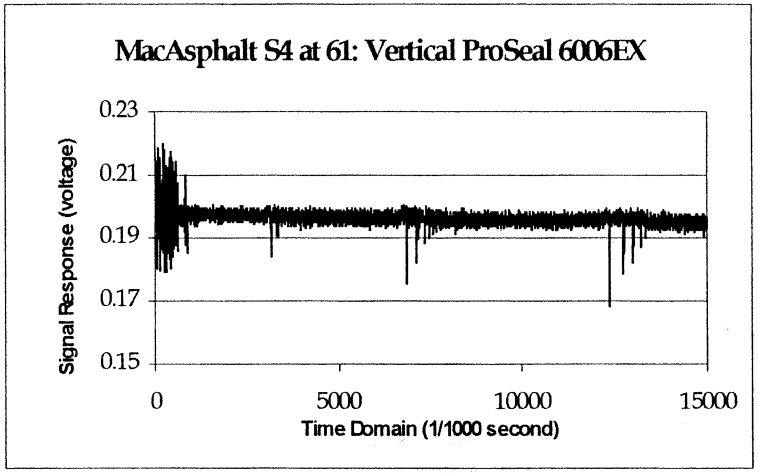
MacAsphalt S4 at 61: Vertical ProSeal 6006EX
Signal Response (voltage)
0.23
0.21
0.19
0.17
0.15
0
5000
10000
15000
Time Domain (1/1000 second)

Deflection Profile for Flexible Pavement Using Falling Weight Deflectometer with Drop Pressure Between 57- 60 psi.

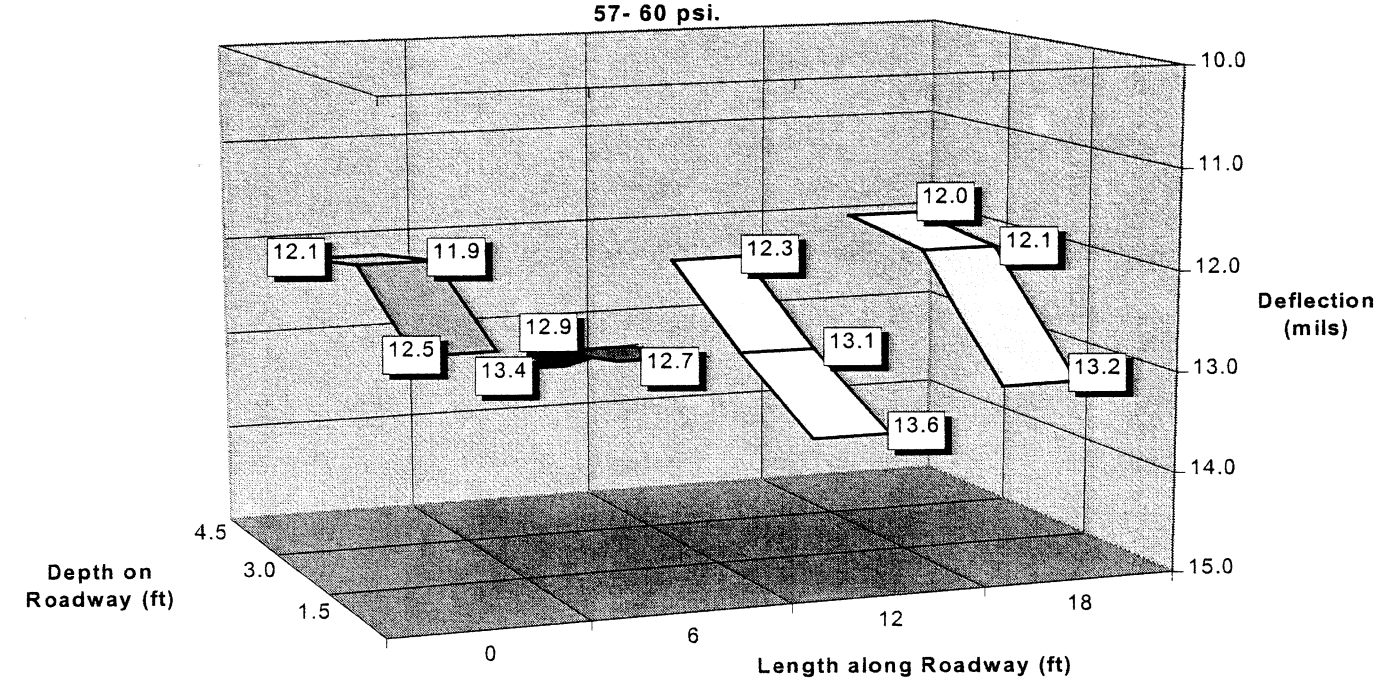

Deflection Profile for Flexible Pavement Using Falling Weight Deflectometer with Drop Pressure Between 74-80 psi.

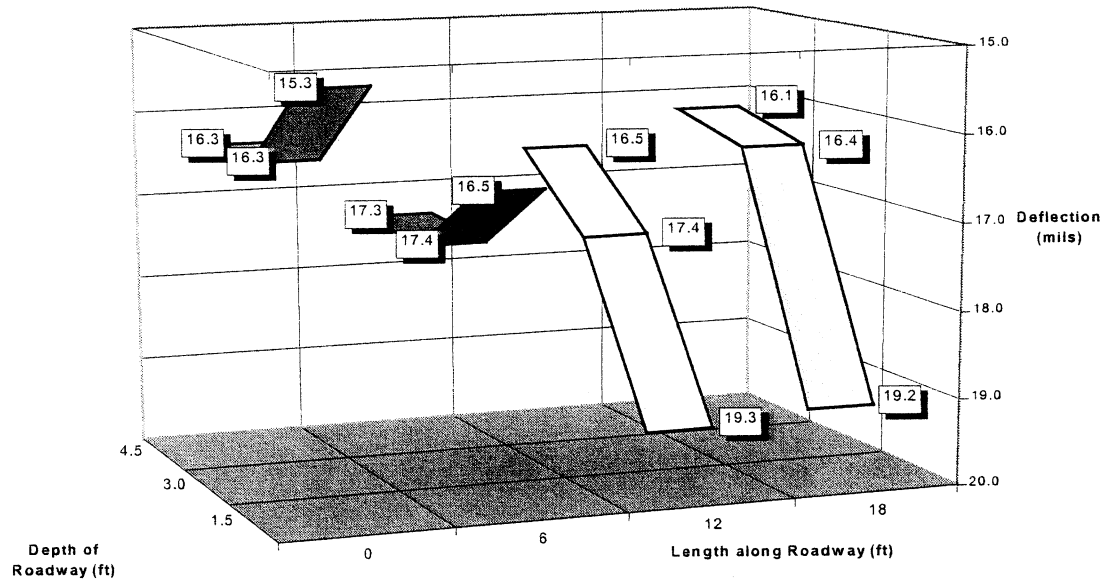

Deflection Profile for Flexible Pavement Using Falling Weight Deflectometer with Drop Pressure Between 132-138 psi.

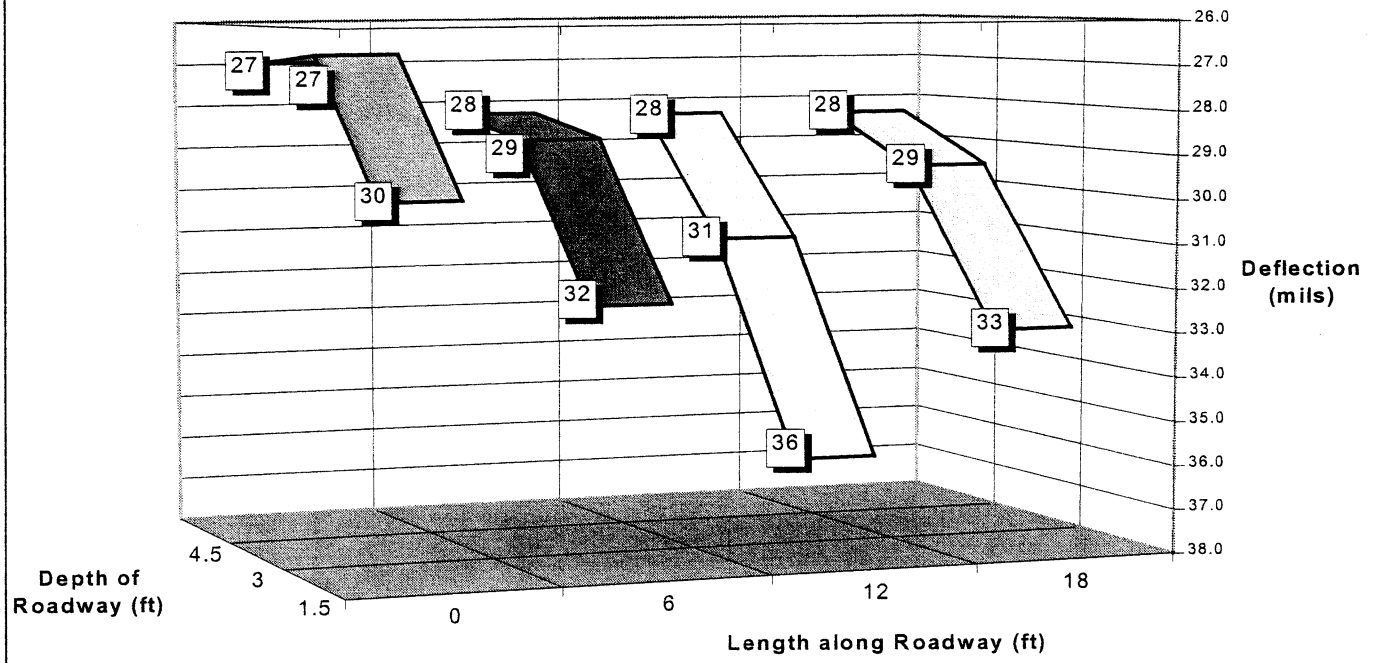

Deflection Profile for Rigid Pavement Using Falling Weight Deflectometer with Drop Pressure Between 57-60 psi.

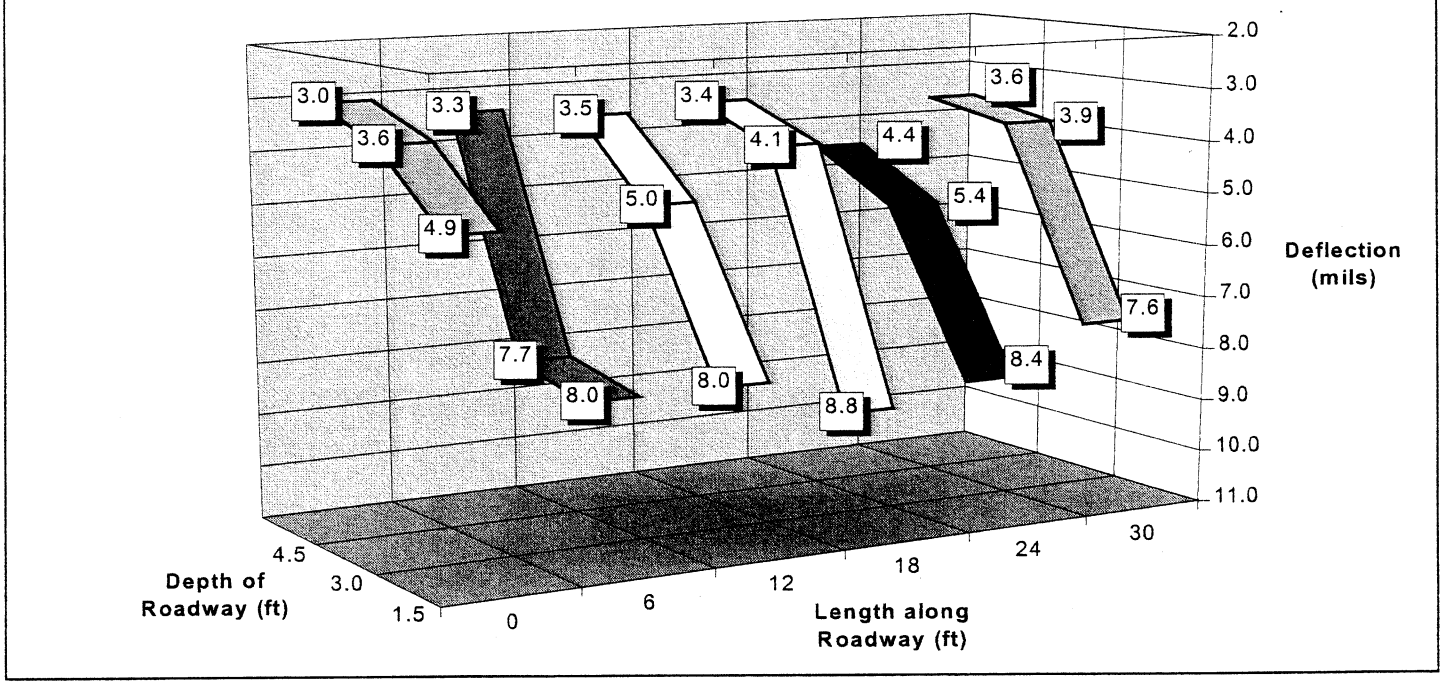

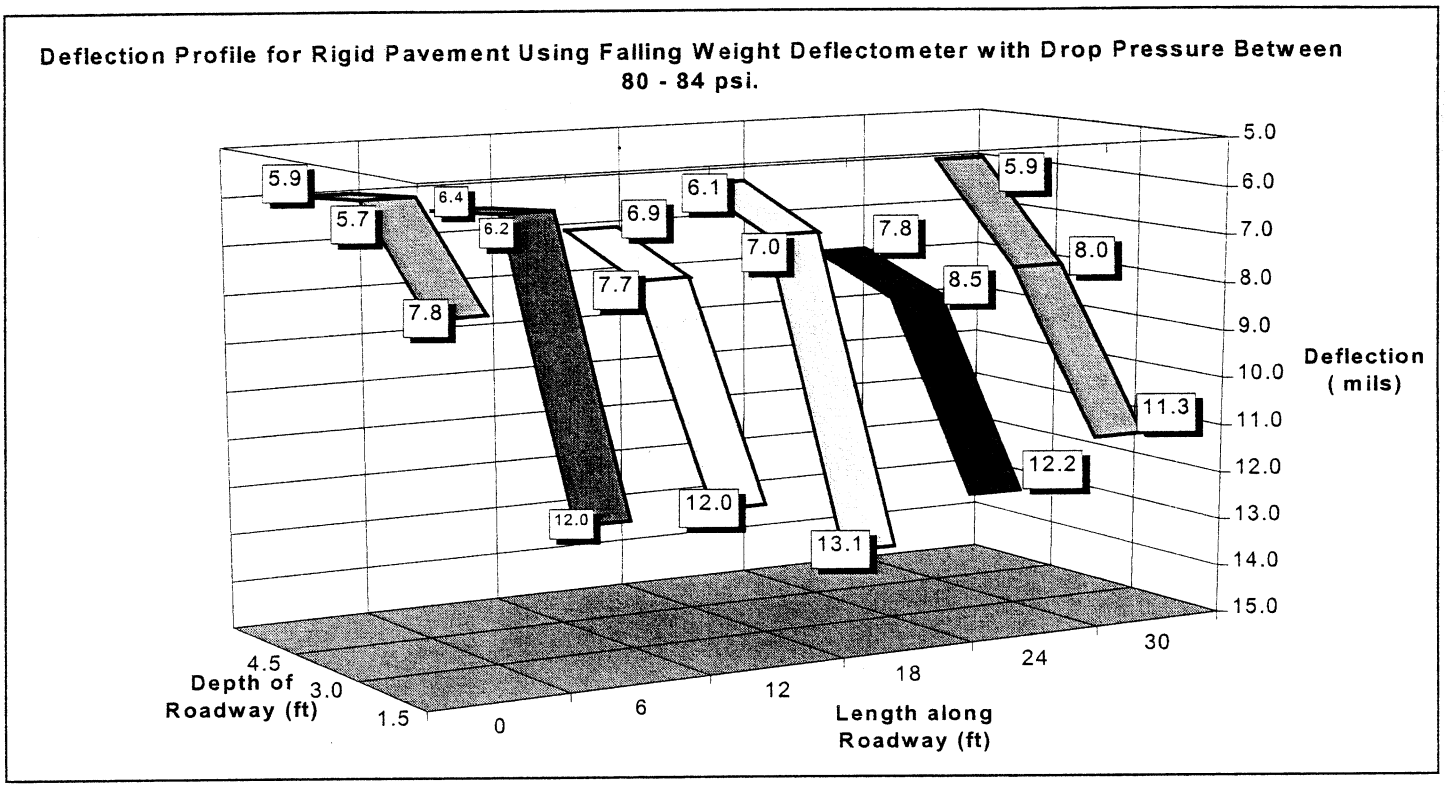
Deflection Profile for Rigid Pavement Using Falling Weight Deflectometer with Drop Pressure Between 80 - 84 psi.
5.9
5.7
7.8
6.4
6.2
12.0
6.9
7.7
12.0
6.1
7.0
13.1
7.8
8.5
12.2
5.9
8.0
11.3
5.0
6.0
7.0
8.0
9.0
10.0
11.0
12.0
13.0
14.0
15.0
Deflection (mils)
4.5
3.0
1.5
Depth of Roadway (ft)
0
6
12
18
24
30
Length along Roadway (ft)

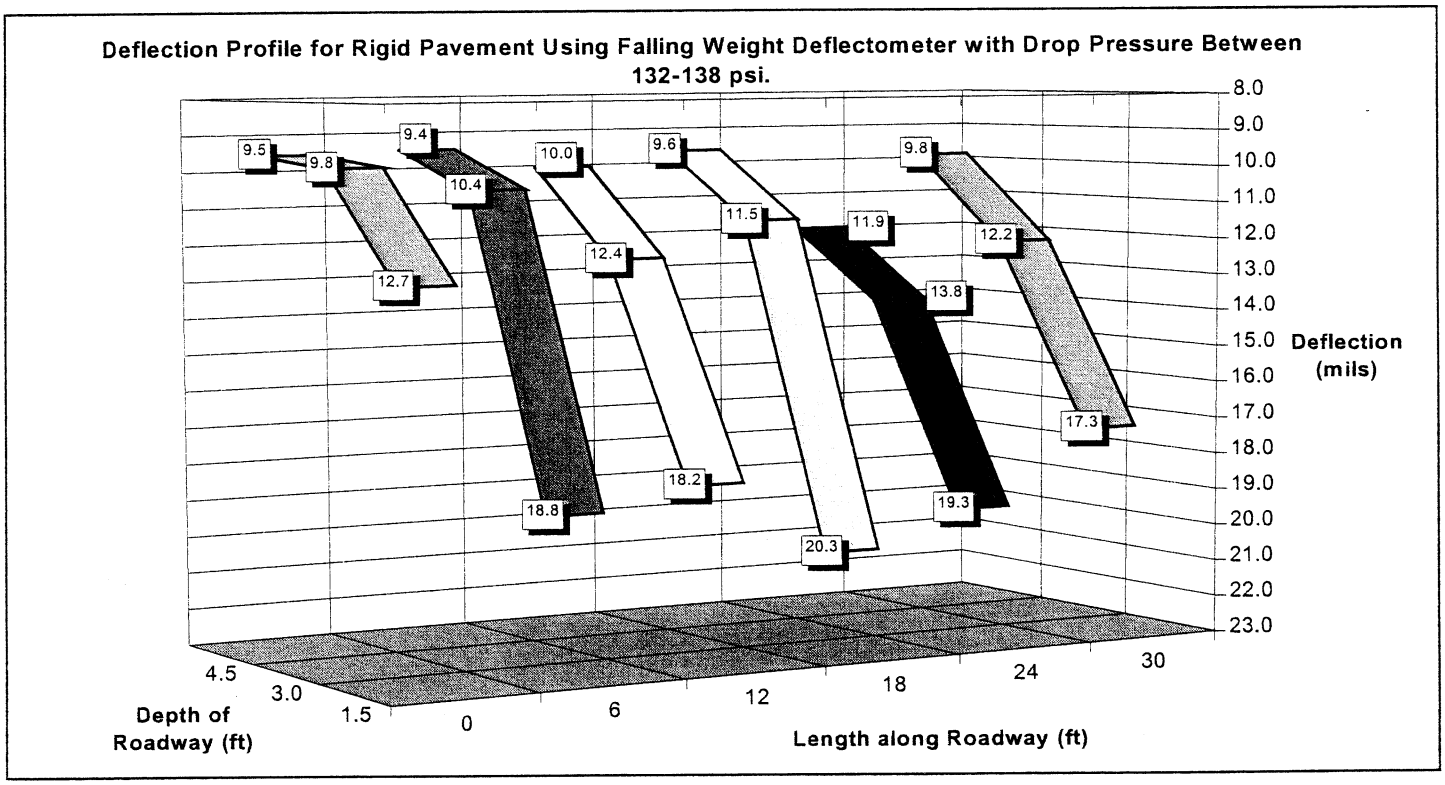
Deflection Profile for Rigid Pavement Using Falling Weight Deflectometer with Drop Pressure Between 132-138 psi.
9.5
9.8
12.7
9.4
10.4
18.8
10.0
12.4
18.2
9.6
11.5
20.3
11.9
9.8
13.8
19.3
12.2
17.3
8.0
9.0
10.0
11.0
12.0
13.0
14.0
15.0
16.0
17.0
18.0
19.0
20.0
21.0
22.0
23.0
Deflection (mils)
4.5
3.0
1.5
Depth of Roadway (ft)
0
6
12
18
24
30
Length along Roadway (ft)

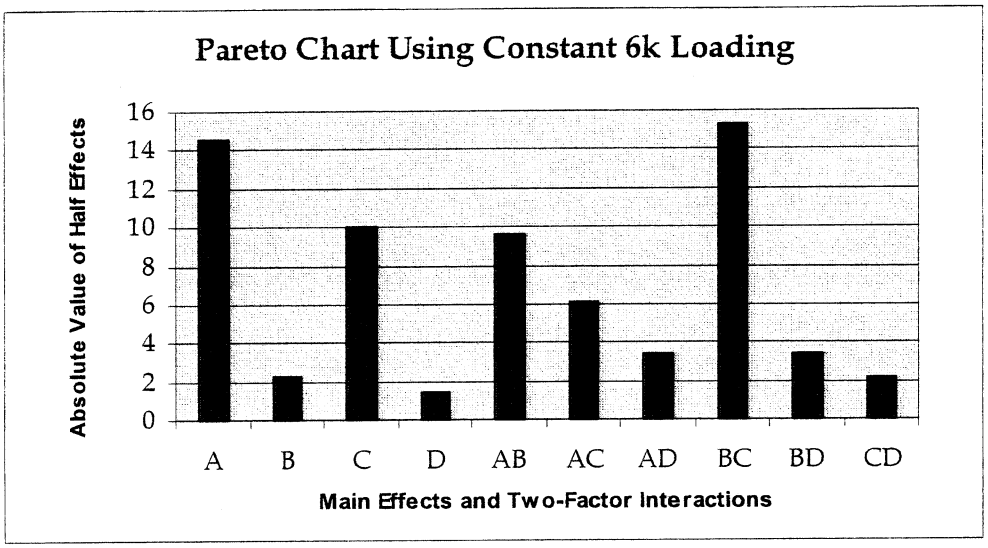

Pareto Chart Showing Absolute Value of Half Effects - 6k Load

A = Pavement Type	C = Sensor Orientation
B = Encapsulant Material	D = Surface Temperature

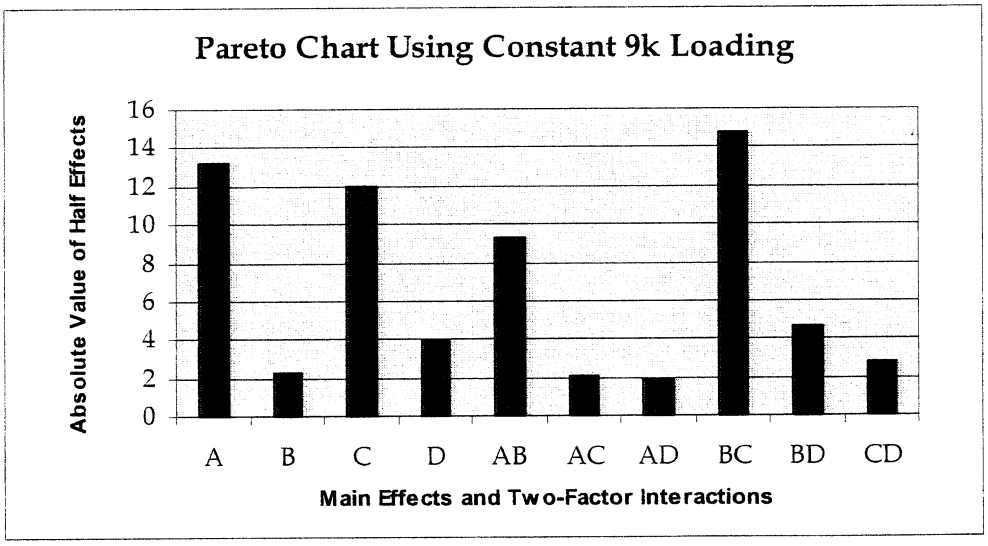

Pareto Chart Showing Absolute Value of Half Effects - 9k Load

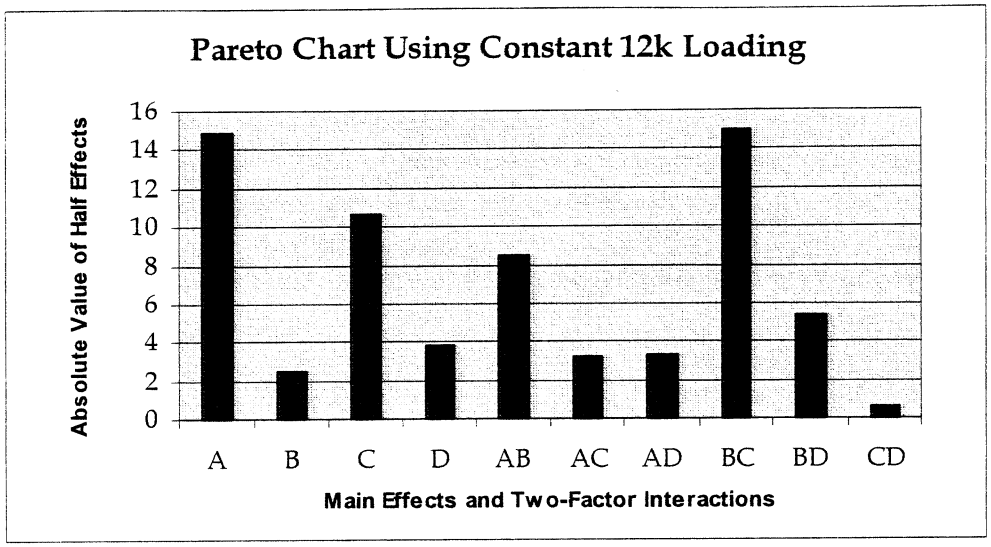

Pareto Chart Showing Absolute Value of Half Effects - 12k Load

A = Pavement Type	C = Sensor Orientation
B = Encapsulant Material	D = Surface Temperature

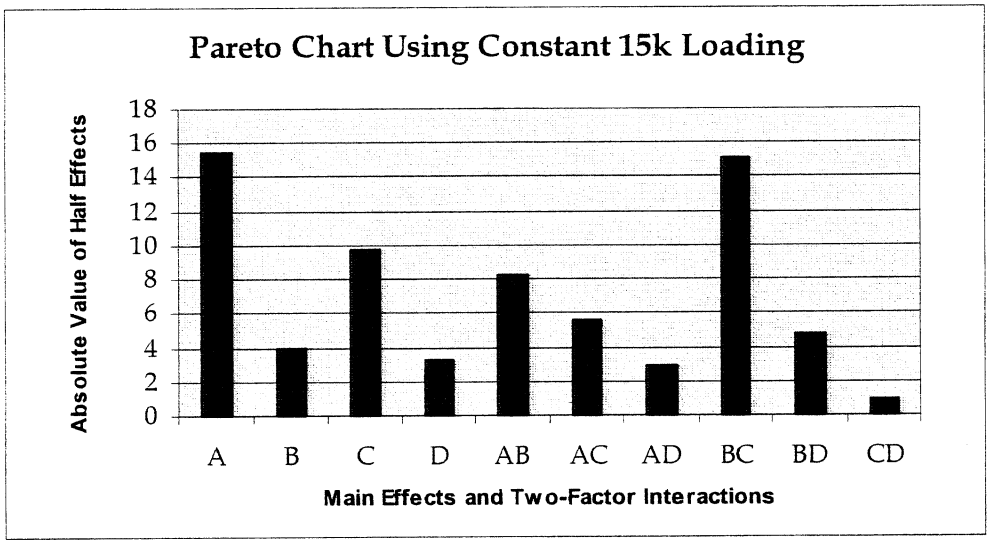

Pareto Chart Showing Absolute Value of Half Effects - 15k Load